



HAL
open science

Designing and building an ultracold Dysprosium experiment : a new framework for light-spin interaction

Davide Dreon

► **To cite this version:**

Davide Dreon. Designing and building an ultracold Dysprosium experiment : a new framework for light-spin interaction. Physics [physics]. Université Paris sciences et lettres, 2017. English. NNT : 2017PSLEE036 . tel-01571420v2

HAL Id: tel-01571420

<https://theses.hal.science/tel-01571420v2>

Submitted on 5 Jun 2018

HAL is a multi-disciplinary open access archive for the deposit and dissemination of scientific research documents, whether they are published or not. The documents may come from teaching and research institutions in France or abroad, or from public or private research centers.

L'archive ouverte pluridisciplinaire **HAL**, est destinée au dépôt et à la diffusion de documents scientifiques de niveau recherche, publiés ou non, émanant des établissements d'enseignement et de recherche français ou étrangers, des laboratoires publics ou privés.

THÈSE DE DOCTORAT
de l'Université de recherche
Paris Sciences Lettres – PSL Research University

préparée à l'École normale supérieure

Conception et construction
d'une expérience de dysprosium ultrafroid :
un nouveau cadre pour l'interaction lumière-spin

*Designing and building an ultracold Dysprosium experiment:
a new framework for light-spin interaction*

École doctorale n°564 Physique en Ile de France
Spécialité: Physique Atomique et Moléculaire Optique

Soutenue par **Davide Dreon**
le 12 Juillet 2017

dirigée par **Jean Dalibard**
& **Sylvain Nascimbène**

Composition du Jury :

M. Olivier Dulieu
LAC - Université Paris-Sud 11
Président du jury

Mme. Francesca Ferlaino
IQOQI - Université de Innsbruck
Rapporteuse

M. Thierry Lahaye
CNRS - Institut d'Optique
Rapporteur

M. Olivier Gorceix
LPL - Université Paris 13
Examinateur

M. Jean Dalibard
LKB - Collège de France
Directeur de thèse

M. Sylvain Nascimbène
LKB - École normale supérieure
Co-directeur de thèse



Résumé / Abstract

DANS CE travail de thèse, je présente la construction d'une nouvelle expérience pour la production de gaz ultra froids de dysprosium. En tirant parti de la structure électronique à couche incomplète de ces atomes, nous visons à la réalisation de champs de jauge synthétiques, qui pourront conduire à l'observation de nouvelles phases (topologiques) de la matière. Le couplage du spin atomique avec le champ lumineux, plus efficace que pour des atomes alcalins, permettra d'atteindre des régimes d'interactions fortes qui restent, jusqu'à présent, hors de portée expérimentale. J'adapte des protocoles existants pour la réalisation de champs de jauge dans le cas de Dysprosium, en tenant compte de son grand spin électronique ($J = 8$ dans l'état fondamental). En outre, le dysprosium a le plus grand moment magnétique parmi les éléments stables, et il est donc le meilleur candidat pour l'étude des gaz dipolaires. Je détaille le dispositif expérimental que nous avons construit et comment nous effectuons le piégeage et le refroidissement du dysprosium. Nous étudions en détail le comportement du piège magnéto-optique, qui est réalisé sur la transition d'intercombinaison $^1S_0 \leftrightarrow ^3P_1$. La raie étroite et le grand spin rendent l'opération du piège très complexe. Néanmoins, je montre que sa compréhension devient assez simple dans le régime où le nuage se polarise spontanément en conséquence de la combinaison des forces optiques et gravitationnelles. Enfin, je décris les dernières étapes du transport optique et de l'évaporation, ce qui conduira à la production d'un gaz dégénéré.

IN THIS thesis I present the construction of a new experiment producing ultra cold gases of Dysprosium. Using the favourable electronic structure of open-shell lanthanide atoms, we aim at the realisation of laser-induced synthetic gauge fields, which could lead to the observation of novel (topological) phases of matter. The coupling of the atomic spin with the light field, improved with respect to alkali atoms, opens the possibility to explore strongly interacting regimes that were up to now out of experimental reach. I adapt existing protocols for the implementation of gauge fields to the case of Dysprosium, taking into account its large electronic spin ($J = 8$ in the ground state). Moreover, Dysprosium has the largest magnetic moment among the stable elements, and is the best candidate for the study of dipolar gases. I describe the experimental setup that we built and how we perform the trapping and cooling of Dysprosium. We study in detail the behaviour of the magneto-optical trap, which is performed on the $^1S_0 \leftrightarrow ^3P_1$ intercombination line. The narrow linewidth and the large spin make the trap operation quite challenging. Nevertheless, I show that its understanding becomes quite simple in the regime where the cloud spontaneously polarises due to the interplay of optical and gravitational forces. Finally I describe the last steps of optical transport and evaporation, which will lead to the production of a degenerate gas.

Contents

I	Why Dysprosium Quantum Gases?	
1	Thesis Introduction	2
2	Dipolar Quantum Gases	7
2.1	From Contact to Long-range Interaction	8
2.2	Feshbach Resonance	10
2.3	Dipolar Bose-Einstein Condensates	12
2.3.1	Mean-Field Model	12
2.3.2	Thomas-Fermi Approximation	13
2.3.3	Elongation of Dipolar Clouds	14
2.4	Condensate Instabilities	15
2.4.1	Phonon Instability	16
2.4.2	Geometrical Stabilisation	16
2.5	Dipolar Relaxation	19
2.5.1	Spin-flip Interaction	19
2.5.2	Dipolar Scattering	20
2.5.3	Effect of Particle Statistics	24
3	Off-Resonant Light-Atom Interaction	26
3.1	AC Stark Interaction	26
3.2	Light Shift Operator	28
3.2.1	Tensor Polarisability	29
3.2.2	Light Polarisation and Fictitious Fields	32
3.3	Alkali Atoms	34
3.3.1	Line Structure	34
3.3.2	Raman Coupling	35
3.4	Dysprosium	37
3.4.1	Line Structure	37
3.4.2	Light Shift Anisotropy at 626 nm	39
3.4.3	Raman Coupling	41
4	Towards Synthetic Gauge Fields	43
4.1	Light-induced Gauge Fields	44
4.1.1	Hamiltonian and Eigenstates	44
4.1.2	Geometric Potentials	46

4.2	Implementation with Dysprosium	47
4.2.1	Experimental Scheme	48
4.2.2	Expected Results	49
4.2.3	Tensor Laser Coupling	51
4.2.4	Experimental Requirements	52

II

A New Experiment on Ultra-cold Dysprosium

5	Experimental Setup	55
5.1	Vacuum System	55
5.1.1	High Vacuum Part	56
5.1.2	Ultra-High Vacuum Part	57
5.2	Laser System for Near-Resonant Light	58
5.2.1	Blue Laser Setup	59
5.2.2	Red Lasers Setup	60
5.3	Magnetic Field Control	64
5.4	Data Acquisition	64
5.5	A Slow Jet of Dysprosium Atoms	66
5.5.1	Effusion Oven	66
5.5.2	Transverse Cooling	68
5.5.3	Zeeman Slower	69
6	Narrow Line MOT	73
6.1	Magneto Optical Trapping of Dysprosium	73
6.1.1	MOT Loading	75
6.1.2	Compressed MOT	76
6.2	MOT Position	77
6.3	Spin Composition	79
6.3.1	Rate Equation Model	79
6.3.2	Stern-Gerlach Imaging	81
6.4	Temperature	83
6.5	Size and Density	86
6.6	Inelastic Light Assisted Collisions	88
6.6.1	Radiative Redistribution	88
6.6.2	Calculation of the two-body loss coefficient β	89
7	Towards Dysprosium BEC	93
7.1	Optical Dipole Trap	93
7.1.1	Trap Frequencies	94
7.1.2	Dipole Trap Loading	95
7.2	Frequency Measurements	96
7.2.1	Sloshing and Breathing Modes	96
7.2.2	Parametric Excitations	98

7.3	Optical Transport	98
7.3.1	Experimental Setup	99
7.3.2	Accelerating Potential	99
7.3.3	Transport Efficiency	102
7.4	Crossed Dipole Trap	102
7.5	Evaporative Cooling	104
7.5.1	The Cooling Process	104
7.5.2	Evaporation with Longitudinal Multimode Laser	106
7.5.3	Second Crossed Trap	107
8	Conclusion and Perspectives	110

III

Appendices

A	Dysprosium	113
A.1	Basic Properties	113
A.2	Atomic Spectrum	114
A.2.1	Laser Cooling Transitions	115
A.2.2	Hyperfine structure	116
A.2.3	Laser spectroscopy	116
A.3	Magnetic Properties	117
A.3.1	Magnetic Moment	118
A.3.2	Zeeman Effect	118
B	Imaging Dysprosium Clouds	120
B.1	Absorption Imaging	120
B.1.1	Dark-frame subtraction	121
B.1.2	Cross section corrections	122
B.2	Thermometry	123
B.2.1	Thermal Clouds	123
C	Notes on the Experiment Database	125
C.1	Database	125
C.1.1	Structure of the database	125
C.2	Data Analysis	127
C.2.1	Image fitting	127
C.2.2	Data processing	128
	Bibliography	139

Remerciements

ÉCRIRE des remerciements plus sincères que ceux qui suivent est impossible. Au cours des années passées j'ai connu des gens merveilleux et je souhaite à tous d'avoir la chance de rencontrer des collègues et des amis pareils.

Tout d'abord, je remercie sincèrement l'équipe BEC de m'avoir accueilli pour mon doctorat et en particulier mes directeurs de thèse, Jean et Sylvain.

Je pense que Jean est le professeur que tout le monde devrait avoir. Dans ta salle de cours, dans ton bureau ou à la cafeteria, je ne me souviens pas d'une seule conversation avec toi qui n'a pas été agréable ou qui ne m'a pas appris quelque chose. Ta passion est un vrai modèle d'inspiration pour tout le groupe.

Sylvain, c'était un plaisir d'être ton premier thésard. Tu es un chef excellent, toujours avec les bonnes idées sur les démarches à suivre pour aller dans la bonne direction. C'était très agréable de te voir nous aider au laboratoire, même pour faire des travaux ennuyants comme assembler la chambre à vide, bobiner, couper le Dysprosium en miettes, ou pour faire d'autres passe-temps plus ou moins relaxants. Je te souhaite des années amusantes avec l'expérience et ce que suivra.

Je souhaite également remercier beaucoup Fabrice et Jérôme. Parler avec vous était toujours très agréable et vos conseils avisés sur n'importe quel sujets ont été toujours utiles.

Entre collègues, on ne partageait pas seulement des montures de miroirs, mais surtout des conversations agréables, la pause de l'après-midi, les discours au déjeuner ou un apéritif le soir à la sortie du laboratoire. Pendant ma thèse j'ai eu énormément de chance parce que beaucoup de mes collègues sont aussi de bons amis, ce qui n'est pas souvent le cas.

Je vais commencer avec l'équipe Dysprosium et le premier remerciement va naturellement à Wilfried. Nous avons commencé à assembler l'expérience dans les locaux futuristes à l'ENS, où perdre des vis est si facile! (n'est-ce pas?) Les pauses consacrées aux «bobo talks» sont encore inégalées, c'était un plaisir de t'avoir comme collègue.

Je remercie évidemment Tian, auto-proclamé *the Lazy One*. Durant l'année qu'il a passée avec nous, il a eu l'occasion de partager son modèle de philosophie, dont les fondements sont gravés dans les «Tian's facts» pour les prochaines générations de thésards.

Je remercie Mama Chayma. La plus grande partie de ma thèse, je l'ai partagée avec toi (*oh-my-glob!*). On a eu beaucoup de mauvaise chance, mais on a mis de côté une bonne dose de karma pour le futur. J'avoue que charcuter des trucs à l'IPG a son style, mais maintenant c'est toi l'«ancienne» de la manip, sois une reine sage!

Un grand merci à Leonid. C'était cool de travailler avec toi ou d'écouter des histoires bizarres sur ton pays. Nos talents de maçons, qui nous ont servi à colmater les fenêtres

du laboratoire, resteront *in secula seculorum*.

Le N°1 de mes stagiaires préférés restera toujours Thomas, dit Tom Tom, est depuis cette année officiellement le dauphin de la manip. J'aurais aimé avoir partagé plus de temps au laboratoire, mais je dois partir et donc -u root -p est à toi. Rappelle toi : «with great power comes great responsibility».

Enfin je souhaite bonne chance à Alexandre, qui a rejoint l'équipe pendant ma rédaction (donc des interactions sociales réduites au minimum), mais sera sûrement bien accueilli comme thésard.

Parmi les autres collègues, je commence avec un merci à Camille, dit Petit Chaton^a. Nous avons commencé nos thèses en même temps et nous avons peut-être partagé plus de choses ensemble qu'avec d'autres. C'était cool d'avoir un jumeau mais, enfin, les gens ne vont plus nous confondre.

Je remercie Andrea^b, ou bien Gianandvea Mavia, dit Meno un Quarto, pour m'avoir aidé à garder un haut niveau d'*italianité* dans l'équipe et pour l'hospitalité chaleureuse de Votre Seigneurie chaque fois que je me suis rendu à Vôte château (celui à Pavmentiev, pas celui au Vomevo).

Je remercie également pour leur sympathie les deux autres membres du groupe historique des trois mousquetaires «the Sodium dream team»^c, Vincent et Tilman.

Merci à Karina, parce que les bonbons mexicains m'ont permis de survivre une bonne semaine.

Je remercie Laura, la dernière highlander de l'ENS, pour avoir été le meilleur exemple de force de volonté pour tout le monde (notamment quand on a découvert que Rb2 allait mourir).

Je remercie Jean-Loup, *alias* Jean-Paul Banana, d'avoir su être un collègue «très agréable». Tu gardes une «bonne ambi» au labo, sinon ce serait «l'enfer».

Raphaël (Rb), j'ai vu que tu aimes aussi décorer les bureaux des collègues de façon créative (une démarche souvent trop peu appréciée). Après mon départ, je te laisse cette responsabilité.

Tom, parce que on t'aime bien même si tu n'arrives pas à terminer un arancino !

Monika, parce que même si tu as passé peu de temps chez nous, tu as introduit des changements radicaux (la cafetière moka !).

Katharina, pour avoir partagé la magique salle S18 et pour les seaux d'eau fraîche sur la terrasse.

Je remercie Manel, *alias* El Spicy Cœurdepierre, même s'il n'a jamais su me dire où se trouve la bibliothèque ou quelle heure il est. «I'll see you again in 25 years».

Raphael (Yb), *a.k.a.* R.A.F., l'Actuel Administrateur-Adjoint de l'Association Amicale des Amateurs d'Andouillette Authentique de l'AURA (9A).

Elisa, parce que tu transpires la Toscane à travers tous tes pores, et ça c'est bien (peut-être), pour les mini saucissons de sanglier et pour ton hospitalité.

Les anciennes membres de l'équipe que j'ai rencontré lors de mon arrivée en stage : Christof, Lauriane, Rémi et spécialement Matthias, Alexandre (et Quentin plus tard), avec qui on a partagé les beaux moments^d du déménagement et reconstruction au Collège de France.

^aet d'autres surnoms que je ne peux pas partager ici...

^bsauf pour l'idée débile de toi et Camille de voir des films tristes lors de la rédaction de la thèse.

^cpeut-être «Sodium beer team»

^dje plaisante, c'était affreux

Le group d'Alexei^a, dit «the climbing team». C'était un plaisir de partager du temps avec Alexei (lui même), Nico et Kilian, *alias* «the handsome» (bien joué Anna) ou «not-the-postdoc-you-want-but-the-postdoc-you-deserve», qui répandait sa bonne humeur dans tout l'étage et qui nous a heureusement permis de faire encore plus de blagues d'italiens vs. allemands (super drôles since '45)!

Je remercie l'ensemble du personnel du Laboratoire Kastler Brossel : son directeur Antoine Heidmann, les autres collègues, les services techniques et administratifs, en particulier Thierry et Audrey. Je remercie beaucoup Pascal et l'équipe de l'atelier mécanique, qui sont vraiment exceptionnels.

Également je remercie les services du Collège de France, son administrateur Alain Prochiantz, et un grand merci à Carmen, notre formidable administratrice.

Je remercie le bureau de l'association Chadocs pour le bon travail qu'on a fait ensemble pour mélanger un peu plus les équipes au Collège de France. En particulier je remercie énormément Florent, le meilleur responsable PR qu'on puisse souhaiter et la superbe vice-presidente Veronica. Et bonne chance au nouveau bureau pour le futur de l'association.

En dehors du labo, je remercie tous les amis qui m'ont accompagné pendant ces années parisiennes, pour avoir fait en sorte que cette ville devienne mon chez moi. Partir sera difficile, vous allez tous me manquer beaucoup.

En particulier, je suis reconnaissant à la «mafia» italienne. Les premiers remerciements seront pour le nucleus original : Chiara, *alias* Pulcina, et Giulio, pour sa gentillesse (seulement Chiara, pas toi Giulio, toi t'es un beau)^b et pour avoir instauré les traditionnels «déjeuners italiens», souvent dans 16 m² d'appart maximum.

Giacomo, *a.k.a.* Sir Jack, pour avoir été la note musicale dans l'équipe italienne.

Lara, *alias* Svetly, parce que ça fait plaisir d'avoir une amie architecte qui amène un peu de sens esthétique. Et pour la mythique et providentielle assiette d'œufs battus.

Oscar pour m'avoir hébergé à plusieurs reprises, spécialement pour les vacances détente avant ma soutenance dans sa magnifique ville natale (et on en revient toujours à la même question...). Visitez la Campanie!^c

Luca Alberto Rizzo, dit Paisà, parce que je suis d'accord avec ton jury de thèse : t'es un bon garçon. Visitez la Campanie!^c

Letizia, pour son esprit toujours joyeux qui met de bonne humeur.

Merci à Stefania, pour les conseils entomologiques et à Andrea (Scotti).

Maria, dite la Reina de las croquetas (true story, vous devriez essayer, elles sont délicieuses), parce que t'es inimitable.

Je remercie beaucoup Mattia, d'avoir su être un bon coloc et une riche cave à musique et à concerts. Enfin quelqu'un avec qui partager la passion pour le reggae^d.

Un grand merci à Mariane, *a.k.a.* MJC, parce que comme membre acquis dans l'équipe t'as amené de la bonne humeur à la cantine et pendant les pauses baby foot, parce que t'étais une voisine super cool, et pour une liste infinie de beaux moments qu'on a partagés (notamment à défier notre faible volonté face à la bouffe).

Je remercie toute l'équipe phénoménale des Restos du Cœur de Denfert (merci

^aje ne sais pas si vous avez un nom officiel

^b♥

^cCette déclaration est à titre gratuit, je ne reçois pas d'argent de la part de la région de Campanie (visitez la Campanie).

^dJe plaisante. On déteste le reggae.

Mariane de m'avoir recruté, merci Marc de m'avoir officialisé). Les mercredis avec vous vont me manquer.

Je remercie les amis de l'université, même s'il est vraiment difficile de se revoir souvent, ça fait toujours plaisir.

Last but not least je remercie ma mère de m'avoir accueilli «mieux que dans un hôtel» (*sic*) au cours des derniers jours de rédaction, quand ma journée se déroulait devant un écran d'ordinateur, et merci pour le magnifique pot de thèse (le San Daniele restera *ad perpetuam rei memoriam*), à mon père pour l'avoir arrosé et merci à mon frère et à ma grand-mère qui ont accompagné ma mère pendant le voyage de l'espoir.

Pour vous toutes et tous je souhaite le meilleur et un futur heureux.

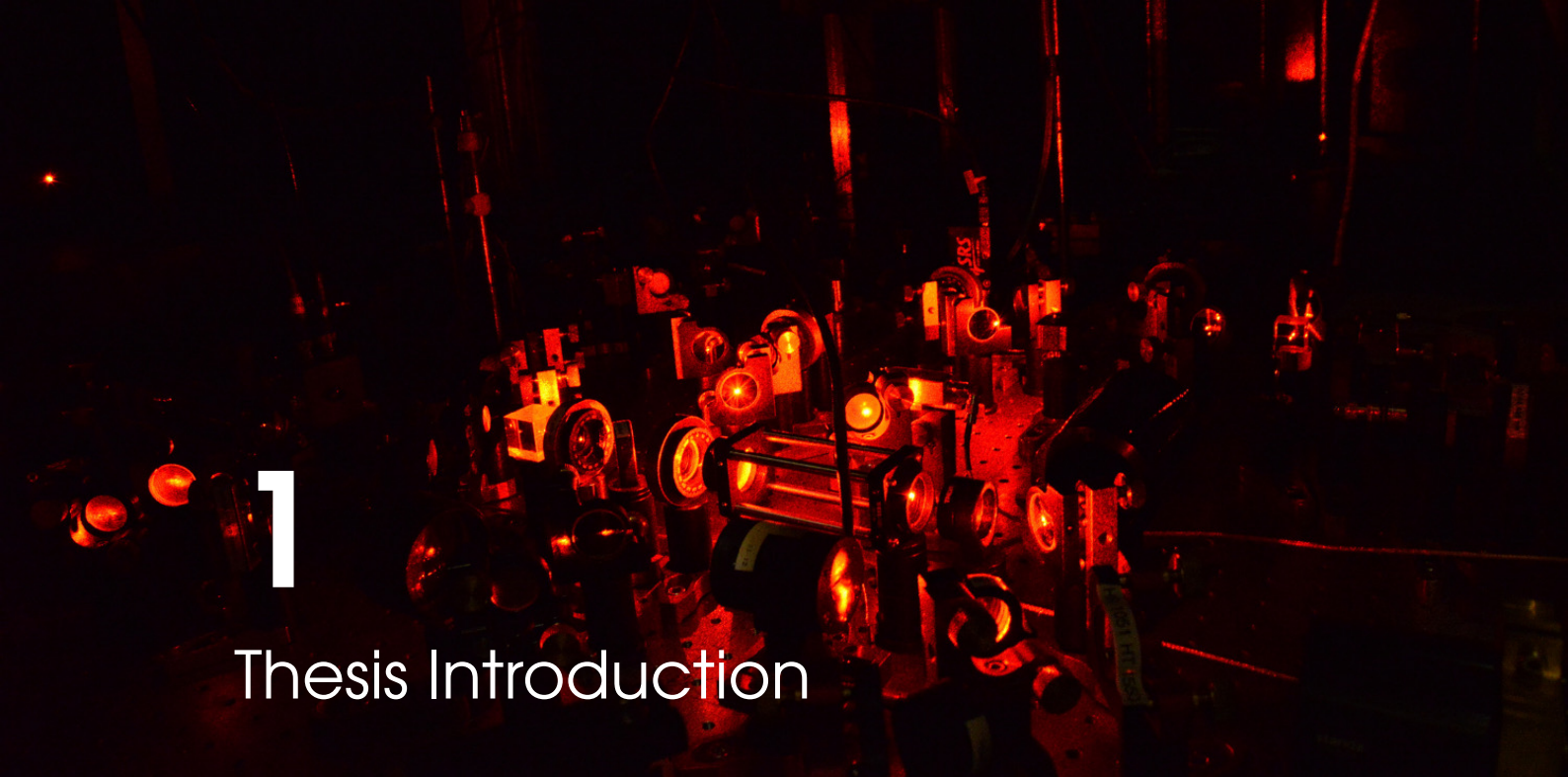
Merci.

Davide



Why Dysprosium Quantum Gases?

1	Thesis Introduction	2
2	Dipolar Quantum Gases	7
2.1	From Contact to Long-range Interaction	
2.2	Feshbach Resonance	
2.3	Dipolar Bose-Einstein Condensates	
2.4	Condensate Instabilities	
2.5	Dipolar Relaxation	
3	Off-Resonant Light-Atom Interaction ..	26
3.1	AC Stark Interaction	
3.2	Light Shift Operator	
3.3	Alkali Atoms	
3.4	Dysprosium	
4	Towards Synthetic Gauge Fields	43
4.1	Light-induced Gauge Fields	
4.2	Implementation with Dysprosium	



1

Thesis Introduction

"[...] we sent the atoms rolling, like so many marbles, and the kid whose atom went farthest won the game. When you made your shot you had to be careful, to calculate the effects, the trajectories, you had to know how to exploit the magnetic fields and the fields of gravity, otherwise the ball left the track and was eliminated from the contest."

Cosmicomics
Italo Calvino

"[...] the Reason, a greedy, grasping thing, is only satisfied when it succeeds in chaining some cosmic geyser, or harnessing an atomic swarm."

The Cyberiad
Stanislaw Lem

THE THESIS work I am about to present deals with ultracold atoms physics, a research field whose roots are found in the second half of past century. Already in the 1950's, experiments on matter control at the atomic scale were quite advanced, although it was still science fiction in popular culture^a. In the first experiments on optical pumping, light produced by gas lamps was used to manipulate the internal (electronic) state of the atoms. Then, the invention of the laser [2] boosted the experimental capabilities. Soon physicists were able to extend the control of an atom's internal state to its external state, affecting its motion. Lasers were used to trap and cool atomic gases down to the microkelvin regime, far beyond any previous reachable limit and much below the coldest temperatures found in nature [3, 4, 5]. From the principles of quantum mechanics, one knows that matter exhibits stronger wave-like properties the lower the temperature is. If we consider a gas of atoms, where each one is described by a wave of size given by the thermal wavelength $\lambda_{dB} \sim T^{-1/2}$, by lowering the temperature enough, λ_{dB} grows

^aNote that the novels I quoted above were written in the same years when Richard Feynman held his famous lecture "There's Plenty of Room at the Bottom" in which he foretold that "ultimately - in the great future - we can arrange the atoms the way we want; the very atoms, all the way down!" [1]

and will eventually become comparable with the distance between the atoms. Below a critical temperature, the waves of the single (bosonic) particles interfere with each other constructively, and give rise to a macroscopic matter wave, the famous Bose-Einstein condensate (BEC). This state of matter had been for long a holy grail of physics, from the time of its theoretical prediction dating back to the 1920's [6, 7]^a. The experimental rush to achieve the critical temperature ended successfully in 1995, when for the first time BEC was observed in dilute ultra cold gases [8, 9]. The following studies on condensates focused on their undulatory nature. In analogy to phenomena observed in light waves, BECs interfere [10], exhibit long range coherence [11] and can be used to create atom "lasers" [12, 13].

Atoms of the same species are by definition identical. In the quantum world, a system of non-interacting indistinguishable particles will occupy a discrete set of energy levels, with a distribution given by the quantum statistics of the particles and the temperature. Considering the statistic, matter exists only in two different flavours: bosons and fermions. Boson statistics do not limit the particle number that can fit a single energy state. For example, a laser is made by bosons (photons) occupying a single energy mode. Bose-Einstein condensation appears when the lowest energy state is macroscopically populated^b. The condition is different for identical fermions, as Pauli exclusion principle prevents them from occupying the same state. When temperature approaches absolute zero, fermions occupy the ladder of available energy states starting from the bottom, up to a maximum value (the Fermi energy). This state of matter, called a degenerate Fermi gas, has many realisations in nature^c. Using laser cooling techniques, it has been realised in atomic gases shortly after the achievement of the first BEC [14, 15, 16].

From Single Particle to Many-Body Physics

Due to the extreme control of the system parameters, ultra cold Bose and Fermi gases became rapidly an ideal platform to explore degenerate states of matter, brought to the understanding of many other research fields in physics. Since the 21st century, novel experimental methods helped the creation of a multitude of complex, strong interacting systems [17].

Interparticle interactions can be controlled both in magnitude and in sign using Feshbach resonances [18], which allowed to access strong interacting regimes for bosons [19] and fermions [20]. In Fermi gases, Feshbach resonances led to the observation of the crossover from a BEC of weakly bound molecules to a superfluid of Cooper pairs [21, 22], as described by the Bardeen-Cooper-Schrieffer theory of superconductors.

Optical manipulation using lasers gives a tremendous control on the geometry and the dimensionality of the system. Confining a Bose gas in a two-dimensional trap, the famous Berezinskii-Kosterlitz-Thouless transition was observed [23] and in 1D traps the Tonks-Girardeau regime was realised [24, 25]. Also, three-dimensional "box" potentials have been implemented to study more text book models of BEC [26].

^aSuperfluid ^4He is partially condensed. Nevertheless, it is a liquid, in which the atoms are strong interacting. The original BEC theoretical prediction (which considers ideal bosonic gases) can not be applied to ^4He . Moreover, the condensed fraction in ^4He is a minority part of the total number of particles.

^bIn contrast with lasing, that is a non-equilibrium process, Bose-Einstein condensation can occur just by lowering the temperature T .

^cThe electrons in a ordinary metal and white dwarfs stars are well known examples.

Using the interference pattern between two or more laser beams, one can create periodic light structures where the atoms arrange themselves, the so-called optical lattices, in a similar fashion of electrons in crystalline solids. This correspondence is a practical realisation of Feynman's famous idea of a quantum computer [27]. Making use of ultra cold atoms, one could realise an ideal copy of the system to study, where to perform "*an exact simulation, that [...] will do exactly the same as nature.*" [28]. In the past years, optical lattices allowed to implement a lot of interesting condensed matter models, such as the Mott insulator phase for bosons [29] and fermions [30] or spin magnetism on a lattice [31, 32]. In recent years, the "large" separation between lattice sites allowed to observe the fluorescence light of individual atoms using standard optical lenses. These "quantum microscopes" offer evocative images, since for the first time is possible to see atoms arranging in lattice structures^a and they permitted to directly probe and manipulate strongly correlated phases of matter. Although the first microscopes studied Bose gases [33, 34], nowadays Fermi gases are also available [35, 36].

Not Only Alkali

In the early 2000's, experimental advances led to degenerate gases of the whole (stable) alkali metal group [37, 38] and of two-electron atoms (1S_0 in the ground state) like Calcium [39], Ytterbium [40] and Strontium [41]. The last two elements gain interest in recent years for the realisation of ultrastable optical lattice clocks [42, 43].

In 2005 Bose-Einstein condensation of Chromium was achieved [44]. It was the first laser cooled atom with a large electronic spin (7S_3 in the ground state), a property that gives Chromium gases a strong magnetic character. Other elements interact mainly via short-range isotropic potentials. On the contrary, the magnetic interaction between atoms, called dipole-dipole interaction, is anisotropic and long-ranged, and thus strongly modifies the behaviour of the gas. Succeeding studies shown the appearance of pure magnetic phenomena in degenerate dipolar gases, such as magnetostriction [45], anisotropic collapse of the BEC [46], spin relaxations [47].

In recent years other atomic species appeared in the dipolar gases panorama: open-shell lanthanides. The incomplete electronic f -shell gives rise to a huge spin in the ground state of these elements, which enhances the dipolar interactions in the gases even more than in Chromium. In particular, Dysprosium (which is the element we consider in this thesis) is found to be naturally in a configuration where the dipolar interaction overcomes in strength the contact interaction. In addition to Dysprosium, the lanthanides Erbium, Thulium and Holmium have also been successfully laser cooled [48, 49, 50, 51]. Magneto-optical trapping of the former two elements were further improved adopting intercombination transitions, like the ones used for two-electron atoms traps [52, 53]. Moreover, Dysprosium and Erbium still remain the only open-shell lanthanides brought to degeneracy, both for bosonic isotopes [54, 55] and for fermions [56, 57]. Their strong dipolar character led to the observation of new manifestations of the magnetic nature of degenerate gases, such as the Rosensweig instability in a quantum gas of Dysprosium [58], typical of the behaviour of ferrofluids, or the Fermi surface deformation in a degenerate Erbium gas [59].

^aI believe that "vision" should involve optical light. Other microscopy techniques (Field Ion Microscopy, Scanning Tunnel Microscopy, Transmission Electron Microscopy, ...) provide images of similar beauty, and better spatial resolution, but one does not "see" atoms *stricto sensu*.

Dysprosium and Gauge Fields

During this thesis, I constructed a new experiment on ultra cold gases of Dysprosium. As a result of its intriguing properties, Dysprosium is now becoming a trend and many experiments are currently under construction. Having three bosonic and two fermionic isotopes with large natural abundance, Dysprosium makes possibility to work with both degenerate gases, separately or in mixtures. By virtue of its extremely large spin (5I_8 in the ground state), Dysprosium is the ideal platform to explore dipolar physics. In this thesis, we are more interested in another aspect, namely its interactions with light, which is strongly spin dependent, and in its peculiar spectrum, which is populated by plenty of electronic transitions having a narrow linewidth.

Despite atoms are neutral, there exist different experimental procedures to simulate the physics of charged particles. The narrow transitions of Dysprosium are found to be ideal for the case of light induced gauge fields [60]. In the past years, alkali atoms have been used by several groups to simulate synthetic gauge fields [61, 62, 63, 64]. Moreover, the momentum transfer to atoms moving in the synthetic fields made possible the realisation of synthetic spin-orbit coupling, both in BECs [65, 66, 67] and in degenerate Fermi gases [68, 69, 70].

The phase diagram of a spin-orbit coupled Bose gases is very rich [71, 72] and leads to novel phases of matter such as superfluids with stripe order [73] or more exotic states resulting from the combination of spin-orbit coupling and dipolar interactions [74, 75]. Strong spin-orbit coupling is also an essential ingredient to prepare cold atoms in new (topological) states of matter, like exotic quantum Hall effects or topological insulators [76, 77]. Topological states recently gained a lot of experimental and theoretical interest, as testified by the past year's Nobel prize, since their interest is not only limited to their appealing quantum properties but could also be useful in quantum computation [78].

Currently, a great experimental challenge is the limited strength of light-induced gauge fields in alkali atoms, due to the large scattering rate from the excited states^a. As a result of alkali small fine structure splitting, the heating rate can not be reduced at will without decreasing at the same time the strength of interactions, and the strongly coupled regime remains out of reach. On the contrary, strong coupling will be much more accessible using Dysprosium [79], opening the doors to a whole new domain of physics yet unexplored.

Thesis Outline

The manuscript is organised in two separate parts. I give here a brief overview of the chapters that will follow. In the first part of this thesis I review some well established theory on dipolar physics and light atom interaction, which are essential to understand the physics of ultra cold Dysprosium gases, and I adapt to the case of Dysprosium some existing protocols for the generation of light-induced gauge fields. I justify in detail the interest in using Dysprosium and what are the differences with respect to most common atomic species. I will particularly stress the contrast with alkali atoms.

Chapter 2 In this chapter I briefly introduce the properties of dipolar cold gases. The subject is quite vast, so I focus more on the problematics that directly affect our experiment. In particular, the dipole-dipole interaction induces an instability in a degenerate gas which can be counteracted by a right choice of the aspect ratio of

^aA different experimental approach to generate gauge fields relies on periodic modulation of the atomic clouds. In this case the heating is induced by the modulation itself.

the trapping potential. Moreover, the dipolar interactions do not conserve the total spin. As I describe, isothermal spin-flip collisions induce heating and population decay in atomic clouds;

Chapter 3 Dysprosium has a large spin in its ground state and a rich spectrum of electronic excitations. In this chapter I explain how these characteristics affect Dysprosium's interaction with off-resonant light. I show that the light shift is strongly dependent on the light polarisation and the electronic spin state, and I give an example of the anisotropy of an optical trap working on the 626 nm transition. I will also explain that there are indeed advantages in using Dysprosium instead of alkali atoms for two-photon transitions;

Chapter 4 I will present a simple scheme that we could implement in our setup to generate synthetic gauge fields, using Raman transitions between ground state levels. Our goal will be to simulate the physics of a charged particle in a strong gauge field, exploiting the reduced scattering rate of Dysprosium atoms to enter strong coupling regimes.

The second part describes our experimental approach to produce ultra cold gases of Dysprosium.

Chapter 5 This chapter describes in detail the experimental apparatus, which was built from scratch during this thesis. I present our vacuum systems and our cooling lasers, which work on a broad transition at 421 nm (used for slowing and imaging) and on a narrow transition at 626 nm (used for the magneto-optical trap and for the Raman coupling). Then, I present our experimental procedure to obtain a cold jet of gaseous Dysprosium;

Chapter 6 I describe our magneto-optical trap. Open-shell lanthanides, such as Dysprosium, exhibit a quite rich physical behaviour, due to their large electronic spin and the narrow linewidth associated to the cooling transition. In particular, a spontaneous spin polarisation happens in the far detuned regime, as a result of the balance between gravitational and optical forces. I report our detailed study on the trap parameters, which was subject of a publication in [80];

Chapter 2 I describe the conservative traps and the experimental procedures to further cool Dysprosium atoms. The atoms are first optically transported from the MOT chamber to a glass cell. Then we increase the phase space density with forced evaporative cooling in a crossed dipole trap. I report our first results on the evaporation and the on going experimental work.

Appendices deal with more technical arguments that can be useful in the laboratory.

Appendix A I give some Dysprosium parameters which are useful to calibrate laser frequency locks on atomic spectra and to calibrate the magnetic splitting due to the Zeeman effect;

Appendix B I describe more in detail the absorption imaging technique with a particular attention to the cross section corrections due to the large spin of Dysprosium;

Appendix C I introduce some of the software I developed during my thesis, with a focus on the database that stores the metadata of the experimental results.



2

Dipolar Quantum Gases

DIFFERENT forces rule the interactions between atoms at low temperatures. In cold atoms experiments, the prominent contribution is the van der Waals interaction, which arise from the induced electrical dipole between atoms. The van der Waals potential scales as $\sim 1/r^6$ for atoms in the electronic ground state, where r is the inter-particle distance, and is thus considered as short-ranged^a. On the other hand, for atoms and molecules having a permanent dipoles (magnetic or electric) the interaction potential falls off as $\sim 1/r^3$ and therefore has a long-range behaviour. This fact, in addition to the anisotropy of the potential, modifies quite strongly the behaviour of a quantum gas. In this chapter I review some well established consequences of working with a dipolar gas and adapt them to the case of Dysprosium. Extensive information on cold dipolar gases can be found in the reviews [81, 82]. In particular, I focus on some main issues that have to be considered while building a new experiment:

- The non local character of the dipolar interactions leads to a spatial deformation of the atomic cloud, which should be compensated by a trap geometry which avoids instabilities;
- In atomic clouds which are not polarised in the ground state, the dipolar interaction induces inelastic collisions. The energy released from the spin-flip events leads to a heating of the cloud and atom loss.

The argument presented below are common with other dipolar atomic species like Erbium and also Chromium, which is the first species that has been extensively studied with this respect.

^aIn three dimension, we define short-ranged any potential decreasing faster than $1/r^3$, for which the integral $\int dr V(r)$ stays finite.

2.1 From Contact to Long-range Interaction

The exact expression of the van der Waals potential can be very difficult to describe theoretically since the high spin of the ground state of Dysprosium gives rise to a very complex net of molecular levels. Nevertheless some theory work has been done in this direction [83, 84].

In cold atoms experiments we only consider scattering events at very low temperatures, *i.e.* at very low kinetic energies. In this regime one knows that for short range potentials (as the van der Waals potential) the asymptotic part of the scattered wave functions has a spherical symmetry (or one can say that at low temperatures collisions happen only in *s*-wave). The amplitude of the scattered wave depends on a unique parameter, the scattering length a , which more importantly is experimentally accessible and may be tunable.

Regardless of the exact expression of the interaction potential, we can replace it by a model potential having the same a , thus leading to the same scattering properties for low energies. The simplest choice of this potential is the Fermi pseudopotential [85]

$$U_{\text{contact}}(r) = \frac{4\pi\hbar^2 a}{m} \delta(r) \frac{\partial}{\partial r} r, \quad (2.1)$$

that is a contact isotropic interaction. The regularising operator $\partial_r r$ prevents divergences of the potential in case the wave function itself has a $1/r$ divergence [86]. The prefactor is often called the coupling constant

$$g = \frac{4\pi\hbar^2 a}{m}. \quad (2.2)$$

Note how g solely depends on the atomic mass m and the scattering length a . It is also interesting to notice that, even if the form is that of a contact interaction, typical values of the scattering length are of the order of hundred Bohr radii a_0 , that is two orders of magnitude larger than the size of an atom ^a.

In the case of magnetic atoms such as Dysprosium, one should additionally consider the interaction due to the permanent dipole moment. Let us consider in the following the case of two interacting magnetic dipoles $\boldsymbol{\mu}_1$ and $\boldsymbol{\mu}_2$ ^b. If the dipoles are separated by a relative distance $\mathbf{r} = \mathbf{r}_1 - \mathbf{r}_2$, the interaction takes the familiar expression:

$$U_{\text{dd}}(\mathbf{r}) = \frac{\mu_0}{4\pi r^3} [(\boldsymbol{\mu}_1 \cdot \boldsymbol{\mu}_2) - \frac{3}{r^2} (\boldsymbol{\mu}_1 \cdot \mathbf{r})(\boldsymbol{\mu}_2 \cdot \mathbf{r})]. \quad (2.3)$$

where μ_0 is the vacuum magnetic permeability. One notices immediately the long-range character of the interaction, due to the slow $1/r^3$ decay at infinity. In the case of atomic magnetic dipole moment one has $\boldsymbol{\mu}_i = \mu_B g_J \mathbf{J}_i$, where g_J is the Landé factor, μ_B the Bohr magneton and \mathbf{J}_i the total angular momentum.

If the sample is spin polarised, for example by applying an external uniform magnetic field, all the dipoles point in the same direction and the expression of the interaction

^aThe order of magnitude of the scattering length is set by the van der Waals interaction range $(mC_6/\hbar^2)^{1/4}$.

^bIn the case of permanent electric dipoles, like for example in molecular gases, the interaction is obtained by the substitution $\boldsymbol{\mu}_i \rightarrow \mathbf{d}_i$ and $\mu_0 \rightarrow 1/\epsilon_0$.

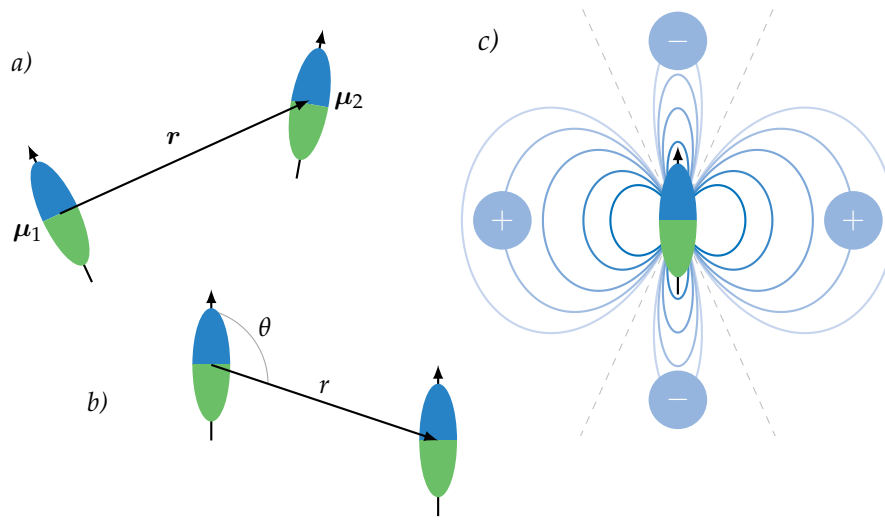


Figure 2.1 – a) Interacting dipoles. b) In case of a polarised sample the interaction depends only on the angle between them. c) Isopotential curves, note how the interaction changes from attractive to repulsive moving from head-to-tail to side-by-side configuration.

simplifies to:

$$U_{\text{dd}}(\mathbf{r}) = \frac{\mu_0 \mu^2}{4\pi} \frac{1 - 3 \cos^2 \theta}{r^3}, \quad (2.4)$$

where θ is the angle between \mathbf{r} and the polarising field (figure 2.1.b). Note that the interaction has a d -wave angular symmetry, which gives to the dipole interaction a strong anisotropic behaviour, in contrast to the contact interaction (2.1). The sign is negative for head-to-tail alignment of the dipoles, hence giving rise to an attractive force, and it is positive (repulsive) for side-by-side dipoles (see 2.1). Notice also that the force vanishes for $\theta \simeq 54.7^\circ$. A complete description of the scattering properties of the dipolar potential is a difficult task and we will review some results at the end of the chapter.

Having defined both the contact interaction and the long-ranged dipole-dipole interaction, one may wish to compare their relative strength. Since the relevant parameter in the first case is the scattering length a , one can define the dipolar length

$$a_{\text{dd}} = \frac{\mu_0 \mu^2 m}{12\pi \hbar^2}. \quad (2.5)$$

The ratio between the two lengths, often called the dipolar strength, is

$$\epsilon_{\text{dd}} = \frac{a_{\text{dd}}}{a}, \quad (2.6)$$

and gives an estimate of the dipolar character of the gas. In table 2.1 is given a short list of ϵ_{dd} for different atomic species. Since the dipolar interaction (2.3) scales as the square of the magnetic dipole $\mu^2 \propto J^2$, for atoms with a large magnetic moment in the ground state (Chromium, Erbium and Dysprosium, the only ones currently cooled to degeneracy) the effect of this interaction is expected to be orders of magnitude stronger

than in alkali (e.g. $J = 1/2$ for Rubidium and $J = 8$ for Dysprosium).

Species	μ [μ_B]	a [a_0]	a_{dd} [a_0]	ϵ_{dd}
^{87}Rb	1	100	0.7	0.007
^{52}Cr	6	102.5	0.15	0.15
^{166}Er	6.98	72	65.4	0.91
^{164}Dy	9.93	100	130.8	1.42

Table 2.1 – Relevant parameters in dipolar gases for some laser cooled species.

2.2 Feshbach Resonance

The dipolar character of the gas, *i.e.* the dipolar strength ϵ_{dd} , can be finely tuned by changing either the value of the dipolar length a_{dd} or the scattering length a . While the first option has been proposed using time varying magnetic fields [87], the scattering length a is commonly finely tuned using Feshbach resonances [88]. A Feshbach resonance occurs in a scattering event whenever the energy of the colliding particles E_{coll} matches the energy of a bound state E_{bound} in a closed scattering channel, leading to a resonant modification of the scattering phase shift. As we expect from a second order perturbation, the effect on the colliding atoms will depend on the energy difference $E_{\text{coll}} - E_{\text{bound}}$ between the incoming state and the resonant bound state. The position of the latter can be tuned using the Zeeman effect, and the resonance can thus be found by varying the external magnetic field B (one speaks of magnetically tuned Feshbach resonance). The scattering length, which has some background value a_{bg} far from the resonance, varies with the magnetic field as

$$a(B) = a_{\text{bg}} \left(1 - \frac{\Delta_B}{B - B_0} \right), \quad (2.7)$$

where Δ_B is the width of the resonance and B_0 is the magnetic field value where the resonance is centred (see figure (2.7)). With a Feshbach resonance both the amplitude and the sign of the scattering length a can be tuned.

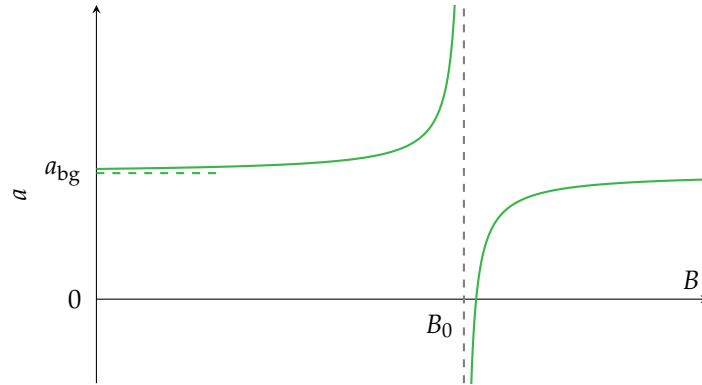


Figure 2.2 – Variation of the scattering length $a(B)$ close to a Feshbach resonance. Crossing the resonance the scattering length changes sign, which results in attractive or repulsive atomic interactions.

The resonance position can be experimentally detected by a simple atom loss spectroscopy as a result of the strong enhancement of three body recombination that leads to inelastic losses close to B_0 . In figure 2.3 we see a plot of a Feshbach loss spectrum of ^{164}Dy around two resonances centred at $B \sim 7.5$ G. A broader scan at low fields (figure 2.4) shows an extremely dense spectrum of narrow resonances.

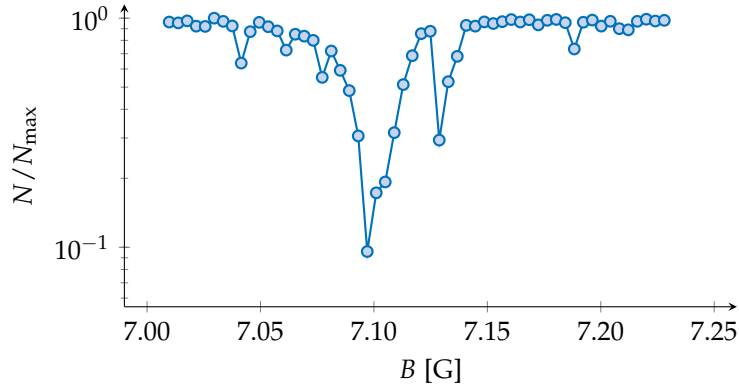


Figure 2.3 – Atom loss spectrum versus magnetic field around two Feshbach resonances of ^{164}Dy . The resonance centred at $B \sim 7.10$ G is quite isolated from the rest of the spectrum at lower fields and we will use it to tune the interatomic interaction during the evaporative cooling. This scan was taken in our laboratory with an optical dipole trap at a temperature of $\sim 2 \mu\text{K}$.

This forest of resonances extends to higher fields and is a common feature of open-shell lanthanides^a, for which the large spin in the ground state generates an intricate web of molecular states. Previous work on Erbium and Dysprosium also demonstrated that

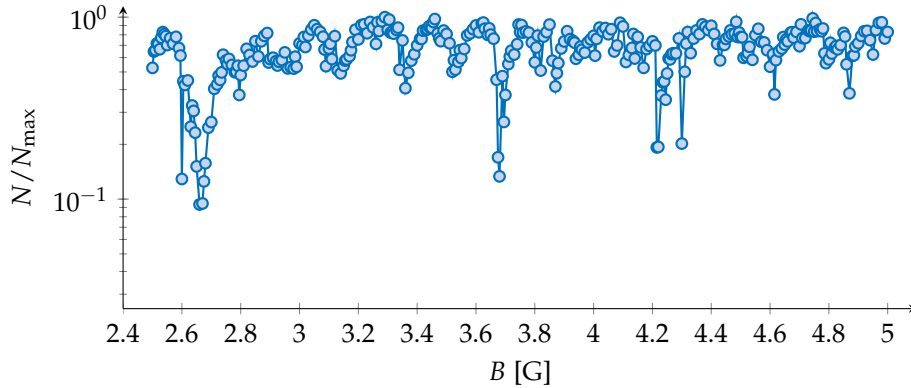


Figure 2.4 – Low field scan of the Feshbach spectrum. Resonances are located by the atom loss versus the magnetic field strength. This scan was taken in a optical dipole trap at a temperature of $\sim 2 \mu\text{K}$.

the mean spacing between nearest-neighbours resonances is described by a Wigner-Dyson distribution, which implies a chaotic behaviour [89, 90]. The chaos finds its origin in the complex ensemble of bound states, which has an intricate net of avoided crossings originating from the strong anisotropy of the interactions [83, 91]. In addition to the

^aDysprosium and Erbium are the only ones studied so far.

rich narrow resonance spectrum of Dysprosium, two broad resonances appear at high field ($B \sim 77$ G and ~ 179 G), which have been extensively studied [92].

Moreover, as it was first observed in reference [93], the number of resonances increases with the temperature of the atomic cloud, which is a clear indication of scattering events in which the incoming wave has a d -wave component [90].

2.3 Dipolar Bose-Einstein Condensates

The anisotropy of the dipolar interaction (2.3) and its alternate attractive and repulsive behaviour drastically changes the interactions in a cold atomic gas. Let us take a look at the main manifestations of the dipolar nature of a degenerate gas, starting with a short reminder of the mean-field theory of condensates which we will need in the following.

2.3.1 Mean-Field Model

Let us consider N interacting bosons in an external potential U_{ext} . The second quantisation hamiltonian has the familiar form [94]

$$\hat{\mathcal{H}} = \int d\mathbf{r} \hat{\Psi}^\dagger(\mathbf{r}) \left(-\frac{\hbar^2}{2m} \nabla^2 + U_{\text{ext}}(\mathbf{r}) \right) \hat{\Psi}(\mathbf{r}) + \frac{1}{2} \int d\mathbf{r} d\mathbf{r}' \hat{\Psi}^\dagger(\mathbf{r}) \hat{\Psi}^\dagger(\mathbf{r}') U_{\text{int}}(\mathbf{r} - \mathbf{r}') \hat{\Psi}(\mathbf{r}) \hat{\Psi}(\mathbf{r}') \quad (2.8)$$

where $\hat{\Psi}^\dagger(\mathbf{r})$ and $\hat{\Psi}(\mathbf{r})$ are the boson field creation and annihilation operators at position \mathbf{r} , and the term $U_{\text{int}}(\mathbf{r} - \mathbf{r}')$ is the two-body interaction potential, which for dipolar gases will be the sum of the contact potential (2.1) and the dipole-dipole interaction (2.3). The external potential U_{ext} in cold atoms experiment is usually a confining trap, which can be created using optical or magnetic forces. As we will see in chapter 7, at lowest order the confining potential can be considered as harmonic. In the following we will then take

$$U_{\text{trap}}(\mathbf{r}) = \frac{1}{2} m \left(\omega_x^2 x^2 + \omega_y^2 y^2 + \omega_z^2 z^2 \right). \quad (2.9)$$

When a condensate is formed, one of the modes of the field, that we should call $\phi(\mathbf{r})$, is macroscopically occupied by an atomic population N_0 close to the maximum number of particles $N_0 \sim N$. Therefore, following Bogoliubov's prescription [95], we can approximate the exact hamiltonian (2.8) by splitting the field operator into condensate and not condensate parts $\hat{\Psi}(\mathbf{r}) = \psi(\mathbf{r}) + \hat{\phi}(\mathbf{r})$, seeing $\hat{\phi}$ as a perturbation to the classical field ψ . This last term is usually called the condensate wavefunction and is normalised to the number of particles

$$\int d\mathbf{r} \psi^*(\mathbf{r}) \psi(\mathbf{r}) = N, \quad (2.10)$$

so that the condensate density is given by $n(\mathbf{r}) = |\psi(\mathbf{r})|^2$. Expanding the hamiltonian in functions of $\hat{\phi}(\mathbf{r})$, the zeroth order is non trivial and gives the energy functional

$$\begin{aligned} \mathcal{H}_0 &= E[\psi] = \\ &= \int d\mathbf{r} \left(\frac{\hbar^2}{2m} |\nabla \psi(\mathbf{r})|^2 + U_{\text{trap}}(\mathbf{r}) |\psi(\mathbf{r})|^2 + \frac{g}{2} |\psi(\mathbf{r})|^4 + \frac{1}{2} \Phi_{\text{dd}}(\mathbf{r}) |\psi(\mathbf{r})|^2 \right), \end{aligned} \quad (2.11)$$

which will be useful in the following to study the stability of the condensate state. In the equation above, g is the contact parameter (2.2) and we introduce the dipolar potential

$$\Phi_{\text{dd}}(\mathbf{r}) = \int d^3r' U_{\text{dd}}(\mathbf{r} - \mathbf{r}') |\psi(\mathbf{r}')|^2. \quad (2.12)$$

The first derivatives of the functional should vanish to have a stable minimum solution. Calculating then $\delta E / \delta \psi = \delta E / \delta \psi^* = 0$ one finds the famous Gross-Pitaevskii equation (GPE)

$$\mu \psi(\mathbf{r}) = -\frac{\hbar^2}{2m} \nabla^2 \psi(\mathbf{r}) + \left(U_{\text{trap}}(\mathbf{r}) + g |\psi(\mathbf{r})|^2 + \Phi_{\text{dd}}(\mathbf{r}) \right) \psi(\mathbf{r}) \quad (2.13)$$

which is used to describe Bose-Einstein condensates [96]. In the formula above we introduced the chemical potential μ . The GPE is also called non-linear Schrodinger equation due to the additional mean-field term $g |\psi|^2$. In addition, the case of a dipolar gas adds a non-local character to the equation, due to the dipolar contribution (2.12). The interaction energy U_{int} will be dominated by the mean-field term $g |\psi|^2$ or the dipolar potential according to the value of the parameter ϵ_{dd} introduced in (2.6). Due to its non linear and non local character the dipolar Gross-Pitaevskii equation does not have an analytical solution, therefore the wave function is usually calculated numerically. Nevertheless, in the following section we discuss some simple cases where an analytical expression for the atomic density can be found using variational calculus.

2.3.2 Thomas-Fermi Approximation

In the limit of vanishing interactions ($U_{\text{int}} = 0$) the cloud size σ is given by the equilibrium between kinetic energy (also called quantum pressure), which scales as $\sim p^2/2m = \hbar^2/2m\sigma^2$, and potential energy, which scales as $\sim m\omega^2\sigma^2/2$. The relevant length scale is then given by the harmonic oscillator length $\sigma \sim a_{\text{ho}} = (\hbar/m\omega)^{1/2}$, which we will use later on.

On the contrary, when the contact interactions are present, since they scale as $\sim gn = gN/\sigma^3$, they tend to increase the cloud size. In the limit of strongly interacting gases, this last term overcomes the kinetic one, which can then be neglected. In the following we will use this approximation (Thomas-Fermi approximation), which is pretty accurate for clouds with a large atom number.

Let us then neglect the kinetic term from the GPE (2.13) and use the definition $n(\mathbf{r}) = |\psi(\mathbf{r})|^2$. We obtain the equation

$$\mu \psi(\mathbf{r}) = \left(U_{\text{trap}}(\mathbf{r}) + gn(\mathbf{r}) + \int d^3r' U_{\text{dd}}(\mathbf{r} - \mathbf{r}') n(\mathbf{r}') \right) \psi(\mathbf{r}), \quad (2.14)$$

which has the following implicit solution for the density profile

$$n(\mathbf{r}) = \frac{1}{g} \left(\mu - U_{\text{trap}}(\mathbf{r}) - \Phi_{\text{dd}}(\mathbf{r}) \right) \quad (2.15)$$

If there is no dipolar interaction ($\Phi_{\text{dd}} = 0$), the insertion of the confining potential gives a parabolic profile, in the three spatial directions, for the equilibrium condensate density. For the sake of simplicity, let us consider an isotropic trap, *i.e.* where the potential is $U_{\text{trap}}(\mathbf{r}) = m\omega r^2/2$. Although an anisotropic trap could be more realistic, it is more

difficult to solve in the dipolar case and this simplification already provides a lot of physical insight. The density profile $n^{(0)}$ in the case $\Phi_{\text{dd}} = 0$ is given by

$$n^{(0)}(\mathbf{r}) = n_0^{(0)} \left(1 - \frac{r^2}{R^2}\right) \Theta(R - r) \quad (2.16)$$

where the cloud semi-axis is $R = (2\mu/m\omega^2)^{1/2}$ and the central density of the cloud $n_0^{(0)} = n^{(0)}(0) = \mu/g$. The Heaviside function Θ explicitly reflects that the density has always to be considered zero outside the Thomas-Fermi radius $n(r > R) = 0$.

2.3.3 Elongation of Dipolar Clouds

We will now consider the dipolar case and proceed with a perturbative treatment. We consider the dipolar potential given by the isotropic density distribution

$$\Phi_{\text{dd}}(\mathbf{r}) = \int d\mathbf{r}' U_{\text{dd}}(\mathbf{r} - \mathbf{r}') n^{(0)}(\mathbf{r}'). \quad (2.17)$$

Let us consider a polarised cloud where the dipoles are aligned in the z direction, so that U_{dd} can be written in the form (2.4). If we express the spatial dependence in the following way [97]

$$\frac{1 - 3z^2/r^2}{r^3} = -\frac{\partial^2}{\partial z^2} \frac{1}{r} - \frac{4\pi}{3} \delta(\mathbf{r}), \quad (2.18)$$

the dipolar potential can then be rewritten as

$$\Phi_{\text{dd}}(\mathbf{r}) = -\frac{\mu_0 \mu^2}{4\pi} \left(\frac{\partial^2}{\partial z^2} \phi(\mathbf{r}) + \frac{1}{3} n_0^{(0)}(\mathbf{r}) \right) \quad (2.19)$$

where we define

$$\phi(\mathbf{r}) = \frac{1}{4\pi} \int d\mathbf{r}' \frac{n^{(0)}(\mathbf{r}')}{|\mathbf{r} - \mathbf{r}'|}. \quad (2.20)$$

In analogy with electrostatic problem, $\phi(\mathbf{r})$ is the electric potential generated by a static charge distribution $n^{(0)}(\mathbf{r})$. The potential obeys Poisson's equation $\nabla^2 \phi = -n^{(0)}(\mathbf{r})$, which is satisfied by a polynom in the form $\phi(\mathbf{r}) = a_0 + a_2 r^2 + a_4 r^4$ for $r < R$, where is easy to check that $a_2 = -1/6$ and $a_4 = 1/(20R^2)$. Making the substitution in the expression of the dipolar energy one finds

$$\Phi_{\text{dd}} = \frac{2}{15} \mu_0 \mu^2 n_0^{(0)} \left(\frac{x^2 + y^2 - 2z^2}{R^2} \right). \quad (2.21)$$

Substituting this expression and the one of the trapping potential in the Thomas-Fermi profile (2.15), we are lead to the density distribution

$$n(\mathbf{r}) = n_0^{(0)} \left(1 - \frac{x^2}{R_x^2} - \frac{y^2}{R_y^2} - \frac{z^2}{R_z^2} \right) \quad (2.22)$$

Like in the non-dipolar case, the profile of the cloud is parabolic but the radii depend on the dipole strength ϵ_{dd}

$$R_x = R_y \simeq R \left(1 - \frac{\epsilon_{\text{dd}}}{5}\right) \quad \text{and} \quad R_z \simeq R \left(1 + \frac{2\epsilon_{\text{dd}}}{5}\right). \quad (2.23)$$

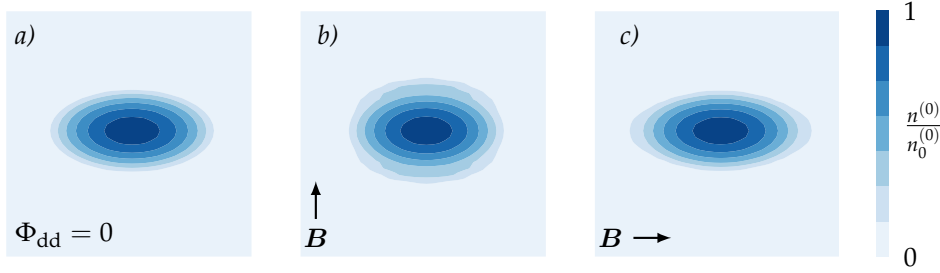


Figure 2.5 – Cloud deformation in the presence of dipolar interaction in a trap with aspect ratio $\lambda = 2$. a) Thomas Fermi profile in an anisotropic potential without the dipolar correction. b) dipoles aligned in e_z direction, c) dipoles aligned in e_x direction. The cloud elongates in one direction and squeezes in the others.

It is now immediate to see how the dipolar interaction deforms the cloud. Starting from the isotropic distribution (2.16) for $\Phi_{\text{dd}} = 0$, the larger ϵ_{dd} , the more the cloud gets elongated in the direction of the dipoles (here z) while it squeezes in the other directions. This effect, known in magnetic materials as magnetostriction, has been experimentally observed in quantum gases of Chromium in [45]. Note that equation (2.23) gives an unphysical solution in the case of strong dipolar interaction $\epsilon_{\text{dd}} > 5$, which gives some insight on the expected instabilities, as we will see in the following.

Let us now consider a more realistic trap with cylindrical symmetry, introducing then a cylindrical coordinate system $\mathbf{r} = (\rho, z)$. Defining the trap aspect ratio $\lambda = \omega_z/\omega_\rho$ and the average trapping frequency $\bar{\omega} = (\omega_\rho^2\omega_z)^{1/3}$, the potential can be written as

$$U_{\text{trap}}(\rho, z) = \frac{m}{2}(\omega_\rho\rho^2 + \omega_z z^2) = \frac{m}{2} \frac{\bar{\omega}}{\lambda^{2/3}}(\rho^2 + \lambda^2 z^2). \quad (2.24)$$

The arguments above still hold, but the calculation of the potential (2.20) is much more involved and has been carried out in [98]. Like in the simple case of isotropic trap, the authors found that for an increasing dipolar strength ϵ_{dd} the cloud elongates in the direction of the polarising field (*i.e.* the condensate aspect ratio $\kappa = R_\rho/R_z$ decreases, see figure 2.5). Physically, this is the effect of the anisotropy of the dipolar potential Φ_{dd} , which minimises the energy by redistributing the atoms in a head-to-tail configuration. These considerations are valid in a perturbative regime, in the following we focus on strongly dipolar gases for which $\epsilon_{\text{dd}} > 1$ (the isotope ^{164}Dy has $\epsilon_{\text{dd}} = 1.42$, away from Feshbach resonances).

2.4 Condensate Instabilities

Under certain conditions, Bose-Einstein condensates with pure contact interactions are unstable: we have seen that crossing a Feshbach resonance the scattering length value a changes from positive to negative values, and thus the inter-particle interaction from

repulsive to attractive. Once the atoms attract each other, they accelerate towards the trap centre^a, and the cloud collapses on itself. As the collapse proceeds, the increased density induces strong three body recombination which leads to atom losses and to the decay of the condensate itself [99, 100, 101]^b.

In the case of dipolar gases the collapse mechanism can be triggered by the dipole-dipole interaction alone, which overcomes the contact interaction in the case $\epsilon_{dd} > 1$ and can thus drive cloud instabilities even for positive a . The following sections describe some effects which have to be taken into account to obtain a stable condensate of Dysprosium. The stabilisation effect has been first observed with Chromium atoms [102] and described theoretically some years before the experimental realisation [103, 104].

2.4.1 Phonon Instability

Let us first consider the case of a homogeneous condensate ($V_{\text{ext}} = 0$) with dipolar interactions. The instability can easily be understood looking at the dispersion relation of the dipolar BEC, which is given by the Bogolyubov excitation spectrum

$$E(p) = \sqrt{E_{\text{free}}^2(p) + 2gn(1 + \epsilon_{dd}(3\cos^2\alpha - 1))} E_{\text{free}}(p). \quad (2.25)$$

The dispersion relation has an angular dependence through α , the angle in between the external polarising field and the wave vector of the excitation p . While at short-wavelengths the spectrum is dominated by free particle excitations $E \sim E_{\text{free}}(p) = p^2/2m$, long-wavelength excitations are phonons, with an anisotropic behaviour

$$E(p) \sim c_s p = \sqrt{\frac{gn}{m}(1 + \epsilon_{dd}(3\cos^2\alpha - 1))} p, \quad (2.26)$$

where c_s is the sound velocity in the gas. From the dispersion relation above, it is evident that for $\alpha \sim \pi/2$ and $\epsilon_{dd} \gtrsim 1$ the excitations are purely imaginary and therefore an homogeneous dipolar condensate is unstable against the density fluctuations which propagate perpendicularly to the dipoles alignment.

2.4.2 Geometrical Stabilisation

Let us now see how the presence of a trap could stabilise a dipolar condensate against its collapse. The problem can be accessed through a variational approach, where the variational parameters will be the cloud sizes. We start by considering the energy functional (2.11), in which we can identify the kinetic, trapping and interacting contributions

$$E[\psi] = E_k[\psi] + E_{\text{trap}}[\psi] + E_{\text{int}}[\psi]. \quad (2.27)$$

We will again consider the interaction dominated regime, so that $E_k[\psi]$ can be neglected. Like in the previous paragraph, the problem can be simplified for a trap with cylindrical symmetry. We will then use the same potential given in equation (2.24). This assumption is not necessary but provides analytical results for the integrals, while in the

^aThe interaction depends linearly on the density, thus it is stronger at the centre of the cloud, where n is higher.

^bNevertheless, below a certain critical atom number, the repulsive interaction due to quantum pressure can stop the cloud collapse, and metastable condensates with negative scattering length can exist.

case of three different trapping frequencies one has to numerically solve the term Φ_{dd} of the energy functional. A good Ansatz for the density distribution is an inverted parabola profile given by the Thomas-Fermi approximation

$$n(\mathbf{r}) = n_0 \left(1 - \frac{\rho^2}{R_\rho^2} - \frac{z^2}{R_z^2} \right) \quad (2.28)$$

where the density at the trap centre is defined as $n_0 = 15N / (8\pi R_\rho^2 R_z)$ and the Thomas-Fermi radii R_z and R_ρ are the variational parameter. The substitution in the energy functional gives

$$\frac{E}{N\hbar\omega} = \frac{1}{14a_{\text{ho}}^2 \lambda^{2/3}} (2R_\rho^2 + \lambda^2 R_z^2) + \frac{15N}{7} \frac{a_{\text{ho}}^2}{R_\rho^2 R_z} (a - a_{\text{dd}} f(\kappa)). \quad (2.29)$$

We introduce here the dipolar function

$$f(\kappa) = \frac{1 + 2\kappa^2}{1 - \kappa^2} - \frac{3\kappa^2 \operatorname{arctanh} \sqrt{1 - \kappa^2}}{(1 - \kappa^2)^{3/2}}. \quad (2.30)$$

which is bounded $f(\kappa) \in [1, -2]$ and monotonically decreasing with the aspect ratio (see the plot in figure 2.6).

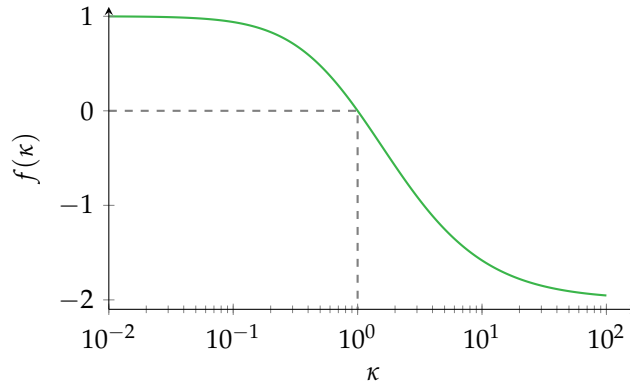


Figure 2.6 – Dipolar function $f(\kappa)$. For isotropic condensates ($\kappa = R_\rho / R_z = 1$) the function vanishes.

The expressions above can be used to evaluate the energy functional for different trap aspect ratios λ and scattering length a . In figure 2.7 is an example for a trap geometry of $\lambda = 2$. For high values of a the cloud deforms and stabilises to a given κ . On the contrary, for low values, there is no local minimum and the cloud implodes.

In the limit $N \rightarrow \infty$ the only term that matters is E_{int} , for which the relevant parameter is $1 - \epsilon_{\text{dd}} f(\kappa)$, which could drive the instability. If N is finite and $E_{\text{int}} > 0$ the condensate is always stable since the term E_{trap} is also positive. The energy is minimised by lowering the density, thus the cloud expands.

On the contrary, the condition $E_{\text{int}} < 0$ is necessary but not sufficient to have an instability. In picture 2.7 one can see the energy landscapes for different values of a and as a function of the cloud sizes. At intermediate values there exist a local minimum, thus the cloud accommodates its shape to minimise the energy. The state is only metastable

since there is also a global minimum which corresponds to an unstable cloud where the energy is minimised by a complete collapse in the ρ direction.

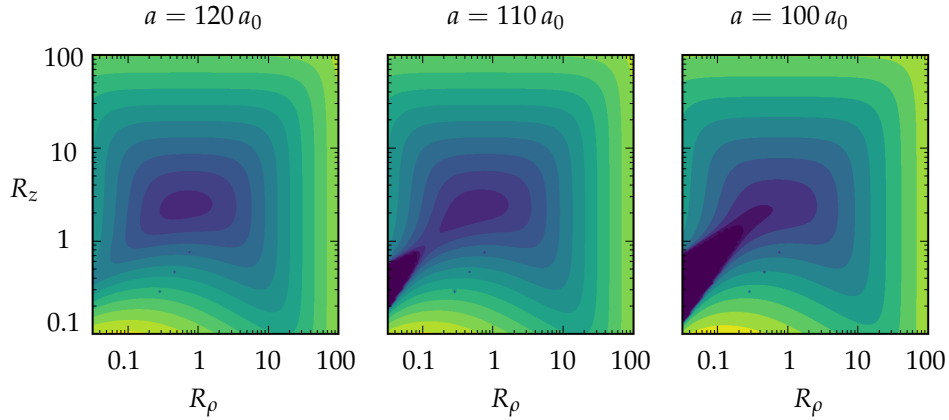


Figure 2.7 – Plot of the energy $E_{\text{tot}}/N\hbar\bar{c}$ obtained with a gaussian Ansatz. The pictures refer to three decreasing values of the scattering length as a function of the cloud sizes R_ρ and R_z for $N = 10^5$ atoms. The confining potential is cylindrical symmetric with trapping frequencies $R_z = 2\pi \times 200$ Hz and $R_\rho = 2\pi \times 100$ Hz. Increasing the value of a , the cloud is stable in a local minimum position (the metastable region in picture 2.6) which is separated by the unstable region appearing at low κ by a saddle point. Below some critical value a_c (right picture), the local minimum merges with the unstable solution and the cloud collapses.

These instabilities were first investigated on Chromium atoms [102], which is not naturally in the unstable regime $\epsilon_{\text{dd}} > 1$. To enter this regime it was necessary to work close to a Feshbach resonance, but the lifetime was in the same time limited [105]. Erbium and Dysprosium have naturally a higher value of ϵ_{dd} without the need of Feshbach resonances. In 2016, new studies on both atoms [106, 107, 108] found surprisingly that the induced instabilities actually do not bring to a total collapse of the cloud as one would have expected. The density of the cloud was indeed increasing, but it saturated to a fixed value where the cloud became stable and self confined. This effect is not expected in the previous mean field analysis, that we obtained by neglecting quantum fluctuations. These fluctuations arise from the term $\hat{\phi}(\mathbf{r})$ that we neglected at the beginning, and they are actually responsible of this new stabilisation mechanism [109]. In fact, if we consider the energy corrections to first order, they result in a positive term which adds to the interactions, which can then be rewritten as

$$E_{\text{int}} \sim gn^2(1 - \epsilon_{\text{dd}}f(\kappa)) + \delta E. \quad (2.31)$$

Here, we recast the interaction energy from (2.29) to explicit the dependence on the density n . For a dipolar gas, the additional term δE is given by the famous Lee-Huang-Yang correction [110] with an additional dependence on the dipolar strength ϵ_{dd} , which has been calculated in [111] and gives

$$\delta E \sim \frac{gn^2}{2} \frac{128\sqrt{na^3}}{15\sqrt{\pi}} \left(1 + \frac{3}{2}\epsilon_{\text{dd}}^2\right). \quad (2.32)$$

The dipole interaction ϵ_{dd} then amplifies this correction term. From (2.31) it is then

evident that when one expects a collapse for $\epsilon_{\text{dd}}f(\kappa) > 1$ the quantum fluctuations could stabilise the cloud.

2.5 Dipolar Relaxation

Up to now we considered elastic interactions between atoms. In this section we will focus on the inelastic character of dipolar collisions, which also leads to a redistribution of the spin states.

In contrast with spin-exchange collisions, which conserve the total spin even if the individual ones can be flipped^a, the dipole-dipole interaction does not commute with the total spin. Therefore, even starting with a polarised cloud, the spins can be flipped by the dipolar interaction. The major problem we will focus on is the dipolar relaxation, which happens in atomic clouds where more than one spin state is present or, in general, if the cloud is not polarised in the absolute ground state. Spin relaxation is a major problem for cold trapped clouds, since the released energy after the collision results in rapid heating or atom loss. As we will see, dipolar relaxation depends on the cloud temperature and the external magnetic fields, but has different behaviour for bosons or fermions.

Let me point out again that, as much of the physics discussed above, these collisions are common to any atomic gas, and can be problematic also for alkali atoms with large spin (for example Cesium).

2.5.1 Spin-flip Interaction

Let us start by rewriting the expression of the dipolar potential (2.3) in a more symmetric way. By explicitly rewriting the scalar products in spherical coordinates $\mathbf{r} = (r, \theta, \phi)$, we obtain the expression

$$U_{\text{dd}} = \frac{\mu_0 \mu_{\text{B}}^2 g_J^2}{4\pi r^3} \sum_{m=-2}^2 \mathcal{T}_{2,m}, \quad (2.33)$$

where $\mathcal{T}_{2,m}$ is a rank 2 spherical tensor whose components are given [112] as

$$\begin{aligned} \mathcal{T}_{2,0} &= (3 \cos^2 \theta - 1) \left(J_{1z} J_{2z} - \frac{1}{4} (J_{1+} J_{2-} + J_{1-} J_{2+}) \right) \\ \mathcal{T}_{2,1} &= \frac{3}{2} \sin \theta \cos \theta e^{-i\phi} (J_{1z} J_{2+} + J_{1+} J_{2z}) \\ \mathcal{T}_{2,-1} &= \frac{3}{2} \sin \theta \cos \theta e^{i\phi} (J_{1z} J_{2-} + J_{1-} J_{2z}) \\ \mathcal{T}_{2,2} &= \frac{3}{4} \sin^2 \theta e^{-2i\phi} J_{1+} J_{2+} \\ \mathcal{T}_{2,-2} &= \frac{3}{4} \sin^2 \theta e^{2i\phi} J_{1-} J_{2-} \end{aligned} \quad (2.34)$$

Here, we used the usual definition of the ladder operator $J_{\pm} = J_x \pm iJ_y$. The angular dependence of the tensor can be rewritten using the spherical harmonics $Y_{\ell,m}$ and by defining the operator $\mathcal{S}_{\ell,m}$, whose components act only in spin space and are given

^aSpin-exchange collisions are $\propto \hat{\mathbf{f}}_1 \cdot \hat{\mathbf{f}}_2$

by [113]

$$\begin{aligned}\mathcal{S}_{2,0} &= -\sqrt{\frac{3}{2}}\left(J_{1z}J_{2z} - \frac{1}{3}\mathbf{J}_1 \cdot \mathbf{J}_2\right) \\ \mathcal{S}_{2,\pm 1} &= \pm \frac{1}{2}(J_{1z}J_{2\pm} + J_{1\pm}J_{2z}) \\ \mathcal{S}_{2,\pm 2} &= -\frac{1}{2}J_{1\pm}J_{2\pm}.\end{aligned}\tag{2.35}$$

We can then rewrite the interaction as

$$U_{\text{dd}} = \sqrt{\frac{24\pi}{5}} \frac{\mu_0 \mu_{\text{B}}^2 g_J^2}{4\pi r^3} \sum_{m=-2}^2 Y_{2,m}^*(\theta, \phi) \mathcal{S}_{2,m},\tag{2.36}$$

Except for the component $\mathcal{S}_{2,0}$, the operator does not conserve the total spin, since $\mathcal{S}_{2,1}$ ($\mathcal{S}_{2,-1}$) flips one spin up (down) and $\mathcal{S}_{2,2}$ ($\mathcal{S}_{2,-2}$) flips both the spins up (down).

We see that the orbital angular momentum ℓ is also not conserved in a dipole-dipole collision, since the calculation of the angular part of the potential expectation value will involve an integral on the spherical harmonics in the form

$$\int d\Omega Y_{\ell',m'} Y_{2,M} Y_{\ell,m} = \sqrt{\frac{5}{4\pi}} (2\ell' + 1)(2\ell + 1) \begin{pmatrix} \ell' & 2 & \ell \\ 0 & 0 & 0 \end{pmatrix} \begin{pmatrix} \ell' & 2 & \ell \\ m' & M & m \end{pmatrix}.\tag{2.37}$$

From the orthogonality relation of the Wigner 3- j symbols, the dipole interaction has a selection rule for the orbital quantum number $\Delta\ell = \ell' - \ell = 0, \pm 2$ and for its projection $m + M + m' = 0$. Note as an example that if two particles collide in s -wave they will scatter in d -wave.

2.5.2 Dipolar Scattering

I show here a simplified model for the calculation of the dipolar scattering cross sections. In the following section I give then the exact result that can be found in the literature. Let us consider the scattering of two atoms interacting via the dipolar potential. We will use standard scattering theory notation in the following. The familiar asymptotic form of the scattered wave function is

$$\lim_{r \rightarrow \infty} \psi_{\text{sc}}(\mathbf{r}) = e^{i\mathbf{k} \cdot \mathbf{r}} + f(\mathbf{k}', \mathbf{k}) \frac{e^{ikr}}{r}\tag{2.38}$$

where $\hbar\mathbf{k}$ and $\hbar\mathbf{k}'$ are the relative momenta for the incoming and outgoing wave respectively. The coefficient of the spherical wave is the scattering amplitude $f(\mathbf{k}', \mathbf{k})$, which contains the information on the scattering potential and is given by

$$f(\mathbf{k}', \mathbf{k}) = -\frac{m}{4\pi\hbar^2} \int d\mathbf{r}' e^{-i\mathbf{k} \cdot \mathbf{r}'} U(\mathbf{r}') \psi_{\text{sc}}(\mathbf{r}').\tag{2.39}$$

The exact expression of the $\psi_{\text{sc}}(\mathbf{r})$ requires to solve the auto consistent equation (2.38) which results in an infinite series (Born series) [114]. The most commonly used approximation is to stop the series at the first term, so that $\psi_{\text{sc}}(\mathbf{r}')$ is the incoming wave $\psi_0(\mathbf{r}') = e^{i\mathbf{k} \cdot \mathbf{r}'}$, and the scattering amplitudes turns out to be the Fourier transform of the

potential (Born approximation)

$$f^{(B)}(\mathbf{k}', \mathbf{k}) = -\frac{m}{4\pi\hbar^2} \int d\mathbf{r}' e^{-i\mathbf{k}\cdot\mathbf{r}'} U(\mathbf{r}') e^{i\mathbf{k}'\cdot\mathbf{r}'} = -\frac{m}{4\pi\hbar^2} U(\mathbf{k}', \mathbf{k}) \quad (2.40)$$

The scattering amplitude is also related to the total scattering cross section $\sigma = \int d\Omega |f(\mathbf{k}', \mathbf{k})|^2$. For colliding bosons, the differential cross section is obtained by symmetrising the scattering amplitude

$$\sigma = \int d\Omega |f(k, \theta) + f(k, \pi - \theta)|^2 \quad (2.41)$$

where the integration should be done only on one hemisphere since the particles are indistinguishable. As we have reminded at the beginning of the chapter, for short range potentials, the scattering amplitude tends to the scattering length at low temperatures $f(\mathbf{k}', \mathbf{k}) \rightarrow -a$, which is symmetric and \mathbf{k} -independent, and gives the well known cross section for two identical bosons

$$\sigma = 8\pi a^2. \quad (2.42)$$

It will be a fundamental parameter for the evaporative cooling as we will see in chapter 7.

We now return to the dipolar potential, for which a scattering event can change the internal spin state of the colliding atoms. We will write the scattering states $|\psi_{sc}\rangle = |\mathbf{k}, \alpha\beta\rangle$, where α and β label the internal (spin) state. The scattering wave function is then written as [115]

$$\psi_{sc}(\mathbf{r}) = e^{i\mathbf{k}\cdot\mathbf{r}} |\alpha\beta\rangle + \sum_{\alpha'\beta'} f_{\alpha'\beta', \alpha\beta}(\mathbf{k}', \mathbf{k}) \frac{e^{i\mathbf{k}'\cdot\mathbf{r}}}{r} |\alpha'\beta'\rangle, \quad (2.43)$$

for which the scattering amplitude (2.40) becomes at the Born approximation

$$f_{\alpha'\beta', \alpha\beta}(\mathbf{k}', \mathbf{k}) = -\frac{m}{4\pi\hbar^2} \langle \alpha'\beta' | U_{dd}(\mathbf{k}', \mathbf{k}) | \alpha\beta \rangle \quad (2.44)$$

Let us consider as an example the single spin-flip event represented in picture 2.8. The cloud is supposed to be completely polarised in a state $|J = 8, m_J = 8\rangle$, which can relax via the dipolar interaction to the state at lower energy $|J = 8, m_J = 7\rangle$. When the released Zeeman energy $\Delta E_Z \gg k_B T$ it leads to atom losses, therefore severely limiting the lifetime of the trapped cloud.

In the following we will proceed with some approximations, that will anyway give some insight of the correct scaling laws for dipolar collisions. Let us consider a polarised sample, with all the atoms in the state $|J, m_J = J\rangle$, which we label $|\uparrow\rangle$. A spin-flip event will change the state to $|J, m_J = J - 1\rangle = |\downarrow\rangle$. When considering a binary system, the initial internal state is then labelled $|\alpha\beta\rangle = |\uparrow\uparrow\rangle$. Following a dipolar collision, the interaction could flip one or both spins

$$|\uparrow\uparrow\rangle \rightarrow |\downarrow\uparrow\rangle + \Delta E_Z \quad (2.45)$$

$$|\uparrow\uparrow\rangle \rightarrow |\downarrow\downarrow\rangle + 2\Delta E_Z. \quad (2.46)$$

The released energy ΔE_Z is equal to the Zeeman splitting between levels (appendix A).

Let us simplify the problem by considering the limiting case of small initial relative

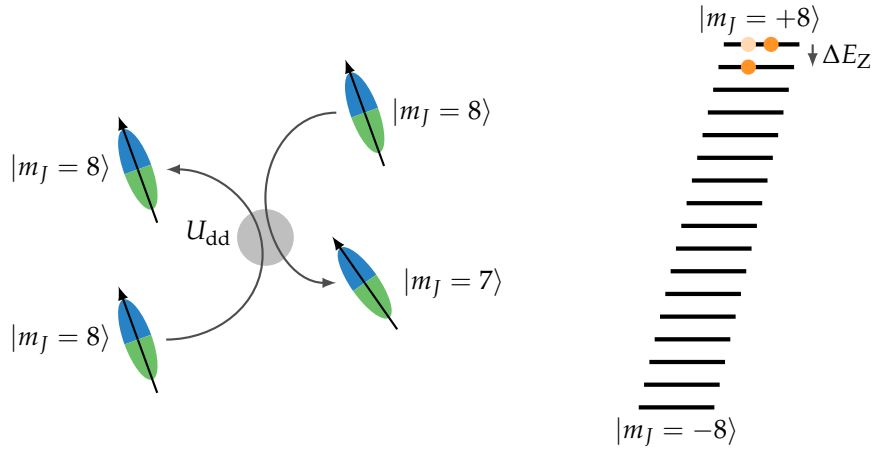


Figure 2.8 – Dipolar collision with a single spin-flip process, starting with the atoms in the stretched state $|J = 8, m_J = 8\rangle$. The energy released after the collision is the Zeeman energy ΔE_Z , which can lead to atom loss.

momentum of the colliding particles with respect to the final one ($k \ll k'$), so that the initial wave function is approximately unity $\psi_0 \rightarrow 1$. The matrix element of the dipole-dipole $U_{\text{dd}}(\mathbf{k}', 0)$ interaction, given by the Fourier transform of the dipole interaction, is

$$U_{\text{dd}}(\mathbf{k}', 0) = \int d\mathbf{r} U_{\text{dd}}(\mathbf{r}) e^{-i\mathbf{k}' \cdot \mathbf{r}}. \quad (2.47)$$

To exploit the symmetries of the dipolar potential in the form (2.36), let us consider the spherical expansion of the plane wave

$$e^{i\mathbf{k}' \cdot \mathbf{r}} = 4\pi \sum_{\ell=0}^{\infty} \sum_{m=-\ell}^{\ell} i^{\ell} j_{\ell}(k'r) Y_{\ell m}^*(\hat{\mathbf{k}}') Y_{\ell m}(\theta, \phi) \quad (2.48)$$

where j_{ℓ} are the spherical Bessel functions and $\hat{\mathbf{k}}'$ is the versor of the momentum \mathbf{k}' . The integral (2.47) can then be separated into radial and angular contributions. From (2.36) and the orthogonality of the spherical harmonics $\int Y_{\ell' m'}^* Y_{\ell m} d\Omega = \delta_{\ell' \ell} \delta_{m' m}$, the only contribution from the plane wave expansion will be the $\ell = 2$ term. The remaining radial contribution to the integration, which is given by

$$R_{\ell} = \int_0^{\infty} dr r^2 j_{\ell}(k'r) \frac{1}{r^3}. \quad (2.49)$$

In the current case one has $R_2 = 1/3$. We can then rewrite the matrix element as

$$U_{\text{dd}}(\mathbf{k}', 0) = \sqrt{\frac{24}{5\pi}} \frac{\mu_0 (g_J \mu_B)^2}{4\pi} \frac{4\pi}{3} \sum_{m=-2}^2 Y_{2,m}^*(\hat{\mathbf{k}}') \mathcal{S}_{2,m} \quad (2.50)$$

For the scattering state (2.43) and in the case of distinguishable particles (we will consider the quantum statistics at the end of the section), the ratio between incoming

and outgoing currents gives the scattering cross section

$$\frac{d\sigma_{\alpha'\beta',\alpha\beta}}{d\Omega} = |f_{\alpha'\beta',\alpha\beta}|^2 \frac{v'}{v} = |f_{\alpha'\beta',\alpha\beta}|^2 \frac{k'}{k}. \quad (2.51)$$

For the initial state $|\uparrow\uparrow\rangle$, we obtain after substituting (2.44) and integrating over the solid angle

$$\sigma_{\alpha'\beta'} = \frac{m^2}{4\pi\hbar^4} \left| \langle \alpha'\beta' | U_{\text{dd}}(\mathbf{k}', 0) | \uparrow\uparrow \rangle \right|^2 \frac{k'}{k}, \quad (2.52)$$

which, explicitly writing the matrix element and again from the orthogonality of the spherical harmonics, gives

$$\sigma_{\alpha'\beta'} = \frac{32\pi}{15} \left(\frac{\mu_0 (g_J \mu_B)^2 m}{4\pi\hbar^2} \right)^2 \sum_m \left| \langle \alpha'\beta' | \mathcal{S}_{2,m} | \uparrow\uparrow \rangle \right|^2 \frac{k'}{k}. \quad (2.53)$$

So we are left with the evaluation of the expectation value of the spin operator (2.35).

Let us consider explicitly the case of the single spin-flip event in figure 2.8. The expectation value of the spin component of the interaction U_{dd} given in equation 2.36 is

$$\langle m'_1, m'_2 | \hat{J}_{1z} \hat{J}_{2-} | m_1, m_2 \rangle = m_1 \sqrt{J(J+1) - m_2(m_2+1)} \delta_{m'_1, m_1} \delta_{m'_2, m_2-1} \quad (2.54)$$

where m_i is the spin projection referring to the i -th particle. In the specific case we are considering, where the atoms start in the state $|\uparrow\uparrow\rangle = |J, J\rangle$, and the expectation value is thus

$$\langle \alpha'\beta' | \hat{J}_{1z} \hat{J}_{2-} | \uparrow\uparrow \rangle = \sqrt{2J^3} \delta_{\alpha', \uparrow} \delta_{\beta', \downarrow} \quad (2.55)$$

Taking the square of the expectation value and substituting in formula (2.53) we finally obtain

$$\sigma^{(1)} = \frac{64\pi}{15} J^3 \left(\frac{\mu_0 (g_J \mu_B)^2 m}{4\pi\hbar^2} \right)^2 \frac{k'}{k} \quad (2.56)$$

as the cross section for a single spin flip event. Notice that the dependence on the atomic species enters only via the mass and the spin $\sigma^{(1)} \propto g_J^4 J^3 m^2$, which justifies the fact that dipolar relaxation is a major problem for large spin atoms. The explicit expression for k'/k for a single spin-flip can be recovered from the energy conservation

$$\frac{\hbar^2 k'^2}{m} = \frac{\hbar^2 k^2}{m} + \Delta E_Z, \quad (2.57)$$

which, writing the formula for the Zeeman energy, gives

$$\frac{k'}{k} = \sqrt{1 + \frac{m\mu_B\mu_0 g_J B}{\hbar^2 k^2}}. \quad (2.58)$$

Note that in the double spin-flip case the released energy is doubled $2\Delta E_Z$ and the matrix element will be different. In both cases, in the limit of low initial energy $k \rightarrow 0$ (*i.e.* low

initial temperature) we expect $k'/k \propto B^{1/2}$.

2.5.3 Effect of Particle Statistics

Extending this calculation to a general case requires more involved calculations, since one has to consider a plane wave expansion (2.48) also for the initial wave function $\psi_0 = e^{ikr}$. In the frame of the Born approximation, the complete expression for the scattering cross section of indistinguishable particles is given in [47]. In this paper one can find the cross section for zero, one or two spin flips events, that are respectively given by

$$\sigma^{(0)} = \frac{8\pi}{15} J^4 \left(\frac{\mu_0(gJ\mu_B)^2 m}{4\pi\hbar^2} \right)^2 \frac{2}{3} [1 \pm h(1)] \quad (2.59)$$

$$\sigma^{(1)} = \frac{8\pi}{15} J^3 \left(\frac{\mu_0(gJ\mu_B)^2 m}{4\pi\hbar^2} \right)^2 [1 \pm h(k^{(1)}/k)] \frac{k^{(1)}}{k} \quad (2.60)$$

$$\sigma^{(2)} = \frac{8\pi}{15} J^2 \left(\frac{\mu_0(gJ\mu_B)^2 m}{4\pi\hbar^2} \right)^2 [1 \pm h(k^{(2)}/k)] \frac{k^{(2)}}{k}. \quad (2.61)$$

The function h is plotted in figure 2.9. The sign \pm above accounts for the particle statistics, $+$ being for the bosons and $-$ for fermions. The dependence on the final momenta is enclosed in the function

$$h(x) = -\frac{1}{2} - \frac{3}{8} \frac{(1-x^2)^2}{x(1+x^2)} \log \frac{(1-x)^2}{(1+x)^2}, \quad (2.62)$$

which is defined in the interval $h(x) \in [1, \infty)$ and is monotonically increasing in its domain from $h(1) = -1/2$ to $h(x \rightarrow \infty) = 1 - 4/x^2$.

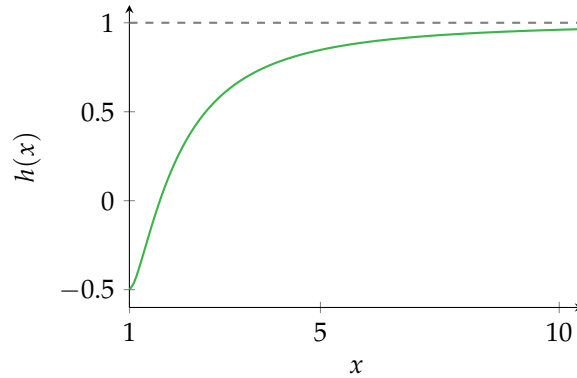


Figure 2.9 – Plot of the $h(x)$ function defined in the main text.

Using the cross section definition, one usually introduces the dipolar relaxation loss rate, which is given by

$$\beta_{\text{dd}} = 2 \langle (\sigma^{(1)} + \sigma^{(2)}) v \rangle_{\text{th}} = 2 \left\langle (\sigma^{(1)} + \sigma^{(2)}) \frac{\hbar k}{m/2} \right\rangle_{\text{th}}, \quad (2.63)$$

where the brackets label the thermal average over the initial relative velocity of the atoms v (or momentum k). The factor 2 accounts for the loss of the pair of atoms after each

collision. The quantity β_{dd} is experimentally accessible by measuring the population decay in the trap.

We now focus on the sign of the function h , which gives opposite behaviour of the cross section for the two statistics. In the asymptotic case $k' \gg k$, which according to (2.58) is the regime of high magnetic fields B or low temperatures, the fermionic inelastic cross sections $\sigma^{(1)}$ and $\sigma^{(2)}$ vanish as $(T/B)^{1/2}$. This suppression has been experimentally observed in ^{161}Dy [116]. On the contrary, in our case we focus on the bosonic isotope ^{164}Dy , for which the cross section increases as $\sigma^{(i)} \sim (B/T)^{1/2}$. Due to the additional dependence on the initial relative momentum k , the loss rate parameters scale as $\beta_{\text{dd}} \sim T/B^{1/2}$ and $\beta_{\text{dd}} \sim B^{1/2}$ for identical fermions and bosons respectively. Therefore, in the case of dipolar bosons the relaxation is suppressed only in the limit $B \rightarrow 0$.

In our case, we will see that the magneto-optical trap polarises the atoms in the absolute ground state $|J = 8, m_J = -8\rangle$. Once we load the atoms in the optical dipole trap, they are thus protected against dipolar relaxation.

In figure 2.10 we plot the loss rate $\beta_{\text{dd}}^{(1)}$ associated with one single spin-flip collision, for both fermions and bosons at different initial temperatures ^a, where the opposite behaviour in the two cases is clear.

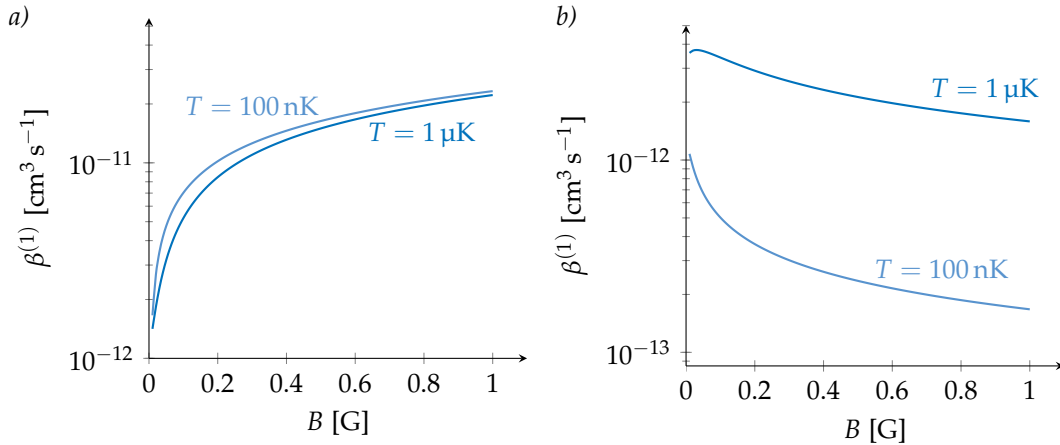


Figure 2.10 – Loss rate parameter for a single spin flip event as given in equation (2.61) as a function of the magnetic field B , for a) identical bosons and b) fermions. Note the different behaviours as a function of initial temperature.

As a final remark, we notice in (2.60) that the elastic cross section remains finite for fermions also in the limit of vanishing k , which means at $T \rightarrow 0$. If the interaction potential was purely short ranged, the elastic scattering of fermions would have been suppressed at low T . On the contrary, collisions between identical fermions are permitted in dipolar gases, and this fact has been successfully exploited in Erbium and Dysprosium gases to reach quantum degeneracy with standard evaporative cooling [57, 56].

With this observation we conclude the considerations on the dipolar nature of Dysprosium. All the problems presented in this chapter had to be carefully considered while constructing an experiment on ultra cold dipolar gases, since they are a clear obstacle to the achievement of Bose-Einstein condensation.

^aWe consider here thermal gases, for which the velocities are calculated from a Maxwell-Boltzmann distribution.

3

Off-Resonant Light-Atom Interaction

IN THIS chapter I review several aspects of the off-resonant interaction between an atom and laser light. Despite dipole forces are usually spin-independent, for Dysprosium atoms the interaction is complicated by its large spin in the ground state and its excitation spectrum with many narrow transitions. I focus mainly on the coupling of the atomic spin to the light polarisation and on the consequent advantages of Dysprosium over other atomic species (in particular over alkali atoms). We first consider a simple two level atomic model before dealing with the whole electronic structure of the atom. At the end of the chapter I consider the specific examples of the anisotropy in conservative traps for Dysprosium (see chapter ??) and the implementation of Raman transitions between ground state levels (see next chapter).

3.1 AC Stark Interaction

Let us consider a monochromatic electromagnetic wave at frequency ω prepared in a quasi-classical state, so that it can be written as:

$$\mathbf{E}_L = \mathbf{e}_L \mathcal{E} e^{-i\omega t} + \text{c.c.}, \quad (3.1)$$

where \mathcal{E} is the field magnitude and \mathbf{e}_L is the polarisation vector. We consider the atom-light coupling to be described by the electric dipole interaction [117]

$$\hat{V}_{AL} = -\hat{\mathbf{d}} \cdot \mathbf{E}_L = -\hat{\mathbf{d}} \cdot \mathbf{e}_L \mathcal{E} e^{-i\omega t} + \text{h.c.}, \quad (3.2)$$

where $\hat{\mathbf{d}}$ is the atomic dipole operator.

In the following we will assume the frequency of the light ω as being far from any atomic resonance. In this case, there is no real transition to any excited state, and we can consider only the ground state being populated. We can analyse the problem in the standard formalism of second order perturbation theory. Via a virtual absorption

and emission of a photon, the dipole operator couples the ground state $|g\rangle$ to all excited states $|e\rangle$ and then back to the ground state. The process mixes the ground state with the excited states, leading to a shift in the energy that can be written as

$$\delta E_g = - \sum_e \left(\langle g | \mathbf{d} \cdot \mathbf{E}_L^* | e \rangle \frac{1}{E_g - E_e - \hbar\omega} \langle e | \mathbf{d} \cdot \mathbf{E}_L | g \rangle + \langle g | \mathbf{d} \cdot \mathbf{E}_L | e \rangle \frac{1}{E_g - E_e + \hbar\omega} \langle e | \mathbf{d} \cdot \mathbf{E}_L^* | g \rangle \right) \quad (3.3)$$

This shift is the well known “light shift”, sometimes called in the literature AC (or dynamical) Stark shift, in contrast with the static Stark effect, which has a similar expression but without the oscillating term for the electric field.

In principle, the energy of the excited levels should be complex to account for their natural lifetime. If Γ_e is the natural decay rate of the state $|e\rangle$, the energy should be written as $E_e - i\hbar\Gamma_e/2$. In this case, the shift will be given by the real part of the formula above, while the imaginary part adds a finite lifetime to the ground state accounting for the photon scattering rate. Introducing the transition frequency $\omega_{eg} = (E_g - E_e)/\hbar$, we can rewrite the previous equation as

$$\begin{aligned} \delta E_g &= - \left[\frac{1}{\hbar} \sum_e \left(\frac{1}{\omega_{eg} - \omega - i\Gamma_e/2} + \frac{1}{\omega_{eg} + \omega - i\Gamma_e/2} \right) |\langle e | \mathbf{d} \cdot \boldsymbol{\epsilon} | g \rangle|^2 \right] |\mathcal{E}|^2 \\ &= -\alpha(\omega) |\mathcal{E}|^2, \end{aligned} \quad (3.4)$$

where we defined the frequency dependent atomic polarisability $\alpha(\omega)$. It is usual to consider separately the real part of the ground state energy shift and the imaginary part

$$\delta E_g = V_g - i\hbar \frac{\Gamma_g}{2}. \quad (3.5)$$

Let us first consider the real part

$$V_g(\omega) = -\text{Re}\{\alpha(\omega)\} |\mathcal{E}|^2. \quad (3.6)$$

Using the expression for the laser intensity $I = 2\varepsilon_0 c |\mathcal{E}|^2$, and explicitly writing the dependence of the intensity on the position $I = I(\mathbf{r})$, we recover the familiar expression of the dipole potential

$$V(\mathbf{r}, \omega) = -\frac{1}{2\varepsilon_0 c} \text{Re}\{\alpha(\omega)\} I(\mathbf{r}), \quad (3.7)$$

which is the basis of conservative optical traps [118]. From the above definition we can write also an expression for the photon (Rayleigh) scattering rate

$$\Gamma_g(\mathbf{r}, \omega) = \frac{1}{\hbar\varepsilon_0 c} \text{Im}\{\alpha(\omega)\} I(\mathbf{r}). \quad (3.8)$$

Let us now put ourselves in the framework of the rotating wave approximation (RWA) and neglect the counter-rotating term in equation (3.4). Within this approximation we recover another well known result. The real part of the ground state energy shift scales

as

$$V_g \propto \frac{\omega - \omega_{eg}}{(\omega_{eg} - \omega)^2 + \Gamma_e^2/4}, \quad (3.9)$$

and the potential is thus attractive for red detuned laser frequencies ($\omega < \omega_{eg}$) and repulsive otherwise. Also, we see that the scattering rate has the expected Lorentzian shape:

$$\Gamma_g \propto \frac{\Gamma_e/2}{(\omega_{eg} - \omega)^2 + \Gamma_e^2/4}. \quad (3.10)$$

As a concluding remark, we point out the different dependence on laser detuning. While the lifetime decreases as $\Gamma_g \sim 1/\Delta^2$, the light shift decay is softer as $V_g \sim 1/\Delta$.

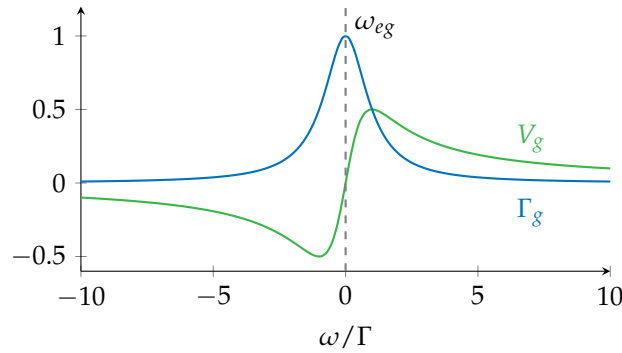


Figure 3.1 – Real and imaginary part of the dynamical Stark shift in the rotating wave approximation, respectively leading to the ground state light shift and scattering rate.

3.2 Light Shift Operator

The last results do not consider the internal structure of the atoms. More formal results are well known from optical pumping theory [119]. In this section, I will briefly sketch the calculation of the light shift, mainly following the treatment of [120], since it clarifies the notation I will use throughout the chapter and allows to easily make some fundamental remarks on the light-atom coupling.

Let us start by rewriting the AC Stark energy shift (3.3) as the expectation value $\delta E_g = \langle g | \hat{\mathcal{H}}_{\text{eff}} | g \rangle$ of an effective hamiltonian

$$\hat{\mathcal{H}}_{\text{eff}} = \hat{P}_g [(\mathbf{E}_L^* \cdot \hat{\mathbf{d}}) \mathcal{R}_{+\omega} (\mathbf{E}_L \cdot \hat{\mathbf{d}}) + (\mathbf{E}_L \cdot \hat{\mathbf{d}}) \mathcal{R}_{-\omega} (\mathbf{E}_L^* \cdot \hat{\mathbf{d}})] \hat{P}_g, \quad (3.11)$$

where we define the frequency-dependent operators

$$\mathcal{R}_{\pm\omega} = -\frac{1}{\hbar} \sum_e \frac{\hat{P}_e}{\omega_{eg} \pm \omega - i\Gamma_e/2}, \quad (3.12)$$

and we defined the projectors on the ground and excited states, respectively $\hat{P}_g = |g\rangle\langle g|$ and $\hat{P}_e = |e\rangle\langle e|$, where $|g\rangle$ and $|e\rangle$ contain all the relevant quantum numbers, that we will explicit in the following.

3.2.1 Tensor Polarisability

We neglect the fast oscillating term $\mathcal{R}_{+\omega}$ in equation (3.11) using the rotating wave approximation. In the case of a laser detuning $\Delta = \omega_{eg} - \omega$ larger than the transition linewidth ($\Delta > \Gamma_e/2$) we can further simplify the expression as

$$\frac{1}{\Delta - i\Gamma_e/2} \simeq \frac{1}{\Delta} + i\frac{\Gamma_e/2}{\Delta^2} \quad (3.13)$$

These assumptions are not necessary, but they give a lighter notation. In the following we will give also the exact formulae.

In the specific case of bosonic isotopes of Dysprosium, for which the nuclear magnetic moment $I = 0$, there is no hyperfine structure. For fermionic isotopes, we will consider the detuning being large with respect to the hyperfine splitting $\Delta \gg \Delta_{\text{HFS}}^a$, so that the projector operator on the excited state couples only to the fine structure basis $\hat{P}'_f = \sum_{m'_j} |J', m'_j\rangle\langle J', m'_j|$.

In the following we will also write explicitly the quantum numbers for the ground state manifold $|g\rangle = |J, m_J\rangle$. Let us consider the real part of the effective hamiltonian^b. We define the light shift operator

$$\hat{V} = -\mathbf{E}_L^* \cdot \hat{\boldsymbol{\alpha}} \cdot \mathbf{E}_L, \quad (3.14)$$

where the atomic polarisability is now a tensor, given by [121]

$$\begin{aligned} \hat{\boldsymbol{\alpha}} &= -\frac{\hat{P}_J \hat{\mathbf{d}} \hat{P}'_f \hat{\mathbf{d}} \hat{P}_J}{\hbar\Delta} \\ &= -\frac{1}{\hbar\Delta} \sum_{J'} \sum_{m'_j} |J, m_J\rangle\langle J, m_J| \hat{\mathbf{d}} |J', m'_j\rangle\langle J', m'_j| \hat{\mathbf{d}} |J, m_J\rangle\langle J, m_J|, \end{aligned} \quad (3.15)$$

Note that the projectors act on the whole ground state J manifold, since the shift may be different for different magnetic levels.

We can use the Wigner-Eckart theorem to factor out the angular dependence of the matrix element on the given Zeeman sub levels

$$\langle J', m'_j | \hat{d}_q | J, m_J \rangle = \langle J', m_J + q | \hat{d}_q | J, m_J \rangle = c_{m_J, q} \langle J || \hat{\mathbf{d}} || J' \rangle, \quad (3.16)$$

where q is the index of the spherical basis

$$\boldsymbol{\epsilon}_+ = -\frac{(\mathbf{e}_x + i\mathbf{e}_y)}{\sqrt{2}}, \quad \boldsymbol{\epsilon}_- = \frac{(\mathbf{e}_x - i\mathbf{e}_y)}{\sqrt{2}}, \quad \text{and} \quad \boldsymbol{\epsilon}_0 = \mathbf{e}_z, \quad (3.17)$$

and $c_{m_J, q}$ is the Clebsch-Gordan coefficient for the transition

$$\begin{aligned} c_{m_J, q} &= \langle J, m_J | 1, q; J', m'_j \rangle \\ &= (-1)^{J'-1+m_J} \sqrt{2J+1} \begin{pmatrix} J' & 1 & J \\ m'_j & q & -m_J \end{pmatrix}. \end{aligned} \quad (3.18)$$

^aA posteriori, this assumption is satisfied since $\Delta_{\text{HFS}} \lesssim 1$ GHz while we will consider detuning of the order of THz.

^bTo get the imaginary part, and hence the scattering rate Γ_{scat} , one should make the substitution $\Delta \rightarrow 2\Delta^2/\Gamma_e$ in the following results and divide by \hbar .

The reduced matrix element $d_{JJ'} = |\langle J || \hat{d} || J' \rangle|$ can be calculated from the Fermi golden rule using the linewidth

$$\Gamma_{JJ'} = \frac{\omega_{JJ'}^3}{3\pi\epsilon_0\hbar c^3} d_{JJ'}^2, \quad (3.19)$$

or from the transition probability coefficients^a

$$A_{JJ'} = \frac{\omega_{JJ'}^3}{3\pi\epsilon_0\hbar c^3} \frac{1}{2J'+1} d_{JJ'}^2. \quad (3.20)$$

As the reduced matrix element is independent on the Zeeman level, we can define the normalised atomic rising operator \hat{D}^\dagger and its hermitian conjugate, the atomic lowering operator \hat{D} , whose components are given by

$$\begin{aligned} \hat{D}_\mu^\dagger &= \frac{(\hat{P}_J \hat{d} \hat{P}_{J'})_\mu}{d_{JJ'}} = \sum_{m'_J} |J', m'_J\rangle \langle J', m'_J| \frac{\hat{d}}{d_{JJ'}} |J, m_J\rangle \langle J, m_J| \\ &= \sum_q \mathbf{e}_\mu \cdot \boldsymbol{\epsilon}_q^* c_{m_J, q} |J', m_J + q\rangle \langle J, m_J|, \end{aligned} \quad (3.21)$$

where the scalar product projects the spherical basis $\boldsymbol{\epsilon}_q^*$ of the operator into the cartesian basis \mathbf{e}_μ . We can use these operators to rewrite the light shift operator as

$$\hat{V} = -\frac{d_{JJ'}^2 |\mathcal{E}|^2}{\hbar\Delta} \mathbf{e}_L^* \cdot \hat{D} \hat{D}^\dagger \cdot \mathbf{e}_L, \quad (3.22)$$

where we separate the electric field amplitude \mathcal{E} from the polarisation \mathbf{e}_L . Note that in the literature, the above formula is often written in terms of the Rabi frequency $\Omega_R = d\mathcal{E}/\hbar$. Substituting the explicit value of the matrix element and expressing the field as light intensity, we get

$$\hat{V} = V_{JJ'} \mathbf{e}_L^* \cdot \hat{D} \hat{D}^\dagger \cdot \mathbf{e}_L \quad (3.23)$$

where using (3.19) the prefactor is

$$V_{JJ'} = -\frac{\hbar\Omega_R^2}{\Delta} = -\frac{3\pi c^2}{2\omega_{JJ'}^3} \frac{\Gamma_{JJ'}}{\Delta} I. \quad (3.24)$$

Let us consider equation (3.23), since all the relevant physics is in there. We see that light shift operator is separated in two different parts. $V_{JJ'}$ contains the information on the strength of the coupling, given by the matrix element and on the laser intensity and detuning. All the angular dependence of the shift is enclosed in the second adimensional part, which describes how the light polarisation couples to the internal spin state of the atoms. In the following we analyse the symmetries of this term.

Let us consider the product of the rising and lowering operators $\hat{D}\hat{D}^\dagger$, which are both vector operators (*i.e.* tensors of rank 1). This kind of product is called a dyad, which using standard tensor properties [123] is usually decomposed into a complete set of

^aThis is the convention for the data from [122].

irreducible spherical tensors $T^{(K)}$ of rank $K = 0, 1, 2$

$$\begin{aligned}\hat{D}_\mu \hat{D}_\nu^\dagger &= T^{(0)} + T^{(1)} + T^{(2)} \\ &= \frac{\hat{\mathbf{D}} \cdot \hat{\mathbf{D}}^\dagger}{3} \delta_{\mu\nu} + \frac{\hat{D}_\mu \hat{D}_\nu^\dagger - \hat{D}_\nu \hat{D}_\mu^\dagger}{2} + \left(\frac{\hat{D}_\mu \hat{D}_\nu^\dagger + \hat{D}_\nu \hat{D}_\mu^\dagger}{2} - \frac{\hat{\mathbf{D}} \cdot \hat{\mathbf{D}}^\dagger}{3} \delta_{\mu\nu} \right).\end{aligned}\quad (3.25)$$

These different components are respectively a scalar, a vector (or antisymmetric tensor) and a traceless symmetric tensor. Therefore, the light shift has the symmetries of this decomposition and is separated accordingly in three parts

$$\hat{V} = \hat{V}_{\text{scal}} + \hat{V}_{\text{vect}} + \hat{V}_{\text{tens}}. \quad (3.26)$$

In the following we will describe the effect of the single components.

No Hyperfine Structure

To further develop the calculation one uses the recursion relations for the Clebsch-Gordan coefficients to rewrite the atomic operator (3.21) in terms of spin operators. We will give the final result as in [124], on which we will base the calculations of the rest of the chapter

$$\hat{V}_{\text{scal}} = \alpha_J^s \hat{1} |E_L|^2 \quad (3.27)$$

$$\hat{V}_{\text{vect}} = -i\alpha_J^v (\mathbf{E}_L^* \times \mathbf{E}_L) \cdot \frac{\hat{\mathbf{J}}}{2J} \quad (3.28)$$

$$\hat{V}_{\text{tens}} = \alpha_J^t \frac{3[(\mathbf{E}_L^* \cdot \hat{\mathbf{J}})(\mathbf{E}_L \cdot \hat{\mathbf{J}}) + (\mathbf{E}_L \cdot \hat{\mathbf{J}})(\mathbf{E}_L^* \cdot \hat{\mathbf{J}})] - 2\hat{\mathbf{J}}^2}{2J(2J-1)}. \quad (3.29)$$

For a given J state, the factors α_J^s , α_J^v , α_J^t are respectively the scalar, vector and tensor polarisabilities, which are given by the following expressions:

$$\alpha_J^s = \sqrt{\frac{1}{3(2J+1)}} \alpha^{(0)} \quad (3.30)$$

$$\alpha_J^v = -\sqrt{\frac{2J}{(J+1)(2J+1)}} \alpha^{(1)} \quad (3.31)$$

$$\alpha_J^t = -\sqrt{\frac{2J(2J-1)}{3(J+1)(2J+1)(2J+3)}} \alpha^{(2)}, \quad (3.32)$$

with the frequency dependent polarisability $\alpha^{(K)}$ given as

$$\alpha^{(K)}(\omega) = (-)^{K+J} \sqrt{2K+1} \sum_{J'} (-)^{J'} \left\{ \begin{matrix} 1 & K & 1 \\ J & J' & J \end{matrix} \right\} \frac{V_{JJ'}}{|\mathcal{E}|^2}, \quad (3.33)$$

where $V_{JJ'}$ was defined in 3.24. The curly brackets stand for the Wigner-6j symbol [125].

The formulae above are valid within the RWA. If we remove this assumption we have to keep the counter rotating term $\mathcal{R}_{+\omega}$ in the light shift operator (3.11). In this case we

get a different expression for the polarisability

$$\alpha^{(K)}(\omega) = (-)^{K+J+1} \sqrt{2K+1} \sum_{J'} (-)^{J'} \left\{ \begin{matrix} 1 & K & 1 \\ J & J' & J \end{matrix} \right\} d_{JJ'}^2 \times \frac{1}{\hbar} \text{Re} \left\{ \frac{1}{\omega_{JJ'} - \omega - i\Gamma_{JJ'}/2} + \frac{(-1)^K}{\omega_{JJ'} + \omega - i\Gamma_{JJ'}/2} \right\}. \quad (3.34)$$

If we consider the imaginary part instead of the real one, we would then get the imaginary part of the operator (3.11), which corresponds to the scattering operator $\hat{\Gamma}_{\text{scat}}$.

With Hyperfine Structure

In the case where the ground state has an hyperfine structure, the expression above are slightly modified, since the relevant quantum numbers are now $|JIF\rangle$. Nevertheless, the dipole operator acts only in the space of the electronic spin and not on the nuclear spin $\hat{\mathbf{d}} = \hat{\mathbf{1}}_I \otimes \hat{\mathbf{d}}_J$, so that the calculation remains the same if we factor out the nuclear spin from the tensor decomposition using the following formula valid for a rank- K tensor [126]

$$\langle JIF || \mathbf{T}^{(K)} || JIF \rangle = (-1)^{F+I+J+K} (2F+1) \left\{ \begin{matrix} F & K & F \\ J & I & J \end{matrix} \right\} \langle J || \mathbf{T}^{(K)} || J' \rangle. \quad (3.35)$$

The expressions above are then modified since the atomic operators project on the F manifold instead of J . The total light shift is thus

$$\hat{V} = \alpha^s |E_L|^2 \hat{\mathbf{1}} - i\alpha^v (\mathbf{E}_L^* \times \mathbf{E}_L) \cdot \frac{\hat{\mathbf{F}}}{2F} + \alpha^t \frac{3[(\mathbf{E}_L^* \cdot \hat{\mathbf{F}})(\mathbf{E}_L \cdot \hat{\mathbf{F}}) + (\mathbf{E}_L \cdot \hat{\mathbf{F}})(\mathbf{E}_L^* \cdot \hat{\mathbf{F}})] - 2\hat{\mathbf{F}}^2 |E_L|^2}{2F(2F-1)}, \quad (3.36)$$

where the polarisabilities are now given by

$$\alpha_F^s = \alpha_J^s, \quad (3.37)$$

$$\alpha_F^v = (-1)^{J+I+F} \sqrt{\frac{2F(2F+1)}{F+1}} \left\{ \begin{matrix} F & 1 & F \\ J & I & J \end{matrix} \right\} \alpha^{(1)}, \quad (3.38)$$

$$\alpha_F^t = (-1)^{J+I+F+1} \sqrt{\frac{2F(2F-1)(2F+1)}{3(F+1)(2F+3)}} \left\{ \begin{matrix} F & 2 & F \\ J & I & J \end{matrix} \right\} \alpha^{(2)}, \quad (3.39)$$

with the same definition of $\alpha^{(K)}$ as before.

3.2.2 Light Polarisation and Fictitious Fields

The tensor decomposition of the polarisability reveals how the different components of the light shift correspond to different physical effects on the ground state spin manifold. The scalar light shift \hat{V}_{scal} is both polarisation and state independent. The energy shift (and the scattering rate) are then the same for all magnetic levels m_F , disregarding of the field polarisation. The rank-1 and rank-2 components of the polarisability are more interesting since they can drive spin dynamics. It is often useful to regard their effect as the action of a fictitious electromagnetic field on the atomic spin space.

Looking at equation (3.36) one can notice that the vectorial part of the light shift is analog to an effective magnetic field giving a Zeeman interaction $\hat{V}_{\text{vect}} = -\mathbf{B}_{\text{eff}} \cdot \hat{\mathbf{F}}$. The magnitude of the fictitious magnetic field is

$$\mathbf{B}_{\text{eff}} = \frac{\alpha^v}{2\mu_B g_F F} i(\mathbf{E}_L^* \times \mathbf{E}_L). \quad (3.40)$$

Since the polarisation of the light is always transverse, \mathbf{B}_{eff} will point in the direction of the light propagation. In the same manner, one can interpret the tensor part of the hamiltonian as an effective electric field \mathbf{E}_{eff} producing a second order Stark effect [119, 127].

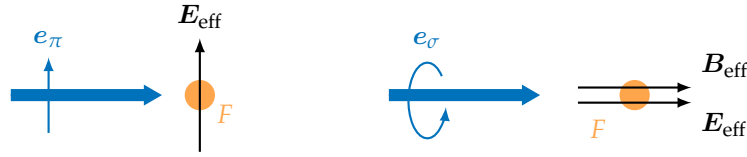


Figure 3.2 – The light shift acts on the atomic spin manifold F as fictitious fields according to the light polarisation.

The symmetries of these fictitious fields correspond to the symmetries of the light polarisation. Take for example the case of the effective magnetic field \mathbf{B}_{eff} , which is a pseudovector. We could not expect to create such a field using linear polarised light, because this one is invariant under reflection. If instead we use circular polarised light, since σ_- and σ_+ light are mirror images one of the other, we expect them to generate opposite \mathbf{B}_{eff} fields, as it is indeed the case.

Let us now consider a general light polarisation, taking the specific case of a laser propagating in the e_z direction. Using Jones notation, the polarisation is an arbitrary transverse vector in the form

$$\mathbf{E}_L = e_L \mathcal{E} e^{ikz} = \begin{pmatrix} \cos \theta \\ \sin \theta e^{i\phi} \end{pmatrix} \mathcal{E} e^{ikz} \quad (3.41)$$

up to a general phase, that here we set equal to unity. Here θ is the angle of polarisation and ϕ is the relative phase. We define also the ellipticity parameter $\mathcal{A} = \sin 2\theta$, which is equal to unity for a perfectly circular polarisation.

Since the scalar part is invariant on polarisation, let us consider first the vector part. Computing the products $(e_L^* \times e_L) \cdot \hat{\mathbf{F}}$ one gets

$$\hat{V}_{\text{vect}} = V_{JJ'} \alpha_F^v \mathcal{A} \sin \phi \frac{\hat{F}_z}{F}. \quad (3.42)$$

As we said, in the case of linearly polarised light the dephasing vanishes $\phi = 0$ and so does the vector light shift. The tensor part depends on the field polarisation via the term $(e_L^* \cdot \hat{\mathbf{F}})(e_L \cdot \hat{\mathbf{F}}) + (e_L \cdot \hat{\mathbf{F}})(e_L^* \cdot \hat{\mathbf{F}})$. The computation gives

$$\hat{V}_{\text{tens}} = V_{JJ'} \alpha_F^t \frac{3}{F(2F-1)} \left(\cos^2 \theta \hat{F}_x^2 + \sin^2 \theta \hat{F}_y^2 + \mathcal{A} \cos \phi \frac{\{\hat{F}_x, \hat{F}_y\}}{2} - \frac{\hat{F}^2}{3} \right), \quad (3.43)$$

where curly brackets denote the anticommutator between the spin operators.

Let us suppose there is an external magnetic field, which is large enough to permit to treat the effect of the light shift operator on a given magnetic level $|F, m_F\rangle$ as a first order perturbation

$$V(m_F) = \langle F, m_F | \hat{V} | F, m_F \rangle. \quad (3.44)$$

Let us study as an example two limit cases which are experimentally relevant. We consider first a linearly polarised light. Setting the quantisation axis along the polarisation direction, say e_x , the light shift has the form [128]

$$V(m_F) = V_0 \left(\alpha_F^s + \alpha_F^t \frac{3m_F^2 - F(F+1)}{F(2F-1)} \right). \quad (3.45)$$

For perfectly circular polarised light we have $\mathcal{A} = 1$, and $\phi = \pm\pi/2$ where the sign stands for right-hand and left-hand polarisation respectively. Choosing the quantisation axis along the light propagation direction e_z , we obtain

$$V(m_F) = V_0 \left(\alpha_F^s \pm \alpha_F^v \frac{m_F}{2F} - \alpha_F^t \frac{3m_F^2 - F(F+1)}{2F(2F-1)} \right). \quad (3.46)$$

Note that all previous results remain valid for atoms without hyperfine structure (just substitute F with J in the formulae), since the α coefficients are independent on the light polarisation.

3.3 Alkali Atoms

Let us now apply the previous results in the specific case of alkali atoms, before comparing to the case of Dysprosium in the next section

3.3.1 Line Structure

Understand the atomic structure of alkali is quite simple since they only have one valence electron. The ground state is a $^2S_{1/2}$ and they are thus spherical in the ground state ($L = 0$). Dipole transition can excite the electron to an upper P state, which the spin-orbit interaction splits in the states $^2P_{1/2}$ and $^2P_{3/2}$. In reminiscence of the Fraunhofer lines these are often called D_1 and D_2 transitions. We will stick to this notation in the following and we will label the (fine structure) energy splitting as $E_{\text{FS}} = \hbar\Delta_{\text{FS}}$.

Since the ground state is spherical, we expect the Stark shift to be isotropic. Anisotropy can thus exist only if the light couples to the electronic or nuclear spin state (if they do not vanish $S, I \neq 0$). Nevertheless, if the detuning with respect to the hyperfine structure is big, only the electron spin plays a role. The alkali spin in the ground state is $J = S = 1/2$, thus the operator $\hat{D}\hat{D}^\dagger$ acts on a two-dimensional manifold. The tensor decomposition (3.25) can have only four independent terms, and hence it stops at the vector contribution. To see that the rank-2 tensor contribution vanishes, one could also notice that the $6j$ -symbol (3.34) vanishes for $J = 1/2$ and $K = 2$.

In the frame of the RWA and using the formulae from the previous section, we can explicitly write the light shift as a sum of the contributions of the D_1 and D_2 lines

$$\hat{V} = \sum_{J'=D_1, D_2} \left(\alpha_{J'}^s \hat{\mathbb{1}} - i\alpha_{J'}^v (e_L^* \times e_L) \cdot \frac{\hat{J}}{2J} \right) = -\hbar\Omega_{\text{R}}^2 \left(\alpha_0 \hat{\mathbb{1}} - i\alpha_1 (e_L^* \times e_L) \cdot \frac{\hat{J}}{2J} \right) \quad (3.47)$$

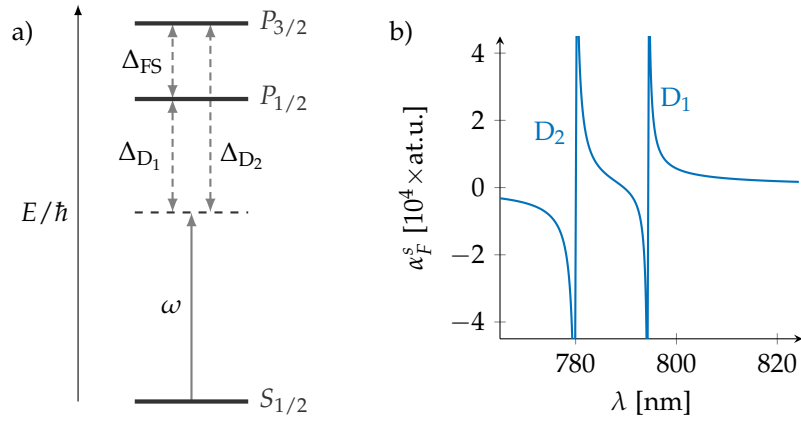


Figure 3.3 – a) Optical transition for an alkali atom. The ground state couples to the excited states $^2P_{1/2}$ and $^2P_{3/2}$ (respectively called D_1 and D_2 line) which are split by the fine structure Δ_{FS} as a consequence of the atomic spin-orbit interaction. b) Scalar part of the atomic polarisability for Rubidium.

Note that, as we have seen, for linear polarisation the vector light shift vanishes and one is left with a pure isotropic scalar shift. We define the coefficient for the scalar polarisability

$$\alpha_0 = \frac{1}{3} \left(\frac{1}{\Delta_{D_1}} + \frac{2}{\Delta_{D_2}} \right) \quad (3.48)$$

and the vector part

$$\alpha_1 = \frac{1}{3} \left(\frac{1}{\Delta_{D_1}} - \frac{1}{\Delta_{D_2}} \right) \quad (3.49)$$

In the case of large detuning with respect to the fine splitting, $\Delta_{D_1} \simeq \Delta_{D_2} = \Delta \gg \Delta_{FS}$, the vector contribution can be approximated as

$$\alpha_1 = \frac{1}{3} \left(\frac{1}{\Delta_{D_1}} - \frac{1}{\Delta_{D_2}} \right) \sim \frac{\Delta_{FS}}{\Delta^2} \quad (3.50)$$

Note that the vector term is strongly suppressed at large detuning, with respect to the scalar one, since they decay differently as $\alpha_0 \sim \Delta^{-1}$ and as $\alpha_1 \sim \Delta^{-2}$. This effect, which physically is due to the destructive interference between the two virtual transitions, should not be surprising. As we mentioned already, the anisotropy in the polarisability is generated solely from the coupling to the excited manifold, if the detuning Δ is too large to resolve the fine structure Δ_{FS} , it is clear that the vector term is suppressed.

3.3.2 Raman Coupling

In the next chapter we will make use of Raman coupling between ground state Zeeman levels. We consider a “ Λ ” configuration (figure 3.4), in which one couples two levels in the ground state manifold via a two photon (Raman) transition. One needs then two laser fields, of frequency ω_1 and ω_2 , having also a different polarisation in order to exchange momentum with the atomic spin. We will further discuss this scheme in the

next chapter, while in the following we focus on the main limitation of this technique, that is the heating induced by the laser coupling.

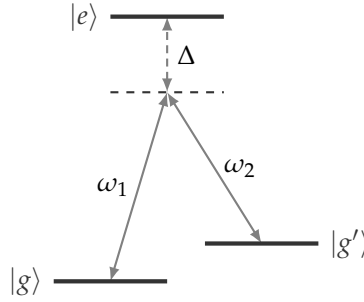


Figure 3.4 – Raman transition in a “ Λ ” configuration coupling two adjacent magnetic levels of the ground state. In the case considered in this paragraph, $|e\rangle$ is the D_1 or D_2 line of the alkali’s excited manifold. In the far detuned case the two lines will be indistinguishable for the laser light.

We have seen that the photon exchange with the light fields leads to a scattering rate Γ_{scat} from the ground state. Every scattered photon will transfer the recoil energy E_r to the atom. The power dissipated in the process is given by

$$P_{\text{scat}} = E_r \Gamma_{\text{scat}} = \frac{\hbar^2 k^2}{2m} \Gamma_{\text{scat}}, \quad (3.51)$$

from which one can get the heating rate $\dot{Q} = P_{\text{scat}}/k_B$.

The coupling between states is driven by the spin-dependent part of the light shift hamiltonian, which in the alkali case reduces solely to the vector term. The relevant figure of merit for Raman coupling is then given by

$$\mathfrak{M} = \frac{V_{\text{vect}}/\hbar}{\Gamma_{\text{scat}}}, \quad (3.52)$$

where we divide by \hbar to have an adimensional definition. The main problem of alkali atoms comes from the fact that the detuning dependence of the vector part, as we have seen in the previous section, is given by

$$V_{\text{vect}} \sim \frac{1}{3} \hbar \Omega_R^2 \frac{\Delta_{\text{FS}}}{\Delta^2} \quad (3.53)$$

and has then the same scaling as the scattering rate

$$\Gamma_{\text{scat}} = \Omega_R^2 \frac{\Gamma}{6} \left(\frac{1}{\Delta_{D_1}^2} + \frac{2}{\Delta_{D_2}^2} \right) \sim \frac{1}{2} \Omega_R^2 \frac{\Gamma}{\Delta^2} \quad (3.54)$$

As a consequence, the ratio between the vector light shift and the scattering rate is bounded. The merit factor is then bounded too and scales as

$$\mathfrak{M} \sim \frac{2}{3} \frac{\Delta_{\text{FS}}}{\Gamma}. \quad (3.55)$$

One is then limited by this ratio and the best coupling can hence be obtained for

alkali atoms having the largest hyperfine splitting Δ_{FS} , such as Rubidium, for which $\mathfrak{M} \simeq 8 \times 10^5$. For this merit factor and for a coupling strength of the order of one recoil energy $V_{\text{vect}}/\hbar = 1E_{\text{r}}/\hbar \simeq 2\pi \times 3.7 \text{ kHz}$, we get a heating rate of $\dot{Q} \simeq 5 \text{ nK s}^{-1}$. Although the heating rate is quite low, it limits significantly the lifetime of Raman coupled samples, for example to 1.4 s in reference [61]. The heating rate is much more dramatic in the case of fermionic alkali, like Lithium or Potassium ($\mathfrak{M} \simeq 1 \times 10^3$ and $\mathfrak{M} \simeq 2 \times 10^5$ respectively), where a significant increase in the gas temperature has been measured for example in reference [69]. For the same coupling strength as above $V_{\text{vect}} = 1E_{\text{r}}$, we get indeed heating rates as large as $\dot{Q} \simeq 115 \text{ nK s}^{-1}$ for Potassium and $\dot{Q} \simeq 1.5 \text{ mK s}^{-1}$ for Lithium.

3.4 Dysprosium

Let us now switch to the case of Dysprosium atoms. Note that the following arguments can also apply to lanthanide atoms with a similar electronic structure, like Erbium (but not Ytterbium which is spherical in the ground state 1S_0).

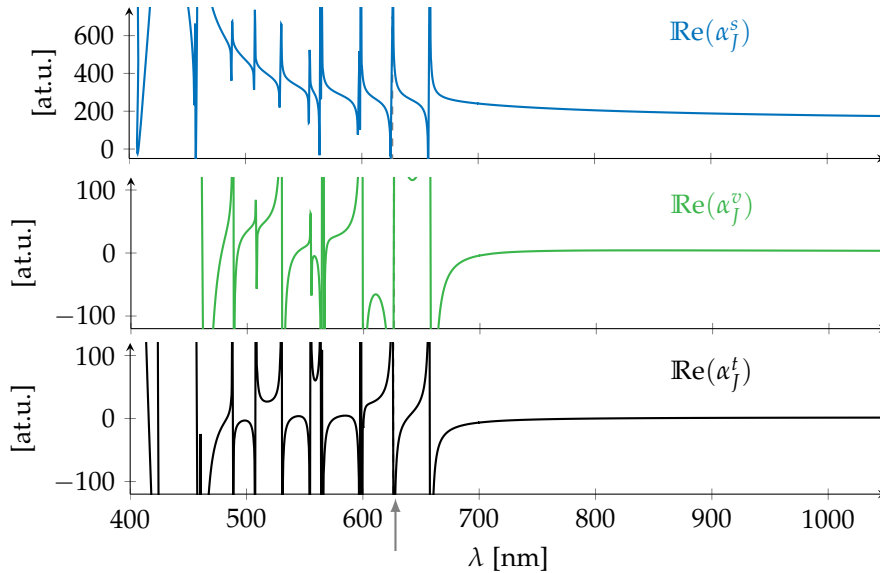


Figure 3.5 – Real part of the polarisability for Dysprosium atoms. The transitions data are taken from [122]. Note that the asymptotic values of vector and tensor part are vanishing, while the scalar contribution remains the finite. The arrow points at the 626.082 nm transition on which we focus on in the following.

3.4.1 Line Structure

The Dysprosium spectrum is characterised by the presence of strong transitions ($\Gamma \simeq 2\pi \times 30 \text{ MHz}$), which are comparable to the D_1 and D_2 lines in alkali. They sit in the blue part of the optical spectrum at 405, 419 and 421 nm. This singlet structure originates from the j - j coupling of the valence electron optical transition $^1S_0 \rightarrow ^1P_1$ to the 5I_8 spectral term of the inner shell electrons (thus $J = 7, 8, 9$ for the three transitions respectively). If these lines alone were present in the spectrum, the tensor part of the light shift would cancel at large detuning like for alkali atoms. On the contrary, Dysprosium's

spectrum has many weaker transitions at lower energies (see appendix A), which are quite far from the strong blue ones and have a large splitting, typically of some nanometers (it is wide due the j - j coupling mechanism, like for the blue lines above).

In figure 3.5 we plot the real part of Dysprosium polarisability calculated using equation (3.39)^a. The calculations are performed on a limited set of energy levels and more complete results are given in reference [84]. In the same study, one finds that the tensor and vector contributions to the polarisability do not vanish at large detunings but tend to finite values, which however are quite weak since they are two orders of magnitude smaller the scalar term.

Our goal will be to exploit the light shift of these resonances, the total scattering rate being drastically reduced with respect to the alkali atoms scenario. In fact, the scattering from these transitions will be small due to their narrow line width. Therefore, as one can see in figure 3.6, far from any narrow transition the scattering is dominated by the background value given by the strong blue transitions (whose scattering is also weak in the red side of the optical spectrum).

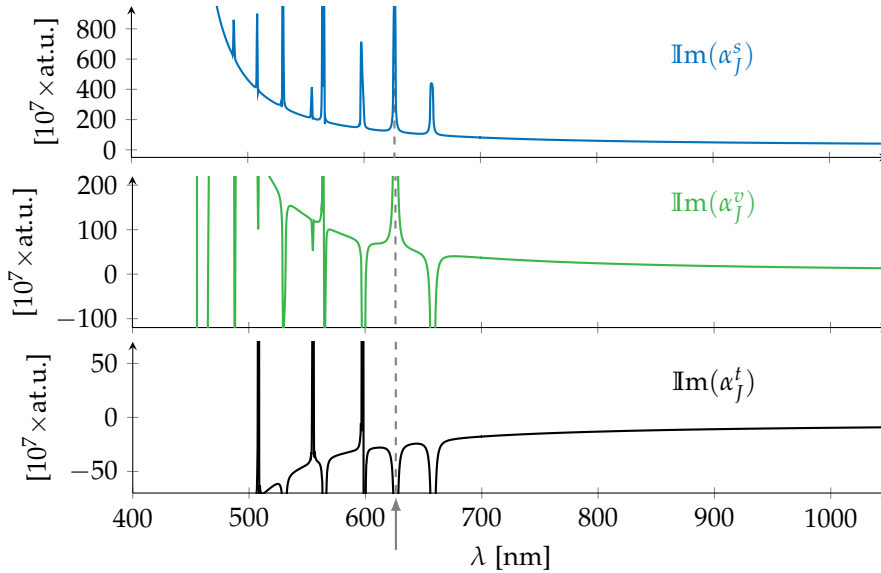


Figure 3.6 – Imaginary part of the polarisability for Dysprosium atoms. As in previous image, data are from [122] and calculation uses equation (3.39). Note that far from any single transition, the only relevant contribution comes from the broad lines at ~ 400 nm.

In figure 3.6 one can also see that at infrared wavelengths all components contribute to the imaginary part of the polarisability, while the real part was essentially dominated by the scalar term. The scattering rate is then expected to depend on the light polarisation for far detuned traps, as it was proved in [84] and in previous similar work on Erbium atoms [129]. The theoretical treatment was recently refined by the addition of configuration-interaction mixing between excited levels in the case of Holmium atoms [130], which is also a lanthanide.

Previous experimental works in the group of Lev in Stanford focused on the narrow-

^aThe results are in atomic units. The conversion factor for the electric polarisability in SI units is $1 \text{ at.u.} = e^2 a_0^2 / E_h = 1.648 \times 10^{-41} \text{ C}^2 \text{ m}^2 \text{ J}^{-1}$

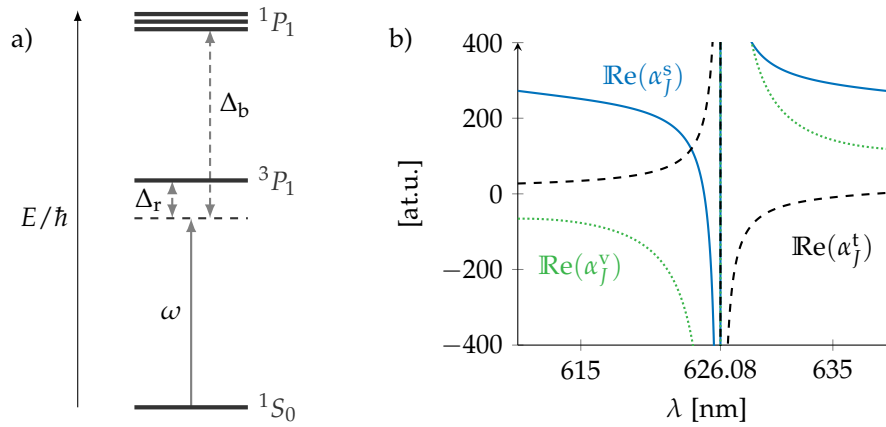


Figure 3.7 – a) Relevant transitions for Dysprosium that we consider in the text. The spectral terms refer only to the valence electrons configuration. The strong transitions in the blue at ~ 400 nm are detuned Δ_b from the laser frequency ω , which is close to a narrow transition. We will consider the transition at 626.082 nm and label the relative detuning as Δ_r . b) Real part of the polarisability close to the 626 nm transition. Real, vector and tensor components are the solid, dotted and dashed lines respectively.

line transition at 741 nm ($\Gamma = 2\pi \times 2$ kHz) [131]. We plan to work instead on the transition at 626 nm, which has a line width $\Gamma = 2\pi \times 135$ kHz. It is the same transition we are using for the magneto optical trapping and is experimentally quite convenient, since we can use the same type of laser setup. In the following we will consider the light shift given by this line alone, since all other transitions are far (with respect to their line widths). On the contrary, we should instead consider the blue lines for the computation of heating rates and scalar polarisability. Figure 3.7 shows this simplified line structure.

3.4.2 Light Shift Anisotropy at 626 nm

We consider here the case of the bosonic isotope ^{164}Dy , which has $I = 0$ and hence no hyperfine interaction. We want to create an optical trap (chapter 7) for Dysprosium atoms using the 626 nm transition. If the laser frequency is close to resonance we can use the RWA formula

$$\hat{V}_r = V_{0,r} \left(\alpha_0 \hat{1} |e_L|^2 - i\alpha_1 (\mathbf{e}_L^* \times \mathbf{e}_L) \cdot \frac{\hat{\mathbf{J}}}{2J} + \alpha_2 \frac{3[(\mathbf{e}_L^* \cdot \hat{\mathbf{J}})(\mathbf{e}_L \cdot \hat{\mathbf{J}}) + (\mathbf{e}_L \cdot \hat{\mathbf{J}})(\mathbf{e}_L^* \cdot \hat{\mathbf{J}})] - 2\hat{\mathbf{J}}^2}{2J(2J-1)} \right) \quad (3.56)$$

where $V_{0,r}$ is the coefficient defined in equation (3.24), which, using the parameters of the red transition, is then

$$V_{0,r} = \frac{3}{16\pi^2 c^2} \frac{\lambda_r^3 \Gamma_r}{\Delta_r} I \quad (3.57)$$

The 626 nm transition couples the ground state $J = 8$ to the excited state $J' = 9$. Following the formulae given in previous sections, the numerical values of the polarisability

coefficients are

$$\alpha_0 = \frac{19}{51} \quad \alpha_1 = \frac{152}{153} \quad \alpha_2 = -\frac{40}{153} \quad (3.58)$$

Notice how the contributions of the different terms are comparable. Therefore one would do a significant error if one would neglect the anisotropic terms.

In our simplified model, the total light shift is the sum of the red and blue lines contributions $\hat{V} = \hat{V}_b + \hat{V}_r$. Since we are far from the blue transition, the same argument that we found in alkali atoms is valid also for Dysprosium: the only non vanishing contribution comes from the scalar polarisability. Moreover, since the detuning is very large, the RWA does not hold. We have then to consider also the counter rotating term, which gives for the light shift

$$\hat{V}_b = V_{0,b} \hat{1} \left(\frac{1}{\omega - \omega_b} + \frac{1}{\omega + \omega_b} \right) = V_{0,b} \hat{1} \frac{2\omega_b}{\omega^2 - \omega_b^2} \quad (3.59)$$

In the specific case of $\lambda \sim 626$ nm, neglecting the counter rotating term will give an error of $\sim 15\%$ on the result. Here, we defined

$$V_{0,b} = \frac{3\pi c^2 \Gamma_b}{2\omega_b^3} I \quad (3.60)$$

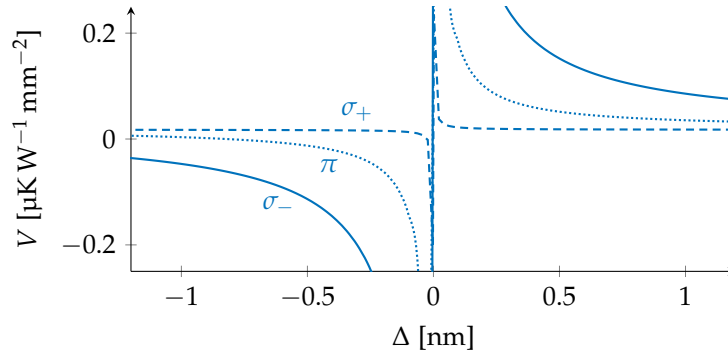


Figure 3.8 – Anisotropy of the trapping potential in the proximity of the 626 nm transition for the atomic state $|J = 8, m_J = -8\rangle$. The three curves show the light shift for different polarisation of the light field.

As a numerical example, let us consider the case of atoms polarised in the absolute ground state $|g\rangle = |J = 8, m_J = -8\rangle$. The total light shift is given by

$$\langle g | \hat{V} | g \rangle = C V_{0,r}(\omega) + V_b(\omega). \quad (3.61)$$

In this expression we can see practically what we observed in the first section: all the angular dependence on the light shift is contained in C , which is a numerical factor. In the case of light polarised linearly along the quantisation axis one finds $C = 37/153$. In the case of right- or left-hand circular polarised beam, propagating in the direction of the quantisation axis, $C = 1$ and $C = -1/153$ respectively.

In figure 3.8 the results are given in μK for circular light and linear light, normalised on a laser intensity of $I = 1 \text{ W mm}^{-2}$. These results coincide with the light shift calculated

from the total spectrum within some per mille error, justifying to consider the red transition “alone”.

Let us remind that the polarisation dependence does not concern the trapping potential alone but also the heating rate associated with the imaginary part of the polarisabilities.

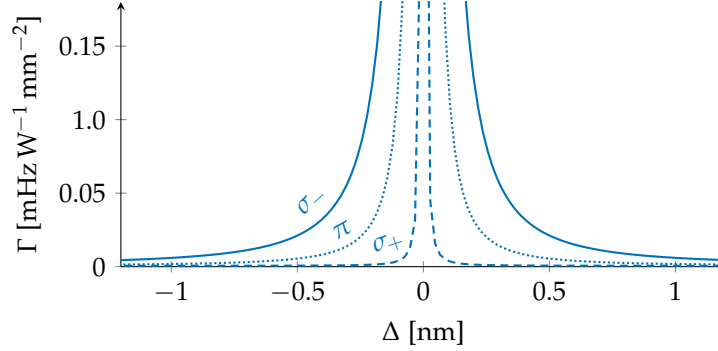


Figure 3.9 – The heating rate associated with the potential taken from the equation (3.56).

An experimental measurement of trap anisotropy was performed in Stanford using linearly polarised light at two different angles with respect to the quantisation axis on the ultra narrow transition at 741 nm [132].

3.4.3 Raman Coupling

We consider now a Raman transition as we did for alkali atoms, but addressing the 626 nm transition of Dysprosium. We already know that the interaction has to take into account the tensor term, since it has the same order of magnitude than the scalar one. The Raman coupling is then proportional to $V_{\text{vect}} \sim V_{\text{tens}} \sim V_{0,r}/\Delta_r$. The blue line is far from resonance and contributes only to the scalar shift, that does not enter the Raman coupling. Nevertheless, the blue transition has instead to be taken into account for the calculation of the total scattering rate

$$\Gamma_{\text{scat}} = \Gamma_{\text{scat},b} + \Gamma_{\text{scat},r} \sim V_{0,b} \frac{\Gamma_b}{\Delta_b^2} + V_{0,r} \frac{\Gamma_r}{\Delta_r^2} \quad (3.62)$$

The merit factor is thus

$$\mathfrak{M} \sim \frac{V_{0,r}}{\Delta_r} \left(V_{0,b} \frac{\Gamma_b}{\Delta_b^2} + V_{0,r} \frac{\Gamma_r}{\Delta_r^2} \right)^{-1} \sim \left(\frac{\Gamma_b^2 \Delta_r}{\Delta_b^2 \Gamma_r} + \frac{\Gamma_r}{\Delta_r} \right)^{-1}, \quad (3.63)$$

which is maximised for a choice of red detuning

$$\Delta_r = \frac{\Delta_b}{\Gamma_b} \Gamma_r. \quad (3.64)$$

Since the ratio between the linewidths is $\Gamma_b/\Gamma_r \simeq 0.5\%$ and $\Delta_b \sim 200$ nm, one should expect an optimum merit factor for $\Delta_r \simeq 1$ nm. For the detuning choice above, one gets

$$\mathfrak{M} \sim \frac{\Delta_b}{\Gamma_b}. \quad (3.65)$$

Therefore, one can easily gain some orders of magnitude with respect to alkali atoms, where the merit factor was $\mathfrak{M} \sim \Delta_{\text{FS}}/\Gamma$, since the fine structure splitting of the D₁ and D₂ lines is only a few nanometers wide ($\Delta_{\text{FS}} \simeq 15$ nm for Rubidium, $\Delta_{\text{FS}} \simeq 3$ nm for Potassium), while here the detuning is $\Delta_b \simeq 205$ nm.

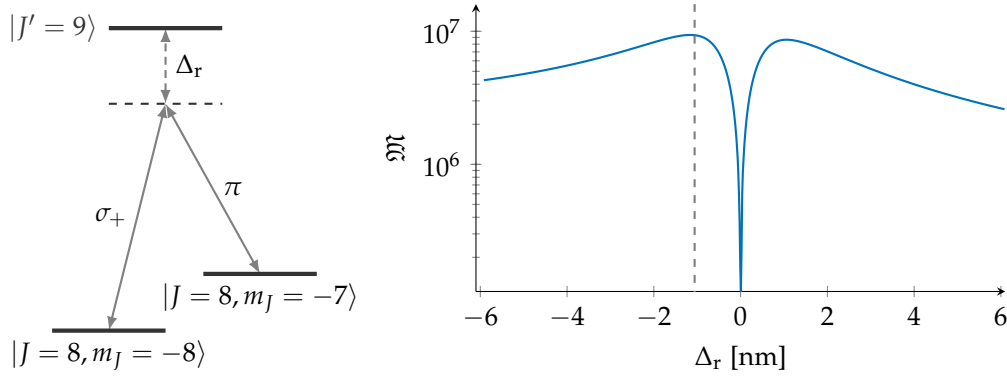


Figure 3.10 – The scheme of the considered example Raman transition $\pi - \sigma_+$ and the calculated figure of merit as a function of the laser detuning from the 626 nm resonance. One finds an optimum at $\Delta_r \simeq -1.1$ nm.

To give a more quantitative estimate of the optimum detuning, we consider as a specific example a Raman transition using a π polarised electric light and a σ_+ polarised one. We suppose that the two lasers have the same intensity $I_\pi = I_{\sigma_+} = I$ and that we couple the states $|J, m_J = -J\rangle$ and $|J, m_J = -J + 1\rangle$ of the ground state $J = 8$ (see figure 3.10). We can then numerically compute the merit factor using the whole expression of the polarisability. The result is plotted in figure 3.10. It is clear that one can find an optimum detuning at $\Delta \simeq -1.1$ nm, which corresponds to the detuning we found by dimensional analysis above. The heating rate at optimum detuning is as low as $\dot{Q} \simeq 0.3 \text{ nK s}^{-1}$ for a coupling strength $V_{0,r} = 1E_r$.

The heating rate is reduced by almost one order of magnitude with respect to Rubidium and by two orders of magnitude with respect to Potassium. This low scattering should lead to much longer lifetimes of the atomic cloud in the presence of a Raman coupling. In the next chapter we will consider a possible implementation of light-induced synthetic gauge fields, which will benefit from the use of Dysprosium over other atomic species.

4

Towards Synthetic Gauge Fields

IN THIS chapter I describe a possible implementation of a synthetic magnetic field in a cloud of ultracold Dysprosium atoms, exploiting the advantages of this atomic species presented in the previous chapter. The motion of a particle of charge q in a magnetic field is driven by the minimal coupling hamiltonian, which is

$$\hat{\mathcal{H}} = \frac{1}{2m} (\hat{\mathbf{p}} - q\mathbf{A}(\hat{\mathbf{r}}))^2, \quad (4.1)$$

where A is the electromagnetic vector potential and $\hat{\mathbf{p}}$ the momentum operator. Despite the simplicity of the hamiltonian, quantum particles in gauge fields give rise to an incredible variety of phenomena of great interest in contemporary physics such as the quantum Hall effect or spin orbit coupling and topological insulators (the latter cases have a non-Abelian gauge potential \hat{A}). *A priori*, ultracold gases might not seem a suitable system to study such physics, since atoms are neutral ($q = 0$) and are thus unaffected by (4.1).

Nevertheless, in the past years different methods have been realised or proposed to engineer gauge fields in cold atoms. These fields are called “synthetic” or “artificial”, meaning that they are not generated from charge distributions or currents as “real” electromagnetic fields, but still they affect the motion of the atoms in the same manner as a real field would do.

The most widely known method that has been implemented is to set the gas in rotation. In fact, in the reference frame co-rotating with the trap, one atom moving with a velocity v will be affected by the Coriolis force $F = 2mv \times \Omega$, where Ω is the angular velocity of the rotating cloud. This fictitious force is clearly equivalent to the Lorentz force by setting $2m\Omega = qB$. The rotation will induce also a centrifugal force, which can be compensated by the confining potential, and the system is then described by a time independent hamiltonian which is equivalent to (4.1). In the case of interacting gases one expects to observe a lattice of vortices in the atomic density, oriented along

the rotation axis (equivalently, along the magnetic field), as it was indeed observed in rotating condensates [133, 134, 135].

In the last years, novel techniques rely instead on clever couplings to the light field (see the extensive reviews [136, 60]). In this chapter we will see that the manipulation of the atomic internal state using Raman transition can give rise to synthetic fields (which, in contrast with rotating condensates, appear directly in the laboratory frame). In the previous chapter we explained that the spectrum and the large spin of Dysprosium can reduce the heating rate of Raman transitions, with respect to an alkali gas having the same coupling strength (or equivalently, one can increase the coupling strength for the same heating rate). Therefore, Dysprosium should allow to reach light-induced gauge fields much stronger in magnitude than what has been realised so far.

4.1 Light-induced Gauge Fields

The basic idea of this method relies on a spatially varying atom-light interaction. Via two-photon transitions, Raman lasers are used to couple neighbouring Zeeman levels $|m_J\rangle$ of the atom, which are degenerate in the absence of external fields. The eigenstates of the coupling hamiltonian, the so called “dressed states”, are linear combinations of the electronic ground state levels $|m_J\rangle$. When the Raman coupling is spatially dependent, the dressed states and their eigenenergies also vary in space. If the system is prepared in one specific dressed state and the atom moves slowly enough to remain in this state (adiabatic following), the atomic wave function can acquire a non-trivial Berry’s phase, whose value depends solely on the geometry of the adiabatic surface where the dressed state is evolving [137]. The acquired phase is equivalent to the Aharonov-Bohm phase that a charge particle picks up moving in a magnetic field [138]. One can thus identify the synthetic gauge field with the engineered Berry’s curvature.

In the following section we give an explicit expression for the synthetic field before describing a practical implementation. For the theoretical derivation I follow closely references [139]. To avoid confusions, I stick to the notation of the previous chapter: \mathbf{B}_{eff} will label the fictitious Zeeman field appearing in the light-atom coupling and I will use calligraphic \mathcal{B} for the synthetic gauge field.

4.1.1 Hamiltonian and Eigenstates

Let us consider the case of an atom moving in an external potential $V(\mathbf{r})$, while the internal variables are subjected to a spatially inhomogeneous coupling $\hat{\mathcal{H}}_{\text{int}}(\mathbf{r})$. The hamiltonian describing the dynamics of both internal (electronic) and external (centre of mass) variables of the atom is

$$\hat{\mathcal{H}}(\mathbf{r}) = \left(\frac{\mathbf{p}^2}{2m} + V(\mathbf{r}) \right) \hat{\mathbb{1}} + \hat{\mathcal{H}}_{\text{int}}(\mathbf{r}), \quad (4.2)$$

where the identity $\hat{\mathbb{1}}$ and the operator $\hat{\mathcal{H}}_{\text{int}}(\mathbf{r})$ act on the internal state of the atom. In the following, we consider the case of a pure vectorial coupling of the light to the spin, equivalent to an effective magnetic field $\mathbf{B}_{\text{eff}}(\mathbf{r})$, as we described in the previous chapter (hence we neglect for the moment the rank-2 tensor part of the light shift). The interaction is written as

$$\hat{\mathcal{H}}_{\text{int}}(\mathbf{r}) = -\hat{\boldsymbol{\mu}} \cdot \mathbf{B}_{\text{eff}}(\mathbf{r}), \quad (4.3)$$

where the operator is defined as $\hat{\mu} = g_J \mu_B \hat{\mathbf{J}}$. The laser frequency is assumed to be far detuned from the excited state, so that the spin dynamics belongs to the $(2J + 1)$ -dimensional ground state manifold. The external potential $V(\mathbf{r})$ appearing in (4.2) is provided by the scalar part of the light shift.

Let us parametrise the effective field as $\mathbf{B}_{\text{eff}} = B_{\text{eff}} \mathbf{e}_B$, where the unit vector $\mathbf{e}_B = (\theta, \phi)$ is given by the spherical angles (see figure 4.1), that one defines as

$$\cos \theta = \frac{B_z^{\text{eff}}}{B_{\text{eff}}} \quad \text{and} \quad \tan \phi = \frac{B_y^{\text{eff}}}{B_x^{\text{eff}}}. \quad (4.4)$$

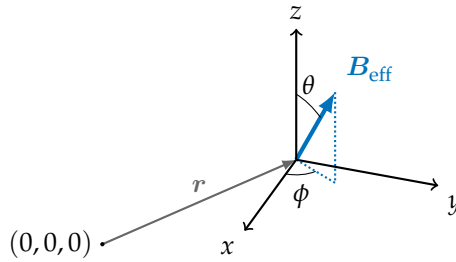


Figure 4.1 – Parametrisation of the effective field $\mathbf{B}_{\text{eff}}(\mathbf{r})$.

Using this parametrisation, equation (4.3) can be written as $\hat{\mathcal{H}}_{\text{int}} = -g_J \mu_B B_{\text{eff}} \hat{\mathbf{J}}_u$, where $\hat{\mathbf{J}}_u$ is the spin operator projected on the effective field direction. One can relate it to $\hat{\mathbf{J}}_z$ by the unitary transformation

$$\hat{\mathbf{J}}_u = \hat{U} \hat{\mathbf{J}}_z \hat{U}^\dagger \quad \text{with} \quad \hat{U} = \hat{\mathcal{R}}_z(\phi) \hat{\mathcal{R}}_y(\theta) \hat{\mathcal{R}}_z^\dagger(\phi), \quad (4.5)$$

where we use the standard definition for the rotation operators

$$\hat{\mathcal{R}}_j(\varphi) = \exp\left(-\frac{i}{\hbar} \hat{\mathbf{J}}_j \varphi\right), \quad (4.6)$$

which rotates of an angle φ around the j -axis. For each atomic position \mathbf{r} , the interaction hamiltonian can be diagonalised using the unitary transformation (4.5), and one finds the eigenstates (dressed states)

$$|\psi_{m_j}\rangle = \hat{U} |m_j\rangle = \exp\left[i\left(m_j - \frac{\hat{J}_z}{\hbar}\right)\phi\right] \exp\left[-i\frac{\hat{J}_y}{\hbar}\theta\right] |m_j\rangle \quad (4.7)$$

with eigenenergies $E_{m_j} = g_J \mu_B m_j B_{\text{eff}}$. If an atom is prepared in a dressed state $|\psi_{m_j}\rangle$ and its kinetic energy is smaller than the splitting $\Delta E = g_J \mu_B B_{\text{eff}}$ between neighbouring energy surfaces, one can neglect the contributions from $m'_j \neq m_j$, since during the atomic motion the internal state will follow adiabatically the space dependence of $|\psi_{m_j}\rangle$.

Separating internal and external atomic variables, we can write the total (space dependent) wave function as

$$|\Psi(\mathbf{r}, t)\rangle = \sum_{m_j} \phi_{m_j}(\mathbf{r}, t) |\psi_{m_j}\rangle \quad (4.8)$$

where $\phi_{m_j}(\mathbf{r}, t)$ is the wave function describing the atom's centre of mass motion.

One can now write the the Schrödinger equation for the wave function $i\hbar\partial_t|\Psi\rangle = \hat{\mathcal{H}}|\Psi\rangle$, project it on the selected state $\langle\psi_{m_J}|$, and find that the evolution of the centre of mass motion $i\hbar\partial_t\phi_{m_J} = \mathcal{H}_{\text{c.m.}}\phi_{m_J}$ is governed by a hamiltonian

$$\mathcal{H}_{\text{c.m.}} = \frac{1}{2m} \left(\mathbf{p} - \mathcal{A}(\mathbf{r}) \right)^2 + E_{m_J}(\mathbf{r}) + \mathcal{V}(\mathbf{r}) + V(\mathbf{r}), \quad (4.9)$$

where the vector potential is defined as

$$\mathcal{A}(\mathbf{r}) = i\hbar\langle\psi_{m_J}|\nabla|\psi_{m_J}\rangle, \quad (4.10)$$

and the scalar potential is given by

$$\mathcal{V}(\mathbf{r}) = \frac{\hbar^2}{2m} \sum_{m'_J \neq m_J} |\langle\psi_{m'_J}|\nabla|\psi_{m_J}\rangle|^2. \quad (4.11)$$

The hamiltonian (4.9) is equivalent to the minimal coupling hamiltonian (4.1) for a particle of electric charge $q = 1$. The differences are in the physical origin of the gauge potential \mathcal{A} and in the presence of the additional potentials $\mathcal{V}(\mathbf{r})$ and $E_{m_J}(\mathbf{r})$. Note that the latter is equivalent to the potential energy surfaces one finds in quantum molecular chemistry. In fact, the analogy emerges from the separation of fast and slow evolution of the variables. Here, we split the internal and external atomic parameters, while in molecules the separation applies to the different time scales of nuclear and electronic motion (the famous Born-Oppenheimer approximation).

4.1.2 Geometric Potentials

It is usual to refer to artificial potentials as "geometrical", in order to stress their origin. In fact, we will see in the following that they indeed are generated from non trivial angles $\theta(\mathbf{r})$ and $\phi(\mathbf{r})$. Let me add an additional *caveat*: here we use the terms "vector potential" and "scalar potential", but they should not be confused with their homonyms in the previous chapter.

Let us explicitly give the dependence of the gauge fields on the Zeeman field \mathbf{B}_{eff} . One should first calculate the matrix elements

$$\langle\psi_{m'_J}|\nabla|\psi_{m_J}\rangle = \frac{i}{\hbar} e^{i(m_J - m'_J)\phi} \langle m'_J | \left[\left(\hbar m_J - \hat{\mathcal{R}}_y^\dagger(\theta) \hat{J}_z \hat{\mathcal{R}}_y(\theta) \right) \nabla\phi - \hat{J}_y \nabla\theta \right] | m_J \rangle. \quad (4.12)$$

Let us remind that the dependence on the spatial position \mathbf{r} is implicit in the angles. From the rotation of the spin operator \hat{J}_z , one gets $\hat{\mathcal{R}}_y^\dagger(\theta) \hat{J}_z \hat{\mathcal{R}}_y(\theta) = \hat{J}_z \cos\theta + \hat{J}_x \sin\theta$.

Taking the diagonal terms of equation (4.12), and using the fact that $|m_J\rangle$ is an eigenstate of the operator \hat{J}_z , we get the expression for the vector potential

$$\mathcal{A}(\mathbf{r}) = \hbar m_J (1 - \cos\theta) \nabla\phi. \quad (4.13)$$

From the potential, one can also calculate the synthetic magnetic field

$$\mathcal{B}(\mathbf{r}) = \nabla \times \mathcal{A}(\mathbf{r}) = \hbar m_J \nabla(\cos\theta) \times \nabla\phi. \quad (4.14)$$

Notice the dependence on m_J of both the potential and the field. Using the large $m_J = 8$

in Dysprosium's stretched spin state, we could gain in magnitude with respect to other atomic species. Note also the constraint given by the equation above to have a non vanishing field \mathcal{B} : both angles should have finite gradients, which should not be parallel.

From equation (4.12) one additionally gets the off diagonal elements, which can be inserted in equation (4.11) to obtain the scalar potential

$$\mathcal{V}(\mathbf{r}) = \frac{\hbar^2}{2m} \left(J(J+1) - m_J^2 \right) \left((\nabla\theta)^2 + \sin^2\theta (\nabla\phi)^2 \right). \quad (4.15)$$

Note that the scalar potential is maximum for $m_J = 0$, where $\mathcal{A} = 0$. This potential will sum to the scalar light shift and one has to ensure that the trapping potential will not be significantly deformed. Physically, we see from equation (4.11) that this potential has the form of a kinetic energy associated to the coupling to the other dressed states. In fact, the adiabatic elimination of these states gives rise to an oscillatory micro-motion of the centre of mass, whose kinetic energy is represented by $\mathcal{V}(\mathbf{r})$ [140].

4.2 Implementation with Dysprosium

Let us now consider a possible implementation in a Dysprosium gas (here bosons). The following calculations are inspired by references [141, 142] using a slightly different geometry. We consider a Raman configuration that induces coupling between ground state levels, where the laser frequency is close to the $\lambda = 626$ nm transition. The laser coupling with the atomic spin is described by the light shift operator that we analysed in detail in the previous chapter and, for the considered transition, we refer to equation (3.56). The laser frequencies are detuned of Δ from the excited state resonance, which we showed to be optimal for $\Delta \sim 1$ nm. In the following we calculate the light shift in the case of a spatially varying beam intensity, and we give an expression for the artificial potentials and magnetic field.

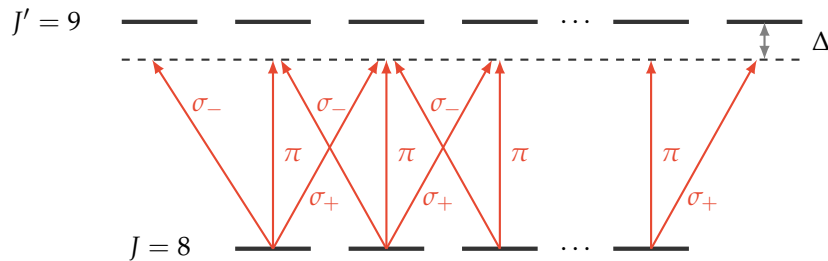


Figure 4.2 – Raman coupling between degenerate ground state levels $|m_J\rangle$, with $-8 < m_J < 8$. In the considered example, the levels correspond to the transition at 626 nm we analysed in the previous chapter.

In contrast with the following calculations, an experimental implementation of synthetic gauge fields in Dysprosium has been realised using the fermionic isotope ^{161}Dy in the presence of a large external magnetic field B , which produces a large quadratic Zeeman effect that restrict the Raman coupling to an effective two-level system [143]. We use instead ^{164}Dy and as we explained in chapter 2, large magnetic fields in a bosonic cloud can not be used, since the dipolar relaxation will induce heating and atom loss in the trap.

4.2.1 Experimental Scheme

In order to couple adjacent Zeeman levels we need two light beams, whose electric fields we label as E_1 and E_2 . The first beam has a linear (π) polarisation and the second a circular (σ_+) one, and they cross at a right angle $k_1 \perp k_2$. The spatial variation of the coupling, *i.e.* of Zeeman field B_{eff} , is provided by an offset in the propagation directions (*i.e.* the laser beams do not overlap), which gives a light intensity gradient in the transverse direction (see figure 4.3).

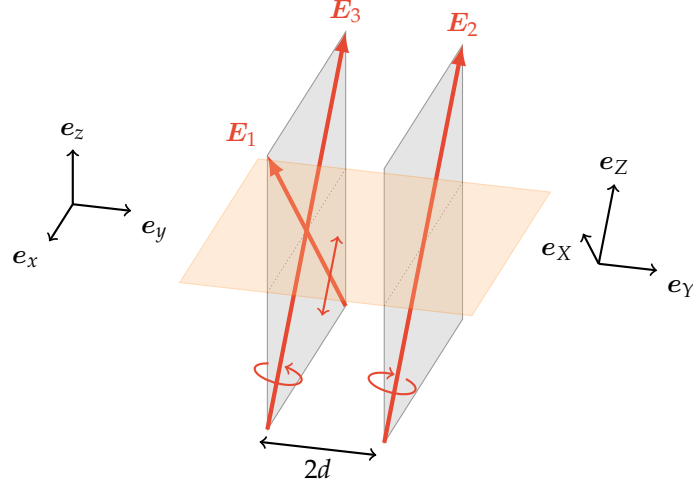


Figure 4.3 – Experimental geometry for the Raman coupling. The two laser beams counter propagate and cross with at a right angle. Beam 1 is linearly polarised along Z while beam 2 and 3 are circularly polarised.

In the following, we assume that the atomic cloud is strongly confined in a quasi bidimensional geometry in the (x, y) plane. We can write the light fields (neglecting the z dependence) as

$$\begin{aligned} E_1 &= e_1 \mathcal{E}_1 \exp\left(-\frac{(y-d)^2}{w^2} + i\frac{kx}{\sqrt{2}}\right), \\ E_2 &= e_2 \mathcal{E}_2 \exp\left(-\frac{(y+d)^2}{w^2} - i\frac{kx}{\sqrt{2}}\right), \end{aligned} \quad (4.16)$$

where w is the beam waist, supposed equal for the two beams, and $2d$ is the distance between the axes of the beams^a. In addition to these fields, we need a third beam

$$E_3 = e_3 \mathcal{E}_3 \exp\left(-\frac{(y-d)^2}{w^2} - i\frac{kx}{\sqrt{2}}\right), \quad (4.17)$$

to obtain a symmetric scalar potential, as we will see in the following.

We will proceed with the calculation in the rotated reference frame whose axes coincide with the propagation directions of the lasers (see figure). We will label the new coordinate system as (X, Y, Z) , where $e_X = (e_x + e_z)/\sqrt{2}$, $e_Y = e_y$ and $e_Z = (e_z - e_x)/\sqrt{2}$.

^aWe consider to work closely to the beam foci, so that we can neglect the dependence of the laser profile on the x direction.

The first beam is linearly polarised along $\mathbf{e}_1 = \mathbf{e}_Z$ axis. The other beams have opposite circular polarisation that we can write as $\mathbf{e}_2 = -(\mathbf{e}_X + i\mathbf{e}_Y)/\sqrt{2}$ and $\mathbf{e}_3 = (\mathbf{e}_X - i\mathbf{e}_Y)/\sqrt{2}$. Let us suppose the third beam has a different frequency with respect to the two others^a, so they do not interfere.

The hamiltonian describing the system is (4.2) and we can use the findings of the previous section. The effective magnetic field for the internal degrees of freedom of the atoms is given by equation (3.40), which in the present case is written as

$$\mathbf{B}_{\text{eff}} = -i \frac{\alpha_1 V_0}{2J\mu_B g_J} [(\mathbf{E}_1 + \mathbf{E}_2)^* \times (\mathbf{E}_1 + \mathbf{E}_2) + \mathbf{E}_3^* \times \mathbf{E}_3]. \quad (4.18)$$

Let us remind that $V_0 \sim \hbar d_{JJ'}^2 / \Delta$, where $d_{JJ'}$ is the matrix element, Δ is the detuning from the excited state, and the coefficient $\alpha_1 = 152/153$ for the 626 nm transition. As we noticed in the previous chapter, the circular beams will create two effective fields pointing along their propagation direction \mathbf{e}_Z , with opposite signs as a result of their opposite circular polarisations, while the cross product of beam 1 and 2 will give a contribution in the (X, Y) plane. The explicit expression of the effective Zeeman field is

$$\mathbf{B}_{\text{eff}} = \frac{\alpha_1 V_0}{2J\mu_B g_J} \left((I_2 - I_3) \mathbf{e}_Z + \sqrt{2I_1 I_2} [\cos(\sqrt{2}kx) \mathbf{e}_X + \sin(\sqrt{2}kx) \mathbf{e}_Y] \right) \quad (4.19)$$

where we introduced the laser intensities I . Note that a different experimental setup can rely on a spatially varying detuning Δ , i.e. V_0 in equation (4.18) to induce a position dependent \mathbf{B}_{eff} . In our case, we use instead the spatial variation of the light intensity. In the paraxial approximation, the intensities depend only on y and are

$$I_{1,3}(y) = |\mathcal{E}_{1,3}|^2 \exp\left(-2\frac{(y-d)^2}{w^2}\right) \quad \text{and} \quad I_2(y) = |\mathcal{E}_2|^2 \exp\left(-2\frac{(y+d)^2}{w^2}\right). \quad (4.20)$$

Using the parametrisation of figure 4.1, we get the effective field angles

$$\theta = \tan^{-1} \frac{\sqrt{2I_1 I_2}}{I_2 - I_3} \quad \text{and} \quad \phi = \sqrt{2}kx \quad (4.21)$$

The necessity of a third beam is clear, otherwise one could not obtain a symmetric expression for the angle θ . For this purpose, in the following we consider $I_1 = 2I_3$ and $I_2 = I_3$ as relative amplitudes of the electric fields. For this choice of intensities, we get

$$\theta = -\frac{1}{\sinh(4dy/w^2)} \quad (4.22)$$

4.2.2 Expected Results

The calculation of the synthetic potentials is straightforward. We suppose the adiabatic condition is verified and the atoms are in the lowest dressed state. Using the formulae given in the previous section we get the vector potential

$$\mathcal{A}(\mathbf{r}) = \sqrt{2}\hbar J \left[1 - \tanh\left(\frac{4dy}{w^2}\right) \right] k \mathbf{e}_X, \quad (4.23)$$

^aThe frequency difference should be small compared to the detuning from the resonance, but this is easily done since $\Delta \sim 1$ THz.

which gives the synthetic magnetic field

$$\mathcal{B}(\mathbf{r}) = 4\sqrt{2}\hbar J \frac{kd}{w^2} \operatorname{sech}^2\left(\frac{4dy}{w^2}\right) \mathbf{e}_Z. \quad (4.24)$$

As we mentioned before, note the pure geometric origin of the potentials. The strength of the field is solely determined by the beams relative position and the waist. Note also that the field vanishes as expected for $d = 0$, since the spatial variation of the angle θ is also vanishing. The formulae are equivalent to the findings of reference [141], but the field magnitude is increased by the large $J = 8$ of Dysprosium (instead of the $1/2$ case considered there). The field magnitude at the origin will be

$$\mathcal{B}(0) = 24\sqrt{2}\hbar \frac{kd}{w^2} \mathbf{e}_Z. \quad (4.25)$$

One also finds that the scalar potential is given by

$$\mathcal{V}(\mathbf{r}) = \frac{\hbar^2 J}{2m} (k^2 + 8d^2/w^4) \operatorname{sech}^2\left(\frac{4dy}{w^2}\right) \quad (4.26)$$

The results are shown in figure 4.4.

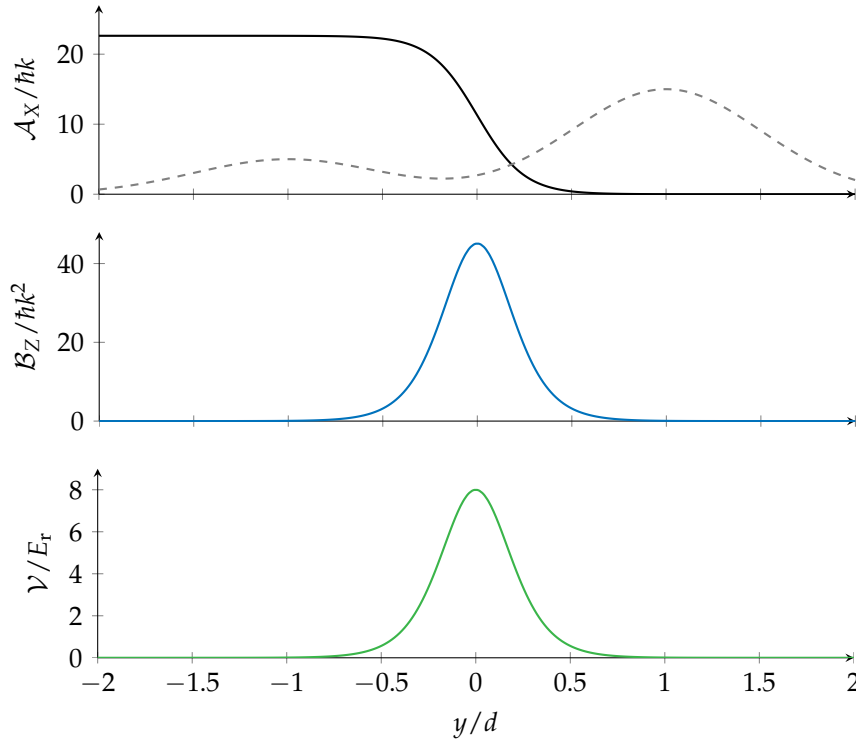


Figure 4.4 – Synthetic fields generated by the considered geometry. The dashed curve in the first plot is the intensity profile of the laser beams along y . This plot is obtained for $w = d = 10 \mu\text{m}$.

A clear indication of the presence of the geometric field would be the observation of

vortices in the condensed cloud. The surface density of such vortices is given by [144]

$$\rho_{\text{vortex}} = \frac{m\omega_c}{2\pi\hbar}, \quad (4.27)$$

where we introduced the cyclotron frequency $\omega_c = q|\mathbf{B}|/m$, in this case for a particle of unit charge $q = 1$. For the magnetic field calculated above, we get

$$\rho_{\text{vortex}} = 24\sqrt{2}\frac{kd}{\pi w^2}, \quad (4.28)$$

from which we can estimate the number of vortices $N_{\text{vortex}} = \pi R^2 \rho_{\text{vortex}}$, with R the cloud size. Assuming for simplicity $w = d$ and choosing the waist of the beams approximately equal to the cloud size, which is typically of the order of $R \sim 10 \mu\text{m}$ for $N \sim 10^4$ condensed atoms [54], we get that the number of observable vortices is $N_{\text{vortex}} \sim 35$.

4.2.3 Tensor Laser Coupling

In the case we include the tensor term, the interacting part of the hamiltonian (4.3) is given by the whole light shift operator (not just the effective magnetic field), and should be properly diagonalised. The tensor part of the interaction can be explicitly calculated for the considered beam configuration. The light shift is given by

$$\hat{V}_{\text{tens}} = \frac{\alpha_2 V_0}{2J(2J-1)} \left(3[(\mathbf{E}_1 + \mathbf{E}_2)^* \cdot \hat{\mathbf{J}}][(\mathbf{E}_1 + \mathbf{E}_2) \cdot \hat{\mathbf{J}}] + 3[(\mathbf{E}_1 + \mathbf{E}_2) \cdot \hat{\mathbf{J}}][(\mathbf{E}_1 + \mathbf{E}_2)^* \cdot \hat{\mathbf{J}}] \right. \\ \left. + 3(\mathbf{E}_3^* \cdot \hat{\mathbf{J}})(\mathbf{E}_3 \cdot \hat{\mathbf{J}}) + 3(\mathbf{E}_3 \cdot \hat{\mathbf{J}})(\mathbf{E}_3^* \cdot \hat{\mathbf{J}}) - 2\hat{\mathbf{J}}^2 \right), \quad (4.29)$$

where V_0 is the same as the vector coupling and the factor $\alpha_2 = -40/153$. The calculation leads to the following potential

$$\hat{V}_{\text{tens}} = \frac{\alpha_2 V_0}{2J(2J-1)} \left(3\sqrt{2I_1 I_2}(\cos\phi \hat{J}_X + \sin\phi \hat{J}_Y) \hat{J}_Z + 3\sqrt{2I_1 I_2} \hat{J}_Z (\cos\phi \hat{J}_X + \sin\phi \hat{J}_Y) \right. \\ \left. + 3(2I_1 - I_2 - 2I_3) \hat{J}_Z^2 + (I_2 - 2I_1 + 4I_3) J(J+1) \right). \quad (4.30)$$

Notice that it appears the same dependence on the operators \hat{J}_X and \hat{J}_Y as in the vector case. We can define the operator \hat{J}_u , acting on the direction defined by $\mathbf{u} = \cos\phi \mathbf{e}_X + \sin\phi \mathbf{e}_Y$ and write the spin-dependent part of the hamiltonian as

$$\hat{V} \propto \sqrt{2I_1 I_2} \left(\hat{J}_u + \epsilon \{ \hat{J}_Z, \hat{J}_u \} \right) + I_2 \hat{J}_Z + \epsilon (2I_1 - I_2 - 2I_3) \hat{J}_Z^2, \quad (4.31)$$

where curly brackets label the anticommutator. Here, we introduce the parameter ϵ , which multiplies the tensor interaction and is given by

$$\epsilon = \frac{3\alpha_2}{(2J-1)\alpha_1} = \frac{8}{152} \simeq 0.053 \quad (4.32)$$

The tensor term is thus a small perturbation to the vector light shift.

To check its contribution to the geometric fields, we diagonalise numerically the total

light shift (3.56). In figure 4.5 we show the resulting geometric gauge field and potential. The tensor term induces an anisotropy in the fields, which can be experimentally compensated by a right choice of the ratio between the laser amplitudes (see figure).

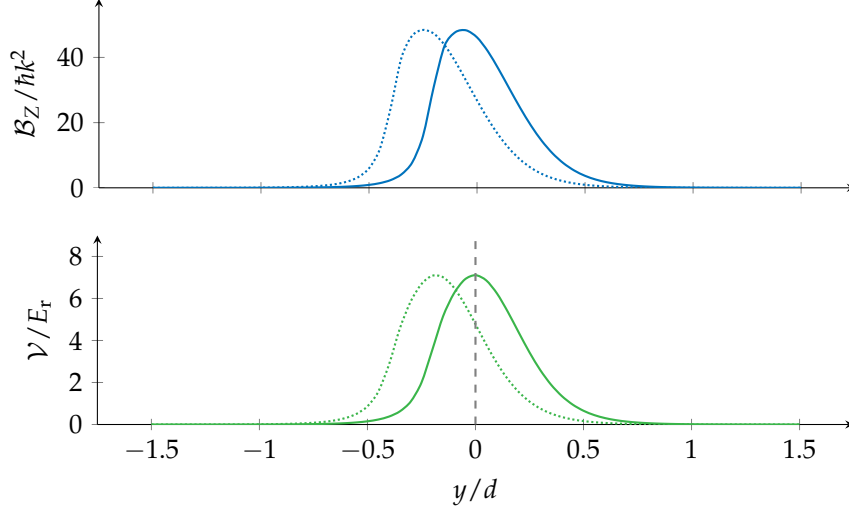


Figure 4.5 – Synthetic fields calculated from the numerical diagonalisation of the light shift operator. The dotted curves correspond to the intensity setup of the previous graph $I_2 = I_3 = I_1/2$. Solid lines are a more symmetric configuration for $I_1 = 2I_3$ and $I_2 = 4.325 I_3$, which guarantees an harmonic potential in $y = 0$.

4.2.4 Experimental Requirements

As we noticed at the beginning of the chapter, the adiabatic approximation adds a constraint on the energy separation between the adiabatic surfaces $g_J \mu_B B_{\text{eff}} = \hbar \Omega_R / \Delta \gg E_r = h \times 3.1 \text{ kHz}$. To check the validity of the findings above one could numerically solve the spinor Gross-Pitaevskii equation describing the different spin states of the condensate, which is a non trivial problem due to the large dimension $(2J + 1) = 17$ of the Hilbert space.

Let us consider the different experimental requirements on the system parameters. The scalar potential adds to the external trapping potential and should be correctly counterbalanced. Close to the origin, we can expand (4.26) up to the second order. Retaining only the terms in k^2 , since $kw \gg 1$, we get

$$\mathcal{V}(\mathbf{r}) = \hbar^2 J \frac{k^2}{2m} - 8\hbar^2 J \frac{d^2 k^2}{mw^4} y^2 + \mathcal{O}(y^4). \quad (4.33)$$

We get then an anti-trapping frequency

$$\omega_{\text{atrap}} = i4\sqrt{J} \frac{\hbar kd}{mw^2}, \quad (4.34)$$

which should be canceled by an additional laser or should be kept smaller than the trapping frequencies. Typically, the final frequencies at the end of evaporative cooling are of the order of $\omega_{\text{trap}} \sim 2\pi \times 100 \text{ Hz}$. Assuming again $w = d$, we should then choose $w \gg 70 \mu\text{m}$ to have a negligible anti trapping contribution.

Let us consider now the constraints on the residual real magnetic fields, whose fluctuations add to the effective \mathbf{B}_{eff} , possibly destroying the synthetic fields.

In the case of an external magnetic field in the X direction $\mathbf{B} = B_X \mathbf{e}_X$, its contribution should be negligible in front of the light-shift induced field $\mathbf{B}_{\text{eff}} \cdot \mathbf{e}_X$ which is $> E_r / g_J \mu_B J$ in the adiabatic regime. This gives the condition $B_X < 220 \mu\text{G}$ for a coupling strength of $1E_r$. Higher coupling strengths require a less demanding constraint. For a field $\mathbf{B} = B_Y \mathbf{e}_Y$ one gets the same result.

If the external field is pointing instead along the Z direction $\mathbf{B} = B_Z \mathbf{e}_Z$, it will add to the term $\propto (I_2 - I_3)$, which is $\sim 4yd/w^2$ close to the origin. The external field B_Z will then shift the centre of the synthetic field. We require the shift to be smaller than d . By taking again $w = d$ and a coupling strength of $1E_r$, we get $B_Z < 7 \text{ mG}$.

This technical requirements are experimentally feasible, but require an excellent stabilisation of the magnetic field fluctuations. Previous data show that the magnetic field fluctuations are currently $\lesssim 10 \text{ mG}$ in our experiment, and an active stabilisation of magnetic noise is an on going work.

In summary, the implementation of gauge fields on Dysprosium with the proposed scheme should constitute a significant improvement over alkali atoms. We expect to enter strongly coupled phases, with more observable vortices and the reduced photon scattering should lead to long lived vortices, which at equilibrium will arrange in the familiar Abrikosov lattice. Previous work on alkali could only obtain a limited number of vortices, which decay fast due to the atom loss induced by the residual photon scattering [61]. Moreover, the dipolar properties of Dysprosium should modify the structure of the vortex lattice, leading to phases of different symmetry [145].



A New Experiment on Ultra-cold Dysprosium

5	Experimental Setup	55
5.1	Vacuum System	
5.2	Laser System for Near-Resonant Light	
5.3	Magnetic Field Control	
5.4	Data Acquisition	
5.5	A Slow Jet of Dysprosium Atoms	
6	Narrow Line MOT	73
6.1	Magneto Optical Trapping of Dysprosium	
6.2	MOT Position	
6.3	Spin Composition	
6.4	Temperature	
6.5	Size and Density	
6.6	Inelastic Light Assisted Collisions	
7	Towards Dysprosium BEC	93
7.1	Optical Dipole Trap	
7.2	Frequency Measurements	
7.3	Optical Transport	
7.4	Crossed Dipole Trap	
7.5	Evaporative Cooling	
8	Conclusion and Perspectives	110



5

Experimental Setup

MOST OF the work I carried out during this thesis was designing and constructing a new apparatus to cool Dysprosium atoms down to degeneracy. In this chapter I describe in detail our experimental setup. I detail the vacuum system, where we produce the atomic gas. Then I continue on the tools we use to manipulate the atoms: lasers and magnetic fields. I also shortly expose the way we pilot the experiment and how we take data.

I subsequently explain how we produce an atomic beam of Dysprosium starting from a high temperature oven. Having cold and slow atoms is essential to capture them in a magneto optical trap, which will be the subject of the next chapter.

5.1 Vacuum System

As any experiment where the contact with the environment should be avoided, the production of degenerate atomic gases requires working in ultra high vacuum (UHV) conditions. The experiments are thus performed in a vacuum chamber, where all residual gas has been pumped away. In fact, collisions with the residual background gas typically lead to atom losses and can limit the trap lifetime. The mean time between collisions τ_{coll} must hence be larger than the desired lifetime of the trap, giving the constraint on pressure. To obtain a BEC via evaporative cooling one typically needs $\tau_{\text{coll}} > 10$ s and hence UHV conditions, which means that the pressure of the environment surrounding the sample should be $p < 10^{-10}$ mbar.

To achieve this low pressure, our vacuum chamber is divided in two main sections. They are separated by a differential pumping stage, that permits to maintain a steady-state pressure difference between both. Ordering by decreasing pressures the various parts, first is the atomic source, followed by the spectroscopy chambers, then the slower, and last come the chambers where we trap and manipulate the atoms.

5.1.1 High Vacuum Part

In the first section of the vacuum chamber the typical pressure is of a few 10^{-9} mbar, so one can only speak of high vacuum (HV). The main limitation to achieve lower pressures is the oven where we evaporate Dysprosium. It is constantly maintained at high temperatures (hundreds of °C), and the induced degassing from the chamber walls contributes to the increase of the pressure.

The oven is facing the rest of the apparatus and is directly connected to a small CF40 cubic chamber, where four windows allow us to perform laser spectroscopy of the 626 nm transition directly on the atomic jet. On top of the cube, a cross piece holds on one side a 40 L ion pump and on the opposite side the main valve of the system. The valve is opened only during the procedures to refill the exhausted oven.

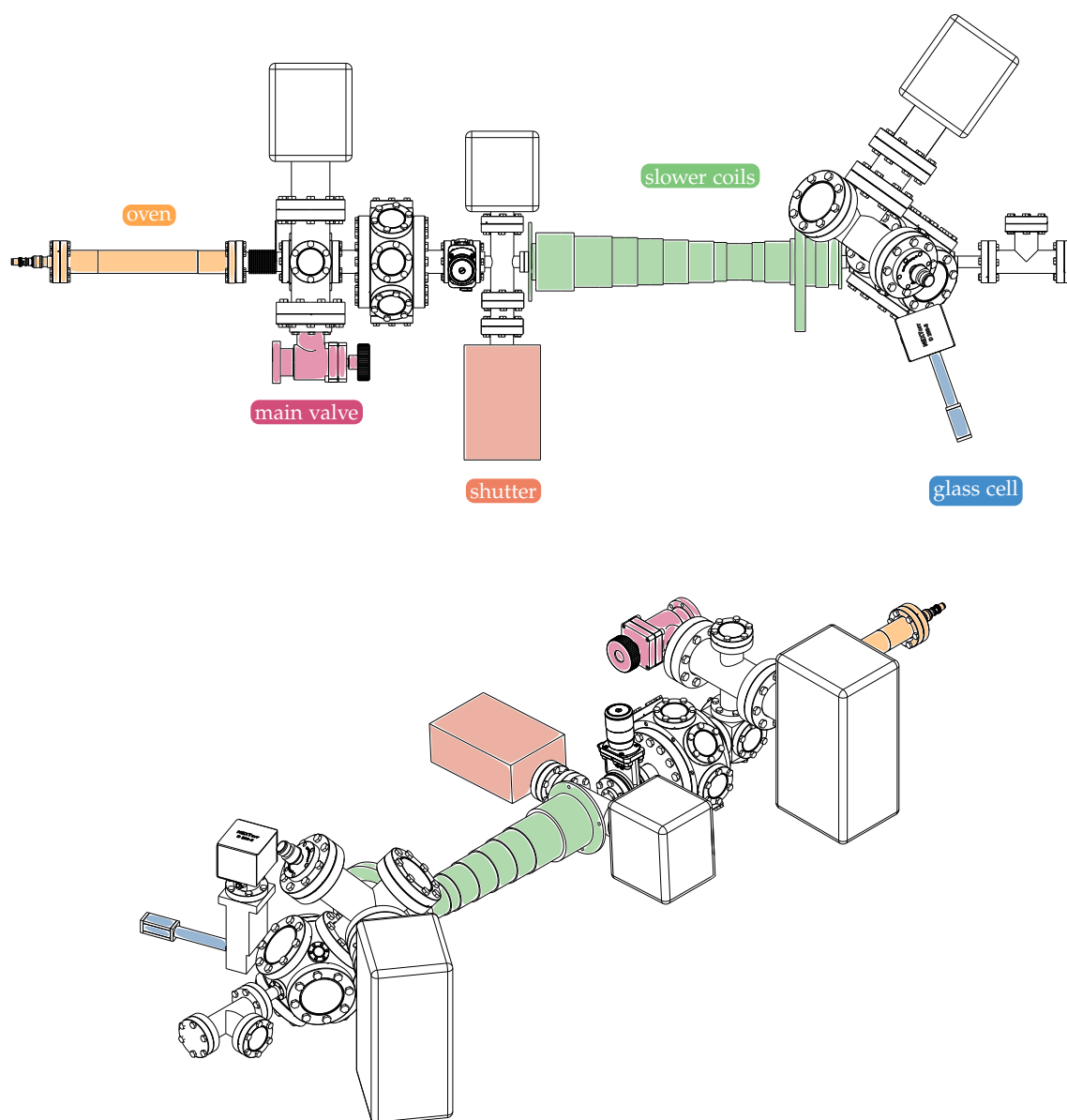


Figure 5.1 – Technical drawing of the vacuum chamber (top and isometric view). A more detailed description is given in the main text.

Following the propagation of the atomic jet, we find an octagonal chamber where eight

CF40 windows are used to send laser cooling beams, to perform saturated absorption spectroscopy on the 421 nm transition and to collect the fluorescence of the beam itself.

After this chamber is mounted a gate valve. This valve is always closed during the oven refill procedure, so that the vacuum in the following section of the chamber is preserved even if the previous is exposed to atmospheric pressure.

Behind the gate valve we have a 20 L s^{-1} ion pump^a and a mechanical shutter^b, both mounted on a cross piece. The latter is simply a metallic rod externally controlled by a linear magnetic actuator, and it can be used to completely block the beam of atoms and prevent them to enter the MOT chamber.

5.1.2 Ultra-High Vacuum Part

After the shutter, the atomic beam enters the Zeeman slower tube, which connects the HV side of the chamber to the UHV section. The tube is 50 cm long and has a increasing internal diameter, thus ensuring a differential pumping stage between the slower entrance and the MOT chamber.

We need to send a laser beam propagating along the atomic jet axis. The easiest way is to have a window facing the oven, but we found that the deposit of Dysprosium is sufficient to metallize the glass in a few hours. We therefore installed in the vacuum chamber a 45° aluminium mirror. The laser beam enters from a window on the side and is reflected in the oven direction. The coating of the aluminium surface with dysprosium does not affect significantly the reflectivity of the mirror itself.

The slower tube and the vacuum piece where the aluminium mirror sits are mounted on opposite connections with respect to the MOT chamber. The latter has the shape of a cube^c with six CF60 windows on the facets and eight CF16 connections on the vertices.

Two coplanar pairs of opposite CF16 connections give the above mentioned Zeeman slower axis and the dipole trap axis. The dipole laser enters the chamber through a 2° angled window, to avoid direct reflections of the beam. On this window we installed a metallic shield equipped with a temperature interlock to avoid excessive thermal heating of the glass-to-metal connection, which may cause (and did) a dangerous vacuum leak. Due to the cube symmetry of the chamber, the two aforementioned axes cross at 70.5° .

The four remaining CF16 flanges have windows that permit additional optical access to the atoms in the MOT. The six CF60 windows are used for two imaging axes and to send the MOT laser beams themselves, the big diameter of the windows allowing a wide diameter (and thus a wide capture region). One of the CF60 windows is actually mounted on the cube via a CF60 cross, where additional pumping is provided by a non evaporable getter pump^d and a 40 L s^{-1} ion pump. Those pumps keep the pressure as low as 4×10^{-10} mbar in the MOT chamber. Note that our entire vacuum apparatus has never been baked out, an operation which could in principle reduce the final pressure. Nevertheless, since the pressure is low enough to ensure stable operation of the traps, we decided to not bake the system.

The production of the degenerate gas of Dysprosium and the following experiments are performed in a glass cell. This ensures much more optical access and permits to work

^aVacIon Plus 20, Varian Inc.

^bLSM DU-30-1,0, MBE-Komponenten GmbH

^cMCF450-SphCube-E6A8, Kimball physics

^dCapaciTorr D400-2, SAES Getters SpA

much closer to the atoms than a standard vacuum chamber would do. The cell^a has a square section of 2.5 cm per side, and is 6 cm long. Every glass facet is 5 mm thick and is not AR coated. It is thus preferable send the laser beams at the Brewster angle in order to avoid troublesome reflections.

The glass cell is connected to the MOT chamber via a differential pumping stage that ensures a pressure lower than 1×10^{-11} mbar. This differential pumping stage consists in a custom Tee shaped piece with two CF16 flanges that link the cell to the chamber, and a larger CF40 side that leaves space to a hybrid ion-getter pump^b.

5.2 Laser System for Near-Resonant Light

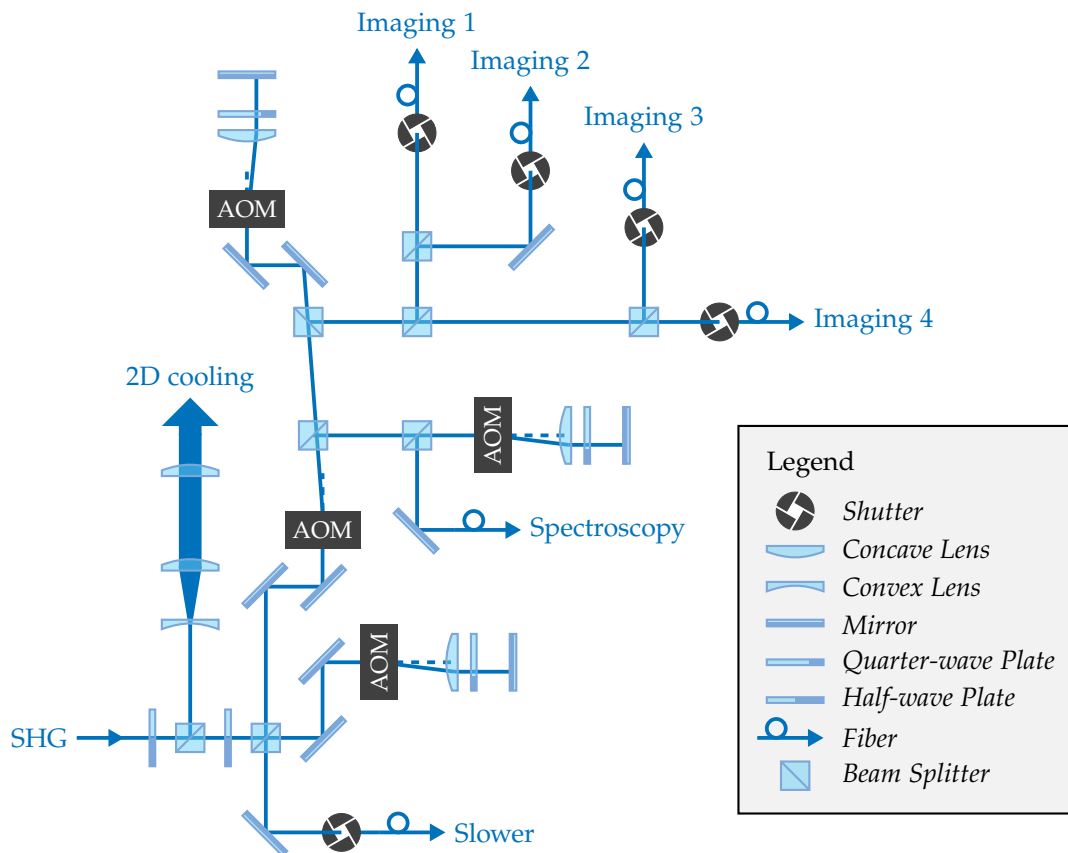


Figure 5.2 – Simplified scheme of the optical setup for the blue light. The main laser is split into different paths, which serve for different purposes, as indicated in the drawing. The frequency of the difference outputs are adjusted by means of acousto optical modulators (AOM). See main text for more details.

Most of the techniques in cold atom experiments rely on the manipulation of atoms by near-resonant light. In the following, we describe the various lasers we use in our experiment and their different purposes. The two laser cooling transitions of Dysprosium are in visible spectrum, at 626 nm and 421 nm. After describing the setup to produce these wavelengths, we will see how we perform the frequency stabilisation for the two lasers.

^amanufactured by Hellma Analytics

^bNEXTorr D 100, SAES Getters SpA

5.2.1 Blue Laser Setup

The source of blue light is a commercial second harmonic generation system^a. It consists in an extended cavity diode laser and a tapered amplifier delivering 1.2 W at 840 nm. The infrared light is then frequency doubled using a non linear crystal placed in a bow tie cavity. At optimum the laser can produce about 600 mW at 421 nm.

Most of the laser power is used for transverse cooling the atomic beam, hence the laser frequency is detuned of $-\Gamma/2$ from the atomic resonance, to maximise the cooling efficiency. About 200 mW are drawn at the laser output and shaped into an elliptical beam. The beam is then split in half and sent on the atomic jet from two orthogonal directions.

The remaining power is dispatched on different paths for imaging, spectroscopy and Zeeman slowing, which uses about 60 mW of power.

Modulation Transfer Spectroscopy

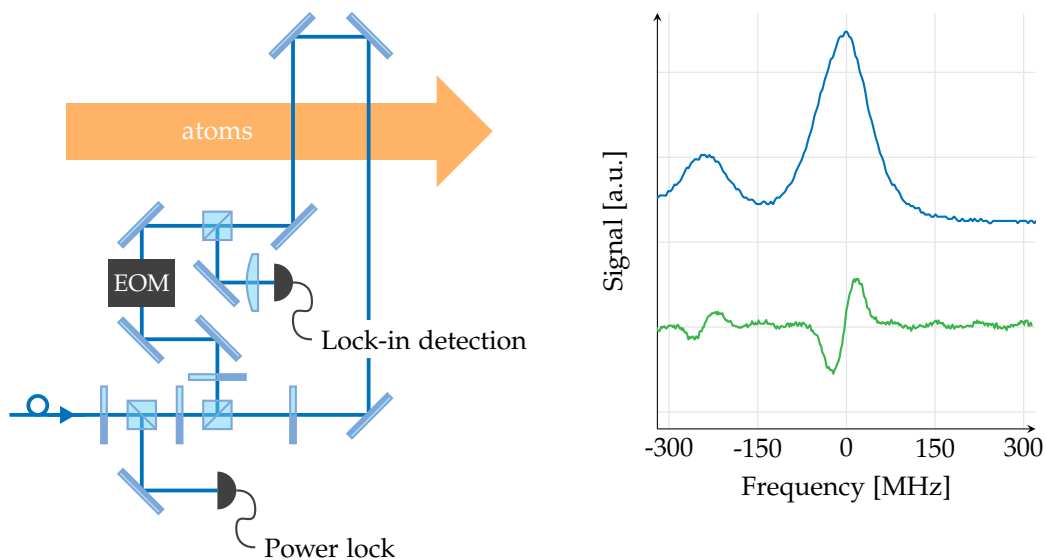


Figure 5.3 – Optical setup for frequency lock of the blue laser. The pump beam is modulated via an EOM and counter propagates along the probe optical path, crossing twice the atomic beam. Probe light is collected by a photodiode and the signal is sent to the lock-in amplifier for the PDH detection. On the right the recorded oscilloscope tracks for both the fluorescence and the error signal after the demodulation. Legend in Figure 5.2.

The frequency lock of the laser is done on the error signal obtained from modulation transfer spectroscopy performed on the atomic jet, in a typical pump and probe experiment. About 2 mW of pump power and 0.5 mW of probe power are sent on the atoms in contra propagating directions. The pump is modulated at 16 MHz using an electro-optical modulator (EOM) and transfers the modulation to the probe beam via the interaction with the atoms. The probe signal is then collected with a rapid photodiode^b with a bandwidth larger than the modulation frequency. The signal is then demodulated by a home made lock-in amplifier to recover the dispersive curve shown in Figure 5.3.

^aTA-SHG Pro, TOPTICA Photonics AG

^bPDA8A/M, Thorlabs Inc.

We then feed back this error signal to the laser diode current. The frequency stability in closed loop operation is ~ 1 MHz. This is good enough for the experiment operation, since the natural linewidth of this transition is very large ($\Gamma = 2\pi \times 32$ MHz).

5.2.2 Red Lasers Setup

We have two identical setups for the red light at 626 nm. The two lasers share the construction design, since we need independent high power sources for the MOT trapping light and the Raman coupling beam. To produce the light we followed the setup described in ref [146] and used on for Be^+ , which consists in a sum-frequency generation (SFG) scheme.

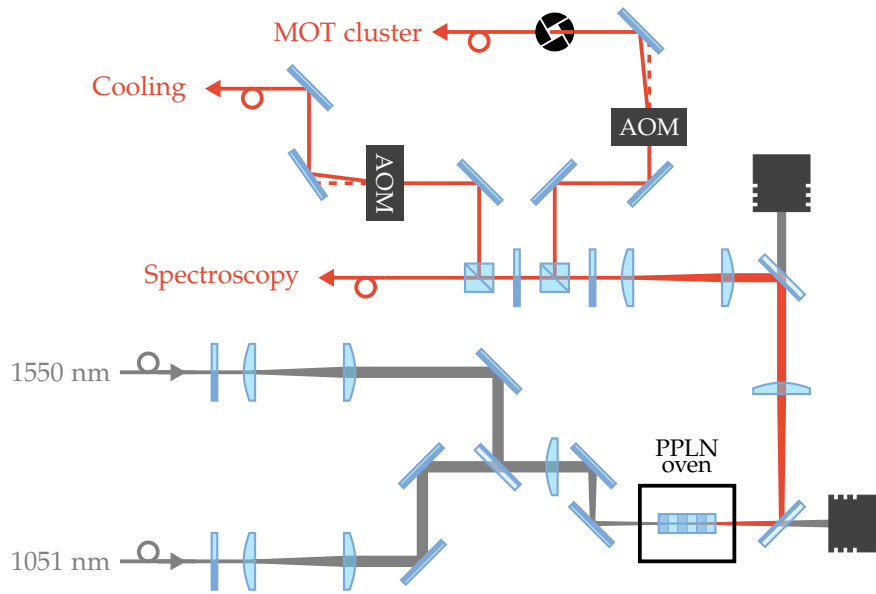


Figure 5.4 – Setup for the sum frequency generation of the MOT light. The two infrared lasers are superimposed with a dichroic mirror and then focalised with a single lens into the non linear crystal. We filter the generated red light from the remaining IR with two additional dichroic mirrors. We then dispatch the red light to the spectroscopy setup, the MOT cluster and the Doppler cooling. Legend in Figure 5.2.

Sum-frequency generation

SFG is a second order nonlinear process used to produce light at the sum of the incoming frequencies. This phenomenon takes place in non-linear material where two photons can be annihilated to create a new photon at the sum of the frequencies $\omega_3 = \omega_1 + \omega_2$.

Unless the phase matching condition $\Delta k = k_3 - k_1 - k_2 = 0$ is maintained all along the crystal, different waves created at the different points in the crystal will interfere destructively if they are generated at a distance $L_c = \pi/\Delta k$.

To prevent this to happen, one uses periodically poled crystals, in our case periodically poled lithium niobate (PPLN), which consists in an array of thin slices of crystal with alternated direction of the optical axis. If the width of every slice Λ is exactly L_c , one recovers the constructive interference between the incoming waves. This condition is called quasi-phase matching.

The crystal is held in a small oven that permits to control its temperature, that in turn permits the regulation of the phase mismatch

$$\Delta k = 2\pi \left(\frac{n_3(T)}{\lambda_3} - \frac{n_1(T)}{\lambda_1} - \frac{n_2(T)}{\lambda_2} \right). \quad (5.1)$$

The values for the refractive indices for different temperatures and wavelengths are calculated from the Sellmeier [147] equation for the lithium niobate.

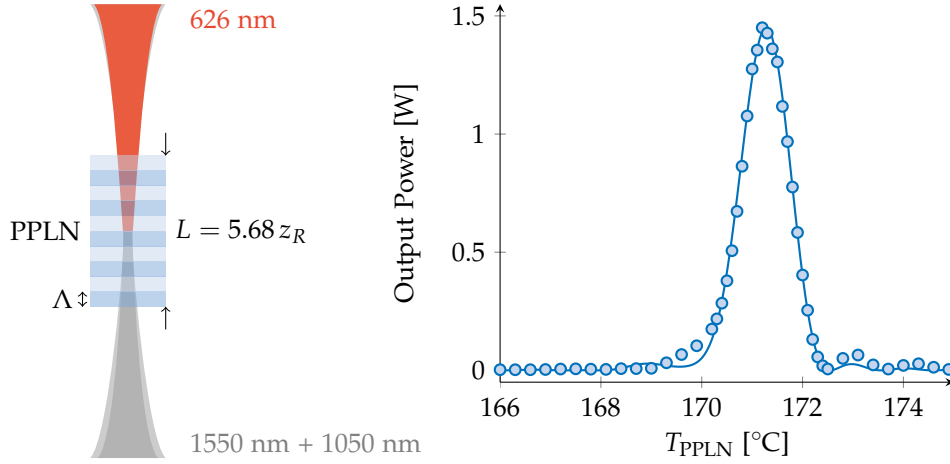


Figure 5.5 – Scheme of the SFG of the red light. The size of the crystal L sets the Rayleigh length z_R for the two focalised IR beams. On the left, the power of the generated red light as a function of crystal temperature. Solid line is the theoretical curve from equation 5.3.

Boyd and Kleinman [148] studied the propagation of two gaussian beams focused in a crystal with second order non linearities: the total output power for the sum frequency wave $\mathcal{P}_3 = n_3 \epsilon_0 c \pi w_0^2 |E_3|^2$ is found by solving the non-linear wave equation for the electric fields by integrating the intensity profile over both the radial direction and the crystal length. For input powers \mathcal{P}_1 and \mathcal{P}_2 of the same order of magnitude, the generated power \mathcal{P}_3 results in simply being proportional to their product

$$\mathcal{P}_3 = \alpha \mathcal{P}_1 \mathcal{P}_2, \quad (5.2)$$

with the proportionality coefficient given by

$$\alpha = \frac{32\pi^2 d_{\text{eff}}^2 L}{\epsilon_0 c \lambda_1 \lambda_2 \lambda_3^3 (n_1/\lambda_1 + n_2/\lambda_2 + n_3/\lambda_3)^2} h(a, b). \quad (5.3)$$

The h factor is called the Boyd and Kleinman factor and its expression is given by

$$h(a, b) = \frac{1}{4a} \left| \int_{-a}^a d\tau \frac{e^{-ib\tau}}{(1+i\tau)} \right|^2 \quad (5.4)$$

where one defines the adimensional parameters $a = L/2z_R$ and $b = (\Delta k - 2\pi/\Lambda)z_R$. From the optimal value $a = 2.84$ and the crystal length $L = 4 \text{ cm}$ one extracts the optimum value $z_R \sim 7 \text{ mm}$ for the two incoming lasers. This length fixes the waist of the

two beams. The optical setup is thus very simple. We adjust the lasers waist with two independent telescopes and then we focus them in the centre of the crystal, after having them superposed using a dichroic mirror.

In our setup we produce the 626 nm light by mixing the output of two fiber amplifiers at 1051 nm and 1550 nm. For this wavelength we expect a typical conversion efficiency of 7 W W^{-2} in front of a $\sim 6.7 \text{ W W}^{-2}$ measured efficiency. The setup for the MOT light uses two amplifiers delivering 5 W each at their respective frequencies^a. The laser amplifiers are seeded by two narrow line diode lasers^b. For the Raman light we expect to use more power, so we have different amplifiers, the one working at 1050 nm delivering 10 W^c. The amplifier at 1050 nm shares the seed laser with the MOT laser setup. On the other hand, since we will need a broader control range in frequency, the 1550 nm amplifier is seeded by a wide scan range laser diode^d.

Lamb-Dip Frequency Stabilization

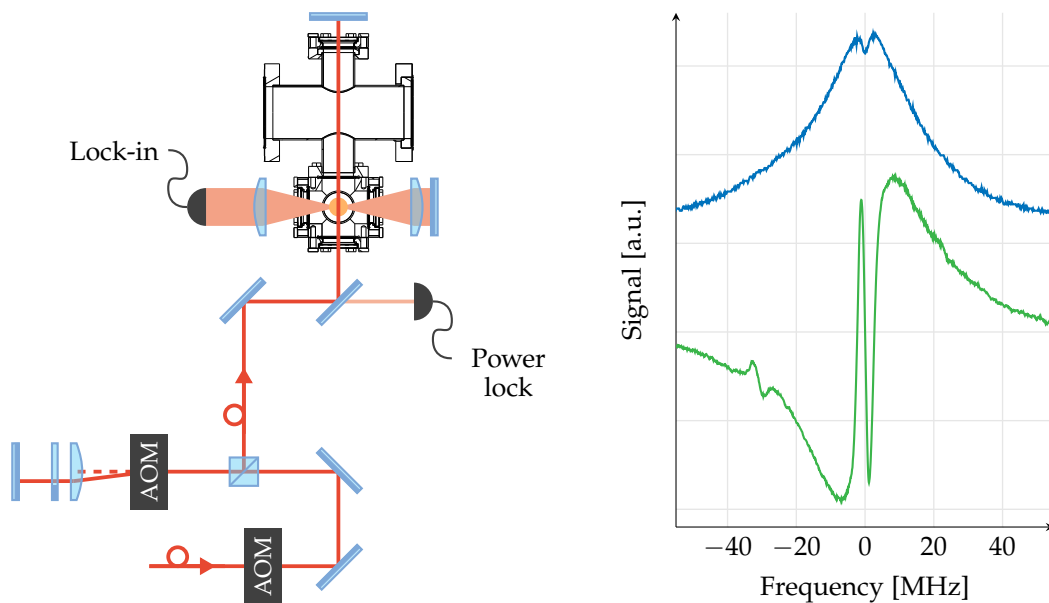


Figure 5.6 – Laser setup for the frequency lock of the 626 nm laser. To increase the signal we use a large area photodiode. The signal is also doubled by collecting the fluorescence from the opposite direction and retroreflecting it on the photodiode. On the right, the Lamb dip signal (red) and the obtained error signal after lock-in detection. Is also visible a small signal of the $15/2 \rightarrow 17/2$ transition of the ^{163}Dy fermionic isotope.

Since the linewidth of the atomic transition is only 135 kHz wide, one needs a very stable frequency lock. One option is to use an ultraslow expansion (ULE) cavity, which normally can provide very narrow frequency lock and has a negligible frequency drift on daily basis.

In our case we obtain a stable lock by spectroscopy techniques on the atomic jet.

^aKeopsys and Koheras Boostik HPA, NKT Photonics

^bKoheras AdjustiK, NKT Photonics

^cALS-IR-1030/1064 High Power, Azur Light Systems

^dDL 100, TOPTICA Photonics AG

The line being so narrow, it was difficult to find a modulation transfer signal. We tried locking on the fluorescence but it could not provide a stable operation of the MOT: due to the large width of the Doppler broadened profile (some tens of MHz), it was difficult to achieve a narrow lock. What turned out to work nicely is a frequency stabilisation on the Lamb dip, which is simply obtained by retro reflecting the laser beam on itself, so one can burn a hole at the fluorescence profile centre.

In strong saturation regime ($s \gg 1$) the Lamb dip profile is given by [149]:

$$a(\omega) = a_0(\omega) \left[1 - \frac{s}{2} \left(1 + \frac{(\Gamma_s/2)^2}{(\omega - \omega_0)^2 + (\Gamma_s/2)^2} \right) \right], \quad (5.5)$$

where $a_0(\omega)$ is the Doppler broadened line shape and $\Gamma_s = \Gamma\sqrt{1+s}$ is the saturation broadened linewidth and ω_0 is the resonance frequency. Both the depth and the width of the peak depend on laser intensity, thus the spectroscopy beam should be stabilised in power to avoid fluctuations of the error signal. The error itself is generated by modulating the spectroscopy beam frequency at 20 kHz and demodulating the collected fluorescence light using a low-signal low-noise lock-in amplifier^a. The spectrum of the ^{164}Dy line and its error signal are plotted in figure 5.6 together with the laser setup. The residual rms noise on the frequency in close loop operation is estimated to be about 5 to 10 kHz, which is enough to ensure a stable operation of the MOT.

Iodine Spectroscopy

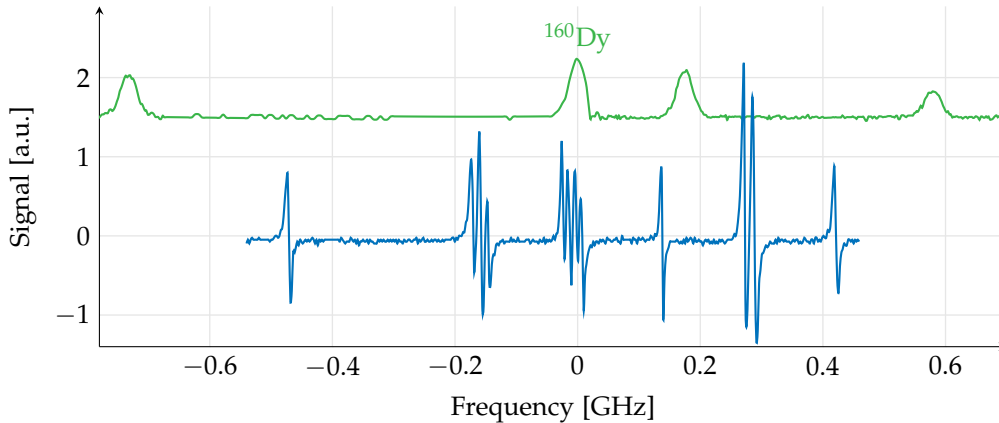


Figure 5.7 – Modulation transfer spectroscopy on the I_2 vapour cell (blue spectrum) and fluorescence spectrum on the 626 nm transition of Dysprosium (green spectrum). The molecular hyperfine structure of Iodine is ~ 1 GHz broad and is centred around the ^{160}Dy peak (see appendix A for the complete spectrum).

The technique described above works quite well for the isotope we currently use in our setup, the ^{164}Dy boson. Nevertheless, in case one needs to change isotope, the fluorescence signal is strongly reduced (see the full experimental spectrum in appendix ??). Molecular iodine I_2 has a very rich spectrum due to the numerous hyperfine and roto-vibrational states of the molecule. Luckily enough there are two absorption peaks in the frequency range of the 626 nm transition of Dysprosium. We have a 50 cm glass cell filled with gaseous I_2 on which we perform saturated absorption spectroscopy. The

^aSRS SR510 Lock-In Amplifier

error curves are similar to the ones obtained by the previously mentioned Lamb-dip stabilisation and are conveniently situated few tens of megahertz away from the relevant transitions for the ^{163}Dy fermionic isotope.

5.3 Magnetic Field Control

As we have seen in the first chapters, working with a dipolar gas of highly magnetic atoms and realising artificial gauge fields require both a precise control of the magnetic fields and gradients.

We have different sets of magnetic coils in our setup, that I will shortly list below.

Zeeman slower coils

A set of coils is mounted in the direction of propagation of the atomic jet and constitute our Zeeman slower. I shall speak more in detail about the way we choose the field profile in section 5.5.3. The coils use currents up to 30 A, which necessitates enough cooling capacity. The coils are wound on a metallic water cooled cylinder – which encloses the vacuum chamber tube where the atoms are moving – and are surrounded by a second water cooled shell. To help dissipate the power we used thermal conducting glue for the cooling shields and for the coils themselves.

MOT chamber coils

The trap gradient is provided by a pair of coils connected in anti-Helmholtz configuration. Since we may need high current, these coils were wound using hollow copper wires, which can be cooled by flowing water inside the wires themselves.

Compensation cage

Three big pairs of coils in Helmholtz configuration provide a general offset field on the experimental table. The coils enclose the UHV section of our experiment and are ~ 1.5 m wide, since we need a uniform magnetic field over a distance of ~ 0.3 m while we perform the optical transport of the atoms from the MOT centre to the glass cell.

Science cell cage

The most crucial part of our setup is the glass cell, where all the future experiments will be performed. To maximise the control of the fields, the glass cell was enclosed in a plastic structure where we have mounted eight pairs of coils. Six pairs of coils are mounted along the three spatial directions, two for each direction. For each axis, one of the pairs is connected in an Helmholtz configuration and the second in anti-Helmholtz, which allow us to apply three independent field gradients and three bias fields. For the vertical direction we have an additional pair of coils made of hollow copper wire, which will be useful in case we need to work with high currents and low inductances.

5.4 Data Acquisition

The typical data we acquire are absorption images of the atomic clouds. The way one takes these images is a quite standard technique, nevertheless Dysprosium requires some additional care since the resonant scattering is strongly dependent on the light polarisation due to the high spin in the ground state (see appendix B).

We currently have six cameras installed on our experiment. To take the images in the MOT chamber which we will see in the next chapter we use a Lumenera camera^a, which is imaging along one of the MOT's proper axis. For a better imaging quality in the science chamber we use a Pixelfly camera^b, which has both lower noise and higher quantum efficiency (~ 0.5 at 421 nm). This optical axis of this imaging is perpendicular to the cell. We have also a second perpendicular axis, from which we image the atoms from the top. Currently it also uses a Lumenera camera but we plan to install a better camera and high numerical aperture lenses in the future. In addition to these cameras, we have additional ones along the propagation direction of each optical dipole trap. These on-axis cameras are used to center the traps on the atoms and eventually to implement a feedback loop to actively cancel pointing errors.

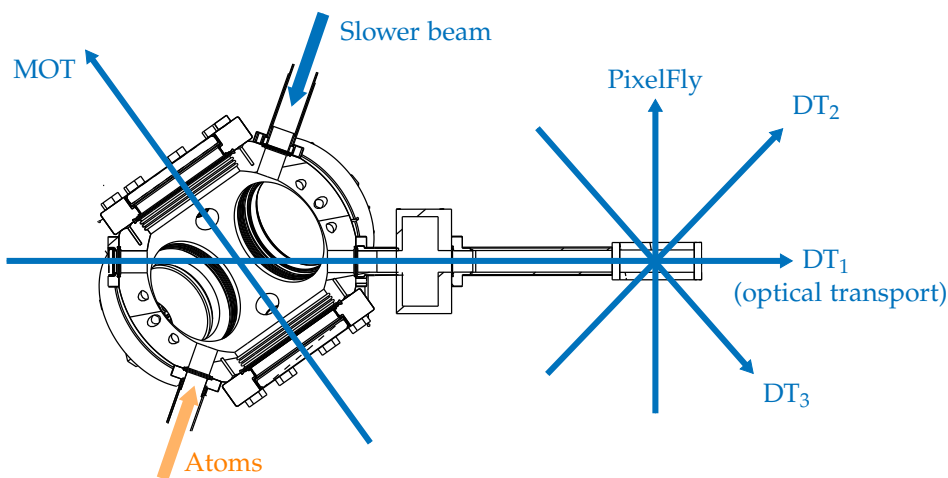


Figure 5.8 – Cut view of the UHV section of the vacuum chamber together with the horizontal images axes. In addition to the MOT imaging, we have one camera for every axis of an optical dipole trap (DT). Not in the drawing: the vertical imaging on the glass cell. The incoming direction of the atoms and of the slower light in the MOT chamber are also shown.

The typical measurements we perform require a lot of sequential steps (before taking the image of the cloud), which constitute a full experimental cycle. In each time step of the experimental sequence we need to send digital or analog signals, often with a time resolution of the order of millisecond or lower.

The experiment is driven via a chassis^c with a PCI bus in which we installed different cards that provide both digital^d and analog^e outputs. The outputs of the cards are synchronised on the clock signal provided by an external FPGA^f with a 10MHz sampling rate. To limit the number of buffer outputs during a sequence we use a variable timebase, meaning that the clock sampling varies according to the time precision we demand along the sequence.

To program the experimental sequence we use the Cicero free software [150]. It

^aLumenera Lm 135

^bPCO pixelfly

^cNational Instruments NI PXIe-1065

^dNI PXIe-6535

^eNI PXI-6713 and NI PXI-6733 for 16 bit resolution

^fFPGA reference

has a practical graphical interface that permits to visually program single outputs of the digital and analog channels. It also has a efficient RS232 interface that we use to communicate with experimental hardware not included in the chassis. The additional possibility to create socket pairs allows to send information via TCP/IP protocol to other computers, thus easily allowing interfacing Cicero with other softwares which I developed during this thesis. These softwares take care of the camera control, of magnetic and temperature probes, and of both live- and post-analysis of the data. Every software relies on a database, where all the metadata concerning a single experimental run are stored (or recovered). More technical details on both the database and the softwares can be found in appendix C.

Cicero itself is the client of a server software called Atticus, which takes care of the communication to the NI cards and the other hardware.

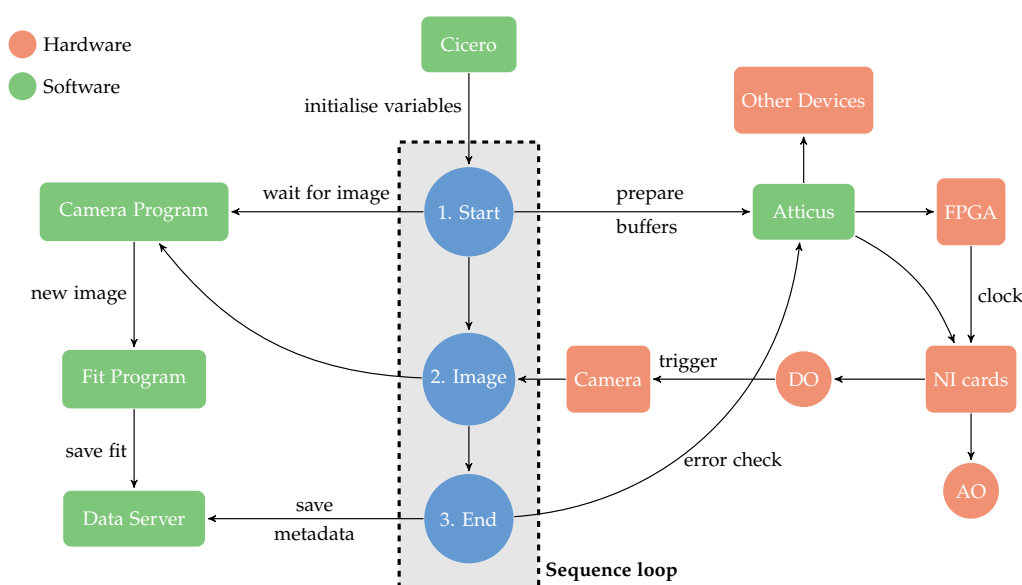


Figure 5.9 – Flow chart of the experimental sequence loop controlled by Cicero: after the initialisation the experiment runs until an image is taken and the data saving is triggered. Arrows show the main communications taking place between software and hardware.

5.5 A Slow Jet of Dysprosium Atoms

Now that I described the experimental setup, I shall focus on how we produce an atomic jet in our vacuum chamber starting from solid Dysprosium. Having atoms in the gas phase inside the vacuum chamber is the very starting point of every cold atom experiment. Atoms having low vapour pressure at ambient temperature, can be evaporated just by heating a small dispenser. In our case, one needs a special oven, since the vapour pressure of Dysprosium is negligible up to ~ 1000 K.

5.5.1 Effusion Oven

An evaporation oven is in principle an elementary device: it consists of a crucible, where the material is stored, surrounded by a cage of wires. As electrical current is let

pass through the wires, they heat up the crucible and the material will start to evaporate. By adjusting the temperature, one can adjust the pressure of the gas at will.

In spite of the simplicity of the principle, care should be taken in the construction of the oven. Since we need high temperature, both the wires and the crucible should be machined from high melting point metals, such as Wolfram (W) or Tantalum (Ta). In our case W forms alloys with Dy at high temperatures, with the risk of serious damaging the oven itself, hence our choice of a Ta crucible.

The wires will heat up not only the crucible but all the rest of the chamber unless some shielding is provided. To prevent this problem, our oven is enclosed in a metallic shelter which is in turn enclosed in a in-vacuum water cooled cylinder. An additional water cooling is externally provided from the outside to further cool the chamber parts facing the oven. With all these precautions, the vacuum chamber stays at room temperature even during normal operation of the oven.

The oven itself is a commercial double effusion cell^a.

We load ~ 10 g of Dysprosium inside the crucible every time we refill the oven. Usual working temperature is around 1050 °C. In this case, the mean free path of an atom in the oven is bigger than the oven size, the dominating interaction being the collisions between the atom and the walls of the oven, not the collision with the surrounding particles. Therefore one can use the theory of effusive flows. Under such conditions, the number of atoms emerging in a solid angle $d\Omega$ (per unit time) will be:

$$d\Phi = n\bar{v} \cos \theta A \frac{d\Omega}{4\pi} \quad (5.6)$$

where n is the atomic density in the oven volume, \bar{v} is the average velocity inside, A is the exit orifice's area and θ is the angle relative to the normal of the plane containing the oven's aperture. Note that in these equations one assumes that the thickness of the aperture is small enough to be neglected.

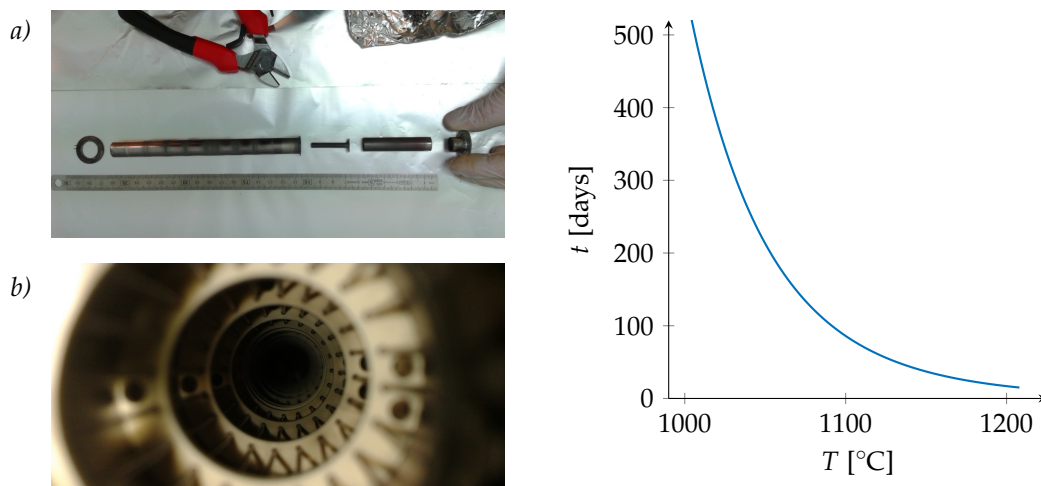


Figure 5.10 – Picture of the disassembled crucible (a) and an inside view of the oven, with the array of heating wires. The graph shows the time needed to exhaust 10g of Dy as a function of the oven temperature.

^aCreaTec DFC-40-10290-WK-SHo-Col

The cosine dependence of the outgoing beam can constitute a problem: a lot of the emerging Dy will simply stick on the chamber's walls and be lost. This problem is solved by replacing the simple aperture with a collimation tube. The atoms escaping at considerably large angles will hit the tube's wall and be either stuck or expelled at smaller angles.

In the presence of this setup modification the approximation made on the thin thickness of the aperture is not valid anymore and the flux is decreased by a factor $1/\kappa$ [151]. The calculation for a cylindrical collimation tube gives $1/\kappa = 8r/3\ell$, where r is the cylinder's radius and ℓ its length. We get:

$$\Phi = \frac{2}{3} \frac{r}{\ell} n \bar{v} A. \quad (5.7)$$

If the temperature of the collimating tube is lower than the effusion cell, Dysprosium could condense and eventually block the tube. The oven we use in our setup has a separate heating part, called the hot lip (HL), which has the purpose to maintain the temperature of the collimating tube higher than the rest of the oven, preventing thus Dysprosium to condensate.

Velocities Distribution for Atomic Jet

On the inside of the oven the velocity v is distributed according to the well known 3-dimensional Maxwell distribution. However, in the light of equation (5.7), one sees that the probability for an atom to emerge from the source is directly proportional to its velocity. Therefore, considering this additional dependence, the probability distribution of the velocities in the atomic jet will be

$$P(v) \propto \left(\frac{v}{v_{\text{mp}}^*} \right)^3 \exp\left(-\frac{v^2}{v_{\text{mp}}^{2*}} \right). \quad (5.8)$$

The distribution is different with respect to a thermal gas and therefore one has new values for both the most probable velocity and the average velocity, respectively $v_{\text{mp}} = \sqrt{3k_{\text{B}}T/m}$ and $\bar{v} = 3/4\sqrt{\pi} v_{\text{mp}}$. For our oven working at 1050 °C and for the ^{164}Dy boson, we get $v_{\text{mp}} = 460 \text{ m s}^{-1}$.

5.5.2 Transverse Cooling

Even in presence of a collimating tube, the atomic jet is diverging with quite a strong angle ($\gtrsim 90^\circ$) after the oven exit. To prevent the atoms to deposit on the windows next to the oven output we installed a pierced gasket to block the most diverging part of the atomic jet. This method will save the windows but has two main disadvantages: first, a lot of atoms will get lost, stick on the collimation walls, and second this kind of collimation does not prevent the beam to further expand. If the path taken by the atoms is long enough, like in our case during the passage through the Zeeman slower, many of the atoms will anyways get lost before reaching the trapping region of the MOT.

A standard method that actually permits both to narrow the atomic beam and to damp the transverse motion of the atoms is to perform Doppler cooling in the transverse direction. This cooling relies on the radiation pressure force due to the momentum kick $\hbar k$ of the absorbed photons. Doppler cooling increases considerably the flux in the beam direction, and one can gain some orders of magnitude on the brightness (and a factor of

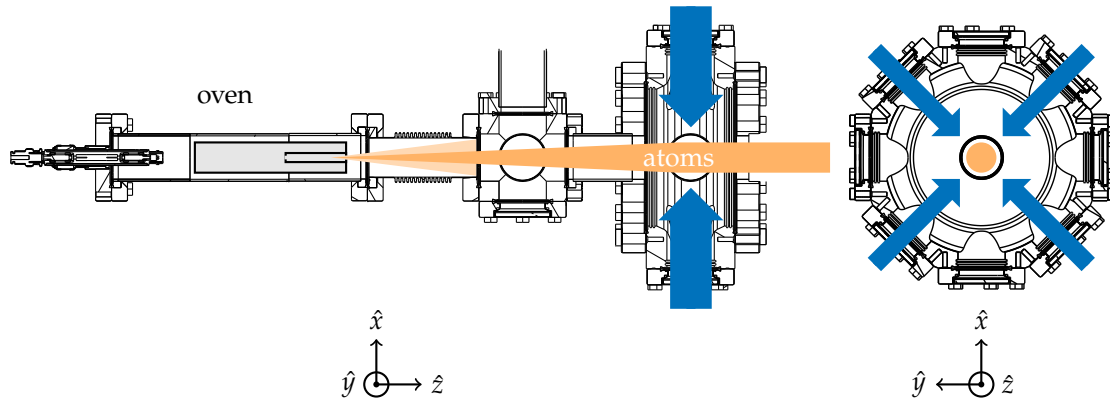


Figure 5.11 – An aperture is placed after the oven exit to block the most diverging part of the atomic jet. We then proceed to a two dimensional transverse cooling of the atomic beam to increase the brilliance and prevent further divergence.

4 in the number of captured atoms in the MOT).

For the transverse cooling of the Dysprosium jet we send two perpendicular laser beams at the 421 nm transition and retro-reflect them on the atoms. In order to maximise the interaction region, we shape the laser beam into an ellipse with 1:3 aspect ratio that better matches the atomic beam profile, the major axis of the ellipse being aligned on the Dysprosium jet direction.

5.5.3 Zeeman Slower

We have seen that the thermal velocity of the atoms right after the oven exit is about $\sim 500 \text{ m s}^{-1}$. They are too fast to be captured in a MOT since, as they fly through the trapping beams, they do not have time to scatter enough photons.

The velocity can be reduced using a Zeeman slower: sending resonant light against the atoms, the radiation pressure force is strong enough to slow them down, provided there are enough scattering events. We remind the familiar expression of the light force, to give then some relevant experimental parameter for Dysprosium

$$F_{\text{rad}} = \hbar k \frac{\Gamma}{2} \frac{s}{1 + s + 4\Delta^2/\Gamma^2} \quad (5.9)$$

which depends on the linewidth Γ and the saturation parameter $s = I/I_s$ and the laser detuning $\Delta = \omega_L - \omega_0$. For resonant light, equation (5.9) gives the deceleration:

$$a(\Delta = 0) = \frac{\hbar k \Gamma}{2m} \frac{s}{1 + s} = \eta a_{\text{max}} \quad (5.10)$$

where the parameter $\eta < 1$ is often called the security parameter, which limits the maximum slower deceleration (depending on the saturation parameter s), which is defined as $a_{\text{max}} = \hbar k \Gamma / 2m$. For the blue transition of Dysprosium $a_{\text{max}} = 5.8 \times 10^5 \text{ m s}^{-2}$.

Let us suppose an atom is moving along \hat{z} at a velocity v , and the laser counter-propagates in the $-\hat{z}$ direction. Due to the Doppler effect, the resonance condition is fulfilled only by a precise velocity class (if the laser frequency is fixed), so that the atoms get off resonance as soon as slow down. The resonance can be maintained using

spatially varying magnetic field B , which adds a Zeeman effect to the local detuning

$$\delta(z) = \Delta - kv(z) + \delta_\mu \frac{B(z)}{\hbar}. \quad (5.11)$$

Here $\delta_\mu = \mu' - \mu = \mu_B(g_{J'}m_{J'} - g_Jm_J)$ is the difference in magnetic moment between the ground state and the excited state, with g_J and $g_{J'}$ the respective Landé g -factors. When the magnetic field profile $B(z)$ is well chosen, it compensates the Doppler effect along the whole deceleration distance, maintaining the atoms always on resonance with the laser light.

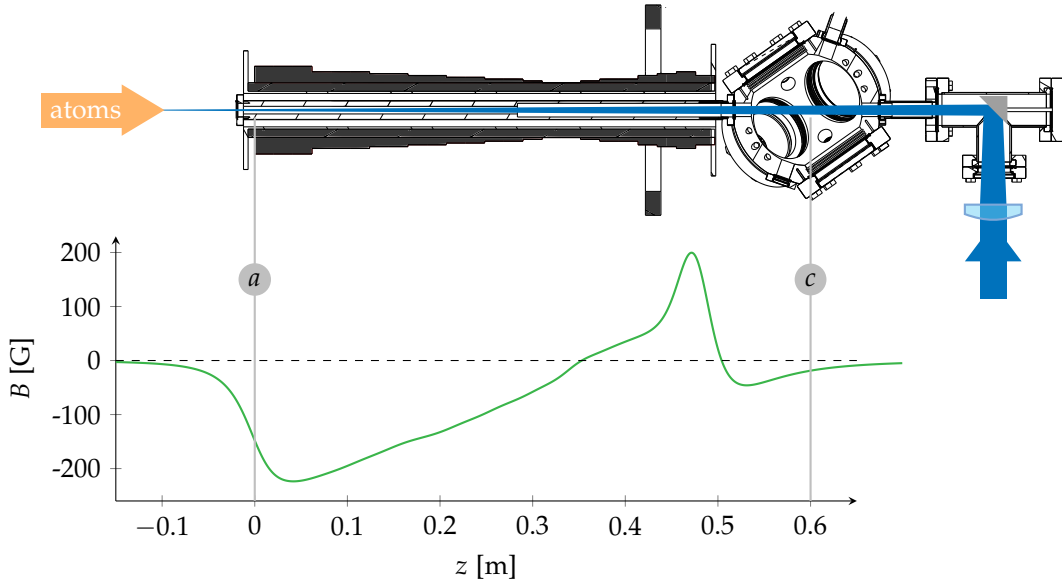


Figure 5.12 – Schematic drawing of the apparatus and plot of the magnetic field B along the slower axis z . The points a) and c) mark the entrance of the slower and the MOT centre position. From the section of the Zeeman slower, one notices that it is constituted by a stack of coils. The blue laser is reflected by an in-vacuum mirror and aligned against the atomic jet. The focus is before the slower entrance, to slow down the atoms in the transverse direction as well.

Imposing the condition of constant deceleration, one gets the velocity profile

$$v(z) = v_0 \sqrt{1 - \frac{2\eta a_{\max} z}{v_c}}. \quad (5.12)$$

The capture velocity v_0 is chosen to be the most probable thermal velocity at the oven exit $v_0 = v_{\text{mp}} = \sqrt{3k_B T/m} = 460 \text{ m s}^{-1}$. Every atom with velocity lower than v_0 could be slowed if the magnetic field has the ideal theoretical profile. The latter could be straightforwardly computed from the condition $\delta(z) = 0$ as

$$B_{\text{ideal}} = B_{\text{bias}} + B_0 \sqrt{1 - \frac{2\eta a_{\max} z}{v_0}}. \quad (5.13)$$

The field has thus a square-root dependence on the distance and a high B_0 , that can be

shifted by a bias component B_{bias} . These two terms are respectively

$$B_0 = -\frac{\hbar k v_0}{\delta_\mu} \quad \text{and} \quad B_{\text{bias}} = -\frac{\hbar \Delta}{\delta_\mu}. \quad (5.14)$$

The choice of the laser detuning Δ is completely free, but it will determine the value of the bias field B_{bias} . Having a small detuning $\Delta \sim 0$ or a very large one both have disadvantages, since in the first case the field will decrease along the slower but at the MOT position the light will be resonant with the trapped atoms (which could then be pushed out of the MOT by the radiation force), in the second case the light will not be resonant at the MOT position but the high value of B_{bias} could deform the MOT quadrupolar field, in particular for low MOT gradient fields.

In our experiment the slower is built in a spin-flip configuration, *i.e.* the magnetic field crosses zero. This allows us to work with lower fields (which also helps to keep residual gradients at the MOT position very low). The laser detuning is $\Delta/2\pi \sim 500$ MHz, which corresponds to $\Delta = -15 \times \Gamma$ from the resonance. Even if this detuning is quite large, the residual optical force is still large enough to perturb the atoms in the trap. For this reason the centre of the MOT is slightly lower than the beam, to avoid undesirable light forces.

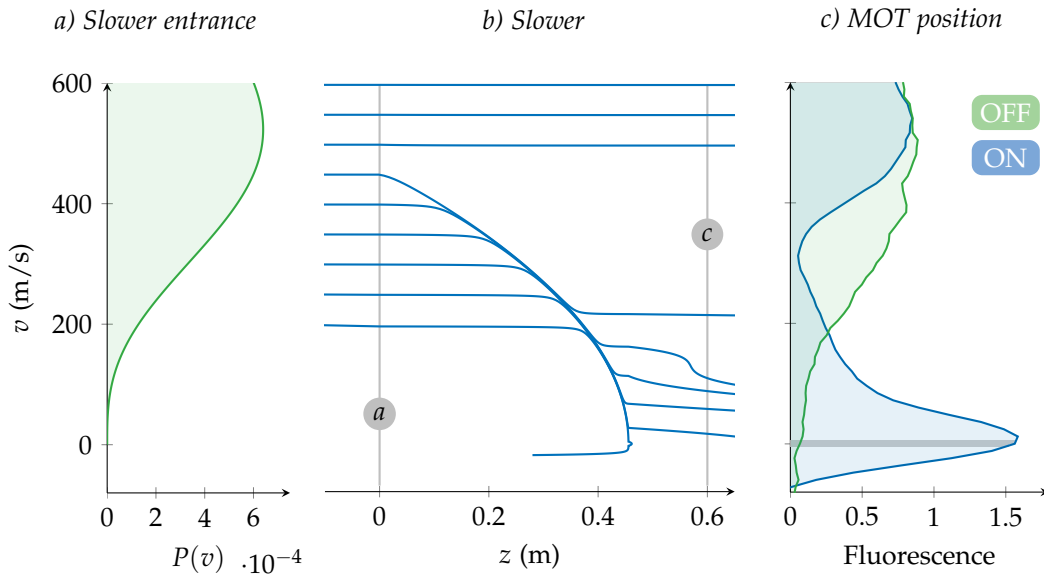


Figure 5.13 – Evolution of the atomic velocity before and after the Zeeman slower. Notice that the three graphs share the same vertical axis. a) Probability distribution of velocities at the oven working temperature. Plot from equation (5.8). b) Trajectories of the velocities along the slower. Two grey vertical lines mark the entrance of the slower and the MOT centre position, at ~ 60 cm distance. c) Fluorescence signal of the ^{164}Dy boson collected at the MOT position as a function of atomic velocity. The green (blue) spectrum shows the fluorescence in the case the slower is off (on). The grey shaded area represents the velocity class that can be captured by the MOT.

The total length L of the slower is fixed by the desired final velocity v_f , which is fixed by the MOT capture velocity. For our experimental parameters $v_f \sim 8 \text{ m s}^{-1}$ (see

chapter 6), and is given by

$$L = \frac{v_0^2 - v_f^2}{2\eta a_{\max}}, \quad (5.15)$$

which in our case is $L = 50$ cm.

Before trying to operate the magneto-optical trap, we separately tested the efficiency of the slower by spectroscopy on the atomic jet. For this purpose we use a laser diode at 421 nm^a. We shine the light on the atoms after the passage into the slower, from an angled direction. In this way we were able to sense the velocity distribution along the propagating direction. Then we collect the fluorescence with a large area photodiode. The calibration of the zero velocity position was done by simultaneously collecting a reference spectrum from a direction perpendicular to the atoms' propagation direction. The results of this measurement are presented in Figure 5.13, along with the theoretical distribution of velocities before the cooling process and the velocity evolution in the Zeeman slower. After this test we are sure the atoms are sufficiently slow to be trapped in the MOT, which is the subject of next chapter.

^aTopic diode reference

6

Narrow Line MOT

TRAPPING atoms in a magneto optical trap (MOT) is the first fundamental step of every ultra cold atoms experiment. Dysprosium MOTs are quite different from the more common alkali or alkali-earth atoms. In particular:

- the optical cooling is performed on a narrow transition, thus the optical forces are much weaker;
- the total angular momentum quantum number in the ground state is $J = 8$, yielding to a rich spin structure.

Indeed, we shall see some interesting consequences of the non trivial physics arising from the combination of these characteristics and I also give a theoretical model to understand them. Before we turn to the analysis of the experimental results, I make a short historical excursus on Dysprosium traps and, starting from the cold atomic jet described in the previous chapter, I describe our experimental realisation of the MOT.

6.1 Magneto Optical Trapping of Dysprosium

The first Dysprosium MOT was realised in Stanford in 2010 using the strong blue line as cooling transition [152], in the light of previous work on repumper-less MOT of Erbium atom carried on by J. J. McClelland at NIST [48]. Even if the blue transition is not completely closed, atoms escaping in dark metastable states can still be magnetically trapped in the quadrupole MOT field thanks to their large magnetic moment, until they relax back in the ground state and enter again the cooling cycle. With this kind of trap one achieves typical temperatures of ~ 1 mK. Lower temperatures can only be obtained with a second MOT, which is loaded from the first one, working on the 1.8 kHz ultra-narrow 741 nm transition, in a similar fashion of how Strontium MOT are produced [153]. In this manner a dense cloud at $2 \mu\text{K}$ can be reached (the temperature being however far from the Doppler limit of 84 nK) [131].

Unlike this previous work, designing our laser cooling apparatus we followed the

scheme for Erbium MOT used of the experimental group in Innsbruck [52], where the cooling is performed using an intercombination line (in our case the 626 nm transition), as it is the case in previous work on Ytterbium atoms [154]. These atomic species are also lanthanides, and thus possess optical transitions with similar properties. In particular the narrow MOT and the strong blue transitions are associated to the same electronic excitations in the three atomic species. At the same time of our studies, this laser cooling scheme has been successfully used in the group of T. Pfau in Stuttgart to produce the first Dy MOT using this transition [53]. Despite these previous works on Erbium and Dysprosium already successfully demonstrate the efficiency of the trapping and, as we will see, the spontaneous polarisation of the atomic cloud, in the following we provide a deeper and more complete analysis of the evolution of the MOT parameters, that we published in [80].

Intercombination lines are very narrow compared to the D_2 lines used in alkali atoms experiments, where linewidths are of the order of few MHz. The Dysprosium transition, having a linewidth as narrow as $\Gamma/2\pi = 135$ kHz permits to have a low Doppler temperature of $T_D = 3.26$ μ K. This lower limit is comparable to the temperature experimentally achieved using the 741 nm. Moreover, since the 626 nm transition is broader, the capture velocity is increased, thus permitting a direct load of the atoms from the Zeeman slowed beam and avoiding the use a double colour MOT.

The geometry of our MOT is represented in figure 6.1. Two MOT beams propagate along the strong gradient axes e_x in the horizontal plane while the other four lie on the plane $(0, y, z)$ and are sent from 45° angled directions.

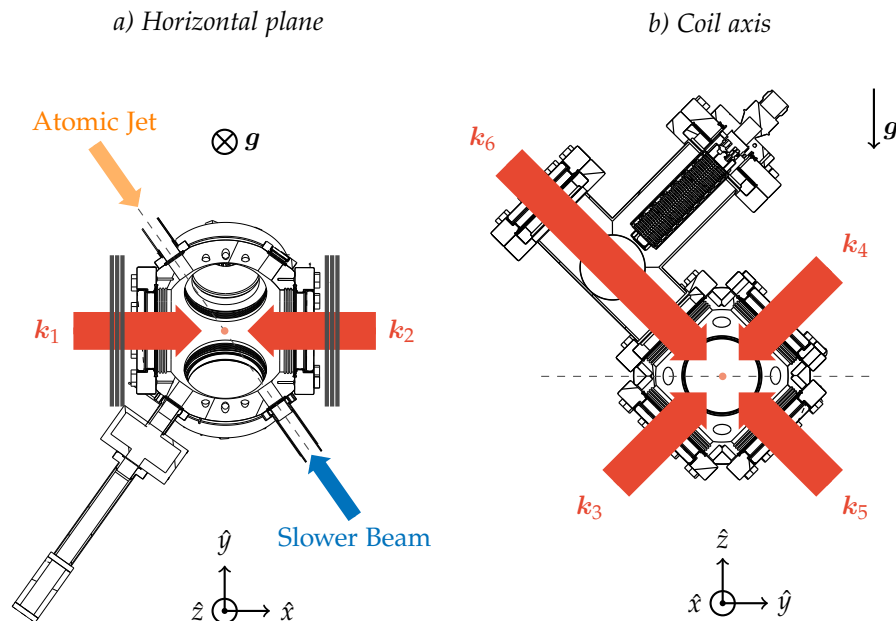


Figure 6.1 – Scheme of the experimental geometry for the magneto optical trap viewed from two different axis. Two beams are in the horizontal plane while the others arrive from 45°. In orange and blue the directions of propagation of the atoms arriving in the MOT and the slowing light. The coils and the gravity direction are also shown in the figures.

6.1.1 MOT Loading

On the previous graph, we can see that the slowing beam is crossing the centre of the chamber. The residual optical force could induce atom losses from the trap. Therefore, as we load the MOT, we shift the zero of the magnetic field quadrupole $\mathbf{B} = b(-x, y/2, z/2)$ below the slower axis by adding a vertical uniform field $\mathbf{B}_{\text{comp}} = -B_0\mathbf{e}_z$.

The narrowness of the line has a direct consequence on the maximum velocity that can be captured in the trap. In fact, only atoms with a velocity up to a certain value v_c can be captured, while the others will simply fly through the MOT. Having defined the maximum deceleration due to the laser light a_{max} in equation (5.10), if the atom interacts with the light in a region given by the beam diameter $2w_0$, the capture velocity will be

$$v_c = \sqrt{a_{\text{max}}2w_0} = \sqrt{\frac{\hbar k\Gamma}{m}}w_0. \quad (6.1)$$

We clearly see the interest of having wide beams as long as we can saturate the optical transition. In our experiment the waist of the beams is $w_0 = 20 \text{ mm}$, leading to a capture velocity of $v_c \sim 8 \text{ m s}^{-1}$.

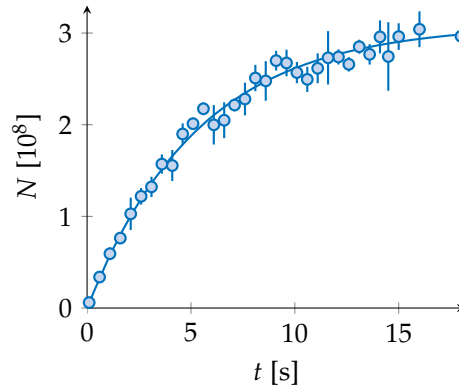


Figure 6.2 – Loading curve of the MOT. Number of atoms as a function of charging time. From the fit we obtain a loading rate $6(1) \times 10^7$ atoms per second and a saturation value $N_{\text{max}} = 3.1(5) \times 10^8$.

Another consequence of working with a narrow line is that the Doppler force will be resonant only with a reduced velocity class of atoms. Thus a very low number of atoms can be captured by the MOT at the exit of the slower, the rest of them being either too fast or too slow to be affected by the light.

We address the problem by two means. First, the line is broadened by using high laser intensity. Since the saturation intensity is just about $72 \mu\text{W cm}^{-2}$ it is easy to work with high saturation parameters. In our case we typically have a power of $P = 50 \text{ mW}$ per beam, resulting in a saturation parameter $s = I/I_s \sim 50$ per beam. Second, the linewidth of the laser is broadened by sideband modulation. This permits to enlarge the velocity class addressed by the laser light and thus increases the efficiency of the MOT loading. By an acousto-optic modulator we introduce sidebands spaced by 135 kHz over a total frequency range of $\delta f \sim 6 \text{ MHz}$. The broadened spectrum and the resulting captured atom number is presented in figure 6.3.

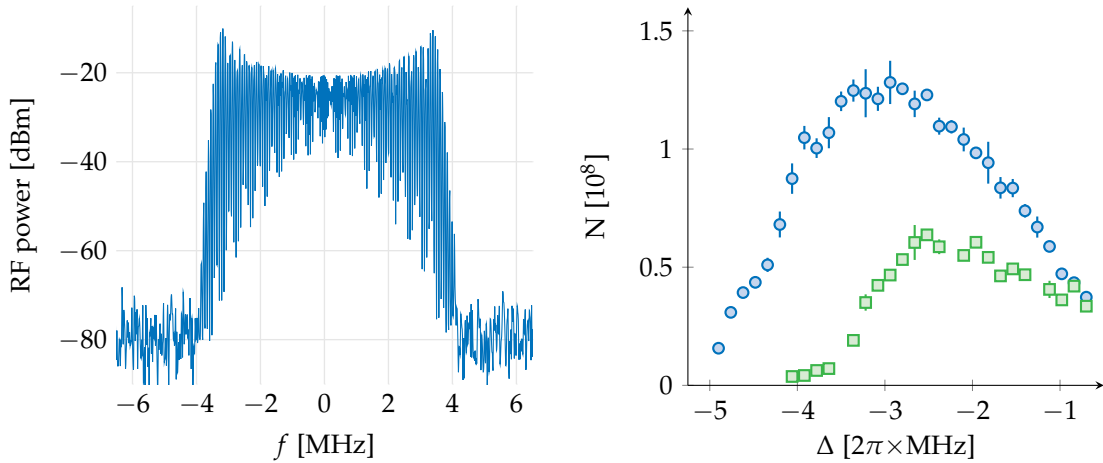


Figure 6.3 – Recorded power spectra of the RF used to modulate the MOT light. Blue (green) curve is with (without) frequency broadening. On the right, the resulting atom number in the MOT after 6 s loading time, as a function of laser detuning Δ , with \circ or without \square broadening. The frequency zero is set at the atomic resonance.

6.1.2 Compressed MOT

After the loading process the MOT is still too large and too hot to permit an efficient loading of the dipole trap. Therefore we proceed with a compression phase in which we reduce the light intensity, reducing the photon scattering and thus the heating of the trapped atoms. At the same time, since the Zeeman light has been turned off after the loading of the MOT, we shift the quadrupole position back into the centre of the chamber, preparing the alignment of the dipole trap.

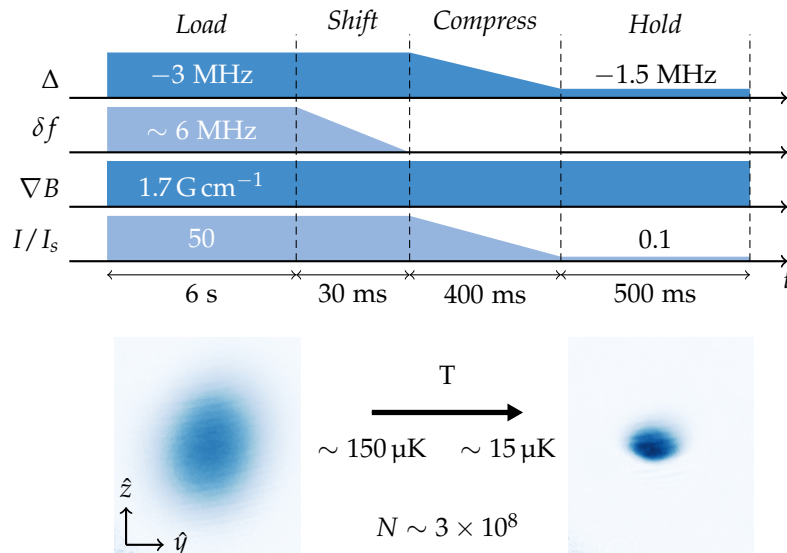


Figure 6.4 – Variation of the MOT parameters along the compression sequence. The laser detuning Δ is diminished while decreasing the light intensity. Below in situ images of MOT before and after compression. The dependence of the MOT parameters on the final values will be the subject of the next sections.

We compensate the loss of intensity, and hence the lowering of the optical force strength, by reducing the detuning Δ . Also, the sideband modulation is turned off during the whole process. A scheme of the changing parameters is presented in figure 6.4, along with the in situ images of the trapped atoms at the beginning and at the end of the compression phase. Temperatures diminish from values higher than 200 μK down to 15 μK .

We experimentally find that the final parameters of the compression phase change quite drastically the behaviour of the MOT. Let us take a closer look to the different regimes we can explore by varying the laser intensity or frequency.

6.2 MOT Position

We first investigate the effect of the laser detuning Δ on the cloud centre position, which drops for increasing values of Δ , as shown in figure 6.5.

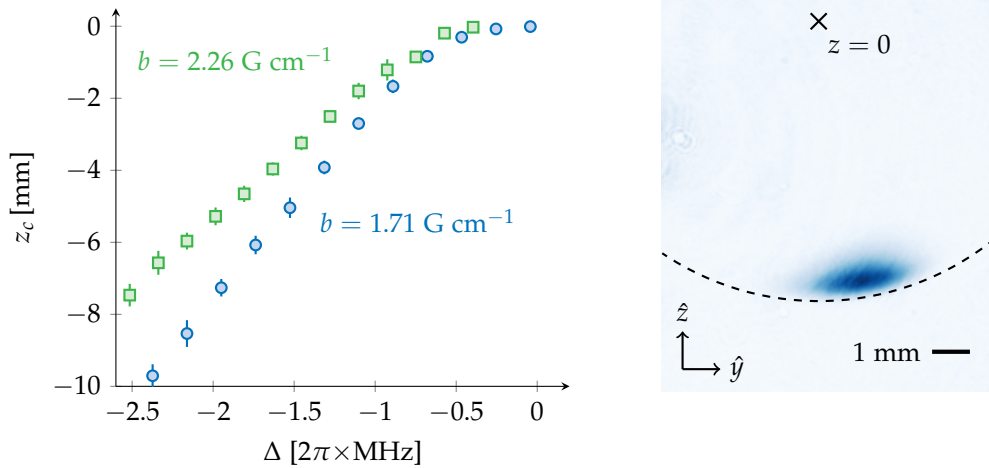


Figure 6.5 – Position of the atomic cloud center z_c as a function of laser detuning Δ . The two data sets are taken for different quadrupole field strengths. On the right: in-situ image of the cloud for large detuning. The atoms are clearly shifted down with respect to the center of the trap, indicated by a cross. The dashed line is an isomagnetic curve.

The key factor to understand the physics of a narrow line MOT is that the optical forces are much lower than for alkali atoms and one should expect gravity force to play a crucial role. To quantify this effect it is useful to introduce the adimensional parameter

$$\eta = \frac{\hbar k \Gamma}{2mg} \sim 168, \quad (6.2)$$

that is the ratio between the maximal optical force and the gravity force. The given value is for our MOT parameter. For comparison, $\eta \sim 10^5$ for alkali MOT working on the D_2 line (while it is smaller than our case for alkali-earth MOTs).

Clearly then, what is happening is that gravity tends to push down the atomic cloud as the optical force gets weaker, since the equilibrium condition requires the two forces to compensate each other $F_{\text{rad}} + mg = 0$. Let us consider for the sake of simplicity a

two-level atomic model driven by σ_- polarised light. If we restrict the calculation of the optical force in the vertical direction e_z , we just have to sum the contributions of the four beams in the (z, y) plane. We get

$$F_{\text{rad}} = \frac{\hbar k \Gamma}{2} \frac{s}{1 + 2s + 4\Delta_{\text{loc}}^2/\Gamma^2} e_z, \quad (6.3)$$

where Δ_{loc} is the local detuning at the position of the atomic cloud centre z_c , which takes into account for the Doppler effect and the local Zeeman effect. The equilibrium condition for the forces leads to

$$\frac{s}{1 + 2s + 4\Delta_{\text{loc}}^2/\Gamma^2} = \frac{1}{\eta'}, \quad (6.4)$$

which gives the interesting result of Δ_{loc} being independent on the laser detuning Δ or the magnetic gradient $\nabla B = (-b, b/2, b/2)$, varying only with the saturation intensity s :

$$\Delta_{\text{loc}} = -\frac{\Gamma}{2} \sqrt{(\eta - 2)s - 1}. \quad (6.5)$$

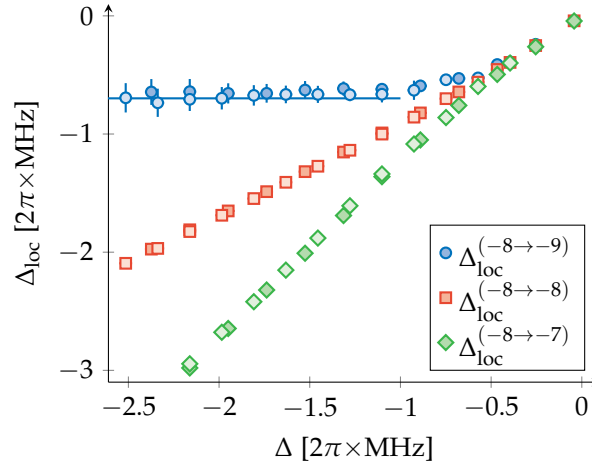


Figure 6.6 – Local detuning $\Delta_{\text{loc}}^{(m_l \rightarrow m'_l)}$ as a function of the laser detuning Δ . Data are calculated from the MOT position taking into account an ambient residual gradient $\nabla B = -0.094(2) \text{ G cm}^{-1}$. Open and filled symbols refer to the different magnetic gradients of figure 6.5. The σ_- component of the light saturates to the constant value. The solid line is the theoretical value calculated from the formula given in the main text.

This can be proved refining the model by taking into consideration different light polarisations. The local detunings $\Delta_{\text{loc}}^{(-8 \rightarrow m'_l)}$ (with $m'_l \in \{-9, -8, -7\}$) are calculated from the data presented in figure 6.5 and using the expression for the position dependent detuning as in formula (5.11). We also plot the value of $\Delta_{\text{loc}}^{-8 \rightarrow -9}$ as calculated from the above equation, which agrees quite well with the data at large laser detuning. One may wonder why a two level model is capable of describing this result, even though Dysprosium has a rich spin structure. Figure 6.6 brings element of understanding. By looking at the local detuning for the three different light polarisations, we see that only σ_-

component saturates to an asymptotic value when increasing $|\Delta|$, while the π and σ_+ get further off resonant. The predominance of σ_- light will therefore lead to optical pumping of the electronic spin to the absolute ground state, the only relevant optical transition remaining $|J = 8, m_J = -8\rangle \longleftrightarrow |J' = 9, m_{J'} = -9\rangle$. The cloud is hence polarised for large laser detunings $\Delta \lesssim -2\pi \times 1 \text{ MHz}$, justifying the two-level assumption.

6.3 Spin Composition

By looking at the previous results, it is interesting to study how the different electronic states will be populated in the small detuning regime, where all polarisations become resonant. We know that when we eventually transfer atoms into the dipole trap, they undergo dipolar relaxation and get lost from the trap if the cloud is not polarised (see chapter 2). In the following let us attempt to write a simple theoretical model for the atoms in the trap, based on optical pumping for the populations in the spin states.

6.3.1 Rate Equation Model

One should in principle solve the optical Bloch equations for the whole electronic spin ensemble to obtain the time evolution of the populations. We can simplify the problem by neglecting the coherences and therefore considering just the pumping rates.

Let us consider the spontaneous emission from the excited state manifold J' . Every relaxation channel from an excited state $|J', m_J + q\rangle \rightarrow |J, m_J\rangle$ will have a decay rate given by

$$\Gamma_{m_J, q} = \Gamma |c_{m_J, q}|^2, \quad (6.6)$$

that is the natural linewidth Γ weighted by the square of the Clebsh-Gordan coefficient

$$c_{m_J, q} = \sqrt{2J' + 1} \begin{pmatrix} J' & 1 & J \\ m_J + q & -q & -m_J \end{pmatrix}, \quad (6.7)$$

where we used the Wigner 3-j symbol notation [94]. The index $q \in \{1, 0, -1\}$ accounts for the light polarisation. For the interested reader, numerical values of the coefficients can be found in figure B.3.

Let us label the MOT beams with the index $p \in \{1, 2, \dots, 6\}$. Each of the beams will couple to the transition $|J', m_J + q\rangle \longleftrightarrow |J, m_J\rangle$ with a rate given by

$$\gamma_{m_J, q, p} = s_{m_J, q, p} \frac{\Gamma}{2} |c_{m_J, q}|^2 \quad (6.8)$$

where we defined the transition-dependent saturation parameter

$$s_{m_J, q, p} = \frac{s_0}{1 + 4\Delta_{m_J, q, p}^2 / \Gamma^2} (\mathbf{e}_q^* \cdot \boldsymbol{\epsilon}_p)^2 \quad (6.9)$$

with s_0 being the resonant saturation parameter for every single beam and the scalar product giving the projection of each beam in the polarisation basis. The detuning accounts for both Zeeman and Doppler effect

$$\Delta_{m_J, q, p} = \Delta + \delta_\mu - \mathbf{k}_p \cdot \mathbf{v}, \quad (6.10)$$

where δ_μ is the difference between the ground state and excited state magnetic moment, as defined in equation (5.11), and k_p is the beam wave vector.

We can now write the rate equations for populations in both the ground and excited electronic states, that we shall respectively call Π_{m_J} and $\Pi'_{m'_J}$. For every state we need to sum the contributions from the coupling to each laser beam and the spontaneous decay. Neglecting coherences, we are lead to the following system of equations

$$\begin{cases} \dot{\Pi}_{m_J} = \sum_q \left(\Gamma_{m_J,q} + \sum_p \gamma_{m_J,q,p} \right) \Pi'_{m_J+q} - \sum_{p,q} \gamma_{m_J,q,p} \Pi_{m_J} \\ \dot{\Pi}'_{m'_J} = \sum_{p,q} \gamma_{m'_J-q,q,p} \Pi_{m'_J-q} - \sum_q \left(\Gamma_{m'_J-q,q} + \sum_p \gamma_{m'_J-q,q,p} \right) \Pi'_{m'_J} \end{cases} \quad (6.11)$$

For the Dysprosium MOT on the 626 nm transition $J' = 9$ and $J = 8$, the absolute ground state being $|g\rangle = |8, -8\rangle$. We thus have a system with $(2J' + 1) + (2J + 1) = 36$ coupled equations. Since we are interested in the equilibrium properties of the MOT we can just consider the solution of the steady state system $\dot{\Pi}_{m_J} = \dot{\Pi}'_{m'_J} = 0$.

Once we have the population in the excited states we can write the total force acting on the atoms. In the case of a two level system, each beam contribution will simply be $F_{\text{rad}} = \hbar k \Gamma \Pi'$. In the low saturation regime, we can consider the beams as independent, hence the total force is given by the sum of the six beams $F_{\text{rad}} = \sum_{p=1}^6 F_{\text{rad},p}$. In our case, we should use the right Clebsh-Gordan coefficients to account for the different Zeeman states, which gives for each beam

$$F_{\text{rad},p} = \hbar k_p \Gamma \sum_{m'_J} \frac{s_{m'_J-q,q,p} |c_{m'_J-q,q}|^2}{\sum_p s_{m'_J-q,q,p} |c_{m'_J-q,q}|^2} \Pi'_{m'_J} \quad (6.12)$$

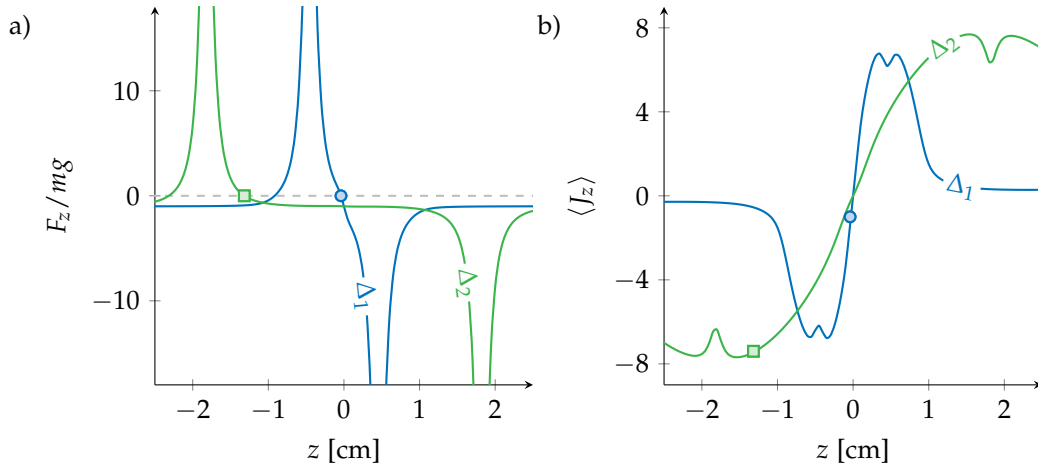


Figure 6.7 – a) Total force in the vertical direction F_z acting on an atom at rest calculated from equation (6.13). b) Average population $\langle J_z \rangle$ as a function of the vertical position z . Different colours are for different laser detuning: green is for $\Delta_2 = -2$ MHz and blue is closer to resonance $\Delta_1 = -0.5$ MHz. The points in the two plots mark the equilibrium position z_c , defined at $F_z = 0$.

Once we have inserted the steady state solution in the previous formula, we can plot

the total force F acting on an atom at rest. The total force should account also for the gravity and the magnetic contribution:

$$F = F_{\text{rad}} - m\mathbf{g} - \frac{\mu_B}{2} \left(g_J \sum_{m_J} \Pi_{m_J} m_J + g_{J'} \sum_{m_{J'}} \Pi_{m_{J'}} m_{J'} \right) \nabla B, \quad (6.13)$$

where $g_J, g_{J'}$ are the Lande's factors for the ground and excited state (see appendix A). A plot of the force in the vertical plane $F_z = F \cdot \mathbf{e}_z$ is shown in figure 6.7. One can see how the gravity breaks the symmetry of the trap, shifting the equilibrium position z_c further below the trap centre for decreasing laser detuning. On the second graph, one can see the average $\langle J_z \rangle$ calculated from the steady state populations Π_{m_J} at different position. From the plot it is clear that the drop of the equilibrium position leads to a progressive spontaneous polarisation of the MOT $\langle J_z \rangle \rightarrow -8$ as the detuning is increased.

6.3.2 Stern-Gerlach Imaging

To validate experimentally the theory we need to measure the population in the different electronic spin states. A simple way of doing so is to perform a Stern-Gerlach imaging.

This technique consists in applying a strong magnetic gradient, say in the z direction^a. The force that one atom experiences depends on its internal magnetic state m_J . Atoms in $|m_J = 0\rangle$ will not be affected, while positive and negative $|m_J\rangle$ will be accelerated in opposite direction with a magnitude given by

$$a(z) = -\frac{\mu_B}{m\hbar} g_J m_J \partial_z |\mathbf{B}|. \quad (6.14)$$

Therefore it is possible to split the cloud according to the internal electronic state of the atoms, provided that one has let enough time for the single components to spatially separate one from each other. It is then easy to recover the population in each $|m_J\rangle$ state just by fitting the single clouds.

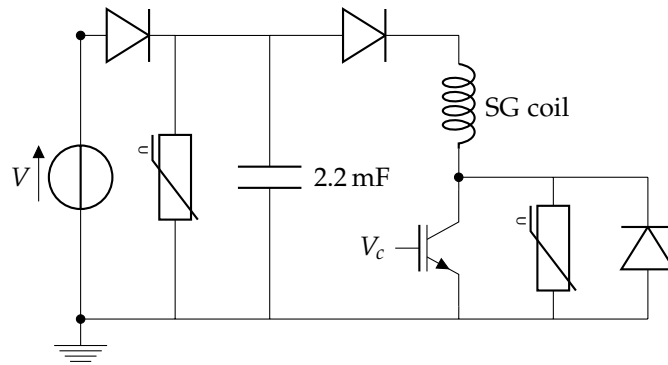


Figure 6.8 – Scheme of the Stern Gerlach circuit. When the IGBT is opened the capacitor discharges on the coil. With our setup we have a peak current of 480 A in 4 ms.

With respect to usual Stern-Gerlach measures with ultra cold atom, our measure shows additional difficulty since the cloud is relatively quite hot and large and the coil

^aHere, we mean that there is a strong magnetic gradient plus a uniform field in the vertical direction. The gradient alone can not be unidirectional because $\nabla \cdot \mathbf{B} = 0$.

is quite far. Normally to have a clear separation of the components it is sufficient to increase the TOF, since the distance grows with the square of the time while the size grows linearly. In our case we could not wait longer since the cloud is already much diluted and the signal gets too weak. Besides, the heating of the coil did not permit to further increase the magnetic gradient.

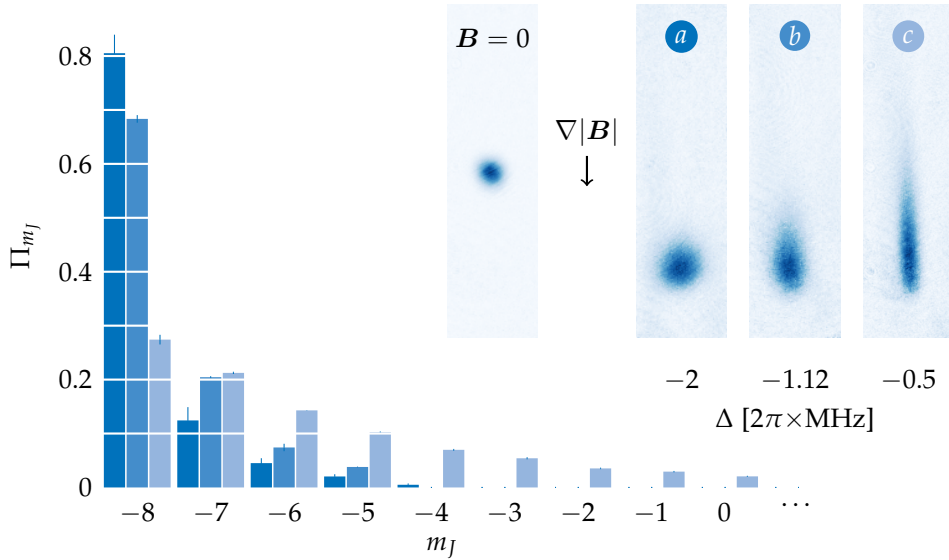


Figure 6.9 – Histogram of population Π_{m_j} in the different Stern Gerlach imaging of the MOT. By applying a magnetic field gradient during the time of flight, the cloud splits into its magnetic states. a , b and c pictures are taken for decreasing values of laser detuning Δ . One can clearly see the polarisation of the MOT in the absolute ground state $|m_j = -8\rangle$ in picture a . The image at $B = 0$ is the reference for picture c .

We generate the field gradient using a coil aligned on the gravity axis, where we discharge a large 2.2 mF capacitor. The electrical circuit is sketched in figure 6.8. The discharge gives a peak current of 480 A in ~ 4 ms, which provides a field of 30 G cm^{-1} at the MOT position. The main limitation in using higher currents is the power dissipation in the coil, since the experimental geometry did not permit to include some cooling element for the wires.

Some images taken for different detuning are presented in figure 6.9. For every detuning a reference image without magnetic gradient is taken. This will be used to recover the position of the $|m_j = 0\rangle$ state, that is not affected by the magnetic force. A multiple gaussian fit of the clouds, weighted with the proper coefficients (see appendix B) is used to recover the relative population in every Zeeman level Π_{m_j} .

Once we obtained the Π_{m_j} we calculate the mean spin projection $\langle J_z \rangle$ for the various detunings. The results are plotted in figure 6.10 and show a quite good agreement with the theory curve calculate from the rate equation model.

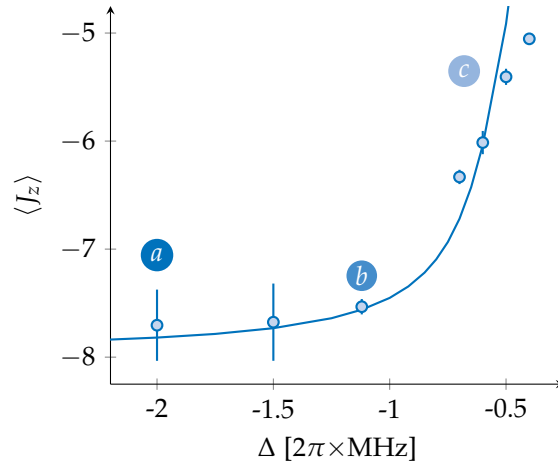


Figure 6.10 – Mean spin projection $\langle J_z \rangle$ for different detunings of the MOT light. Data points are the average population obtained from the Stern-Gerlach measure. The data points a,b and c refer to the previous image. The solid line is the theoretical value from the model.

6.4 Temperature

As we have mentioned, the narrow line width of our MOT transition width gives a Doppler limit temperature of $T_D \sim 3 \mu\text{K}$. In our setup we achieve T as low as $15 \mu\text{K}$ on normal operation. This value depends strongly on the laser detuning Δ and the saturation parameter s as we will see. Let us now provide some quantitative formulae in the simple case of polarised MOT. We previously mentioned that for large detuning that the only relevant optical transition is driven by σ_- light between the $|J = 8, m_J = -8\rangle \leftrightarrow |J' = 9, m_{J'} = -9\rangle$ states. In this case we recover an effective two level system and we can derive some analytical expressions for the MOT temperature.

For very low velocities, the force can be expanded linearly $F = m\alpha v$. This permits to define an effective friction coefficient α . Nevertheless the radiative forces we have considered so far are assumed to be average values. The total force has also a random fluctuating component $\delta F(t)$, which is the Langevin force associated to the stochastic radiative process, and that we neglect since $\langle \delta F(t) \rangle = 0$. Nevertheless, the fluctuations of the force $\langle \delta F(t) \delta F(t') \rangle = 2D\delta(t - t')$ (where D is the diffusion coefficient), affect the position of an atom at the centre of the trap, which is described by a Brownian motion. This diffusive behaviour of the atoms gives a lower bound to the achievable temperature in the trap, which can be recovered using the Einstein relation

$$T = \frac{D}{m\alpha k_B}, \quad (6.15)$$

provided that one can give an expression for the diffusion coefficient D .

Let us now attempt to derive the temperature T . Let us start by the linearisation of the radiative pressure force around the equilibrium point r_c , which gives

$$F_{\text{rad}}(v) = -m\alpha \left(\frac{2}{3} v_x e_x + v_y e_y + v_z e_z \right) + \mathcal{O}(v^2). \quad (6.16)$$

Here, the α coefficient has the following expression

$$\alpha = \frac{3\sqrt{s_0(\eta - 2) - 1} E_r}{\eta^2 s_0 \hbar} \quad (6.17)$$

where η has been already defined in equation and $E_r = \hbar k/2m$ is the recoil energy associated to a photon momentum kick. The damping coefficient α is directly related to the equilibration time $\tau = 1/(2\alpha)$, which one can access experimentally. In figure 6.11 we plot the relaxation of the MOT temperature to the equilibrium value for $\Delta = -2\pi \times 1.84$ MHz and $s = 0.65$. The time constant that we get from an exponential fit is $\tau \sim 29(11)$ ms, which corresponds to a value of $\alpha = 17(6) \text{ s}^{-1}$, which is smaller than the calculated value $\alpha = 47(2) \text{ s}^{-1}$ given by the equation above but of the right order of magnitude.

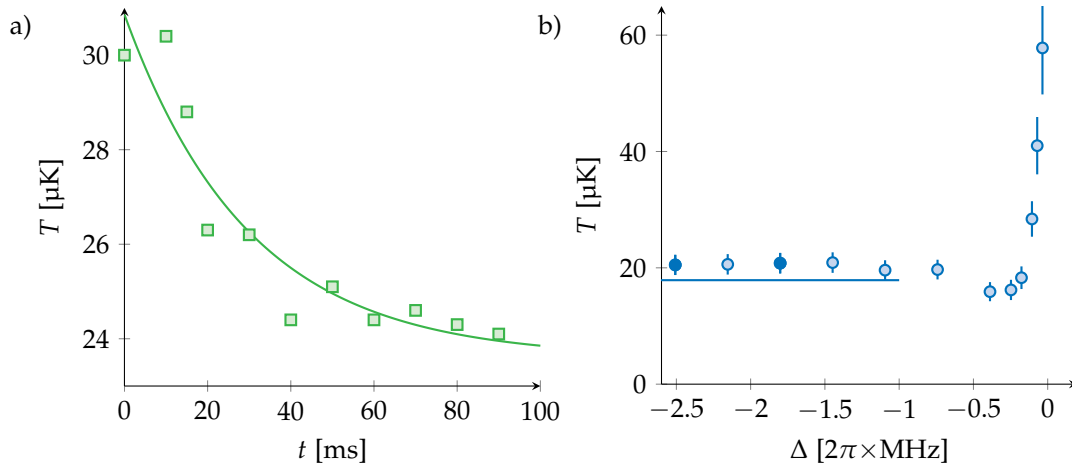


Figure 6.11 – a) Evolution of the MOT temperature T after the compression phase. The equilibration time is directly related to the velocity damping coefficient α . b) Temperature as a function of laser detuning Δ at fixed saturation parameter $s = 0.65$. In the polarised regime, T saturates to a finite value, calculated from equation (6.20) and shown as a solid line. The dark circles will be referred to in picture 6.12.

Let us now consider the diffusion coefficient D , which is given by the sum of two different contributions, since both the absorption of a photon and the spontaneous emission are stochastic processes. Let us label the two different contributions D^{abs} and D^{em} .

To obtain the absorption D^{abs} one needs to calculate the rate at which every single beam is scattered. In the (x, y, z) basis defined in figure 6.1, the diffusion matrix is diagonal and is given by

$$D^{\text{abs}} = \frac{1}{16\eta} \hbar^2 k^2 \Gamma \begin{pmatrix} 2 & 0 & 0 \\ 0 & 3 & 0 \\ 0 & 0 & 3 \end{pmatrix}. \quad (6.18)$$

The diffusion due to the spontaneous emission is also anisotropic due to the intrinsic

anisotropy of the dipole scattering

$$D^{\text{em}} = \frac{1}{20\eta} \hbar^2 k^2 \Gamma \begin{pmatrix} 3 & 0 & 0 \\ 0 & 3 & 0 \\ 0 & 0 & 4 \end{pmatrix} \quad (6.19)$$

Summing the two diffusion coefficients and using the expression given above, we finally get the following expression for the equilibrium temperature

$$\begin{pmatrix} T_x \\ T_y \\ T_z \end{pmatrix} = \frac{\hbar\Gamma}{k_B} \frac{s\eta}{2\sqrt{s(\eta-2)}-1} \begin{pmatrix} 33/120 \\ 27/120 \\ 31/120 \end{pmatrix}. \quad (6.20)$$

Note the slight anisotropy in the three directions, which however is below the experimental resolution of our setup.

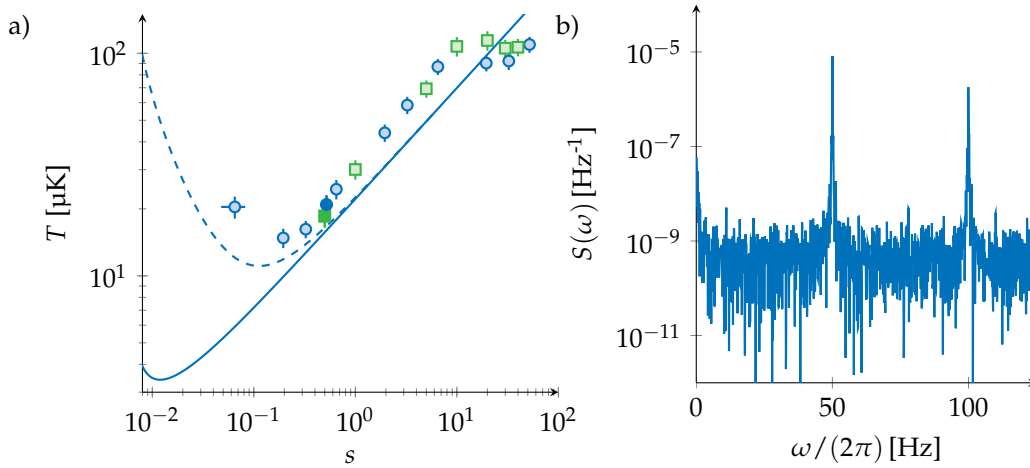


Figure 6.12 – a) Evolution of the asymptotic value (at large detuning) of T as a function of the saturation intensity s . Points taken for two different detunings: $\Delta = -2\pi \times 1.84$ MHz and $\Delta = -2\pi \times 2.54$ MHz. The solid line represents the values given by equation (6.20). The filled points were presented in figure 6.11. We attribute the deviation from theory at low s to the residual noise in the intensity lock, the frequency spectrum of which is presented in b). The expected increase in T is plotted as a dashed line in a).

In the figures and in the following formula we will consider $T = T_z$. The minimum temperature is achievable for $s = 2/(\eta - 2)$, which corresponds to a local detuning $\Delta_{\text{loc}} = -\Gamma/2$ (as in standard Doppler cooling theory), and is given by

$$T_{\text{min}} = \frac{31}{60} \frac{\eta}{(\eta - 2)} \frac{\hbar\Gamma}{k_B} \simeq 3.4 \mu\text{K} \quad (6.21)$$

that as $\eta \gg 1$ is very close to the standard Doppler limit $T_D = \hbar\Gamma/2k_B$. We measure the temperature in our MOT using standard time-of-flight technique (see appendix B.2 for more details). Temperatures as a function of the light intensity are plotted in figure 6.12. The two data set presented are taken at two different laser detunings Δ in the spin polarised regime and are consistent with an independence of T on Δ . We see that the data

agree with the theory in a range of two order of magnitude for the saturation parameter $0.1 \leq s \leq 10$. At higher values, we expect a depolarisation of the cloud and hence the previous formulae are not valid. For lower values, we notice significant heating for $s \leq 0.1$, while we expect to reach a minimum temperature at $s \sim 0.01$. This is due to a technical limitation of our setup. During the MOT operation the intensity of the cooling laser is servo-locked to a PID controller. Nevertheless, as we can see in figure 6.12.b, the spectral density of the servoed intensity has some residual noise, leading to a time dependent saturation parameter $s(t)$. The fluctuations in intensity shake the position the trap equilibrium position $z_c(t)$. In the z axis the atom dynamics will be described by Newton's equation

$$m\ddot{z} = -m\omega_0^2\kappa_z(z - z_c(t)) - m\alpha\dot{z} + \delta F(t), \quad (6.22)$$

where $\omega_0 = \sqrt{\kappa_z/m}$ is the trap frequency (additional details in the next paragraph, see equation (6.27)) and, as we have seen above, $\delta F(t)$ is the stochastic force. Integrating the equation of motion and taking the rms value for the velocity, we get

$$\langle \dot{z}^2 \rangle = \frac{D}{m^2\alpha} + \left(\frac{dz_c}{ds} \right)^2 \int d\omega \frac{\omega_0^4 \omega^2}{(\omega_0^2 - \omega^2)^2 + \omega^2 \alpha^2} S(\omega). \quad (6.23)$$

We can get the temperature by $T = m\langle \dot{z}^2 \rangle / k_B$, which we represent in figure 6.12 as a dashed line. If the noise was not present we recover of course Einstein's relation. In principle, improving the electronics of our intensity lock could reduce the final temperatures that we achieve in the MOT. Since we already vary the intensity over a range of almost three orders of magnitude, further improvements will require a better electronic circuit with a logarithmic amplifier.

6.5 Size and Density

Let us now consider the variations of MOT dimension and density, which are both fundamental parameters for the charging of an optical dipole trap. In the proximity of the centre of the MOT, where the force vanishes at the equilibrium position, the force is linear in the displacement. To first order in position it can be written as

$$\mathbf{F}_{\text{rad}}(\mathbf{r}) = -\kappa_x x \mathbf{e}_x - \kappa_y y \mathbf{e}_y - \kappa_z z \mathbf{e}_z + \mathcal{O}(\mathbf{r}^2) \quad (6.24)$$

The spring constants obtained after linearisation are then

$$\kappa_x = \frac{2mg}{|z_c|}, \quad (6.25)$$

$$\kappa_y = \kappa_x / 2, \quad (6.26)$$

$$\kappa_z = \frac{4mg \delta_\mu \nabla B |\Delta_{\text{loc}}|}{s \eta \hbar \Gamma^2}. \quad (6.27)$$

It is interesting to notice how the constants in the horizontal plane do not depend explicitly on the parameters of the laser light, which appear only in the position of the cloud z_c . The one half factor between κ_x and κ_y can be easily understood, since \hat{x} is the strong axis of the magnetic quadrupole, where the field gradient is twice larger than in the other directions.

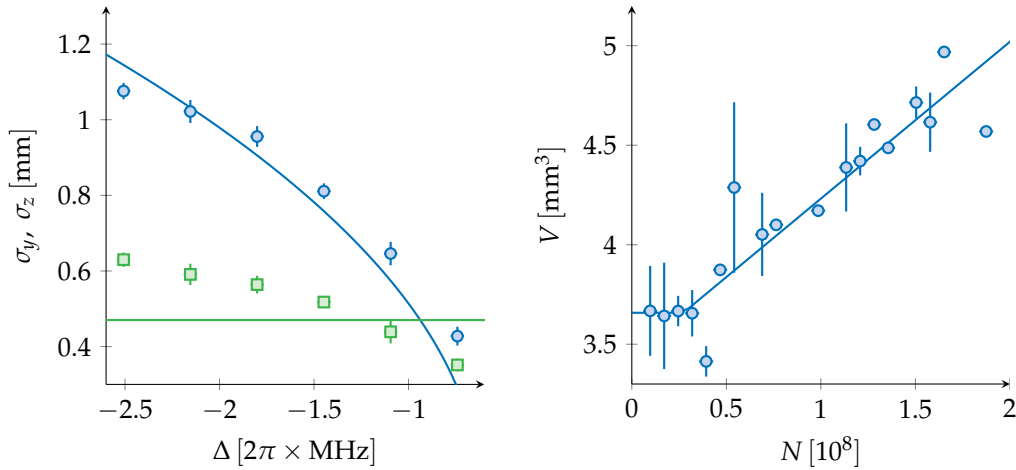


Figure 6.13 – MOT size as a function of laser detuning (green squares are for σ_z and blue circles for σ_y). Data points are standard deviation σ assuming a gaussian shape as fitting function. On the right, volume V of the cloud for different atom numbers N , which shows two different regimes: a linear increase and a saturation for low N .

For every spatial direction $i \in \{x, y, z\}$ we can derive an expression of the rms radius of the cloud σ_i via the thermodynamic relation

$$k_B T = \kappa_i \sigma_i^2. \quad (6.28)$$

As one can clearly see in the in-situ images of the atoms, the cloud has a non gaussian shape which should in principle be taken into account. Nevertheless, looking at figure 6.13, the simple formulae provided above capture quite well the variation of the sizes with the laser detuning. The agreement is less good for the vertical direction, where we expect a constant behaviour for σ_z as both the temperature and the local detuning are constant in the polarised regime, as we have seen in the previous sections. This variation can originate from non linear effects, which are not completely negligible given the non-gaussian cloud shape.

For a given value of laser detuning and intensity, we observe an increase of the cloud volume V with the atom number N . This should not be surprising, since atoms in the trap experience a repulsive force between them due to the radiation pressure generated by the spontaneous emission of photons. In this regime, we expect the MOT to have a core of uniform density n_{\max} , hence a linear increase of the MOT size with the atom number [155, 156]. For atom numbers lower than a threshold value N_c , we expect this effect to be weak and thus the volume $V = (2\pi)^{3/2} \sigma_x \sigma_y \sigma_z$ almost independent of the number atoms N . From our imaging axis we do not have direct access to σ_x , that is thus taken to be twice larger than σ_y following equation 6.26.

To account for the two regimes observed experimentally, we fit the data with the empirical formula

$$V = V_{\text{single atom}} + c (N - N_c) \Theta(N - N_c), \quad (6.29)$$

where c is the curve slope and Θ the Heaviside step function.

6.6 Inelastic Light Assisted Collisions

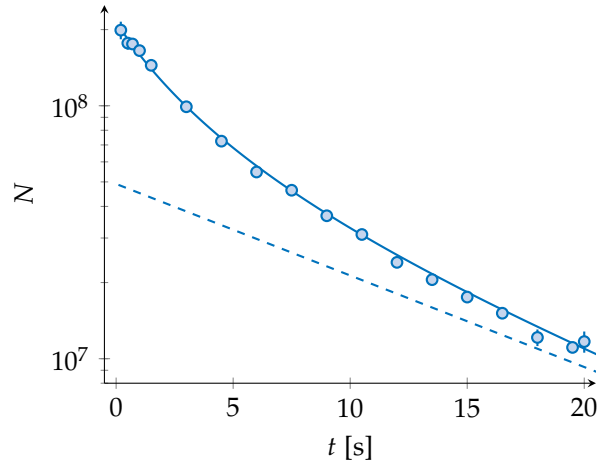


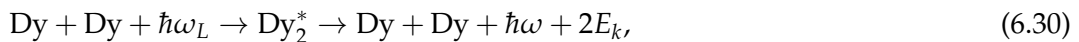
Figure 6.14 – Decay of the atom number in the magneto optical trap for a laser detuning $\Delta = -2.54 \times 2\pi$ MHz and a saturation parameter $s = 0.65$. The plots are in log scale. The dashed curve represent the asymptotic one-body decay at large time scales. Data are fitted using expression 6.31.

Having a look at the MOT sizes in figure 6.13, one may think that working close to resonance is the best option since it gives denser clouds, thus improving the subsequent loading of the dipole trap. Unfortunately, we observe a reduction in the lifetime of the MOT when we get closer to the resonance. Typical data are presented in figure 6.14.

We attribute these losses to light assisted collisions. I shall briefly explain the underlying mechanism of the losses and show how it is possible to get a qualitative agreement with our data using simple arguments.

6.6.1 Radiative Redistribution

Let us consider a binary collision in the presence of laser light. The absorption of a photon of frequency $\hbar\omega_L$ excites one of the two atoms in an upper molecular potential. The atoms will then approach each other until the excited atom relaxes back to the ground state by spontaneously emitting a red detuned photon at an energy $\hbar\omega < \hbar\omega_L$ (see figure 6.15). This kind of process is called radiative redistribution [157] and can be described by the following kind of reaction



where the internal electronic energy $\hbar(\omega_L - \omega)$ has been converted in kinetic energy E_k for the two atoms. If the gained energy exceeds the capture capabilities of the MOT, the pair of atoms is lost from the trap.

Experimentally we can investigate the loss of atoms by looking at the decay of the number of trapped atoms in the MOT. After a loading period, the Zeeman slower light is turned off. The decay of the population N in the trap is described by

$$\dot{N} = -\frac{N}{\tau} - \beta \bar{n}N, \quad (6.31)$$

with τ being the one-body lifetime, which accounts for collisions with the residual gas

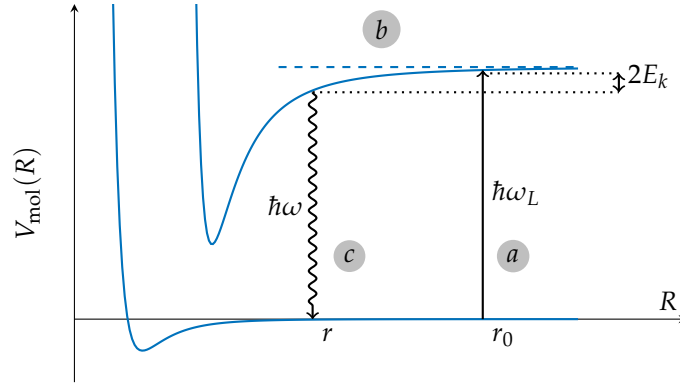


Figure 6.15 – Scheme of a radiative redistribution process for an atom pair. r is the relative distance between the particle. a) The absorption of a photon $\hbar\omega_L$ excites one of the two atoms to an upper molecular potential. b) The atom pair shrinks along the excited molecular potential. c) Relaxation to the ground state via spontaneous emission. The internal energy has been converted to kinetic energy for the two atoms.

in the chamber, and β the two-body loss coefficient. Before turning to the experimental results, let us discuss a theoretical calculation that agrees quite well with the observed losses.

6.6.2 Calculation of the two-body loss coefficient β

Let us consider two atoms in their electronic ground state with a relative internuclear distance $r = r_1 - r_2$. The rate at which one atom can get excited in the upper level is given by

$$\Gamma_{\text{asso}}(r) = |c_{m_j, q}|^2 \frac{\Gamma_m}{2} \frac{2s}{1 + 4(\Delta(r)/\Gamma_m)^2}, \quad (6.32)$$

where Γ_m and $\Delta(r)$ are the lifetime of the molecular state and the detuning at the position where the excitation occurs. The detuning $\Delta(r) = \Delta_{\text{loc}} + V(r)/\hbar$ can be explicitly written if one knows the form of the molecular state. Molecular potentials arise from resonant dipole-dipole interactions, the main interaction scaling thus with the usual $-C_3/r^3$ dependence. For Dysprosium atoms, there are $2(2J' + 1)(2J + 1) = 646$ molecular states. In order to simplify the problem we consider a toy-model with only one single effective molecular potential

$$V(r) = -\lambda \frac{\hbar\Gamma_m}{(kr)^3}, \quad (6.33)$$

where we defined an effective lifetime $\Gamma_m = \mu\Gamma^a$ and the parameter λ which accounts for the average of all possible excited states. The mean values of these parameters averaged over the 323 attractive molecular potentials are $\bar{\lambda} \simeq 0.68$ and $\bar{\Gamma}_m = \bar{\mu}\Gamma \simeq 1.05\Gamma$.

As pointed out in last section, an atom pair can be lost if the acquired kinetic energy after the relaxation E_k is larger than a threshold energy E^* , corresponding to the maximum that can be captured in the MOT. From the capture velocity defined in

^aThe parameter μ accounts for the difference in lifetimes of the excited states with respect to the bare linewidth Γ .

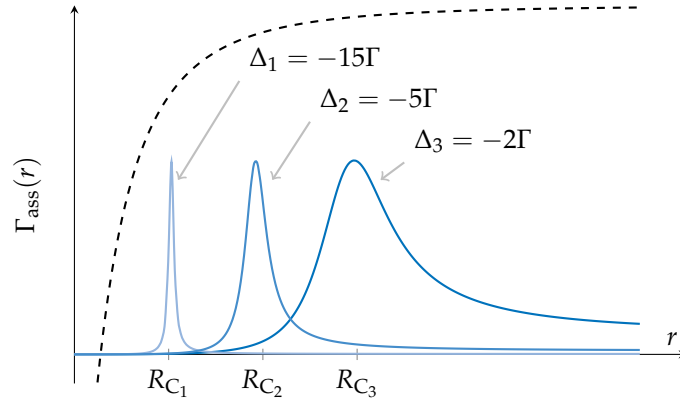


Figure 6.16 – Association rate $\Gamma_{\text{asso}}(r)$ to the excited state for different values of the local detuning Δ_{loc} . The maxima occur at the Condon distance R_C , defined for $V(R_C) = \hbar\Delta_{\text{loc}}$. Note that for large detuning, substituting $\Gamma_{\text{asso}}(r)$ by a Dirac- δ distribution is better justified.

equation (6.1), one gets $E^* \simeq 500\hbar\Gamma$. We can then define the probability P_{loss} of losing one atom that was previously excited in the molecular state at position r_i by calculating the probability for that atom to relax back into the ground state with its kinetic energy $E_k > E^*$. Therefore we can write

$$P_{\text{loss}}(r_i) = \int_0^\infty dt \Gamma_m e^{-\Gamma_m t} \Theta [E_k(r_i, t) - E^*], \quad (6.34)$$

where $\Gamma_m e^{-\Gamma_m \tau}$ is the probability density of a spontaneous emission event to occur at time τ and Θ is the Heaviside step function. The meaning of this integral is that we have just to consider times long enough for the atoms to acquire enough kinetic energy. In order to get an explicit expression, let us consider the energy conservation of the radiative redistribution process (6.30). Let us also neglect the initial kinetic energy of the atom pair, since the typical velocities in the MOT are much lower than the ones acquired after the relaxation. In the centre of mass frame we can then write

$$\lambda \frac{\hbar\Gamma_m}{(kr_0)^3} = \frac{1}{2} m_r \dot{r}^2 - \lambda \frac{\hbar\Gamma_m}{(kr)^3}, \quad (6.35)$$

where r_0 is the initial relative distance between the atoms, r is the distance when the relaxation event occurs and $m_r = m/2$ is the reduced mass. We can rewrite the previous expression as

$$dr \sqrt{\frac{1}{(r_0/r)^3} - 1} = 2 \sqrt{\frac{\lambda \hbar \Gamma_m}{m (r_0 k)^3}} dt. \quad (6.36)$$

Recasting the variable r/r_0 as x and performing the integration, we get

$$t = f(x) \frac{r_0^{5/2}}{2} \sqrt{\frac{mk^3}{\lambda \hbar \Gamma_m}} = f(x) \frac{(kr_0)^{5/2}}{2} \sqrt{\frac{\hbar}{2\lambda E_r \Gamma_m}} \quad (6.37)$$

where we defined the integral

$$f(x) = \int_x^1 du \sqrt{\frac{1}{u^3 - 1}} \quad (6.38)$$

Since when the relaxation occurs, the final distance is very small compared to the initial one ($r \ll r_0$), we can safely set $r \sim 0$ ($x = 0$). The integral has then an exact expression using Euler's gamma function as $f(0) = \sqrt{\pi}/3 \Gamma_E(5/6)/\Gamma_E(4/3) \sim 0.747$. Substituting the time expression in the formula (6.34) and performing the integration, we obtain the following equation for the loss coefficient

$$P_{\text{loss}}(r_i) = \exp \left(-\frac{\mu}{2\sqrt{\lambda}} (kr_i)^{5/2} \sqrt{\frac{\hbar\Gamma}{2E_r}} f \left[\left(1 + \frac{E^*}{|V_{\text{mol}}(r_i)|} \right)^{-1/3} \right] \right), \quad (6.39)$$

where the argument of $f(r/r_0)$ is obtained by energy conservation and by the condition $E_k > E^*$.

Let us now put the pieces together. Assuming a constant density in the trap n , the atom number decay will be given by integrating the association rate and the consequent loss probability over every atom pair in the cloud:

$$\dot{N} = -\frac{n^2}{2} \int d\mathbf{r}_1 d\mathbf{r}_2 \Gamma_{\text{asso}}(|\mathbf{r}_1 - \mathbf{r}_2|) 2P_{\text{loss}}(|\mathbf{r}_1 - \mathbf{r}_2|). \quad (6.40)$$

The factor 1/2 is necessary to avoid double counting, while the loss coefficient has to be counted twice since losses occur in pairs. Recasting the integral in relative coordinates and carrying out the integration over the volume of the cloud, we obtain $\dot{N} = -\beta n N$, with the two body coefficient given by

$$\beta = 4\pi \int dr r^2 \Gamma_{\text{asso}}(r) P_{\text{loss}}(r). \quad (6.41)$$

By substituting (6.32) and (6.39) into the previous equation, we can proceed to numerical integration. The full curve of $\beta(\Delta)$ is shown in figure 6.17 to have a good agreement with the experimental data points obtained from the fit of population decay (6.31).

It is also possible to write an analytical expression of β if we consider a strict resonance condition, *i.e.* substituting the Lorentz profile of equation (6.32) with a Dirac δ distribution. As one can see from figure 6.16, this approximation is more justified for large detuning. Therefore, making the substitution we finally find the expression for the loss parameter

$$\beta_{m_J, q} = \Pi_{m_J} \frac{2\pi^2 \lambda^2 \mu}{3} |c_{m_J, q}|^2 \left(\frac{\Gamma}{\Delta_{\text{loc}}^{(m_J \rightarrow m_J + q)}} \right)^2 \exp \left[-C \left| \frac{\Gamma}{\Delta_{\text{loc}}^{(m_J \rightarrow m_J + q)}} \right|^{5/6} \sqrt{\frac{\hbar\Gamma}{E_r}} \right] \frac{s\Gamma}{k^3}, \quad (6.42)$$

where we introduced the numerical constant

$$C = \sqrt{\frac{\pi}{2}} \frac{\Gamma_E(5/6)}{6\Gamma_E(4/3)} \lambda^{1/3} \mu \simeq 0.264 \lambda^{1/3} \mu. \quad (6.43)$$

and Γ_E comes from using the expression of $f(0)$ given above for $x \sim 0$. The formula is valid for a given spin level m_J and light polarisation q .

As we described in the previous sections, for large laser detuning Δ the only relevant

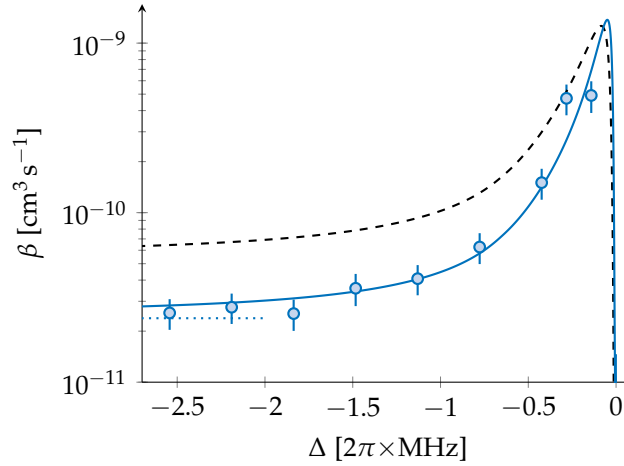


Figure 6.17 – Two-body loss coefficient β as a function of the laser detuning Δ . At large detuning we observe a saturation as we enter the spin polarised regime. The dashed black line is the theoretical prediction obtained from equation (6.41) using $\bar{\Gamma}_m$ and $\bar{\lambda}$, while the solid blue line is a fit obtained with the two parameters as free parameters. The dotted line is the asymptotic expression in the polarised regime given by equation (6.44).

transition is $|J = 8, m_J = -8\rangle \leftrightarrow |J' = 9, m_{J'} = -9\rangle$. The loss coefficient in this case is then

$$\beta = \beta_{-8,-1} = \frac{2\pi^2\lambda^2\mu}{3} \left(\frac{\Gamma}{\Delta_{\text{loc}}} \right)^2 \exp \left[-C \left| \frac{\Gamma}{\Delta_{\text{loc}}} \right|^{5/6} \sqrt{\frac{\hbar\Gamma}{E_r}} \right] \frac{s\Gamma}{k^3}, \quad (6.44)$$

which is independent of the laser detuning. As one can see in figure 6.17, this formula gives the asymptotic behaviour we observe when entering the spin polarised regime at $\Delta \leq -2\pi \times 1.5$ MHz.

As a conclusion, we emphasise that a large laser detuning is the best choice in order to minimise atom losses. Therefore in the following we shall work in the spin polarised regime. In the next chapter we shall see how we transfer the atoms from the MOT into a conservative trap and we further cool them to lower temperatures.



7

Towards Dysprosium BEC

THE LAST step towards the achievement of a Bose-Einstein condensate is evaporative cooling, which is the universally used technique to reach quantum degeneracy in atomic gases. Dysprosium may add some difficulties compared to other atomic species for the reasons we have seen in the first chapters: the trap aspect ratio influences the stability of condensed clouds and the magnetic field has to be carefully calibrated as well to avoid (or exploit) the Feshbach resonances. In this chapter I describe the final optical traps and our optimisation of the evaporation process.

7.1 Optical Dipole Trap

Further cooling of the atoms requires traps where the lowest achievable temperature is not limited by photon scattering. We have seen in chapter 3 that intense light fields induce a displacement of the atomic energy levels and that, far from resonances, the associated scattering rate is strongly suppressed. One can then use the light shift to create conservative traps for the atoms, called optical dipole traps (DT). The traps can be designed by carefully choosing the intensity profile of the laser $I(\mathbf{r})$, which is indeed directly proportional to the optical dipole potential

$$U_{\text{dip}}(\mathbf{r}) = -\frac{1}{2\epsilon_0 c} \text{Re}\{\alpha(\omega)\} I(\mathbf{r}), \quad (7.1)$$

where $\text{Re}\{\alpha(\omega)\}$ is the real part of the polarisability of the atom at the laser frequency ω , which was largely discussed in chapter 3. In this chapter we consider traps operating with near-infrared frequencies, where the light shift is independent on the atomic spin. In the following we focus on the trap engineering and characterisation.

7.1.1 Trap Frequencies

We start by defining some known quantities that we will use to describe our optical traps. Let us consider light propagating as an ideal gaussian beam along the z axis. Let us remind that the intensity profile for a gaussian beam is given by

$$I(\rho, z) = I_0 \left(\frac{w_0}{w(z)} \right)^2 \exp\left(-\frac{2\rho^2}{w^2(z)} \right) \quad (7.2)$$

where ρ is the radial coordinate (with respect to the propagation axis z) and w_0 is the $1/e^2$ radius of the beam at the focus position $z = 0$, called the beam waist. The beam radius expands along the propagation direction as $w(z) = w_0 (1 + (z/z_R)^2)^{1/2}$, where one defines the Rayleigh length $z_R = \pi w_0^2 / \lambda$. The intensity at the waist position is defined as:

$$I_0 = I(0, 0) = \frac{2P}{\pi w_0^2}, \quad (7.3)$$

where P is the laser beam total power. Far from focus ($z \gg z_R$) the beam diverges in a cone like shape, where the angle between the propagating direction and the beam radius $w(z)$ is given by $\theta = \lambda / (\pi w_0)$. If the beam is not perfectly gaussian, it will have a larger diffraction angle. This deviation is usually quantified by the quality factor M^2 , so that the angle becomes $\theta = M^2 \lambda / (\pi w_0)$, and hence the ratio between z_R and w_0 is modified accordingly. We should keep in mind that a quality factor $M^2 \neq 1$ will modify the following formulae, but we suppose to work with perfect beams, which is experimentally a good assumption since our dipole traps are laser outputs from single mode optical fibres.

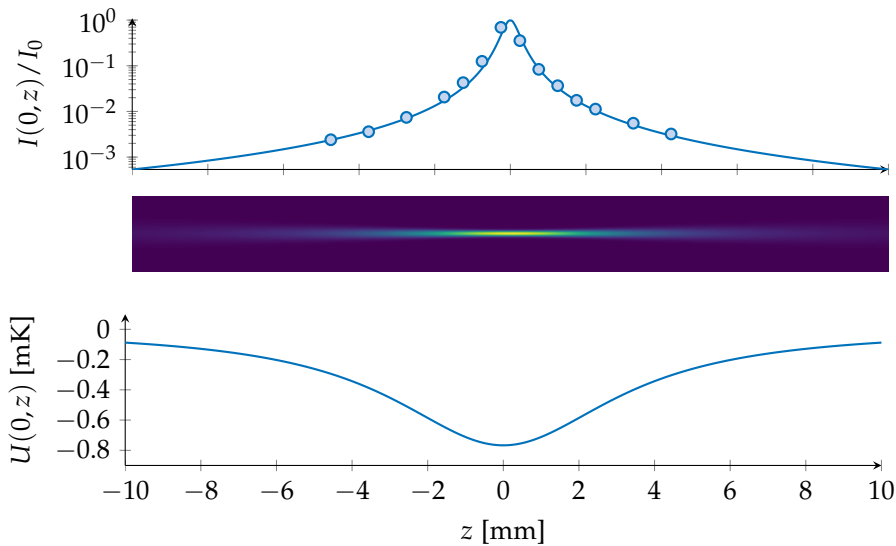


Figure 7.1 – The measured intensity profile of the laser beam is plotted above, the solid line being a lorentzian fit giving the waist w_0 . Below, a 2D plot of the same beam in the (ρ, z) plane (it has a cylindrical symmetry). On the bottom, the expected trap depth for the measured parameters $P = 40$ W and $w_0 = 35\mu\text{m}$ assuming $\alpha = 160$ a.u..

In the radial and axial directions, the beam intensity follows a gaussian and a lorentzian distribution respectively. When the dimensions of the atomic cloud are sufficiently smaller than the beam sizes ($\sigma_\rho \ll w_0$ and $\sigma_z \ll z_R$), at lowest order the exact potential can be approximated by a three dimensional harmonic trap

$$U_{\text{DT}}(\rho, z) = -\frac{U_0}{1 + (z/z_R)^2} \exp\left(-\frac{2\rho^2}{w_0^2(1 + z^2/z_R^2)}\right) \quad (7.4)$$

$$\simeq -U_0 + \frac{m}{2} \left(\omega_\rho^2 \rho^2 + \omega_z^2 z^2 \right),$$

where we defined the radial and axial trapping frequencies

$$\omega_\rho = \frac{2}{w_0} \sqrt{\frac{U_0}{m}}, \quad (7.5)$$

$$\omega_z = \frac{1}{z_R} \sqrt{\frac{2U_0}{m}}. \quad (7.6)$$

Note that the ratio of the two frequencies $\sqrt{2} z_R/w_0$ is given by the geometry of the gaussian beam and is independent of both the atomic parameters and the laser power. U_0 is the potential at the trap centre and, according to the above definitions, is defined as

$$U_0 = \frac{1}{2\epsilon_0 c} \text{Re}\{\alpha\} I_0 \propto \frac{P}{w_0^2}. \quad (7.7)$$

Therefore, to generate deeper potentials one should increase the laser power or focalise the beam to a tighter spot. In figure 7.1 the profile of our dipole trap is given.

7.1.2 Dipole Trap Loading

Starting with the MOT at a temperature $T \sim 15 \mu\text{K}$ we can transfer the atoms directly into a dipole trap, provided that the potential is deep enough. We use a (longitudinal) multimode fibre laser emitting 50 W at 1070 nm^a. The laser is tightly focused on the MOT centre position, with a measured waist of $w_0 = 30.8(1) \mu\text{m}$ and $M^2 = 1.32$. Due to losses along the optical path, only ~ 40 W shine on the atoms, still this power is sufficient to provide a trap depth $U_0 \sim 1.0$ mK.

To load the dipole trap we switch on the IR light right after the MOT has been compressed. The MOT is left on during 600 ms to increase the captured atom number, and then the red light is switched off. During the first milliseconds after the loading we observe fast losses in the optically trapped atoms, due to the equilibration dynamics in the dipole trap.

We transfer $\sim 10\%$ of the atoms from the MOT into the dipole trap. Even if the potential is deep enough, the size mismatch is very large, since the dipole trap is radially at least one order of magnitude smaller than the MOT. To increase the transfer efficiency we actually do not load the atoms at the trap centre but at $z \simeq 1.25 z_R$ from the beam focus, where the radial size of the dipole trap is slightly larger. Further away from focus the loading is less efficient because the DT is shallower. The loading procedure is summarised in figure 7.2, in which we see that the maximum number of atoms that we can transfer from the MOT is $\sim 4.5 \times 10^6$.

^aYLR 50W, IPG Photonics

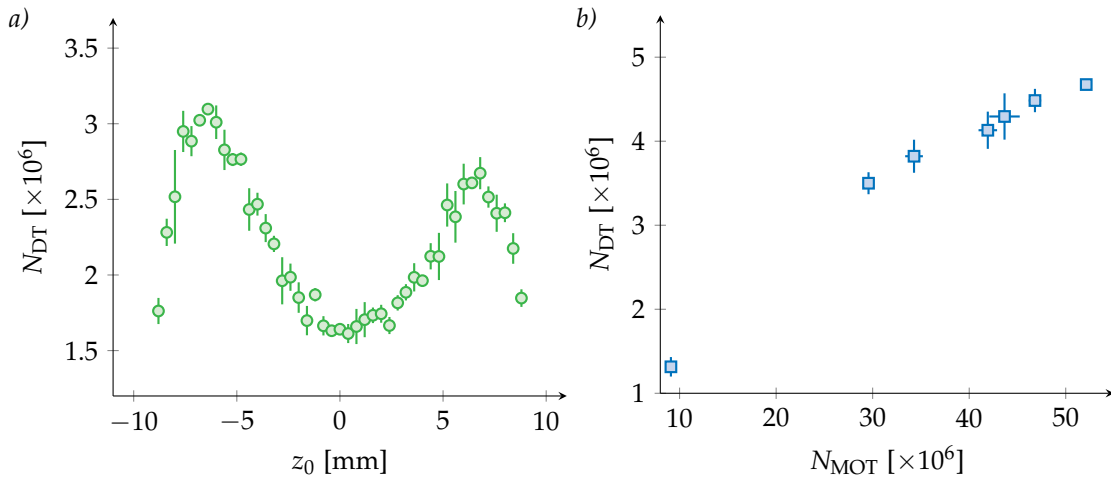


Figure 7.2 – a) Atoms loaded in the dipole trap as a function of the dipole trap focus position. We load more atoms if we are off centred, where the size of the trap is ~ 2.5 times larger. At larger distances the trap is weaker and we lose the atoms. b) Atoms charged in the dipole vs total atom number in the MOT.

In the following we investigate a precise characterisation of the dipole trap by frequency measurements.

7.2 Frequency Measurements

To calculate a priori the potential U_{dip} one measures the beam profile of the trap in situ, to exclude the presence of optical aberrations, and then use equation (7.1) if one knows exactly the value of the atomic polarisability $\alpha(\omega)$. For Dysprosium, there are different experimental values of $\text{Re}\{\alpha\} = 102(20)$ a.u. at 1070 nm [158], $\text{Re}\{\alpha\} = 136(15)$ a.u. and 116 a.u. at 1064 nm [158, 54], which all disagree with the theoretical prediction $\text{Re}\{\alpha\} = 164$ a.u. [84].

We rely then on experimental measurements, where we obtain U_{dip} by direct measuring the trapping frequencies and recovering the value of the potential with equations (7.6). At equilibrium the atoms sit at the trap bottom with a spatial extent given by the Boltzmann distribution (for a thermal cloud). We then excite an oscillation mode and observe the cloud response. The measurement can be repeated at different laser power to check the expected scaling $\omega_i \propto P^{1/2}$ and deduce the value of α . Note that the main error comes from the waist measurement precision since $\alpha \propto w_0^4$ or $\alpha \propto w_0^6$ if one uses the radial or axial frequency respectively.

7.2.1 Sloshing and Breathing Modes

Measurements of radial and axial frequency are achieved in different manners. In the axial direction, we “kick” the atoms and then observe the cloud sloshing back and forth in the trap. The “kick” is done by a sudden displacement of the focus position by a distance $\Delta z \sim z_R/10$. The following oscillation of the centre of mass position is shown in figure 7.3. The damping we observe is indeed expected if one takes into account the dephasing of the oscillations due to the trap anharmonicity and the frequency distribution resulting from the initial thermal energy distribution of the atoms.

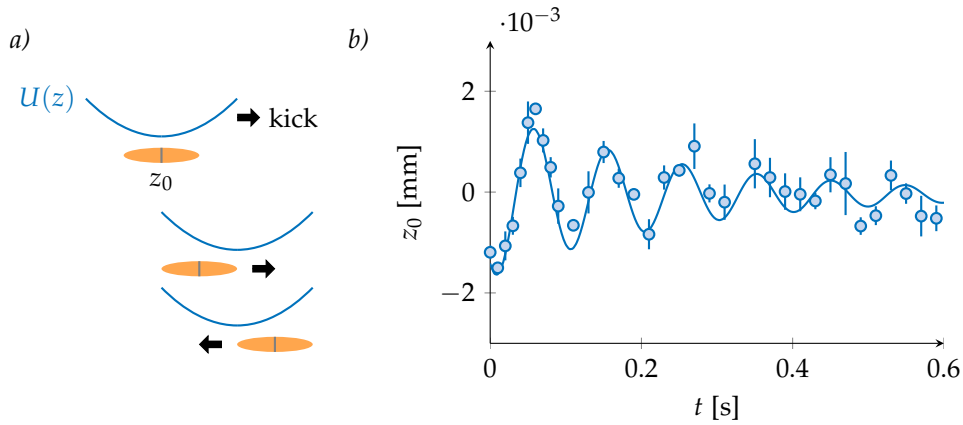


Figure 7.3 – a) Kick excitation of the axial mode: the oscillation is triggered by a sudden displacement of the trap position. b) The oscillation of the cloud's centre of mass position after the trap kick. A fit with the response function of a damped oscillator gives the trap frequency.

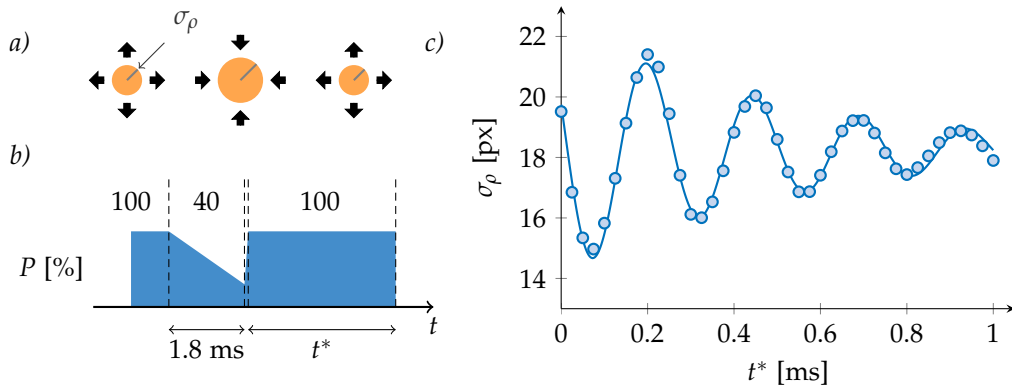


Figure 7.4 – a) Breathing (monopole) mode of the cloud. b) Excitation ramp and c) data for the trap transverse sizes σ_ρ (errors are smaller than the point size). After the sudden restore of the initial power, the size is measured after a variable time t^* . In this case also the data are fitted using the response function of a damped oscillator.

In our setup we can only shift the focus axially, so for the radial frequency we excite instead the breathing mode of the trap, *i.e.* the monopole oscillation of the transverse size σ_ρ . The excitation is obtained by lowering the beam intensity to $\sim 40\%$ of the initial power, before rapidly jumping back to the initial value. The sudden recompression of the trap triggers the breathing mode. We show the experimental results in figure 7.4.

Both measurements were done at full laser power and the result of the fits gives $f_\rho = 1.96(4)$ kHz and $f_z = 10.7(8)$ Hz.

Using the experimental values together with equations (7.6), we obtain a polarisability $\Re\{\alpha\} = 117$ a.u. As we already mentioned, this value is subject to a strong dependence on the experimental uncertainties, such as the error in the beam waist. In addition, the measurement of trap frequencies supposes that all the atoms sit at the bottom of the harmonic potential well, thus neglecting anharmonic effects which can lower the effective frequency, leading to an underestimation of the polarisability. These facts can explain the

discrepancy we find with the theoretical value, which should in principle give a lower bound (if not coincide) to the experimental measurement.

7.2.2 Parametric Excitations

A second method to characterise the trapping frequencies is a parametric excitation. Parametric excitations occur in harmonic systems whenever one of the oscillator parameters is varied in time, for example the frequency ω_0 :

$$\ddot{\rho} + \omega^2(t)\rho = 0 \quad \text{with} \quad \omega(t) = \omega_0(1 - \epsilon \cos(\Omega t)) \quad (7.8)$$

If the system is driven at the double of its trap frequency ($\Omega = 2\omega_0$), the amplitude of the oscillations increases exponentially [94]. In our case, we modulate the power of the laser $P(t) = P_0(1 - \epsilon_P \cos(\Omega t))$, with Ω being close to the expected trap frequency. The modulation amplitude ϵ_P should not be too large, to avoid atom losses. The data in figure 7.11 are taken for $\epsilon_P = 0.035$. We then measure the heating rate (*i.e.* the increase in σ_ρ) to locate the parametric resonance and recover ω_ρ . A fit on the resonance position gives $2f_y = 3.7$ kHz, which is in agreement with the breathing mode measurement. Figure 7.11 also shows a minimum at frequencies slower than the resonance. This cooling is justified by the selective evaporation of more energetic atoms, which experience a different resonant frequency as a result of the trap anharmonicity [159].

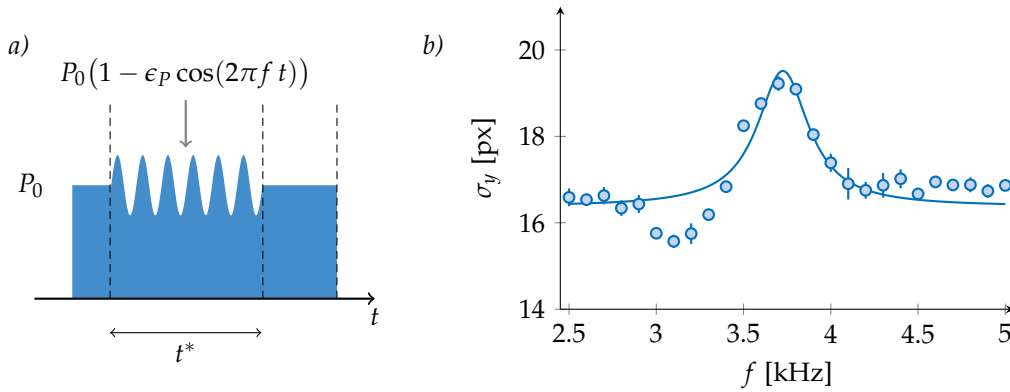


Figure 7.5 – a) Laser power ramp. The power is modulated during a time $t^* = 100$ ms. b) The transverse size of the cloud σ_y , which is directly related to the atoms' temperature, is increasing as soon as the modulation frequency approaches the trap frequency.

7.3 Optical Transport

As we have seen in chapter 5 the MOT and the glass cell, where we perform the final stages of the cooling, are on different parts of the experimental chamber. Therefore, we need to move the atoms from one place to the other, over a distance of ~ 28 cm. The transport consists in displacing the trapping potential, *i.e.* the beam focus position, and letting the atoms follow the movement of the trap. Transport of atomic clouds has been experimentally realised both in magnetic and optical traps. For the second case, there are two possible ways to proceed: either the focus is shifted by mechanically moving the focalising lens [160], or the setup is in a static configuration but one uses adaptive optics

such as focus-tunable lenses [161]. Following previous work in our research team, we choose the first option, using a magnetic levitating translation stage^a.

7.3.1 Experimental Setup

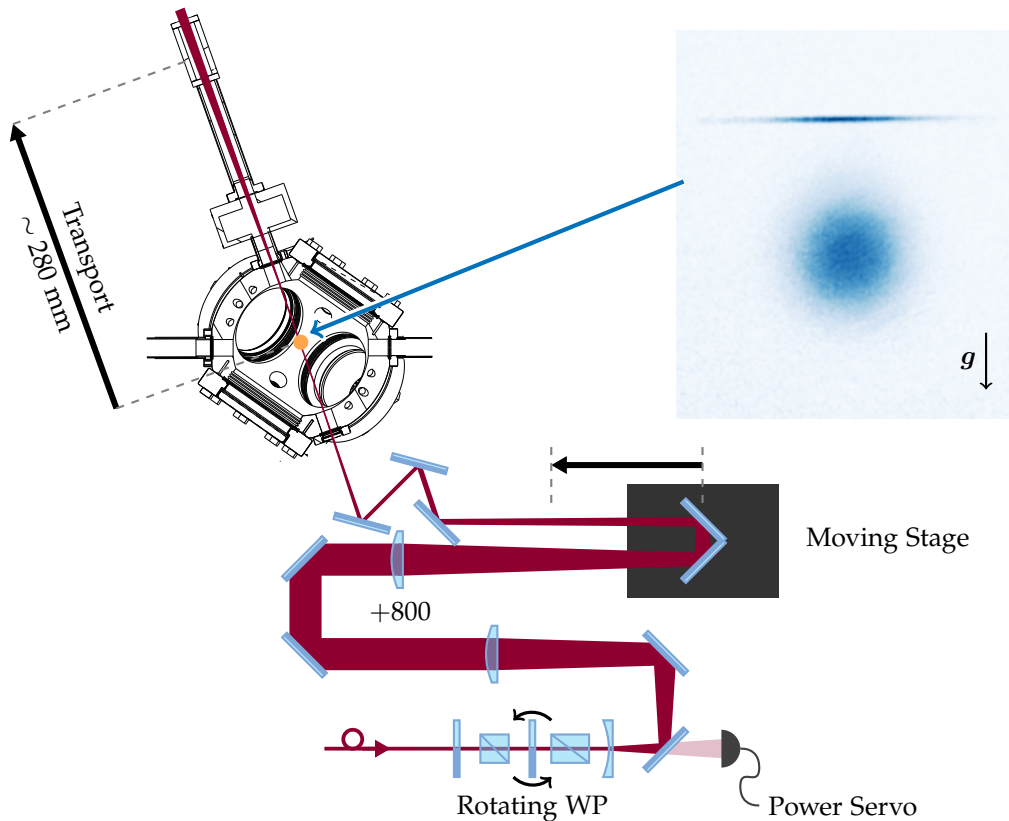


Figure 7.6 – Scheme of the experimental setup for the dipole trap. The IPG laser is focused on the MOT. After $\sim 10\%$ of the atoms are loaded into the DT, the translation stage is moved, shifting the focus position (and hence moving the atoms) into the glass cell. The picture shows the trapped atoms in the DT after the release of the atoms in the MOT. The uncultured atoms are falling below the dipole trap.

A scheme of our experimental setup is shown in figure 7.6. The IPG laser is filtered in polarisation by a first polarising cube. Then we use a rotating wave plate on a servomotor and a Glan-Taylor polariser to control the laser power. The analog control of the laser is not sufficient to achieve low intensities, since it is limited to 10% of the maximum power. To control the power we rather use a rotating wave plate instead of an AOM for different reasons: it preserves the good beam mode quality from the fibre output, there is no loss of power and we avoid thermal lensing issues. On the other hand the response time of the rotating plate is quite slow (40 Hz bandwidth). This is not an issue in our case, since the typical time scales of the evaporation power ramps are some seconds. High frequency noise is canceled by working with the laser analog control in closed loop operation on a faster PID controller.

^aANT130-160-L-PLUS-25DU-MP, Aerotech

The laser beam diameter is broadened with a telescope and focused by a +800 mm lens on the atoms, after passing through a retro reflector, which is on the moving stage. By moving it, we reduce the optical path of the beam before it enters the chamber, and thus we move further the focus position.

All mechanical vibrations of the stage couple to the trap position and, as we have seen already for the MOT, shaking the trap heats up the cloud and can eventually lead to atom losses. For this reason, instead of displacing the lens we displace the reflector. The retro reflector is built with three mirrors mounted on three orthogonal planes, therefore by geometry the reflected beam will exit parallel to the incoming one^b, whatever the incoming angle of incidence. This should sensibly reduce the coupling of pitch and jaw mechanical noise to the beam pointing position [162].

7.3.2 Accelerating Potential

The relevant time scale for the transport is set by the axial trapping frequency. If the acceleration is too fast, the sloshing motion after the transport stops can heat up the cloud and lead to losses. We mention that it has been shown that a right choice of the acceleration (and deceleration) profiles avoids atom losses even with ramps faster than the adiabatic limit (in literature this is called shortcut to adiabaticity [163]). In our case the cloud is relatively hot and a linear acceleration ramp provides almost perfect ($\gtrsim 90\%$) transfer efficiency.

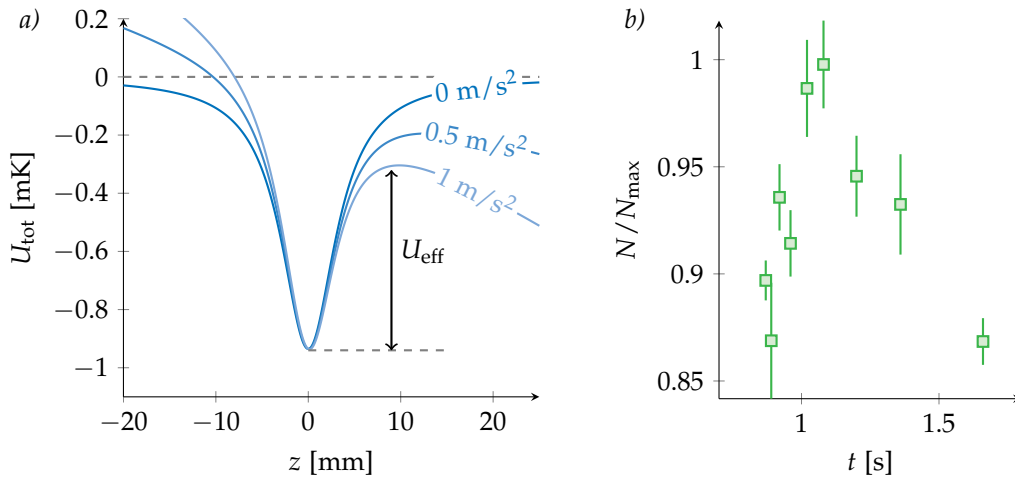


Figure 7.7 – a) Trap deformation along the axial direction z for different accelerations a during the transport. The tilt lowers the trap depth to an effective value U_{eff} . b) Transported atom number as a function of time, i.e. of the acceleration, for a fixed maximum velocity. Slow transport induces also losses due to lifetime limitation.

In our setup, we have to consider two additional problems. First, the lifetime of the dipole in the MOT chamber is quite poor (~ 1 s) and we should then transfer the atoms quite rapidly (see figure 7.8). Second, during the transport the trap potential along the optical axis z is deformed by the acceleration a of the trap

$$U_{\text{tot}}(\rho, z) = -\frac{U_0}{1 + (z/z_R)^2} \exp\left(-\frac{2\rho^2}{w(z)^2}\right) + maz. \quad (7.9)$$

^bit is the same principle of bicycle retroreflectors.

The additional term tilts the trap in the transport direction which is the weak confining axis. In the limit $a_{\max} \sim U_0/mz_R \sim 10 \text{ m s}^{-2}$, the tilt is strong enough that the potential has no longer a minimum and one completely loses the atoms^a.

In figure 7.7.b we plot the transported atom number versus transport time (shorter times have stronger accelerations). The maximum at $t = 1.1 \text{ s}$ ($a_{\max} = 1 \text{ m s}^{-2}$) is a compromise between moving fast enough to avoid losses due to the poor vacuum of the MOT chamber and slow enough to avoid spilling atoms from the trap and to avoid the non adiabatic effects that we mentioned above.

7.3.3 Transport Efficiency

In figure 7.8, we plot transport data for different final positions of the trap, taken after a back and forth path. The furthest point is at the centre of the glass cell, at $z \sim 280 \text{ mm}$ from the starting position. We attribute the strong atom loss in the central region of the transport to the presence of magnetic gradient from a nearby ion pump. Experimentally, we maximise the number of transported atoms adding a small bias magnetic field when the atoms pass in the region $100 \lesssim z \lesssim 200 \text{ mm}$. We also find that the lifetime of the trap depends crucially of the polarisation angle of the trapping light with respect to the field. We find that the optimal polarisation is linear and perpendicular to the direction of the guiding magnetic field.

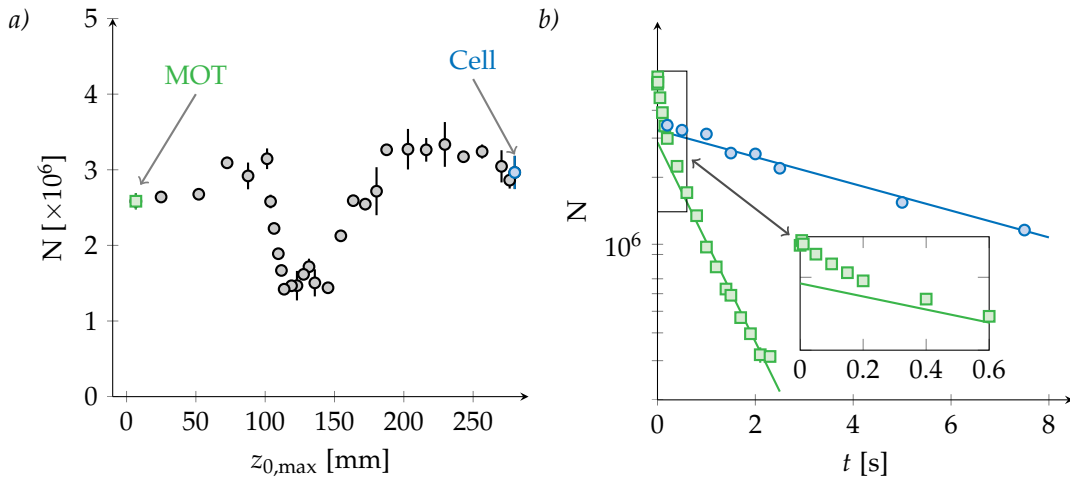


Figure 7.8 – a) Back and forth transport curve. Here $z_{0,\max}$ is the furthest position reached before bringing back the cloud. The cloud is displaced to $z_{0,\max}$, where we wait a variable amount of time in order to have all data points taken after the same total time. b) Lifetime curves in the MOT chamber (green squares) and in the science cell (blue dots). The number of atoms in the dipole trap is plotted as a function of the holding time t , the solid lines give the respective lifetimes $\tau = 1.03(5) \text{ s}$ and $\tau = 7.2(3) \text{ s}$. The inset shows the fast relaxation in the MOT chamber in the first 200 ms due to plain evaporation.

^aWe mention that to provide a much tighter confinement in the axial direction a possible solution is to use a standing wave trap. By changing the phase of one of the interfering beams the lattice position is shifted and the atoms will move as if they were on a conveyor belt [164]. We did not implement this setup since it is more technically demanding and it requires a single mode laser.

7.4 Crossed Dipole Trap

Due to the different frequencies in z and ρ axes, a single beam trap is elongated in the weak z direction, resulting in a cigar shaped trap. To obtain a tight confinement along the three axes, we cross a second laser beam from a transverse direction. The passage to a cross dipole trap (CDT) has two main benefits. First, the squeezing of the cloud size increases the density, and hence the collision rate, which is fundamental for the subsequent evaporative cooling. Furthermore, the passage from a cigar shape to a pancake shape gives the right geometry for stabilising the cloud against dipolar collapse (see chapter 2).

We use a single mode laser as second dipole trap (which we label DT_2), delivering 7 W at 1064 nm^a, propagating along Z direction. DT_2 enters the glass cell at the Brewster angle (see picture 7.10) so it crosses DT_1 roughly at an angle $\theta \simeq 35^\circ$. To obtain an oblate trap ($\omega_Y > \omega_X$) the cross section of the beam is shaped into an ellipse of aspect ratio 1:1.65 using cylindrical lenses (with measured beam waists $w_X = 44.8(2)\mu\text{m}$ and $w_Y = 28.3(1)\mu\text{m}$). The potential is no more cylindrically symmetric along the propagation axis

$$U_{DT_2}(X, Y, Z) = -\frac{U_0}{w_X(Z)w_Y(Z)} \exp\left(-2\left(\frac{X^2}{w_X^2(Z)} + \frac{Y^2}{w_Y^2(Z)}\right)\right) \quad (7.10)$$

$$\simeq -U_0 + \frac{m}{2}\left(\omega_X^2 X^2 + \omega_Y^2 Y^2 + \omega_Z^2 Z^2\right),$$

where ω_X and ω_Y are now calculated from formula 7.6 using their respective waists. At full power we measure ~ 5 W on the atoms, giving as maximum trapping frequencies $f_X = 424(3)$ Hz, $f_Y = 699(5)$ Hz and $f_Z = 3.9(1)$ Hz. A measurement of the trap frequency of DT_2 in a wide range of power is plotted in figure 7.9. The fit shows the expected square root dependence on the laser power $\omega \propto \sqrt{P}$.

At low power the trap is sufficiently shallow that the gravitational energy $mgw_0 \sim U_0$ and thus the atoms can spill out of the trap, like it was the case in the accelerating transport ramp. Since in this case the trap is static, we compensate the effect of the gravity by adding an opposite magnetic force

$$U_{\text{tot}}(\mathbf{r}) = U_{DT}(\mathbf{r}) + mgz\mathbf{e}_z + U_{\text{mag}}(\mathbf{r}). \quad (7.11)$$

For a Dysprosium cloud in the ground state $|J = 8, m_J = -8\rangle$, a vertical magnetic field gradient of $\partial_z|B| \simeq 3 \text{ G cm}^{-1}$ cancels completely the gravity field and the centre of mass of the cloud levitates even if the trap beams are switched off.

The CDT is obtained by superposing the focus of DT_1 and DT_2 . To get the frequencies of the crossed trap, we have to consider the sum of the two harmonic potentials from the two separate trapping beams. In the horizontal plane, the sum of the potentials gives

$$U_{\text{CDT}}(x, z) = U_{DT_1}(x, z) + U_{DT_2}(x, z)$$

$$= \begin{bmatrix} x & z \end{bmatrix} \left(\begin{bmatrix} \omega_{x,1}^2 & 0 \\ 0 & \omega_{z,1}^2 \end{bmatrix} + R(\theta) \begin{bmatrix} \omega_{x,2}^2 & 0 \\ 0 & \omega_{z,2}^2 \end{bmatrix} R^T(\theta) \right) \begin{bmatrix} x \\ z \end{bmatrix}, \quad (7.12)$$

where we arbitrarily choose the reference frame (x, z) as the proper directions of the first

^aALS-IR-10-1064-SF, Azur Light System

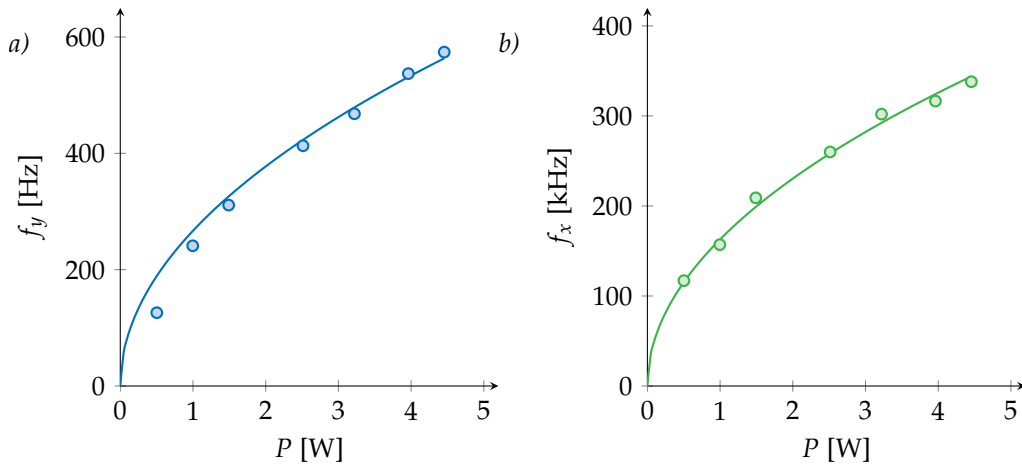


Figure 7.9 – Measurement of the trapping frequencies in the transverse directions for the elliptic dipole trap DT_2 . The fit shows the expected behaviour $f \propto \sqrt{P}$. The deviations for low power along the vertical direction y are due to the gravity deformation of the trap.

beam and $R(\theta)$ is the two dimensional rotation matrix by an angle θ . The diagonalisation of the resulting matrix gives the eigenaxes and eigenfrequencies of the total ellipsoid potential. In the vertical direction y (which is the same for the two laser beams) the total frequency is the quadratic sum

$$\omega_y = (\omega_{y_1}^2 + \omega_{y_2}^2)^{1/2}. \quad (7.13)$$

From the measured values at maximum laser power, the crossed dipole trap has the frequencies $f_{x'} = 2030$ Hz, $f_{z'} = 239$ Hz and $f_y = 2120$ Hz (x' and z' are the eigenaxes resulting from the diagonalisation of 7.12).

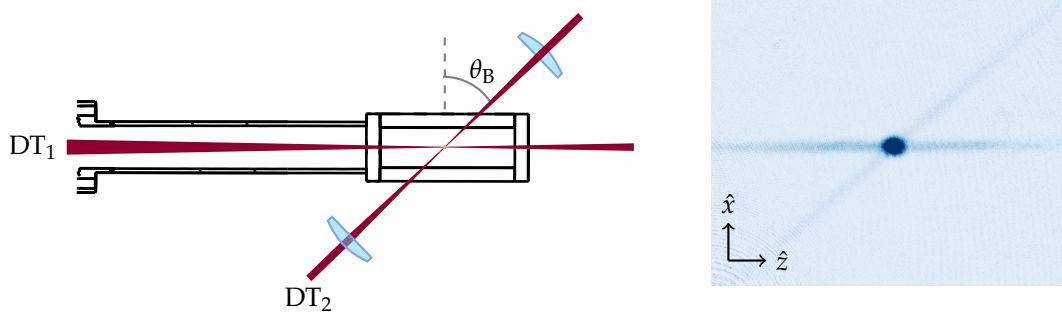


Figure 7.10 – Crossed dipole trap configuration. The atom cloud is at the glass cell centre. One finds the effective trapping frequencies from the contribution of the two separate traps. The second trap is horizontally polarised and it enters the cell at Brewster's angle $\theta_B \simeq 53^\circ$ to minimise reflections from the uncoated glass surface. The picture is taken after a first evaporation in DT_1 .

7.5 Evaporative Cooling

The goal of the following experimental procedure is to further reduce the temperature of the cloud. We will use evaporative cooling, whose basic principle consist in letting the hottest particles (those with an energy larger than the trap depth U_0) escape the trap, so that the remaining atoms eventually thermalise at a much lower temperature. The decrease of the temperature slows down the process, since the average energy of the particles becomes much smaller compared to U_0 . Since the atoms in the trap have a finite lifetime, the evaporation needs to be forced by continuously lowering the trap depth.

7.5.1 The Cooling Process

The thermalisation process relies on elastic collisions between the atoms in the trap. The time scale of the forced evaporation has then to be larger than the average time between collisions τ_{coll} . In a cloud of density n and with average thermal velocity v , the elastic collision rate is given by

$$\Gamma_{\text{coll}} = \tau_{\text{coll}}^{-1} = n\sigma v, \quad (7.14)$$

where σ is the scattering cross section for identical bosons. At low temperatures $\sigma = 8\pi a^2$ (see chapter 2), so $\Gamma_{\text{coll}} = 8\pi n a^2 v$. In the trap DT₁, just after the atoms have been transported in the glass cell, we have $\Gamma_{\text{coll}} \simeq 130 \text{ s}^{-1}$ (away from Feshbach resonances).

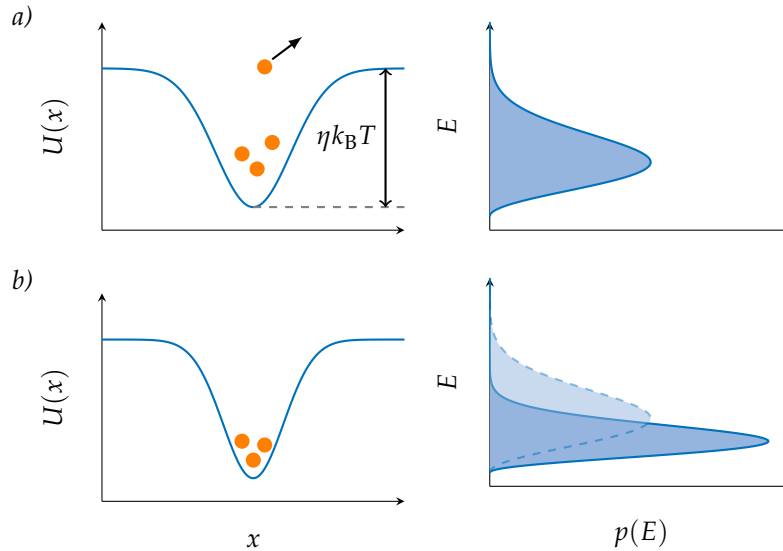


Figure 7.11 – Scheme of the evaporation process. The trap has a depth $U_0 = \eta k_B T$. After the particles in the high-energy tail of the distribution ($E_k > U_0$) are lost from the trap, the remaining particles thermalise at a lower energy via elastic collisions. If the trap depth is kept constant the process slows down, so one lowers the potential to force the evaporation.

Other processes different from evaporation make the atoms escape from the trap without decreasing the temperature. These processes mainly consist of collisions with the background gas, inelastic collisions in the cloud and additional heating due to technical limitation (e.g. fluctuations of the laser intensity). Experimentally, this limits the total time of the evaporation and one has to find the right compromise between τ_{coll} and the

timescale dictated by atom losses τ_{loss} .

The final goal of the evaporation process is to reach quantum degeneracy. The relevant parameter is in this case the phase space density $\mathcal{D} = n\lambda_{\text{dB}}^3$. For a perfect (non interacting) Bose gas in a harmonic confining potential, the phase space density is given by

$$\mathcal{D} = \left(\frac{\hbar\bar{\omega}}{k_{\text{B}}} \right)^3 \frac{N}{T^3}. \quad (7.15)$$

where $\bar{\omega} = (\omega_x\omega_y\omega_z)^{1/3}$ is the geometric mean of the trapping frequencies. The condensation threshold is attained at $\mathcal{D} = 2.61$, which gives as critical temperature for the phase transition

$$T_{\text{c}} = 0.94 \frac{\hbar}{k_{\text{B}}} \bar{\omega} N^{1/3}. \quad (7.16)$$

The cooling is performed in a discrete set of steps where one lowers the trap depth. After each step the atom number reduces from an initial value N_i to a final number N_f . In heuristic models of evaporation, all relevant quantities scale as $(N_f/N_i)^x$, where x is a power coefficient. We are particularly interested in the increase in phase space density, which gives the cooling efficiency of the process. In order to characterise the efficiency, it is usual to define the parameter

$$\gamma = -\frac{\log(\mathcal{D}_f/\mathcal{D}_i)}{\log(N_f/N_i)}, \quad (7.17)$$

which compares the increase in phase space density with the atom loss.

7.5.2 Evaporation with Longitudinal Multimode Laser

At full laser power, the ratio between the potential depths of the trapping lasers in (7.12) is $U_{\text{DT}_2}/U_{\text{DT}_1} \sim 0.1$. The atoms are mostly trapped in DT_1 (the transport beam) and we proceed to lower its power to reach comparable trap depths. We perform a first evaporation, decreasing linearly the power of the IPG down to 10% of its initial value. In the process we reduce the atom number from $N \simeq 4.5 \times 10^6$ (just after transport) to $N \simeq 5 \times 10^5$, while the temperature decreases from $T = 120 \mu\text{K}$ to $T = 14 \mu\text{K}$.

At the end of this first evaporation, the atoms are mostly trapped in the crossed region. In the following steps we lower the depths of the two lasers together. To optimise the evaporation we split the ramps of the laser power into linear steps of which we vary the duration, the slope and the final power to find the optimum experimental values. In figure 7.12 we show the result after an optimisation of a two-step evaporation ramp. The total cooling efficiency of the ramp is $\gamma \simeq 0.9$.

At low intensities, the trap is quite deformed by the gravity. We have found experimentally that the tilt of the trap actually helps the cooling process since it reduces the trap depth for a given frequency.

At laser power lower than $U_{\text{CDT}}/k_{\text{B}} \sim 10 \mu\text{K}$ we expect to completely lose the atoms if we do not counterbalance the gravity, as in equation (7.11). The use of magnetic field appeared to be problematic, as we can see in figure 7.13. We observe strong heating for increasing strength of the magnetic field, which severely limits the lifetime of the atoms in the trap. We attribute the heating and the atoms loss to the multimode structure of

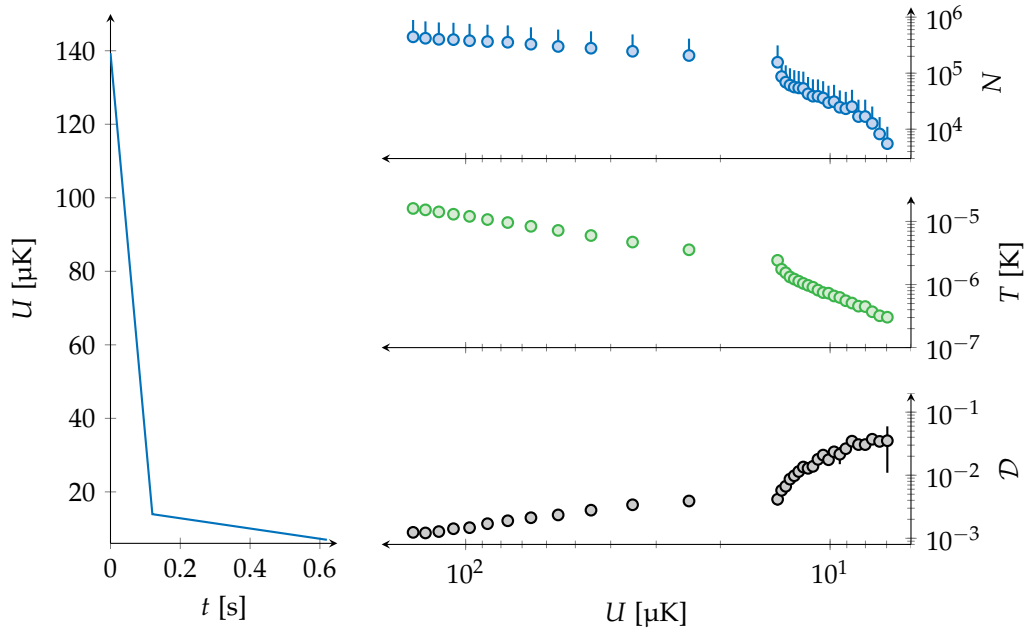


Figure 7.12 – Evaporation in the crossed trap with DT_1 and DT_2 . On the left, the trap depth as a function of time. The evaporation ramp is made of two linear steps. On the right the evolution of the atom number, the temperature and the phase space density as a function of the potential depth.

the laser we use for the DT_1 . A similar problem was observed in the Stuttgart group when using a similar multimode laser [165]. We are then forced to work at very low

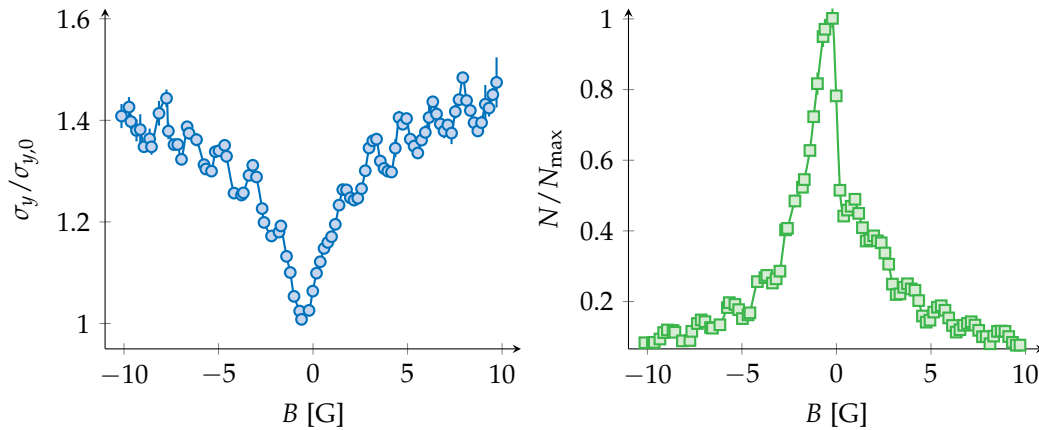


Figure 7.13 – Increase in the cloud size (i.e. in the temperature) and atom loss as a function of the magnetic field $\mathbf{B} = (0, 0, B)$. We attribute the modulation to the mode spacing of the DT_1 laser.

fields to avoid heating and losses while proceeding with the evaporation. Moreover, the control of Feshbach resonances in the crossed trap is spoiled by the heating, so we can not control the scattering length in this crossed trap. The best measures values after evaporation optimisation were $N = 1.5 \times 10^3$ atoms at $T = 50$ nK, with a phase space density of $\mathcal{D} \sim 0.1$.

7.5.3 Second Crossed Trap

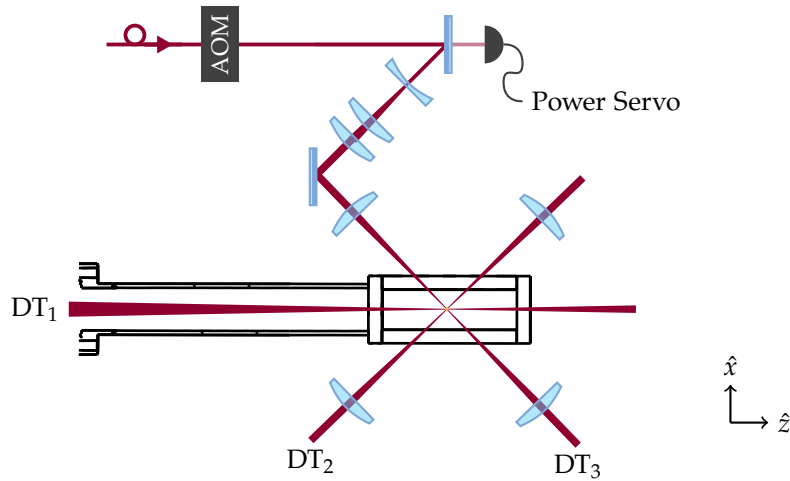


Figure 7.14 – Scheme of the laser setup for the third trap dipole trap DT_3 , which mirrors the setup for DT_2 . We servo the laser power using an AOM and the beam is elliptically shaped by a telescope using cylindrical lenses.

In order to get rid of the multimode laser, we then installed a third dipole trap (DT_3), which uses the same model of single mode laser as DT_2 . The optical setup mirrors the one for DT_2 , with an AOM to control the laser power and a cylindrical telescope to shape the beam cross section into an ellipse. The measured frequencies of the third trap are $f_x = 380(10)$ Hz, $f_y = 575(15)$ Hz and $f_z = 3.06(3)$ Hz at full power (~ 8 W on the atoms). The beam is sent on the atoms from the opposite site of the glass cell with respect to DT_2 , and the two traps cross at an angle of $\simeq 90.1^\circ$ (see picture 7.14). Since the beams are perpendicular, the crossed trap frequencies in the horizontal plane are well approximated by the f_x of the single beams, while vertically one has $f_y = 905$ Hz according to formula (7.13).

As for the previous case, we first lower the power of the multimode laser DT_1 to 20% of its initial value, having $N \simeq 1.5 \times 10^6$ left in the trap. In the crossed dipole trap we typically load $N \simeq 4.5 \times 10^5$ at a temperature $T = 14 \mu\text{K}$. The three beams are present at this instant, then the power in DT_1 is slowly ramped to zero before starting the evaporation in DT_2 and DT_3 .

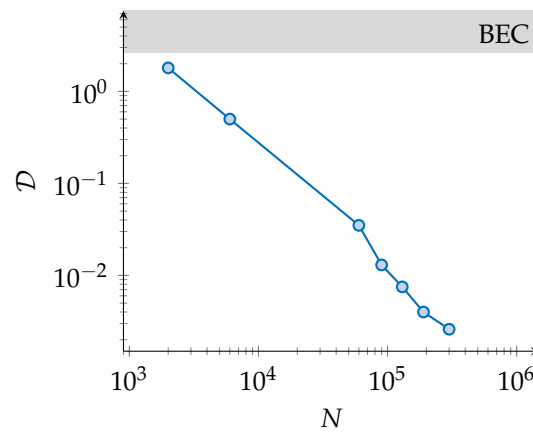


Figure 7.15 – Preliminary results on evaporative cooling in the new crossed dipole trap.

Preliminary evaporation ramps seem promising. At the time of this thesis writing, we reach temperature as low as $T \simeq 30$ nK with $N \simeq 2 \times 10^3$. The phase space density is close to the condensation threshold (see picture 7.15), but we are not expecting a stable condensate for our trap aspect ratio. To reach a stable configuration, we are currently characterising the evaporation ramps at different background scattering lengths, that we can now tune using Feshbach resonances since we are no more limited by the magnetic field induced losses as in the previous trap.



8

Conclusion and Perspectives

IN this manuscript I presented the construction of a new experiment on ultracold Dysprosium gases. The experiment was built from scratch three years ago, in the new laboratories of the Collège de France in Paris, and is now fully working and producing ultracold gas of Dysprosium. I gave a detailed description of the setup and of our experimental procedures to trap and cool the atoms. I presented a detailed study of the magneto optical trap, that we published in [80].

After the first studies of forced evaporative cooling in a crossed dipole trap using a (longitudinal) multimode laser, we currently changed our experimental setup and we load the atoms in a second crossed trap, which uses only single mode lasers. The results on the new setup look promising and we expect to achieve soon the condensation threshold. At the time of this thesis writing, we reach temperatures as low as $T \simeq 40$ nK with $N \simeq 2 \times 10^3$ and phase space density $\mathcal{D} \sim 1$.

In the manuscript I explained that working with Dysprosium is quite different than the most common laser cooled atomic species due to its peculiar characteristics, which manifest in different ways the experiment.

I illustrate how the combination of Dysprosium's large spin and the characteristics of two-electron atoms traps (which work on narrow linewidth transitions) gives rise to interesting mechanisms in the MOT. In particular, gravity plays a crucial role due to its interplay with optical forces, leading to a spin polarisation of the trapped atoms.

Dysprosium is the most magnetic element in the periodic table, which makes it the best candidate to study dipolar physics. On the other hand, I review some consequences of the dipole-dipole interaction which introduce experimental challenges, such as dipolar relaxation and dipolar instability, the latter requiring a good design of the optical traps geometry.

The spin-light coupling has a tensorial nature that offers interesting possibilities. The polarisation of the laser beams and the internal atomic state drastically influence the behaviour of conservative traps, which are usually considered as spin-independent. More-

over, the electronic spin can be manipulated with the right choice of light polarisation. I showed that the residual heating of two-photon transitions between ground state Zeeman levels is considerably reduced with respect to alkali atoms, making Dysprosium a great system for the study of spin-light coupling. Raman transitions are also a fundamental ingredient to generate light-induced artificial gauge fields in ultracold atomic clouds. I discussed a practical implementation in our setup and evaluated the experimental requirements and the expected results.

On the experimental setup, we are currently building the optical dipole trap using light at 626 nm, which is the transition I considered in detail to study spin-light coupling.

Future Perspectives

During this thesis we worked solely with the isotope ^{164}Dy , which is a boson. In our future plans we will proceed to trap and cool ^{161}Dy , a fermion. Evaporative cooling should work straightforwardly [56], as a result of the finite cross-section for dipolar elastic-collisions at low temperatures.

Following the implementation of synthetic gauge fields, we will focus on the study of spin-orbit coupled gases, in a gas of fermionic Dysprosium. We are particularly interested in the study of topological superfluids and insulators, which can be realised using spin-orbit coupling. Topological insulators are extremely interesting systems which are insulating in the bulk and have gapless states at the edges [76]. In our future project, we will study a p -wave superfluid (which is an exotic superconductor with an anti-symmetric Cooper pairing), which can be realised in one dimensional atomic wires [166]. Also in this case we should benefit from the reduced heating from atomic species as Dysprosium [167].

The interest of such a system relies on its exotic edge excitations. In particular it exhibits zero-energy modes, which are Majorana bound states. These quasi-particles are linked to the famous Majorana fermions, which are fundamental particles that are their own antiparticles [168].

In the last years Majorana quasi-particles have been observed in condensed matter topological superconductors [169]. The realisation of such a system within our setup should benefit from the standard techniques of ultracold atoms physics, which can provide a clearer indication of a topological order in the system [170]. The principal interests in Majorana excitations are their non-locality and their non-Abelian statistics. These properties can be exploited to encode extremely robust qubits with respect to environment perturbations (the so-called “topologically protected” qubits), due to the negligible probability of unwanted non-local processes that destroy the coherence. In this respect, Majorana fermions are one of the best candidates to realise quantum computation protocols [171].



Appendices

A	Dysprosium	113
A.1	Basic Properties	
A.2	Atomic Spectrum	
A.3	Magnetic Properties	
B	Imaging Dysprosium Clouds	120
B.1	Absorption Imaging	
B.2	Thermometry	
C	Notes on the Experiment Database ..	125
C.1	Database	
C.2	Data Analysis	
	Bibliography	139



A

Dysprosium

DYSPROSIUM (Dy) still remains uncommon in cold atoms experiments, so it can be worth introducing its physical properties. In order to find this element on the periodic table we have to look into the lanthanides line (the so called rare earth metals), where it sits at number 66.

Dysprosium is found in nature as a bright silver-coloured metal. It crystallises in a hexagonal closed-packed form. Dysprosium is also very soft to be machined, which makes it very easy to cut if bought in large chunks.

One of the most striking properties of Dysprosium is the fact that it possesses the highest magnetic dipole moment among all elements, 10 Bohr magnetons (μ_B). This characteristic makes it one of the best suitable candidates for the study of strong dipole-dipole interactions.

A.1 Basic Properties

In comparison to other laser-cooled species, one good characteristic of Dysprosium is the presence of two stable fermionic isotopes and two stable bosonic isotopes, each of them with a natural abundance close to 25%. In total Dysprosium is found in nature as a mixture of seven stable isotopes, the most common among them are listed in figure A.1.

Dysprosium's melting point at 1 atm is quite elevated: 1412 °C. For this reason one needs a high temperature oven to evaporate the sample. The black body radiation of the oven keeps heating a part of our UHV vessel, which in general causes degradation of the vacuum quality (due to the increased desorption rate from the chamber walls). Luckily it turns out that Dy exhibits getter properties, which means that particles in the chamber stick on the coating generated by the lost atoms on the vacuum walls and thus lowering the vacuum pressure.

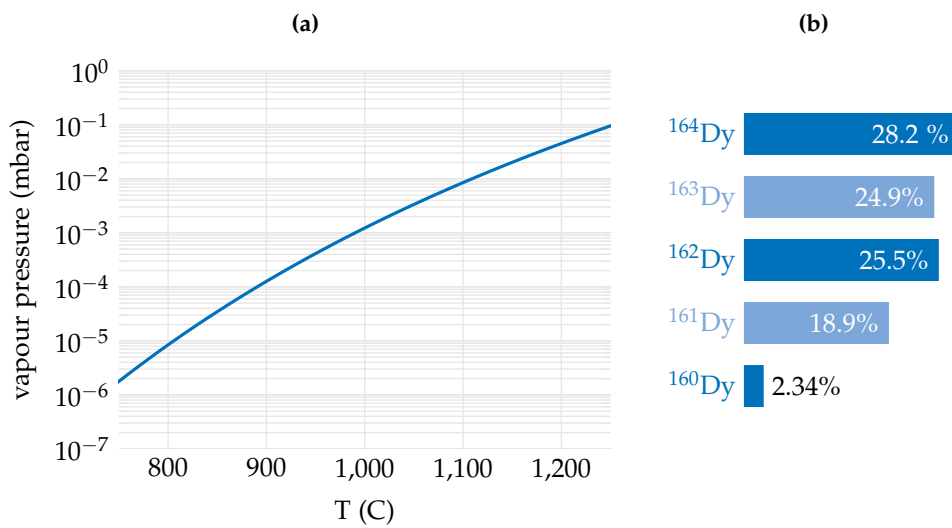
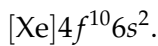


Figure A.1 – (a) Dysprosium vapour pressure as a function of temperature. The typical oven operation is at 1050 °C. (b) Natural isotopes of Dysprosium. Fermions are in lighter blue.

A.2 Atomic Spectrum

Dysprosium belongs to the family of elements possessing a submerged electron shell. Its valence shell has 12 more electrons than the previous noble gas, Xenon. These electrons first occupy the 6s states, leaving the underlying 4f shell partially unfilled. The electronic configuration of the ground state is thus



The spin-orbit interaction of the electrons in the incomplete 4f shell gives rise to a huge 5I_8 spectral term for the ground state (as written in the standard Russell-Saunders notation $^{2S+1}L_J$).

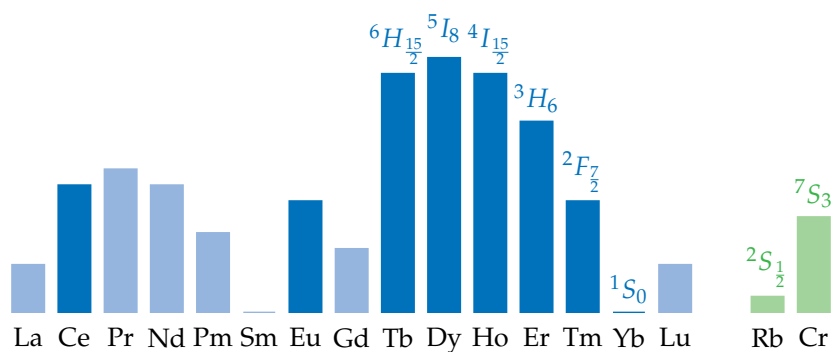


Figure A.2 – Ground state total angular momentum J of lanthanides. For atoms that had been laser cooled is also indicated the spectral term of the ground state [172]. The atomic species in lighter colour can not be laser cooled since they do not have an inverted fine structure multiplet in the ground state. Rb and Cr are aside for comparison.

Among all natural stable elements, Dysprosium possesses the largest spectral term in the ground state (see figure A.2 to compare to other Lanthanides).

A.2.1 Laser Cooling Transitions

The level scheme of Dysprosium presents plenty of lines (Figure A.3). Nevertheless, as we will see below, the only transitions that are actually interesting for our purposes are the ones regarding the 6s-electrons, while the f shell will mostly be responsible of the magnetic properties of the atom. From a laser cooling perspective, Dysprosium seems to be equivalent to an alkali-earth atom, which has only two valence electrons.

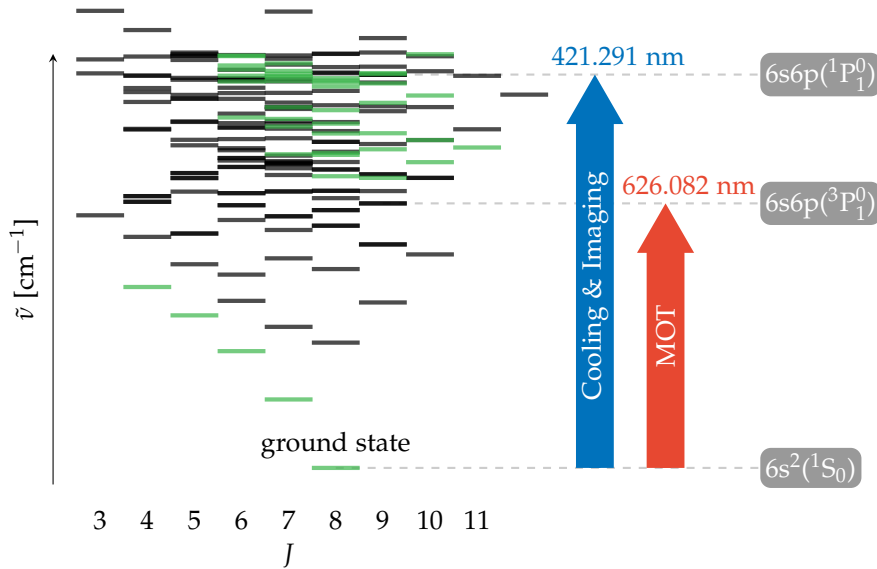


Figure A.3 – Dy energy level structure. Green and black lines refer respectively to the even and odd parity of the levels. The red and blue optical transitions used for laser cooling are the triplet and singlet excitation of one electron from the outer shell.

The transitions we consider are due to the promotion of one 6s electron to the upper 6p state, which can happen both in a singlet or triplet state. Remember also that for heavy atoms the electronic spin-orbit interaction is stronger than the individual spin-spin or orbit-orbit interactions. For the excited states of Dysprosium, the spin and orbital angular momentum of the outer 6s6p and the submerged 4f shells will individually couple to total angular momenta, j_1 and j_2 respectively, which subsequently couple together. For this jj -coupling we use the standard spectroscopic notation $(j_1, j_2)_J$. The two mentioned lines are:

- The first case is the blue transition at 421 nm between the $[\text{Xe}]4f^{10}6s^2\ ^5I_8$ ground state and the $[\text{Xe}]4f^{10}(^5I_8)6s6p(^1P_1^0)(8,1)_9^0$ excited state. This strong transition has a broad linewidth $\Gamma = 2\pi \times 32.2$ MHz, which makes it suitable for cooling and slowing the Dy atoms.
- The second case is the 626 nm closed transition between the ground state and the $[\text{Xe}]4f^{10}(^5I_8)6s6p(^3P_1^0)(8,1)_9^0$ excited state. Since the ground state is a singlet state $6s^2\ (^1S_0)$, it is a spin changing transition (so-called intercombination line) that is partially electric-dipole-forbidden, resulting in a narrow linewidth $\Gamma = 2\pi \times 135$

kHz. This fact gives rise to some peculiar properties of the MOT, as explained in detail in chapter 6.

The fundamental parameters of these two transitions are summarised in A.1: Γ is the spontaneous decay rate, $\tau = 1/\Gamma$ is the natural lifetime. From these parameters and the wavelength we can calculate the useful quantities for laser cooling and trapping, like the saturation intensity $I_s = \pi\hbar c/3\tau\lambda^3$, the Doppler cooling temperature limit $T_D = \hbar\Gamma/2k_B$ and the limit temperature due to photon recoil $T_r = \hbar k^2/mk_B$.

λ	Γ	τ	$\Gamma/2\pi$	I_{sat}	T_D	T_r
421.291 nm	$2.02 \times 10^8 \text{ s}^{-1}$	4.94 ns	32.2 MHz	56.4 mW cm^{-2}	774 μK	660 nK
626.082 nm	$8.5 \times 10^5 \text{ s}^{-1}$	1.2 μs	135 kHz	$72 \mu\text{W cm}^{-2}$	3.2 μK	298 nK

Table A.1 – Laser cooling parameters for the 421 nm and the 626 nm optical transitions. Data from [131, 173].

A.2.2 Hyperfine structure

Hyperfine structure summarises the deviation in the atomic spectrum from the most simple atomic picture – the one that considers the nucleus as being a point like source of infinite mass for the central potential. In reality, the nucleus does not have an infinite mass, nor is a perfect electric monopole, and this gives rise to additional corrections.

For atoms where the nucleus has a nuclear spin $I \neq 0$, the fine structure energy levels are further split into more components, due to the interaction of the electron total angular momentum and the nucleus magnetic moment $\mathcal{M} = g_I \mu_N I/\hbar$. The good quantum number will be in this case $F = I + J$ and the states will be labeled according to the usual angular momentum sum rule. Bosons and fermions have integer or half integer nuclear spin. In the case of Dysprosium $I = 0$ for the bosons, so there is no hyperfine structure, while $I = 5/2$ for the fermionic isotopes. Therefore we expect that the energy levels of the fermions are split into 6 hyperfine levels.

In addition to this effect one has to consider that different isotopes have different nuclear mass, which gives rise to an isotopic shift. The shift is linear in the mass change. In the fermion case one has to consider the weighted centre of the hyperfine levels to calculate the shift.

We performed high resolution spectroscopy on the atoms and we were capable to resolve the whole hyperfine structure.

A.2.3 Laser spectroscopy

In A.4 one can see the experimental spectra of the two optical transitions previously considered in this chapter. The laser frequency was varied by some GHz around

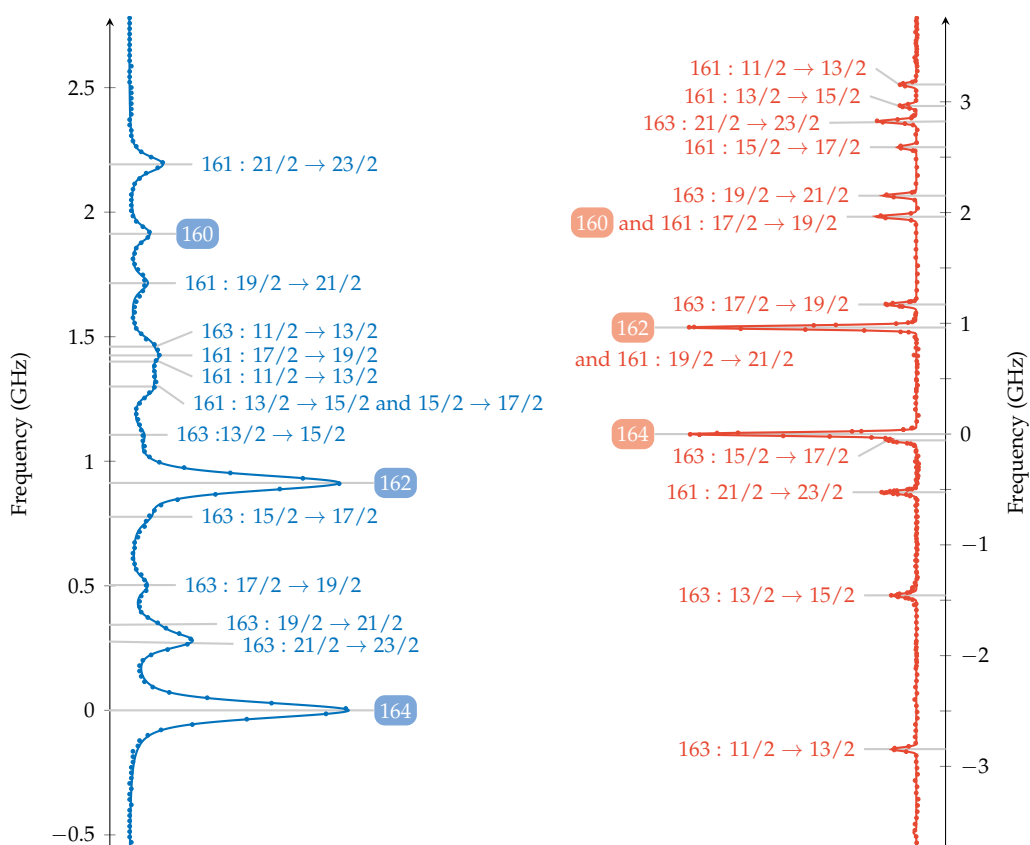


Figure A.4 – Experimental spectra (points) and Voigt fit (solid line) for the two considered optical transitions. Bosonic isotopes are indicated by boxes. Both frequency axes are centred on the ^{164}Dy line. Note that the red transition extends over a broader frequency range.

the resonance and the fluorescence was collected on a large area photodiode. Every fluorescence peak in the data is fitted using a Voigt function, which is a convolution of a Lorentzian and a Gaussian profile. These two profiles respectively account for the natural linewidth of the transition and for the broadening effects of the line. The latter effects are mainly due to the temperature (Doppler) broadening, since in our case we are performing the spectroscopy on the thermal jet at the output of the high temperature oven.

One can clearly see the hyperfine structure of the ground state of the two stable fermionic isotopes. The two isotopes have the nuclear spins with opposite sign, which results in a relative inversion of the hyperfine levels.

A.3 Magnetic Properties

In the following paragraph I will list some formulae that can be useful when dealing with the magnetic properties of Dysprosium.

A.3.1 Magnetic Moment

The magnetic moment of an atom is given by:

$$\mu = m_J g_J \mu_B \quad (\text{A.1})$$

where m_J is the considered magnetic sub-level, μ_B is the Bohr magneton and g_J is the Lande's g-factor. The latter can be calculated using the following formula in the case of pure spin-orbit interaction (as in the ground-state):

$$g_J = 1 + (g_S - 1) \frac{J(J+1) - L(L+1) + S(S+1)}{2J(J+1)}. \quad (\text{A.2})$$

g_S is the gyromagnetic ratio of electron, given within the first order correction from quantum electro-dynamics by:

$$g_S = 2 \left(1 + \frac{\alpha}{2\pi} + \dots \right) \sim 2.0023. \quad (\text{A.3})$$

For Dysprosium, the ground state g-factor calculated from the formula above is $g_J \sim 1.251$. More precise theoretical values should include relativistic corrections that give slightly lower values. Experimentally, the measured value is $g_J = 1.241$. The absolute ground state $|J = 8, m_J = -8\rangle$ then has a magnetic moment:

$$\mu = m_J g_J \mu_B = -9.93 \mu_B \quad (\text{A.4})$$

which is the highest magnetic moment among all elements already cooled to quantum degeneracy, and is only exceeded in nature by Terbium (Tb) which has $\mu = -9.94 \mu_B$ in its ground state.

In the case of the excited states, one also has to additionally consider the jj -coupling scheme. If the coupling happens between two states j_1 and j_2 , the formula of g_J is then given by:

$$g_J = g_{j_1} \frac{J(J+1) - j_2(j_2+1) + j_1(j_1+1)}{2J(J+1)} + g_{j_2} \frac{J(J+1) - j_1(j_1+1) + j_2(j_2+1)}{2J(J+1)}. \quad (\text{A.5})$$

For the transitions we considered in this thesis $j_1 = 8$ and $j_2 = 1$. Only $g_{j_1} \neq g_{j_2}$ since the transition on the blue has $S = 0$ while the red has $S = 1$. The formula gives $g_J = 1.223$ for the blue transition and $g_J = 1.278$ for the red. The result is precise within a few per mille error from the measured values, which are $g_J = 1.22$ and $g_J = 1.29$ respectively.

In the case of fermionic isotopes one expects also the splitting for the hyperfine structure to follow

$$g^F = g_J \frac{F(F+1) - I(I+1) + J(J+1)}{2F(F+1)} \quad (\text{A.6})$$

A.3.2 Zeeman Effect

The presence of a magnetic field B lifts the degeneracy of the magnetic sublevels inside a J manifold, in the same way that the spin-orbit interaction gives rise to the fine structure. In the case of weak fields (weak compared to the fine structure splitting), the

shift is of first order in the magnetic field B and can be written as

$$\Delta E_{\text{Zee}} = \mu_B m_J g_J B, \quad (\text{A.7})$$

where the ΔE is with respect to the energy at $B = 0$. In practice, it is more useful to rewrite the shift in terms of frequencies:

$$\Delta \nu_{\text{Zee}} = m_J g_J \frac{\mu_B}{h} B, \quad (\text{A.8})$$

where h is the Planck constant, so that $\mu_B/h \sim 1.4 \text{ MHz G}^{-1}$. We mainly work with a polarised cloud in the $|J = 8, m_J = -8\rangle$ ground state and figure A.5 lists the Zeeman shifts for the two optical transitions we consider in this thesis. These values can be useful e.g. for calibrating the magnetic field during the imaging process. The shift can be written simply as

$$\Delta \nu_{\text{Zee},q} = \frac{\mu_B}{h} (m_J g_J - m_{J+q} g_{J'}) B \quad (\text{A.9})$$

where the index $q \in \{-1, 0, 1\}$ accounts for the polarisation of the light (σ_- , π and σ_+ respectively). Remember that for fermions, in the case of small magnetic fields compared to the hyperfine structure, the shift will be given instead by

$$\Delta E_{\text{Zee}} = \mu_B m_F g_F B. \quad (\text{A.10})$$

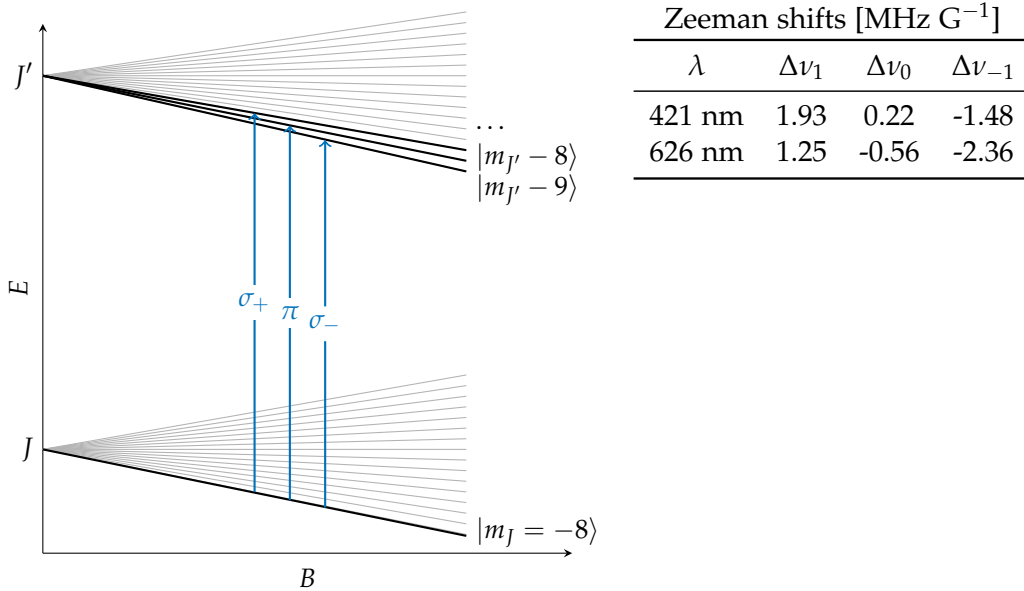


Figure A.5 – Zeeman shifts for the ground state and the excited state addressed by the two optical transition considered before. Since the atomic cloud is polarised in the $|J = 8, m_J = -8\rangle$ state, we consider the only three transition starting from this state.



B

Imaging Dysprosium Clouds

MOST of the data presented in this thesis are obtained by the analysis of pictures of the atomic cloud. In the following I will briefly summarise the most important ideas on imaging.

B.1 Absorption Imaging

In our setup we use absorption imaging. Despite the existence of other imaging technics (fluorescence, phase contrast imaging, ...), absorption imaging is quite easy to setup and calibrate and provides high signal to noise results. In brief it consists in shining resonant light on the atoms and collecting the casted shadow on a CCD.

A light beam propagating along the z direction through an atomic cloud of density $n(x, y, z)$ will be absorbed accordingly to the Lambert-Beer law, thus the collected intensity on the camera chip will be

$$I(x, y) = I_0(x, y) \exp\left(-\int dz n(x, y, z) \sigma(\delta)\right). \quad (\text{B.1})$$

The atomic density, integrated along the cloud thickness, is multiplied by the light scattering cross section:

$$\sigma(\delta) = \frac{\sigma_0}{1 + 4(\delta/\Gamma)^2} \quad (\text{B.2})$$

where $\sigma_0 = 3\lambda^2/2\pi$ is the resonant absorption cross section for a two level system. Note how the cross section depends only on the wavelength of the optical transition and is thus much bigger than the size of an atom. The resonance frequency is easily located after a frequency scan like the one in figure B.1.

Setting the imaging frequency exactly at resonance ($\delta = 0$) we can directly recover

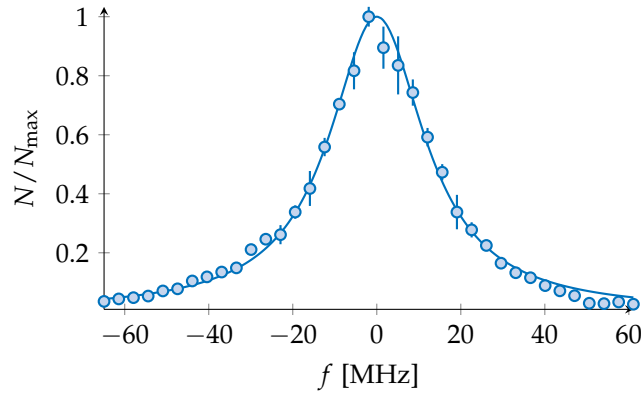


Figure B.1 – Resonance curve using light at 421 nm. The profile is Lorentzian, following the scattering cross section expression (B.2), the width being the natural line width $\Gamma = 2\pi \times 32$ MHz.

the atomic column density by analysing the transmitted intensity:

$$\bar{n}(x, y) = \int dz n(x, y, z) = -\frac{1}{\sigma_0} \ln\left(\frac{I(x, y)}{I_0(x, y)}\right) = \frac{1}{\sigma_0} \text{OD}(x, y) \quad (\text{B.3})$$

Here, the last equality should be taken as a definition for the optical density OD.

B.1.1 Dark-frame subtraction

Various noise sources may reduce the image quality: dark currents (charge carriers excited by thermal energy), transfer noises, read out noise (from the amplification stage in the ADC), hot pixels (due to charge leaks from the electronics to the image sensor), etc. Some of this noise constitutes a fixed pattern and only depends on the exposure time of the chip.. This kind of noise can be reduced or even canceled by using the dark field correction: we collect a dark image I_{bgd} with the same exposition time than the image we want to analyse. Then we subtract the dark frame to the image and obtain a picture clean from fixed pattern noise and from any background light that might still be present.

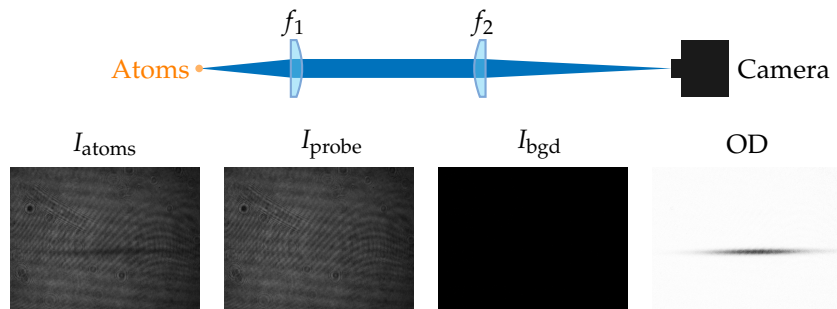


Figure B.2 – Typical imaging setup. Below, the construction of an image of the atoms in the dipole trap. The image with atoms, without atoms and the dark frame are combined together to give the optical density of the cloud as in equation (B.4).

If we want to get the collected intensity with only the probe beam present I_0 or with the probe beam and the atoms I we simply take the two pictures and a background image with same exposure time, so that $I_0 = I_{\text{probe}} - I_{\text{bgd}}$ and $I = I_{\text{atoms}} - I_{\text{bgd}}$. It is thus

very simple to obtain the optical density from equation B.3:

$$\text{OD} = \ln\left(\frac{I_{\text{probe}} - I_{\text{bgd}}}{I_{\text{atoms}} - I_{\text{bgd}}}\right) \quad (\text{B.4})$$

B.1.2 Cross section corrections

Formula B.3 is in general underestimating the density, since the cross section formula is valid for a two level system. In the real atom this can almost be realised imaging the most stretched states with perfectly circular light. In general one has to multiply the expression for the cross section B.2 by the correct Clebsch-Gordan coefficient. For the imaging transition used in our experiment, the coefficient are plotted in figure B.3.

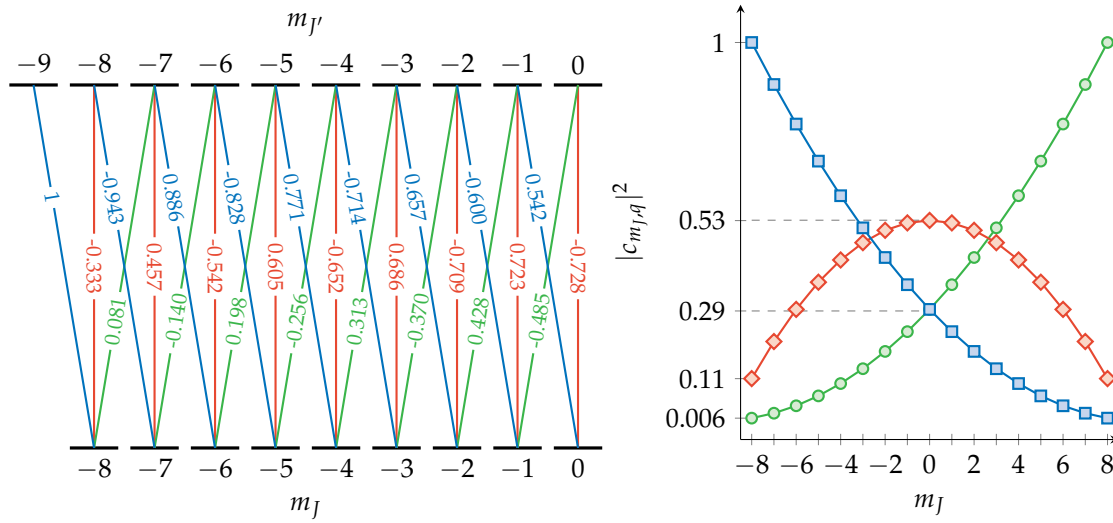


Figure B.3 – Clebsch-Gordan coefficients $c_{m_J, q}$ for the Zeeman states $m_J < 0$. The values are symmetric for positive states $c_{m_J, q} = c_{-m_J, -q}$. In green and blue are the coefficients for σ_+ and σ_- light respectively ($q = \pm 1$) and in red for π polarisation ($q = 0$).

We typically work with a spin polarised cloud in the $|J = 8, m_J = -8\rangle$ ground state. Therefore we should take into account the cross section reduction if we are not imaging on the cycling transition. According to the light polarisation, the effective cross section is:

$$\sigma = \sigma_0 \left(e_{\sigma_-} + \frac{1}{9} e_{\pi} + \frac{1}{153} e_{\sigma_+} \right) \cdot \epsilon, \quad (\text{B.5})$$

where ϵ is the polarisation of the imaging light in the circular basis. Taking this into account is mandatory to get the right atom number in Stern Gerlach images, like the one presented in chapter 6. A good calibration requires also checking the guiding field direction and strength, in order to be certain of the quantification axis.

Nevertheless, this is still an approximation, valid only for very low saturation parameters and short pulses (compared to the optical pumping time). In fact, the imaging light will in general optically pump the atoms and a cloud prepared $|J = 8, m_J = -8\rangle$ will depolarise during the imaging pulse. Thus, a more careful estimation of the cross section

requires to solve the optical Bloch equations to recover the dynamics in the electronic spin states undergoing optical pumping from imaging light (see an example in figure B.4). The total cross section should be then calculated using the time dependent populations.

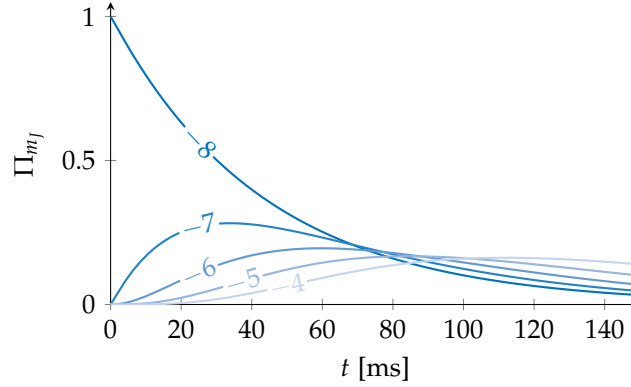


Figure B.4 – Evolution of the population in the ground state spin states when atoms interact with a π polarised light with saturation parameter $s = 0.1$. The number on the solid lines refers to the considered $|m_J\rangle$ state.

B.2 Thermometry

Temperature measurement are performed by time-of-flight imaging (TOF): as the trap is suddenly switched off, the cloud start to fall and to ballistically expand due to atoms initial velocity.

B.2.1 Thermal Clouds

Let us consider the case of an atomic cloud at a temperature above the condensation threshold $T > T_c$. In the classical limit the phase space density follows a Maxwell distribution:

$$f(\mathbf{r}, \mathbf{p}) = e^{(\mu - E(\mathbf{r}, \mathbf{p})) / k_B T}. \quad (\text{B.6})$$

The spatial density in the trap $n(\mathbf{r})$ is then obtained by integrating $f(\mathbf{r}, \mathbf{p})$ over the momenta \mathbf{p} . Turning off the trap, the gas will expand freely according to the initial velocity of atoms $\mathbf{r}(t) = \mathbf{r}_0 + \mathbf{p}t/m$. The integration over the initial positions and the momenta give in this case:

$$n_{\text{TOF}}(\mathbf{r}, t) = \frac{1}{\lambda_{\text{dB}}^3} \prod_i \frac{1}{\sqrt{1 + \omega_i^2 t^2}} e^{(\mu - m\omega_i^2 r_i^2 / 2(1 + \omega_i^2 t^2)) / k_B T} \quad (\text{B.7})$$

At times t longer than the inverse frequency $1/\omega_i$ the width of the exponential is no more anisotropic since it loses the dependence on the initial frequency. The cloud then expands isotropically, the rms sizes $\sigma_{x,z}$ will increase linearly with the time t according to the initial thermal temperature. We can then fit the size using the following function to recover the temperature in the trap:

$$\sigma_i^2(t) = \sigma_{0,i}^2 + \frac{k_B T}{m} t^2 \quad (\text{B.8})$$

By varying the flight time, i.e. the waiting time after which the image is taken, one can get the velocity of the cloud and hence its temperature.

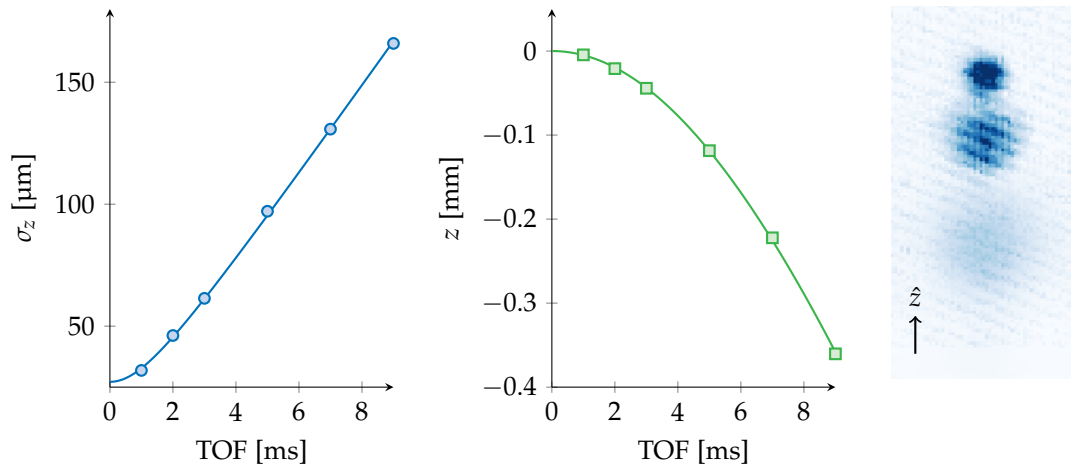


Figure B.5 – Vertical size σ_z and position z of the cloud as a function of time of flight. On the right, a stroboscopic picture of the falling cloud.

Note that in the absence of any magnetic field, the centre of mass motion can be used to calibrate the imaging magnification with the local gravity.

```
313941 | 234225_test_DummyAverage = 1_DipoleTOF = 5_Pixelflycamera_With.tif | 2017-02-24 23:42:25 | 50
20 |
| 313940 | 234207_test_DummyAverage = 1_DipoleTOF = 5_Pixelflycamera_With.tif | 2017-02-24 23:42:07 | 50
20 |
| 313939 | 234152_test_DummyAverage = 1_DipoleTOF = 5_Pixelflycamera_With.tif | 2017-02-24 23:41:52 | 50
20 |
| 313938 | 234136_test_DummyAverage = 1_DipoleTOF = 5_Pixelflycamera_With.tif | 2017-02-24 23:41:36 | 50
20 |
+-----+
---+
10 rows in set (0,00 sec)

mysql> select * from Measures_sequence where id = '50';
+-----+
| id | name | date |
+-----+
| 50 | TOF1 | 2015-05-06 |
+-----+
1 row in set (0,00 sec)

mysql> █
```

Notes on the Experiment Database

SINCE during this thesis I worked on the construction of a new experimental apparatus, one has to know I put a lot of effort in designing the softwares that we use on a daily basis. The main point is the implementation of the database that stores every metadata related to the images. In addition to the database the programs I developed take care of fitting the pictures and recover and analyse the data once they are stored into the database.

C.1 Database

As any respectful experiment we need a lot of statistics to have meaningful results. Statistics means lots of data, and lots of data need some kind of organisation. The usual way informatics deals with a big quantity of information is databases.

A database is an organised data structure that permits very fast operations on the stored informations (searching, ordering, filtering, etc.), and can easily link to external files that are not actually part of the database itself.

We choose to use the MySQL language, which is one of the most spread database management systems (DMS), being also the basis of the common open-source LAMP (Linux-Apache-MySQL-Perl/PHP/Python) servers.

MySQL is a relational DMS. It means that data are stored using relations between them (in databases jargon, the relations are called tables). Each single value recorded in the database should be univocally recovered by resorting the combination of the relation (i.e. the table name), a primary key and of a column name. The examples presented in the next section will make all of this much more understandable.

C.1.1 Structure of the database

During the design of the database, one should also pay attention to avoid single big tables. The relations should be made as fundamental as possible, without of course losing

any information, such that any possible modification can be made on the small tables without affecting the rest of the database nor the definition of the tables themselves. This process is called database normalisation.

To be more clear, let us give an example. Let us suppose that for every measure we take in our experiment we want to store details about the laser powers, the voltage we read on some photodiodes, etc. The simplest idea is to organise the data as the table shown below, storing in a single line of the table all informations regarding a certain measure.

```
1 mysql> SELECT * FROM simple_table;
2 +-----+-----+-----+-----+-----+
3 | id | date                | blue power | MOT fluo  | V photodiode 1 | ...
4 +-----+-----+-----+-----+-----+
5 | 1 | 2015-11-05 09:27:35 | 2.1        | 7.7       | 1.2             | ...
6 | 2 | 2015-11-05 09:27:43 | 2.4        | 7.5       | 1.3             | ...
7 ...
```

This will definitely permit to univocally recover any value we want. Moreover, here one can see the interest of having a database for later data analysis. For example, recover data where the fluorescence of the MOT was bigger than some value reads simply:

```
1 mysql> SELECT id FROM simple_table WHERE MOT fluo >= 3.0;
```

The problem in this example is that the database is not in a normalised form. What will happen if one day we want to add a variable? Or if at some point we remove the variable `blue_laser_pow` and we don't want to register its value anymore? In the first case we will be obliged to modify the table definition and, in the second case, we have to keep a column that we are never going to use anymore.

Let us look at the normalised version of the previous simple example. The single table get decomposed into more fundamental information:

```
1 mysql> SELECT * FROM measures;
2 +-----+-----+
3 | id | date                |
4 +-----+-----+
5 | 1 | 2015-11-05 09:27:35 |
6 | 2 | 2015-11-05 09:27:43 |
7 ...
8 mysql> SELECT * FROM parameters;
9 +-----+-----+
10 | id | name                |
11 +-----+-----+
12 | 1 | blue power          |
13 | 2 | MOT fluo            |
14 ...
15 mysql> SELECT * FROM parameter_values;
16 +-----+-----+-----+
17 | measure_id | variable_id | value |
18 +-----+-----+-----+
19 | 1          | 1           | 2.1   |
20 | 1          | 2           | 7.7   |
21 ...
22 | 2          | 1           | 2.4   |
23 ...
```

One can clearly see that decomposing the information in more fundamental relations, the problems mentioned above are solved. Adding a new variable simply requires to add

a new line on the table with the variables definitions. If one measurement does not use a variable, simply it will not be saved on the results table.

After these premises, the structure of our database should be more clear. This is a scheme of our current databases table:

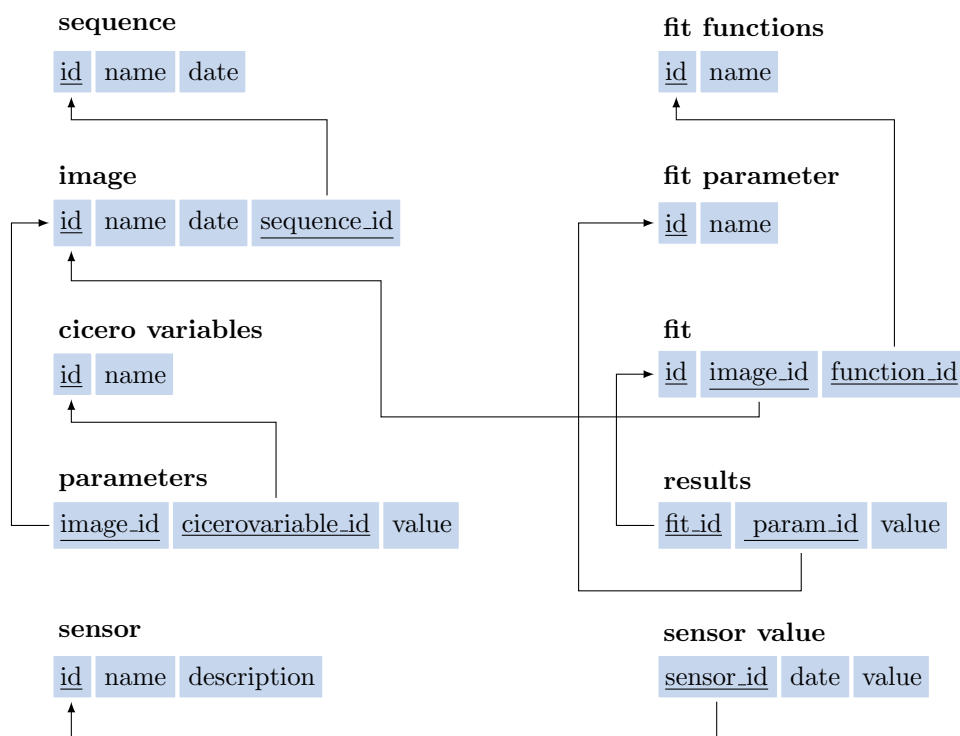


Figure C.1 – Current relational scheme of our database. Arrow indicate foreign keys to a given table and were they are stored.

Note that the database includes also to the storage of the data analysis results, as we will see in the following section. An additional database stores the values read from different sensors connected to a data logger running on a Raspberry Pi server. we typically monitor the temperatures in the room and the magnetic field at different positions.

C.2 Data Analysis

The database stores all the metadata and the path to the actual data, which are the images taken at the end of a sequence. The model operation we perform on these images is first getting the optical density and than perform some kind of fit.

C.2.1 Image fitting

For usual fitting function (2D gaussian, etc.), results can be analysed both in real time (during a sequence) or at any later moment using the program `fit.py`. The program uses the `ipython qt` console to have an immediate visual feed of optical density plot, marginal distributions and fit result, giving a rapid information on the cloud position and atom number.

The results of the fit of every single image constitute a dictionary that looks like the following:


```
1 data = {  
2   'fit function' : fit_name,  
3   'fit results' : {'center_x': x0, 'center_y': y0, 'sigma_y': y0, ...  
4   'fit errors' : {'center_x_e': x0, 'center_y_e': y0, 'sigma_y_e': y0, ...  
5   'N' : atom_number,  
6   'N_error' : atom_number_error,  
7   'variables' : scanning_sequence_variables,  
8   'camera': {'name' : camera_name, 'magnification' : M, 'pixel_size': pxs}  
9 }
```

Once the single images have been fitted these results are then serialised in a python pickle file as backup and are uploaded in the database along with all the other measurements metadata.

C.2.2 Data processing

The informations stored in the database can be recovered and analysed via the program `data_analysis.py`.

The program starts a connection with the database and permits the more usual operation that we perform on the fit results. Typically it is possible to plot one of the scanning variable vs some result, average or rescale the data. The communication with the database is useful to filter the results using any other stored metadata (for example we may want to retrieve the atom number restrictedly for measurements when the power in the slower was a certain value, the magnetic field of a coil was inside a given range, etc.). The program contains also the mostly used fit functions for the routine measurements (like decay curves, TOF sequences) and allows to easily add any custom function that one may need for future use.

Bibliography

- [1] Richard P Feynman. There's plenty of room at the bottom. *Engineering and science*, 23(5):22–36, 1960.
- [2] Theodore H Maiman. Stimulated optical radiation in ruby. 1960.
- [3] William D Phillips. Nobel lecture: Laser cooling and trapping of neutral atoms. *Reviews of Modern Physics*, 70(3):721, 1998.
- [4] Steven Chu. Nobel lecture: The manipulation of neutral particles. *Reviews of Modern Physics*, 70(3):685, 1998.
- [5] Claude N Cohen-Tannoudji. Nobel lecture: Manipulating atoms with photons. *Reviews of Modern Physics*, 70(3):707, 1998.
- [6] Albert Einstein. *Quantentheorie des einatomigen idealen Gases*. Akademie der Wissenschaften, in Kommission bei W. de Gruyter, 1924.
- [7] Satyendra Nath Bose. Plancks gesetz und lichtquantenhypothese. *Z. phys*, 26(3):178, 1924.
- [8] Mike H Anderson, Jason R Ensher, Michael R Matthews, Carl E Wieman, and Eric A Cornell. Observation of bose-einstein condensation in a dilute atomic vapor. *science*, 269(5221):198, 1995.
- [9] Kendall B Davis, M-O Mewes, Michael R Andrews, NJ Van Druten, DS Durfee, DM Kurn, and Wolfgang Ketterle. Bose-einstein condensation in a gas of sodium atoms. *Physical review letters*, 75(22):3969, 1995.
- [10] MR Andrews, CG Townsend, H-J Miesner, DS Durfee, DM Kurn, and W Ketterle. Observation of interference between two bose condensates. *Science*, 275(5300):637–641, 1997.
- [11] I Bloch, Th W Hänsch, and T Esslinger. Measurement of the spatial coherence of a trapped bose gas at the phase transition. *Nature*, 403(6766):166–170, 2000.
- [12] Immanuel Bloch, Theodor W Hänsch, and Tilman Esslinger. Atom laser with a cw output coupler. *Physical Review Letters*, 82(15):3008, 1999.
- [13] EW Hagley, L Deng, M Kozuma, J Wen, K Helmerson, SL Rolston, , and WD Phillips. A well-collimated quasi-continuous atom laser. *Science*, 283(5408):1706–1709, 1999.
- [14] Brian DeMarco and Deborah S Jin. Onset of fermi degeneracy in a trapped atomic gas. *Science*, 285(5434):1703–1706, 1999.
- [15] Andrew G Truscott, Kevin E Strecker, William I McAlexander, Guthrie B Partridge, and Randall G Hulet. Observation of fermi pressure in a gas of trapped atoms. *Science*, 291(5513):2570–2572, 2001.
- [16] F Schreck, Lev Khaykovich, KL Corwin, G Ferrari, Thomas Bourdel, Julien Cubizolles, and Christophe Salomon. Quasipure bose-einstein condensate immersed in a fermi sea. *Physical Review Letters*, 87(8):080403, 2001.

- [17] Immanuel Bloch, Jean Dalibard, and Wilhelm Zwerger. Many-body physics with ultracold gases. *Reviews of Modern Physics*, 80(3):885, 2008.
- [18] S Inouye, MR Andrews, J Stenger, H-J Miesner, DM Stamper-Kurn, and W Ketterle. Observation of feshbach resonances in a bose–einstein condensate. *Nature*, 392(6672):151–154, 1998.
- [19] Simon L Cornish, Neil R Claussen, Jacob L Roberts, Eric A Cornell, and Carl E Wieman. Stable 85 rb bose-einstein condensates with widely tunable interactions. *Physical Review Letters*, 85(9):1795, 2000.
- [20] KM O’hara, SL Hemmer, ME Gehm, SR Granade, and JE Thomas. Observation of a strongly interacting degenerate fermi gas of atoms. *Science*, 298(5601):2179–2182, 2002.
- [21] Thomas Bourdel, Lev Khaykovich, Julien Cubizolles, Jun Zhang, Frédéric Chevy, M Teichmann, L Tarruell, SJJMF Kokkelmans, and Christophe Salomon. Experimental study of the bec-bcs crossover region in lithium 6. *Physical Review Letters*, 93(5):050401, 2004.
- [22] M Bartenstein, A Altmeyer, S Riedl, S Jochim, C Chin, J Hecker Denschlag, and R Grimm. Crossover from a molecular bose-einstein condensate to a degenerate fermi gas. *Physical review letters*, 92(12):120401, 2004.
- [23] Zoran Hadzibabic, Peter Krüger, Marc Cheneau, Baptiste Battelier, and Jean Dalibard. Berezinskii–kosterlitz–thouless crossover in a trapped atomic gas. *Nature*, 441(7097):1118–1121, 2006.
- [24] Toshiya Kinoshita, Trevor Wenger, and David S Weiss. Observation of a one-dimensional tonks–girardeau gas. *Science*, 305(5687):1125–1128, 2004.
- [25] Belén Paredes, Artur Widera, Valentin Murg, Olaf Mandel, Simon Fölling, Ignacio Cirac, Gora V Shlyapnikov, Theodor W Hänsch, and Immanuel Bloch. Tonks–girardeau gas of ultracold atoms in an optical lattice. *Nature*, 429(6989):277–281, 2004.
- [26] Alexander L Gaunt, Tobias F Schmidutz, Igor Gotlibovych, Robert P Smith, and Zoran Hadzibabic. Bose-einstein condensation of atoms in a uniform potential. *Physical review letters*, 110(20):200406, 2013.
- [27] Richard P Feynman. Simulating physics with computers. *International journal of theoretical physics*, 21(6):467–488, 1982.
- [28] Immanuel Bloch, Jean Dalibard, and Sylvain Nascimbene. Quantum simulations with ultracold quantum gases. *Nature Physics*, 8(4):267–276, 2012.
- [29] Markus Greiner, Olaf Mandel, Tilman Esslinger, Theodor W Hänsch, and Immanuel Bloch. Quantum phase transition from a superfluid to a mott insulator in a gas of ultracold atoms. *nature*, 415(6867):39–44, 2002.
- [30] Robert Jördens, Niels Strohmaier, Kenneth Günter, Henning Moritz, and Tilman Esslinger. A mott insulator of fermionic atoms in an optical lattice. *Nature*, 455(7210):204–207, 2008.
- [31] Julian Struck, Christoph Ölschläger, R Le Targat, Parvis Soltan-Panahi, André Eckardt, Maciej Lewenstein, Patrick Windpassinger, and Klaus Sengstock. Quantum simulation of frustrated classical magnetism in triangular optical lattices. *Science*, 333(6045):996–999, 2011.
- [32] Jonathan Simon, Waseem S Bakr, Ruichao Ma, M Eric Tai, Philipp M Preiss, and Markus Greiner. Quantum simulation of antiferromagnetic spin chains in an optical lattice. *Nature*, 472(7343):307–312, 2011.

- [33] Waseem S Bakr, Jonathon I Gillen, Amy Peng, Simon Fölling, and Markus Greiner. A quantum gas microscope for detecting single atoms in a hubbard-regime optical lattice. *Nature*, 462(7269):74–77, 2009.
- [34] Jacob F Sherson, Christof Weitenberg, Manuel Endres, Marc Cheneau, Immanuel Bloch, and Stefan Kuhr. Single-atom-resolved fluorescence imaging of an atomic mott insulator. *Nature*, 467(7311):68–72, 2010.
- [35] Elmar Haller, James Hudson, Andrew Kelly, Dylan A Cotta, Bruno Peaudecerf, Graham D Bruce, and Stefan Kuhr. Single-atom imaging of fermions in a quantum-gas microscope. *Nature Physics*, 11(9):738–742, 2015.
- [36] Lawrence W Cheuk, Matthew A Nichols, Melih Okan, Thomas Gersdorf, Vinay V Ramasesh, Waseem S Bakr, Thomas Lompe, and Martin W Zwierlein. Quantum-gas microscope for fermionic atoms. *Physical review letters*, 114(19):193001, 2015.
- [37] Giovanni Modugno, Gabriele Ferrari, Giacomo Roati, Robert J Brecha, A Simoni, and Massimo Inguscio. Bose-einstein condensation of potassium atoms by sympathetic cooling. *Science*, 294(5545):1320–1322, 2001.
- [38] Tino Weber, Jens Herbig, Michael Mark, Hanns-Christoph Nägerl, and Rudolf Grimm. Bose-einstein condensation of cesium. *Science*, 299(5604):232–235, 2003.
- [39] Sebastian Kraft, Felix Vogt, Oliver Appel, Fritz Riehle, and Uwe Sterr. Bose-einstein condensation of alkaline earth atoms: Ca 40. *Physical review letters*, 103(13):130401, 2009.
- [40] Yosuke Takasu, Kenichi Maki, Kaduki Komori, Tetsushi Takano, Kazuhito Honda, Mitsutaka Kumakura, Tsutomu Yabuzaki, and Yoshiro Takahashi. Spin-singlet bose-einstein condensation of two-electron atoms. *Physical Review Letters*, 91(4):040404, 2003.
- [41] Simon Stellmer, Meng Khoon Tey, Bo Huang, Rudolf Grimm, and Florian Schreck. Bose-einstein condensation of strontium. *Physical review letters*, 103(20):200401, 2009.
- [42] N Hinkley, JA Sherman, NB Phillips, M Schioppo, ND Lemke, K Beloy, M Pizzocaro, CW Oates, and AD Ludlow. An atomic clock with 10–18 instability. *Science*, 341(6151):1215–1218, 2013.
- [43] BJ Bloom, TL Nicholson, JR Williams, SL Campbell, M Bishof, X Zhang, W Zhang, SL Bromley, and J Ye. An optical lattice clock with accuracy and stability at the 10-18 level. *Nature*, 506(7486):71–75, 2014.
- [44] Axel Griesmaier, Jörg Werner, Sven Hensler, Jürgen Stuhler, and Tilman Pfau. Bose-einstein condensation of chromium. *Physical Review Letters*, 94(16):160401, 2005.
- [45] Jürgen Stuhler, Axel Griesmaier, Tobias Koch, Marco Fattori, Tilman Pfau, Stefano Giovanazzi, Paolo Pedri, and Luis Santos. Observation of dipole-dipole interaction in a degenerate quantum gas. *Physical Review Letters*, 95(15):150406, 2005.
- [46] J Metz, T Lahaye, B Fröhlich, A Griesmaier, T Pfau, H Saito, Y Kawaguchi, and M Ueda. Coherent collapses of dipolar bose-einstein condensates for different trap geometries. *New Journal of Physics*, 11(5):055032, 2009.
- [47] S Hensler, J Werner, A Griesmaier, PO Schmidt, A Görlitz, T Pfau, S Giovanazzi, and K Rzazewski. Dipolar relaxation in an ultra-cold gas of magnetically trapped chromium atoms. *Applied Physics B: Lasers and Optics*, 77(8):765–772, 2003.

- [48] Jabez J McClelland and James L Hanssen. Laser cooling without repumping: a magneto-optical trap for erbium atoms. *Physical review letters*, 96(14):143005, 2006.
- [49] Seo Ho Youn, Mingwu Lu, Ushnish Ray, and Benjamin L Lev. Dysprosium magneto-optical traps. *Physical Review A*, 82(4):043425, 2010.
- [50] D Sukachev, A Sokolov, K Chebakov, A Akimov, S Kanorsky, N Kolachevsky, and V Sorokin. Magneto-optical trap for thulium atoms. *Physical Review A*, 82(1):011405, 2010.
- [51] Jinlu Miao, James Hostetter, Georgios Stratis, and Mark Saffman. Magneto-optical trapping of holmium atoms. *Physical Review A*, 89(4):041401, 2014.
- [52] A Frisch, K Aikawa, M Mark, A Rietzler, J Schindler, E Zupanič, R Grimm, and F Ferlaino. Narrow-line magneto-optical trap for erbium. *Physical Review A*, 85(5):051401, 2012.
- [53] T Maier, H Kadau, M Schmitt, A Griesmaier, and T Pfau. Narrow-line magneto-optical trap for dysprosium atoms. *Optics letters*, 39(11):3138–3141, 2014.
- [54] Mingwu Lu, Nathaniel Q Burdick, Seo Ho Youn, and Benjamin L Lev. Strongly dipolar bose-einstein condensate of dysprosium. *Physical review letters*, 107(19):190401, 2011.
- [55] K Aikawa, A Frisch, M Mark, S Baier, A Rietzler, R Grimm, and F Ferlaino. Bose-einstein condensation of erbium. *Physical review letters*, 108(21):210401, 2012.
- [56] Mingwu Lu, Nathaniel Q Burdick, and Benjamin L Lev. Quantum degenerate dipolar fermi gas. *Physical Review Letters*, 108(21):215301, 2012.
- [57] K Aikawa, A Frisch, M Mark, S Baier, R Grimm, and F Ferlaino. Reaching fermi degeneracy via universal dipolar scattering. *Physical review letters*, 112(1):010404, 2014.
- [58] Holger Kadau, Matthias Schmitt, Matthias Wenzel, Clarissa Wink, Thomas Maier, Igor Ferrier-Barbut, and Tilman Pfau. Observing the rosenzweig instability of a quantum ferrofluid. *Nature*, 530(7589):194–197, 2016.
- [59] K Aikawa, S Baier, A Frisch, M Mark, C Ravensbergen, and F Ferlaino. Observation of fermi surface deformation in a dipolar quantum gas. *Science*, 345(6203):1484–1487, 2014.
- [60] Nathan Goldman, G Juzeliūnas, P Öhberg, and Ian B Spielman. Light-induced gauge fields for ultracold atoms. *Reports on Progress in Physics*, 77(12):126401, 2014.
- [61] Y-J Lin, Rob L Compton, K Jimenez-Garcia, James V Porto, and Ian B Spielman. Synthetic magnetic fields for ultracold neutral atoms. *Nature*, 462(7273):628–632, 2009.
- [62] Yu-Ju Lin, Robert L Compton, Karina Jimenez-Garcia, William D Phillips, James V Porto, and Ian B Spielman. A synthetic electric force acting on neutral atoms. *Nature Physics*, 7(7):531–534, 2011.
- [63] Monika Aidelsburger, Marcos Atala, Sylvain Nascimbène, Stefan Trotzky, Y-A Chen, and Immanuel Bloch. Experimental realization of strong effective magnetic fields in an optical lattice. *Physical review letters*, 107(25):255301, 2011.
- [64] Julian Struck, Malte Weinberg, Christoph Ölschläger, Patrick Windpassinger, Juliette Simonet, Klaus Sengstock, Robert Höppner, Philipp Hauke, André Eckardt, Maciej Lewenstein, et al. Engineering ising-xy spin-models in a triangular lattice using tunable artificial gauge fields. *Nature Physics*, 9(11):738–743, 2013.

- [65] Zhengkun Fu, Pengjun Wang, Shijie Chai, Lianghai Huang, Jing Zhang, et al. Bose-einstein condensate in a light-induced vector gauge potential using 1064-nm optical-dipole-trap lasers. *Physical Review A*, 84(4):043609, 2011.
- [66] Y-J Lin, K Jiménez-García, and IB Spielman. Spin-orbit-coupled bose-einstein condensates. *Nature*, 471(7336):83–86, 2011.
- [67] Jin-Yi Zhang, Si-Cong Ji, Zhu Chen, Long Zhang, Zhi-Dong Du, Bo Yan, Ge-Sheng Pan, Bo Zhao, You-Jin Deng, Hui Zhai, et al. Collective dipole oscillations of a spin-orbit coupled bose-einstein condensate. *Physical review letters*, 109(11):115301, 2012.
- [68] Lawrence W Cheuk, Ariel T Sommer, Zoran Hadzibabic, Tarik Yefsah, Waseem S Bakr, and Martin W Zwierlein. Spin-injection spectroscopy of a spin-orbit coupled fermi gas. *Physical Review Letters*, 109(9):095302, 2012.
- [69] Pengjun Wang, Zeng-Qiang Yu, Zhengkun Fu, Jiao Miao, Lianghai Huang, Shijie Chai, Hui Zhai, and Jing Zhang. Spin-orbit coupled degenerate fermi gases. *Physical review letters*, 109(9):095301, 2012.
- [70] RA Williams, MC Beeler, LJ LeBlanc, K Jiménez-García, and IB Spielman. Raman-induced interactions in a single-component fermi gas near an s-wave feshbach resonance. *Physical review letters*, 111(9):095301, 2013.
- [71] Chunji Wang, Chao Gao, Chao-Ming Jian, and Hui Zhai. Spin-orbit coupled spinor bose-einstein condensates. *Physical review letters*, 105(16):160403, 2010.
- [72] Yun Li, Lev P Pitaevskii, and Sandro Stringari. Quantum tricriticality and phase transitions in spin-orbit coupled bose-einstein condensates. *Physical review letters*, 108(22):225301, 2012.
- [73] Jun-Ru Li, Jeongwon Lee, Wujie Huang, Sean Burchesky, Boris Shteynas, Furkan Çağrı Top, Alan O Jamison, and Wolfgang Ketterle. A stripe phase with supersolid properties in spin-orbit-coupled bose-einstein condensates. *Nature*, 543(7643):91–94, 2017.
- [74] Ryan M Wilson, Brandon M Anderson, and Charles W Clark. Meron ground state of rashba spin-orbit-coupled dipolar bosons. *Physical review letters*, 111(18):185303, 2013.
- [75] Sarang Gopalakrishnan, Ivar Martin, and Eugene A Demler. Quantum quasicrystals of spin-orbit-coupled dipolar bosons. *Physical review letters*, 111(18):185304, 2013.
- [76] M Zahid Hasan and Charles L Kane. Colloquium: topological insulators. *Reviews of Modern Physics*, 82(4):3045, 2010.
- [77] Xiao-Liang Qi and Shou-Cheng Zhang. Topological insulators and superconductors. *Reviews of Modern Physics*, 83(4):1057, 2011.
- [78] Chetan Nayak, Steven H Simon, Ady Stern, Michael Freedman, and Sankar Das Sarma. Non-abelian anyons and topological quantum computation. *Reviews of Modern Physics*, 80(3):1083, 2008.
- [79] Xiaoling Cui, Biao Lian, Tin-Lun Ho, Benjamin L Lev, and Hui Zhai. Synthetic gauge field with highly magnetic lanthanide atoms. *Physical Review A*, 88(1):011601, 2013.
- [80] Davide Dreon, Leonid A Sidorenkov, Chayma Bouazza, Wilfried Maineult, Jean Dalibard, and Sylvain Nascimbene. Optical cooling and trapping of highly magnetic atoms: the benefits of a spontaneous spin polarization. *Journal of Physics B: Atomic, Molecular and Optical Physics*, 50(6):065005, 2017.

- [81] Mikhail A Baranov. Theoretical progress in many-body physics with ultracold dipolar gases. *Physics Reports*, 464(3):71–111, 2008.
- [82] Thierry Lahaye, C Menotti, L Santos, M Lewenstein, and T Pfau. The physics of dipolar bosonic quantum gases. *Reports on Progress in Physics*, 72(12):126401, 2009.
- [83] Svetlana Kotochigova and Alexander Petrov. Anisotropy in the interaction of ultracold dysprosium. *Physical Chemistry Chemical Physics*, 13(42):19165–19170, 2011.
- [84] Hui Li, Jean-Francois Wyart, Olivier Dulieu, Sylvain Nascimbene, and Maxence Lepers. Optical trapping of ultracold dysprosium atoms: transition probabilities, dynamic dipole polarizabilities and van der waals c 6 coefficients. *Journal of Physics B: Atomic, Molecular and Optical Physics*, 50(1):014005, 2016.
- [85] Enrico Fermi. Sul moto dei neutroni nelle sostanze idrogenate. *Ricerca scientifica*, 7(2):13–52, 1936.
- [86] Yvan Castin. Bose-einstein condensates in atomic gases: simple theoretical results. In *Coherent atomic matter waves*, pages 1–136. Springer, 2001.
- [87] Stefano Giovanazzi, Axel Görlitz, and Tilman Pfau. Tuning the dipolar interaction in quantum gases. *Physical review letters*, 89(13):130401, 2002.
- [88] Cheng Chin, Rudolf Grimm, Paul Julienne, and Eite Tiesinga. Feshbach resonances in ultracold gases. *Reviews of Modern Physics*, 82(2):1225, 2010.
- [89] Albert Frisch, Michael Mark, Kiyotaka Aikawa, Francesca Ferlaino, John L Bohn, Constantinos Makrides, Alexander Petrov, and Svetlana Kotochigova. Quantum chaos in ultracold collisions of gas-phase erbium atoms. *Nature*, 507(7493):475–479, 2014.
- [90] T Maier, H Kadau, M Schmitt, M Wenzel, I Ferrier-Barbut, T Pfau, Albert Frisch, Simon Baier, Kiyotaka Aikawa, Lauriane Chomaz, et al. Emergence of chaotic scattering in ultracold er and dy. *Physical Review X*, 5(4):041029, 2015.
- [91] Alexander Petrov, Eite Tiesinga, and Svetlana Kotochigova. Anisotropy-induced feshbach resonances in a quantum dipolar gas of highly magnetic atoms. *Physical review letters*, 109(10):103002, 2012.
- [92] Thomas Maier, Igor Ferrier-Barbut, Holger Kadau, Matthias Schmitt, Matthias Wenzel, Clarissa Wink, Tilman Pfau, Krzysztof Jachymski, and Paul Sebastian Julienne. Broad universal feshbach resonances in the chaotic spectrum of dysprosium atoms. *Physical Review A*, 92(6):060702, 2015.
- [93] Kristian Baumann, Nathaniel Q Burdick, Mingwu Lu, and Benjamin L Lev. Observation of low-field fano-feshbach resonances in ultracold gases of dysprosium. *Physical Review A*, 89(2):020701, 2014.
- [94] Lev Davidovich Landau and Evgenii Mikhailovich Lifshitz. *Quantum mechanics: non-relativistic theory*, volume 3. Elsevier, 2013.
- [95] N Bogoliubov. On the theory of superfluidity. *J. Phys*, 11(1):23, 1947.
- [96] Lev Pitaevskii and Sandro Stringari. *Bose-Einstein condensation and superfluidity*, volume 164. Oxford University Press, 2016.
- [97] Duncan HJ O’Dell, Stefano Giovanazzi, and Claudia Eberlein. Exact hydrodynamics of a trapped dipolar bose-einstein condensate. *Physical review letters*, 92(25):250401, 2004.

- [98] Claudia Eberlein, Stefano Giovanazzi, and Duncan HJ O'Dell. Exact solution of the thomas-fermi equation for a trapped bose-einstein condensate with dipole-dipole interactions. *Physical Review A*, 71(3):033618, 2005.
- [99] Christoph Eigen, Alexander L Gaunt, Aziza Suleymanzade, Nir Navon, Zoran Hadzibabic, and Robert P Smith. Observation of weak collapse in a bose-einstein condensate. *Physical Review X*, 6(4):041058, 2016.
- [100] Yu Kagan, AE Muryshev, and GV Shlyapnikov. Collapse and bose-einstein condensation in a trapped bose gas with negative scattering length. *Physical Review Letters*, 81(5):933, 1998.
- [101] Elizabeth A Donley, Neil R Claussen, Simon L Cornish, Jacob L Roberts, Eric A Cornell, and Carl E Wieman. Dynamics of collapsing and exploding bose-einstein condensates. *Nature*, 412(6844):295–299, 2001.
- [102] Tobias Koch, Thierry Lahaye, Jonas Metz, Bernd Fröhlich, Axel Griesmaier, and Tilman Pfau. Stabilization of a purely dipolar quantum gas against collapse. *Nature physics*, 4(3):218–222, 2008.
- [103] L Santos, GV Shlyapnikov, P Zoller, and M Lewenstein. Bose-einstein condensation in trapped dipolar gases. *Physical Review Letters*, 85(9):1791, 2000.
- [104] S Yi and L You. Trapped condensates of atoms with dipole interactions. *Physical Review A*, 63(5):053607, 2001.
- [105] Thierry Lahaye, Tobias Koch, Bernd Fröhlich, Marco Fattori, Jonas Metz, Axel Griesmaier, Stefano Giovanazzi, and Tilman Pfau. Strong dipolar effects in a quantum ferrofluid. *Nature*, 448(7154):672–675, 2007.
- [106] Igor Ferrier-Barbut, Holger Kadau, Matthias Schmitt, Matthias Wenzel, and Tilman Pfau. Observation of quantum droplets in a strongly dipolar bose gas. *Physical review letters*, 116(21):215301, 2016.
- [107] Matthias Schmitt, Matthias Wenzel, Fabian Böttcher, Igor Ferrier-Barbut, and Tilman Pfau. Self-bound droplets of a dilute magnetic quantum liquid. *Nature*, 539(7628):259–262, 2016.
- [108] L Chomaz, S Baier, D Petter, MJ Mark, F Wächtler, L Santos, and F Ferlaino. Quantum-fluctuation-driven crossover from a dilute bose-einstein condensate to a macrodroplet in a dipolar quantum fluid. *Physical Review X*, 6(4):041039, 2016.
- [109] F Wächtler and L Santos. Quantum filaments in dipolar bose-einstein condensates. *Physical Review A*, 93(6):061603, 2016.
- [110] Tsin D Lee, Kerson Huang, and Chen N Yang. Eigenvalues and eigenfunctions of a bose system of hard spheres and its low-temperature properties. *Physical Review*, 106(6):1135, 1957.
- [111] Aristeu RP Lima and Axel Pelster. Beyond mean-field low-lying excitations of dipolar bose gases. *Physical Review A*, 86(6):063609, 2012.
- [112] C Cohen-Tannoudji, B Diu, and F Laloe. *Mecanique Quantique*, volume II. Hermann, Paris, 1977.
- [113] Tomasz Świśtocki, Tomasz Sowiński, Joanna Pietraszewicz, Mirosław Brewczyk, Maciej Lewenstein, Jakub Zakrzewski, and Mariusz Gajda. Tunable dipolar resonances and einstein-de haas effect in a rb 87-atom condensate. *Physical Review A*, 83(6):063617, 2011.

- [114] Charles Jean Joachain. *Quantum collision theory*. 1975.
- [115] HTC Stoof, JMVA Koelman, and BJ Verhaar. Spin-exchange and dipole relaxation rates in atomic hydrogen: Rigorous and simplified calculations. *Physical Review B*, 38(7):4688, 1988.
- [116] Nathaniel Q Burdick, Kristian Baumann, Yijun Tang, Mingwu Lu, and Benjamin L Lev. Fermionic suppression of dipolar relaxation. *Physical review letters*, 114(2):023201, 2015.
- [117] Claude Cohen-Tannoudji, Jacques Dupont-Roc, Gilbert Grynberg, and Patricia Thickstun. *Atom-photon interactions: basic processes and applications*. Wiley Online Library, 1992.
- [118] Rudolf Grimm, Matthias Weidemüller, and Yurii B Ovchinnikov. Optical dipole traps for neutral atoms. *Advances in atomic, molecular, and optical physics*, 42:95–170, 2000.
- [119] Claude Cohen-Tannoudji. Théorie quantique du cycle du pompage optique. vérification expérimentale des nouveaux effets prévus., 1962.
- [120] Ivan H Deutsch and Poul S Jessen. Quantum control and measurement of atomic spins in polarization spectroscopy. *Optics Communications*, 283(5):681–694, 2010.
- [121] JM Geremia, John K Stockton, and Hideo Mabuchi. Tensor polarizability and dispersive quantum measurement of multilevel atoms. *Physical Review A*, 73(4):042112, 2006.
- [122] Alexander Kramida, Yuri Ralchenko, Joseph Reader, et al. Nist atomic spectra database (ver. 5.2). *National Institute of Standards and Technology, Gaithersburg, MD*, 2013.
- [123] Jun John Sakurai. *Advanced quantum mechanics*. Pearson Education India, 1967.
- [124] P Rosenbusch, S Ghezali, VA Dzuba, VV Flambaum, K Beloy, and A Derevianko. ac stark shift of the cs microwave atomic clock transitions. *Physical Review A*, 79(1):013404, 2009.
- [125] Daniel A Steck. Rubidium 87 d line data, 2001.
- [126] Fam Le Kien, Philipp Schneeweiss, and Arno Rauschenbeutel. Dynamical polarizability of atoms in arbitrary light fields: general theory and application to cesium. *arXiv preprint arXiv:1211.2673*, 2012.
- [127] Claude Cohen-Tannoudji and Jacques Dupont-Roc. Experimental study of zeeman light shifts in weak magnetic fields. *Physical Review A*, 5(2):968, 1972.
- [128] NL Manakov and VD Ovsyannikov. Stark effect in hyperfine structure sublevels and splitting of $n2s$, states of alkali atoms in a nonresonant optical field. *Zh. Eksp. Teor. Fiz*, 75:803–815, 1978.
- [129] Maxence Lepers, J-F Wyart, and Olivier Dulieu. Anisotropic optical trapping of ultracold erbium atoms. *Physical Review A*, 89(2):022505, 2014.
- [130] Hui Li, Jean-François Wyart, Olivier Dulieu, and Maxence Lepers. Anisotropic optical trapping as a manifestation of the complex electronic structure of ultracold lanthanide atoms: the example of holmium. *arXiv preprint arXiv:1704.04134*, 2017.
- [131] Mingwu Lu, Seo Ho Youn, and Benjamin L Lev. Spectroscopy of a narrow-line laser-cooling transition in atomic dysprosium. *Physical Review A*, 83(1):012510, 2011.
- [132] Wil Kao, Yijun Tang, Nathaniel Q Burdick, and Benjamin L Lev. Anisotropic dependence of tune-out wavelength near dy 741-nm transition. *arXiv preprint arXiv:1609.02111*, 2016.
- [133] Michael Robin Matthews, Brian P Anderson, PC Haljan, DS Hall, CE Wieman, and EA Cornell. Vortices in a bose-einstein condensate. *Physical Review Letters*, 83(13):2498, 1999.

- [134] KW Madison, F Chevy, W Wohlleben, and JI Dalibard. Vortex formation in a stirred bose-einstein condensate. *Physical Review Letters*, 84(5):806, 2000.
- [135] JR Abo-Shaeer, C Raman, JM Vogels, and Wolfgang Ketterle. Observation of vortex lattices in bose-einstein condensates. *Science*, 292(5516):476–479, 2001.
- [136] Jean Dalibard, Fabrice Gerbier, Gediminas Juzeliūnas, and Patrik Öhberg. Colloquium: Artificial gauge potentials for neutral atoms. *Reviews of Modern Physics*, 83(4):1523, 2011.
- [137] Michael V Berry. Quantal phase factors accompanying adiabatic changes. In *Proceedings of the Royal Society of London A: Mathematical, Physical and Engineering Sciences*, volume 392, pages 45–57. The Royal Society, 1984.
- [138] Yakir Aharonov and David Bohm. Significance of electromagnetic potentials in the quantum theory. *Physical Review*, 115(3):485, 1959.
- [139] G Juzeliūnas and IB Spielman. Flux lattices reformulated. *New Journal of Physics*, 14(12):123022, 2012.
- [140] Marc Cheneau, Steffen Patrick Rath, Tarik Yefsah, Kenneth John Günter, G Juzeliūnas, and Jean Dalibard. Geometric potentials in quantum optics: A semi-classical interpretation. *EPL (Europhysics Letters)*, 83(6):60001, 2008.
- [141] G Juzeliūnas, J Ruseckas, P Öhberg, and M Fleischhauer. Light-induced effective magnetic fields for ultracold atoms in planar geometries. *Physical Review A*, 73(2):025602, 2006.
- [142] Kenneth J Günter, Marc Cheneau, Tarik Yefsah, Steffen P Rath, and Jean Dalibard. Practical scheme for a light-induced gauge field in an atomic bose gas. *Physical Review A*, 79(1):011604, 2009.
- [143] Nathaniel Q Burdick, Yijun Tang, and Benjamin L Lev. Long-lived spin-orbit-coupled degenerate dipolar fermi gas. *Physical Review X*, 6(3):031022, 2016.
- [144] Richard P Feynman. Chapter ii application of quantum mechanics to liquid helium. *Progress in low temperature physics*, 1:17–53, 1955.
- [145] NR Cooper, EH Rezayi, and SH Simon. Vortex lattices in rotating atomic bose gases with dipolar interactions. *Physical review letters*, 95(20):200402, 2005.
- [146] Andrew C Wilson, Christian Ospelkaus, AP VanDevender, Jonas A Mlynek, KR Brown, Dietrich Leibfried, and DJ Wineland. A 750-mW, continuous-wave, solid-state laser source at 313 nm for cooling and manipulating trapped ${}^9\text{be}^+$ ions. *Applied Physics B*, 105(4):741–748, 2011.
- [147] Dieter H Jundt. Temperature-dependent sellmeier equation for the index of refraction, n_e , in congruent lithium niobate. *Optics Letters*, 22(20):1553–1555, 1997.
- [148] GD Boyd and DA Kleinman. Parametric interaction of focused gaussian light beams. *Journal of Applied Physics*, 39:3597, 1968.
- [149] Wolfgang Demtröder. *Laser spectroscopy*, volume 1. Springer, 2008.
- [150] Aviv Keshet and Wolfgang Ketterle. A distributed, graphical user interface based, computer control system for atomic physics experiments. *Review of Scientific Instruments*, 84(1):015105, 2013.

- [151] Norman F. Ramsey. *Molecular Beams*. International series of monographs in physics. Oxford University Press, 1st edition, 1956.
- [152] Mingwu Lu, Seo Ho Youn, and Benjamin L Lev. Trapping ultracold dysprosium: a highly magnetic gas for dipolar physics. *Physical review letters*, 104(6):063001, 2010.
- [153] Hidetoshi Katori, Tetsuya Ido, Yoshitomo Isoya, and Makoto Kuwata-Gonokami. Magneto-optical trapping and cooling of strontium atoms down to the photon recoil temperature. *Physical Review Letters*, 82(6):1116, 1999.
- [154] Takeshi Kuwamoto, Kazuhito Honda, Yoshiro Takahashi, and Tsutomu Yabuzaki. Magneto-optical trapping of yb atoms using an intercombination transition. *Physical Review A*, 60(2):R745, 1999.
- [155] CG Townsend, NH Edwards, CJ Cooper, KP Zetie, CJ Foot, AM Steane, P Szriftgiser, H Perrin, and J Dalibard. Phase-space density in the magneto-optical trap. *Physical Review A*, 52(2):1423, 1995.
- [156] Thad Walker, David Sesko, and Carl Wieman. Collective behavior of optically trapped neutral atoms. *Physical Review Letters*, 64(4):408, 1990.
- [157] Alan Gallagher and David E Pritchard. Exoergic collisions of cold na-na. *Physical review letters*, 63(9):957, 1989.
- [158] Thomas Maier. *Interactions in a Quantum Gas of Dysprosium Atoms*. PhD thesis, Universit t Stuttgart, 2015.
- [159] Nicola Poli, Robert J Brecha, Giacomo Roati, and Giovanni Modugno. Cooling atoms in an optical trap by selective parametric excitation. *Physical Review A*, 65(2):021401, 2002.
- [160] TL Gustavson, AP Chikkatur, AE Leanhardt, A Görlitz, Subhadeep Gupta, DE Pritchard, and Wolfgang Ketterle. Transport of bose-einstein condensates with optical tweezers. *Physical Review Letters*, 88(2):020401, 2001.
- [161] Julian Léonard, Moonjoo Lee, Andrea Morales, Thomas M Karg, Tilman Esslinger, and Tobias Donner. Optical transport and manipulation of an ultracold atomic cloud using focus-tunable lenses. *New Journal of Physics*, 16(9):093028, 2014.
- [162] Matthias Scholl. Probing an ytterbium bose-einstein condensate using an ultranarrow optical line, 2014.
- [163] E Torrontegui, S Ibáñez, Xi Chen, A Ruschhaupt, D Guéry-Odelin, and JG Muga. Fast atomic transport without vibrational heating. *Physical Review A*, 83(1):013415, 2011.
- [164] Stefan Schmid, Gregor Thalhammer, Klaus Winkler, Florian Lang, and Johannes Hecker Denschlag. Long distance transport of ultracold atoms using a 1d optical lattice. *New Journal of Physics*, 8(8):159, 2006.
- [165] Matthias Wenzel. A dysprosium quantum gas in highly controllable optical traps a dysprosium quantum gas in highly controllable optical traps, 2015.
- [166] Liang Jiang, Takuya Kitagawa, Jason Alicea, AR Akhmerov, David Pekker, Gil Refael, J Ignacio Cirac, Eugene Demler, Mikhail D Lukin, and Peter Zoller. Majorana fermions in equilibrium and in driven cold-atom quantum wires. *Physical review letters*, 106(22):220402, 2011.

-
- [167] Sylvain Nascimbene. Realizing one-dimensional topological superfluids with ultracold atomic gases. *Journal of Physics B: Atomic, Molecular and Optical Physics*, 46(13):134005, 2013.
- [168] Ettore Majorana. Teoria simmetrica dell'elettrone e del positrone. *Nuovo Cimento*, 14:171, 1937.
- [169] Stevan Nadj-Perge, Ilya K Drozdov, Jian Li, Hua Chen, Sangjun Jeon, Jungpil Seo, Allan H MacDonald, B Andrei Bernevig, and Ali Yazdani. Observation of majorana fermions in ferromagnetic atomic chains on a superconductor. *Science*, 346(6209):602–607, 2014.
- [170] Christina V Kraus, Sebastian Diehl, Peter Zoller, and Mikhail A Baranov. Preparing and probing atomic majorana fermions and topological order in optical lattices. *New Journal of Physics*, 14(11):113036, 2012.
- [171] Frank Wilczek. Majorana returns. *Nature Physics*, 5(9):614–618, 2009.
- [172] Jean E Sansonetti, WC Martin, and SL Young. Handbook of basic atomic spectroscopic data. *Carbon*, 100:1634, 2005.
- [173] Seo Ho Youn. Bose-fermi mixtures of ultracold gases of dysprosium. Phd thesis, 2011.

DAVIDE.DREON AT COLLEGE-DE-FRANCE.FR

Paris,

July 2017

Résumé

Dans ce travail de thèse, je présente la construction d'une nouvelle expérience pour la production de gaz ultra froids de dysprosium. En tirant parti de la structure électronique à couche incomplète de ces atomes, nous visons à la réalisation de champs de jauge synthétiques, qui pourront conduire à l'observation de nouvelles phases (topologiques) de la matière. Le couplage du spin atomique avec le champ lumineux, plus efficace que pour des atomes alcalins, permettra d'atteindre des régimes d'interactions fortes qui restent, jusqu'à présent, hors de portée expérimentale. J'adapte des protocoles existants pour la réalisation de champs de jauge dans le cas de Dysprosium, en tenant compte de son grand spin électronique ($J = 8$ dans l'état fondamental).

En outre, le dysprosium a le plus grand moment magnétique parmi les éléments stables, et il est donc le meilleur candidat pour l'étude des gaz dipolaires.

Je détaille le dispositif expérimental que nous avons construit et comment nous effectuons le piégeage et le refroidissement du dysprosium. Nous étudions en détail le comportement du piège magnéto-optique, qui est réalisé sur la transition d'intercombinaison $^1S_0 \leftrightarrow ^3P_1$. La raie étroite et le grand spin rendent l'opération du piège très complexe. Néanmoins, je montre que sa compréhension devient assez simple dans le régime où le nuage se polarise spontanément en conséquence de la combinaison des forces optiques et gravitationnelles.

Enfin, je décris les dernières étapes du transport optique et de l'évaporation, ce qui conduira à la production d'un gaz dégénéré.

Mots Clés

dysprosium, gaz ultra froids, champ de jauge artificiel, gaz dipolaires.

Abstract

In this thesis I present the construction of a new experiment producing ultra cold gases of Dysprosium. Using the favourable electronic structure of open-shell lanthanide atoms, we aim at the realisation of laser-induced synthetic gauge fields, which could lead to the observation of novel (topological) phases of matter. The coupling of the atomic spin with the light field, improved with respect to alkali atoms, opens the possibility to explore strongly interacting regimes that were up to now out of experimental reach. I adapt existing protocols for the implementation of gauge fields to the case of Dysprosium, taking into account its large electronic spin ($J = 8$ in the ground state).

Moreover, Dysprosium has the largest magnetic moment among the stable elements, and is the best candidate for the study of dipolar gases.

I describe the experimental setup that we built and how we perform the trapping and cooling of Dysprosium. We study in detail the behaviour of the magneto-optical trap, which is performed on the $^1S_0 \leftrightarrow ^3P_1$ intercombination line. The narrow linewidth and the large spin make the trap operation quite challenging. Nevertheless, I show that its understanding becomes quite simple in the regime where the cloud spontaneously polarises due to the interplay of optical and gravitational forces.

Finally I describe the last steps of optical transport and evaporation, which will lead to the production of a degenerate gas.

Keywords

Dysprosium, ultracold gases, synthetic gauge field, dipolar gases.